RADIO EMISSION FROM HOT STARS AND PLANETS

BY

SIMON DALEY-YATES

A thesis submitted to
The University of Birmingham
for the degree of
DOCTOR OF PHILOSOPHY

Astrophysics and Space Research Group
School of Physics and Astronomy
College of Engineering and Physical Sciences
University of Birmingham
July 2018

"Perhaps I'm old and tired, but I always think that the chances of finding out what really is going on are so absurdly remote that the only thing to do is to say hang the sense of it and just keep yourself occupied."

– Douglas Adams, *The Hitchhiker's Guide to the Galaxy*

Abstract

The winds of hot massive stars and hot giant planets grant us insight into the mechanisms by which the interstellar medium is enriched and the history behind planetary system formation. This thesis comprises a series of studies investigating the magnetospheric dynamics and emission properties of both of these astronomical bodies.

An analytic study of thermal radio and sub-mm emission from the winds of massive stars investigates the contribution from acceleration and wind clumping. The results show strong variation of the spectral index, corresponding to the wind acceleration region and clumping of the wind. This shows a strong dependence of the emission on the wind velocity and clumping profile.

By performing simulations of a magnetic rotating massive star with a non-zero dipole obliquity, it has been shown that the predicted radio and sub-mm observable light curves and continuum spectra are highly dependent on the magnetic confinement of the stellar wind close to the surface, and that understanding the observer inclination and magnetic dipole obliquity are vital for determining the stellar mass-loss rate from radio observations.

Hot Jupiter exoplanets are expected to produce strong radio emission in the MHz range but such emission has not been detected. To explain the absence of observational results, simulations of the interactions between a solar type star and hot Jupiter were conducted and used to calculate the efficiency of radio emission generation within the planet's magnetosphere. Results show that it is completely inhibited by the planet's expanding atmosphere.

Finally, the first simulations of wind-wind interactions between a solar type star and a short period hot Jupiter exoplanet that resolves accretion onto the surface of the star are presented. The accretion point, rate and periodicity are quantified, with the results indicating that material accreting onto the star perturbs surface density and temperature in a periodic manner, in agreement with observations.

Statement of Originality

I declare that the work I submit in this thesis is my own and has been carried out under the supervision of Dr Ian R. Stevens. Chapters 1, 2, 3 and 8 contain introductory and conclusionary material which is fully referenced. Chapters 4, 5, 6 and 7 reformatted copies of publications and in preparation publications of which I am the first author. All material is original and clearly referenced. Contributions from co-authors are listed below:

- Chapter 4 is a reformatted copy of the paper Daley-Yates et al. (2016): "Sub-mm free-free emission from the winds of massive stars in the age of ALMA" and is my own work, aside from Sections 4.3.4 and 4.3.5 which contain text and calculations form co-authors.

- Chapter 5 is a reformatted copy of the paper Daley-Yates et al. in preparation: "3D MHD simulation of a oblique rotating magnetic massive star and synthetic thermal radio emission" and is my own work.

- Chapter 6 is a reformatted copy of the paper Daley-Yates & Stevens (2018): "Inhibition of the electron cyclotron maser instability in the dense magnetosphere of a hot Jupiter" and is my own work, aside from Section 6.1.4 contains text form the co-author.

- Chapter 7 is a reformatted copy of the paper Daley-Yates & Stevens submitted: "It's raining hot Jupiters: 3D MHD simulations of star-planet wind interaction" and is my own work.

Acknowledgements

Firstly I thank my supervisor, Ian Stevens, without whose knowledge and guidance this thesis would not have be possible. It has been a privilege to both work with and been your student over the past years.

I thank my mother, Sue, for all her words of encouragement and support during my studies. Without you I would not have made it this far.

I also thank my father, Stephen, and his wife, Beverly, for their continued support from the start of my studies to fruition.

Finally, I would like to thank my partner, Ricarda, whose patience, encouragement and morale support, both and academically and otherwise, have kept me sane, and more importantly, in tea and biscuits during the final year of my studies.

Contents

Bibliography

List of Figures

List of Tables

1

Introduction

> *"It's a little experiment that might win me the Nobel Prize." "Which field?" said Leela "I don't care - they all pay the same."*
>
> – Professor Hubert J. Farnsworth (Billy West), *Futurama*

Throughout their lifetimes, stars and planets form closely bound, highly evolving systems driven by a large range of simultaneous physical processes. Magnetic fields are an innate property of stellar and planetary bodies on all length scales, from small surface features to extended winds. The question of what fundamental role magnetic fields play in shaping the environment around stars and planets is central to understanding stellar and planetary formation and evolution, together with properties of large scale structures such as the Interstellar Medium (ISM), star clusters and beyond.

The aim of this thesis is to understand the role magnetic fields play in shaping the environment around stars and planets, together with how stars form connections with the planets and disks they host. This has been accomplished by modelling the winds and environment of main sequence stars, and Jupiter-type exoplanets with an emphasis on how they interact with each other and with the structures which form in their winds.

This thesis is comprised of two main areas of work, falling under the topics of massive star winds and the interactions between the magnetospheres of short period Jupiter-type exoplanets and their host solar-type stars. While the two topics may appear unrelated, both massive stars and giant planets exist at the extrema of their respective class of object. While consideration of this quasi-symmetry of topics does not directly inform our physical understanding of the astrophysical bodies in question, it does help to focus attention on the theme of extrema of stellar and planetary physics.

Massive stars, representing the spectral types O and B, are the largest stellar objects by mass, as their name implies. Giant gaseous planets on the other hand are below the limit of hydrogen burning and are therefore substellar objects. The winds of these two class of bodies are distinctly different due to the fundamental physical processes behind their driving mechanisms. To respect this distinction, discussion is divided between chapters according to topic, while theory, which is general to both, is presented in a manner independent from the physical situation.

This introductory chapter presents the above topics in the broadest scene and describes the thesis structure as a whole. Chapter 2 covers the physics of winds from stars, both massive and solar type, together with the planetary winds from the atmospheres of short period Jupiter type planets. The paradigm used for studying these systems is the equations of Magnetohydrodynamics (MHD) and specifically the numerical solution of these equations via the finite volume method of Godunov (Godunov, 1959), which is described and discussed in Chapter 3. Chapters 4, 5, 6 and 7 form the main body of the thesis and the result of the work and are briefly introduced in the remaining sections of this chapter. As the topics of these chapters are not directly related, each is presented in a self-contained manner with an introduction, detailed review of the theory used, results and conclusions. Finally, I conclude the thesis as a whole in Chapter 8 and summarise the work and findings I have presented together with extensions to the work in possible future studies.

1.1 Introduction to massive stars

Early type massive stars comprise approximately 0.1% of all main-sequence stars (Walder et al., 2012). This apparent lack of abundance when compared to lower mass stars is more than compensated for by their contribution to the interstellar medium. Heavier elements such as O, C and Fe are produced in the intense fusion reactions which take place within the interiors of these stars.

The study of how stars disseminate their material into the ISM, the rate and structure of winds which carry away this material from the stellar surface, is vital for understanding the composition of the ISM, metallicity of star-forming regions and the formation of protoplanetary disks and planets which eventually form around more common, lower mass stars are also dependent upon this mechanism. The impact of these large stars upon the galaxy in which they reside can be seen most vividly in the violent cataclysmic events which spread the elements they produce into interstellar space and provide the largest contribution of kinetic energy input into the galaxy, supernova (Leitherer et al., 1992; Lozinskaya, 1997). However, it is during their time on the main sequence that they provide important feedback on the interstellar medium (Fall et al., 2010) in the form of intense radiation at all wavelengths (De Becker, 2007) and strong dense winds leading to the development of shocks in nebulae (Elmegreen & Elmegreen, 1978). This feedback can provide the necessary conditions for star formation in such nebulae and play an important role in the formation of the galaxy as a whole, in which they reside (Ceverino & Klypin, 2009).

The Hertzsprung Russell (HR) diagram, shown in Fig. 1.1, illustrates the range of parameters possible for all stellar spectral types, with masses and luminosities from 0.1 $M_\odot$ and 10^{-3} $L_\odot$ in the case of dwarf stars through to Supergiant O stars with masses and luminosities upwards of 60 $M_\odot$ and 10^6 $L_\odot$ respectively.

Amongst this range, a division occurs at a mass roughly between 1.2 - 1.4 $M_\odot$, where more massive stars have radiative outer envelopes while lower mass stars have convective outer envelopes. However, it is not until a stars mass is ≥ 5 $M_\odot$, corresponding to a late B-type or early A-type star, that the star's wind can be said to be driven primarily by absorption in spectral lines and are therefore known as line driven winds (Lamers & Cassinelli, 1999). As this thesis is considering stellar winds and not internal structure, I will only consider stars with masses ≥ 5 $M_\odot$, as massive.

These winds are distinct from thermal or wave driven winds in that the acceleration of the wind, due to absorption of spectral lines, is a non-linear function of both the local

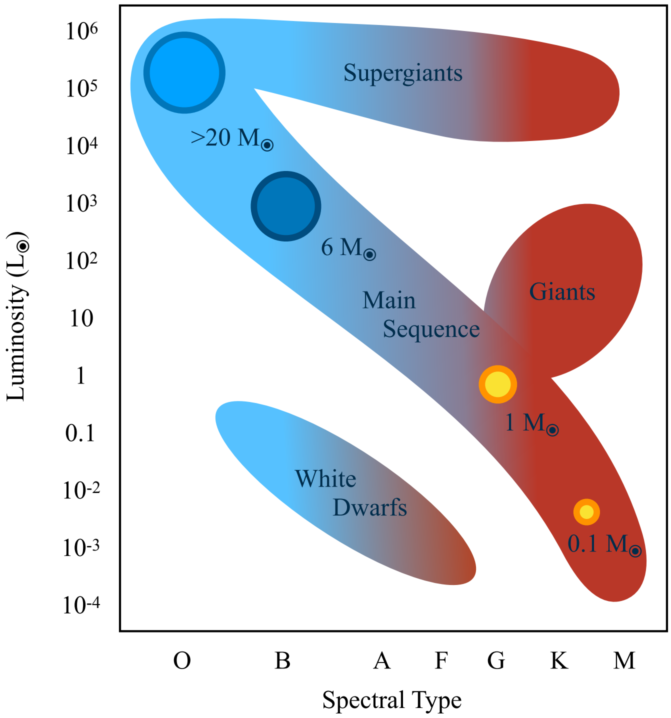

Figure 1.1: HR diagram illustrating the relationship between spectral type, mass and luminosity for main sequence, giants, supergiants and white dwarfs. The position of low, solar and high mass stars are indicated along with the approximate transition between solar and high mass stars occurring at 6 $M_\odot$.

density and velocity gradient within the wind (Castor et al., 1975). As a result, the wind structure is highly unstable and dynamic in nature (Runacres & Owocki, 2002). These effects make the analysis of the wind structure challenging and their theoretical treatment is an ongoing area of research. Observations of massive star winds is a principle avenue for diagnosing stellar properties and observations are conducted at many wavelengths. Both thermal and non-thermal radiation is detectable from these stellar winds, but thermal free-free emission provides a large spectral window for characterising the wind properties and has historically be used to determine the stellar mass-loss rate (Wright & Barlow, 1975; De Becker, 2007). These observations have largely been conducted at frequencies < 100 GHz due to the limitations of telescope technology. However, this situation is likely to change as new instruments and observatories capable of observing massive stars above 100 GHz come online. Observing massive stars at these frequencies results in a greater resolving power and penetration of the stars' extended wind, as such observations become susceptible to changes in the wind structure which impact mass-loss rate estimation, and additional physics such as wind acceleration and magnetic fields must be incorporated to accurately interpret observational results.

In Chapter 4, I address the issue of correctly estimating massive star mass-loss rates when observed at radio and sub-mm frequencies. With the advent of the Atacama Large Millimeter Array (ALMA), the high frequency radio and sub-mm spectrum is available for observing such stars. These high frequency observations probe wind regions close to the stellar surface where the wind accelerates. If this wind acceleration is not accounted for, mass-loss rates will be miscalculated by as much as a factor of 5. This has direct repercussions for any area of astrophysics which relies on accurate mass-loss rates of O-stars, such as X-ray binaries, stellar population synthesis and stellar mass black hole formation. To address this, I developed a quasi-analytic method for calculating this radio/sub-mm emission emitted from the accelerating winds for a range of O-star parameters and thus show the deviation in mass-loss rate between accelerating and non-accelerating wind models.

Approximately 10% of massive stars have detectable magnetic fields ($>$ 100 G) (Wade et al., 2016) which are global, large scale and dynamically significant (Petit et al., 2013). Despite observing eighteen known magnetic O- and B-type stars, a recent JVLA survey, conducted as part of the Magnetism in Massive Stars (MiMeS) project by Kurapati et al. (2016), only reported a detection rate of 20% in cm radio wavelengths from a sample of known magnetic massive stars. Free-free absorption by material in the extended wind of the stars has been suggested as an explanation. In Chapter 5, I investigate this conclusion and demonstrated that magnetic confinement of the stellar wind leads to a departure of spherical and cylindrical symmetry, resulting in a reduction of the continuum radio/sub-mm flux, together with a rotation and observer inclination dependence of the radio light curves. These factors directly impact the estimation of mass-loss rates of massive stars and must be accounted for when interpreting observational results.

1.2 Introduction to hot Jupiter exoplanets

Giant gaseous exoplanets comprise the most commonly detected type of planetary body. As their mass and radii are close to those of their host stars, they are susceptible to detection via both the transit and radial velocity measurement methods (Wright & Gaudi, 2012). Indeed the first detected exoplanet orbiting a non-degenerate star, 51 Peg b, falls into this class of planet (Mayor & Queloz, 1995). They are observed orbiting cool stars in the mass range between 0.0156 $M_\odot$ (Albrow et al., 2018) and 4.5 $M_\odot$ (Nordström et al., 2004), however such extremes of host masses are outliers and the majority of exoplanets are found orbiting stars with masses comparable to the Sun[1].

After initial formation and migration, giant planets are found in close orbits ($<$ 10 days) where the intense radiation of the host is absorbed by the planet's upper atmosphere. This energy input, predominately in the form of Ultraviolet (UV) radiation, promotes the transition from a hydrostatic to a hydrodynamic atmosphere and the planet begins to loss substantial mass through the establishment of a planetary wind. This later stage of evolution is known as the hot Jupiter (HJ) phase where, as the name suggest, the planet's temperature can exceed several 10^3 K.

As hot Jupiters (HJs) are found in close orbit with their hosts, where stellar feedback inhibits planet formation (Murray-Clay et al., 2009), they must undergo migration to their observed orbital radii. The implications of this constraint on formation distance is that over the course of a HJ's evolution and migration to the inner stellar system, it will impact the development of all other disks and planets which it encounters (Fogg & Nelson, 2005); leaving its mark on the entire system. Eventually, the HJ will form close interactions with the host star both through the establishment of the planetary wind and via magnetic phenomena such as reconnection and Alfvénic perturbation (Strugarek et al., 2015b). As such, understanding the observable signatures of this late stage of their evolution is vital for developing our understanding of planetary system dynamics from

---

[1] I refer the interested reader to the exoplanet database at `http://www.exoplanet.eu` for data on the mass distribution of exoplanet hosts.

the early protoplanetary disk stage through to the HJ dominated stage.

Observations of HJ hosting systems have been conducted at multiple wavelengths for numerous purposes, including initial detection and direct planet imaging in order to characterise the properties of both the host star and the HJ itself. As the planet appears dim compared to its host, direct detection remains a challenge. However, theoretical work predicts that HJs will be brighter than their hosts at MHz frequencies due to interactions between free electrons and the magnetosphere of the HJ (Zarka, 1998; Stevens, 2005; Zarka, 2007). However, to date there have been no confirmed observations of radio emission from hot Jupiter exoplanets. These systems are expected to be strong non-thermal radio emitters, via the Electron Cyclotron Maser Instability (ECMI) (Stevens, 2005; Zarka, 2007). In Chapter 6, I provide an explanation for this lack of observational results by conducting magnetohydrodynamic simulations of a magnetised HJ exoplanet orbiting a G-type star identical to the sun. HJs undergo mass-loss induced by photo-evaporation. I demonstrate how the planetary mass-loss increases the plasma density and therefore the plasma frequency in the planets magnetosphere, inhibiting the production of radio emission via the ECMI, thus providing a compelling explanation for the lack of observations.

In addition to direct observation of HJs, enhanced chromospheric activity in the form of increased emission in metal spectral lines. has been proposed as an observational signature of star-planet interaction for a number of stars hosting HJs, including HD 179949 and HD 189733 (Shkolnik et al., 2008; Pillitteri et al., 2015). Star-planet interaction via mass transfer, from planet to star, is thought to be responsible for this enhancement. In Chapter 7, I investigate this hypothesis by tracking the dynamic behaviour of evaporating planetary material in a HJ hosting system, via MHD simulations. Channelled by both the stellar and planetary magnetic fields, significant planetary material is accreted onto the stellar surface. This leads to the development of a spot on the stellar surface, which possesses a periodic accretion rate together with density and temperature perturbations.

2

Stellar and planetary winds

> *"Science has achieved some wonderful things of course, but I'd far rather be happy than right any day." "And are you?" "No. That's where it all falls down of course."*
>
> – Douglas Adams, *The Hitchhiker's Guide to the Galaxy*

Stars from all corners of the Hertzsprung Russell (HR) diagram loss mass through winds. These winds form a continuous flow of material from the stellar surface out past disks, planets and the constituents which form a star system, and finally terminate at the surrounding Interstellar Medium (ISM) in a bow shock. Over the course of a star's life, a wind can remove up to 50% of its mass (Lamers & Cassinelli, 1999), impacting the evolution of both the star, its system and the surrounding ISM. A physical understanding of these winds provides us with both a mechanism to understand observations and a window onto phenomena including subsurface structure and spin down through angular momentum loss (Weber & Davis, 1967).

This Chapter introduces the concept of stellar winds, distinguishes between the types of winds according to the physical driving mechanisms and presents their theoretical basis. I begin with the radiation driven winds of massive stars and follow with the thermal winds of solar type stars and hot Jupiter (HJ) planets and finally give a short overview of the wind types not directly used or modelled in this thesis.

2.1 Line driven winds

The winds of massive stars are driven by the intense radiation escaping form the photosphere. These winds are therefore governed by the physics of radiation transport, which require an understanding of the concepts of opacity and emissivity. For these reasons, a full description of line driven winds first necessitates introducing the equation of radiation transfer, the concept of optical depth and the approximation of Sobolev (1960).

2.1.1 Radiation transfer and optical depth

To determine the intensity of radiation along a given path, the equation of radiative transfer incorporates the collective effects of both the emission and absorption properties of the medium along a path, S, which the photons are travelling (Rybicki & Lightman, 1985). In its simplest form this equation is:

$$\frac{\mathrm{d}I_\nu}{\mathrm{d}S} = -\kappa_\nu \rho(S) I_\nu + j_\nu. \tag{2.1}$$

I_ν is the intensity of radiation at frequency ν, $\mathrm{d}S$ is an infinitesimal distance along path S and the coefficients κ_ν and j_ν are the absorption and emission coefficient at frequency ν respectively. Finally $\rho(S)$ is the density along S. Equation (2.1) can be simplified by replacing the infinitesimal path length $\mathrm{d}S$ with another variable known as the optical depth, and specifically the infinitesimal optical depth, $\mathrm{d}\tau_\nu$, defined as:

$$\mathrm{d}\tau_\nu = \kappa_\nu(S)\rho(S)\mathrm{d}S. \tag{2.2}$$

Integrating equation (2.2) between the site of emission S_0 and the total path length S yields:

$$\tau_\nu(S) = \int_{S_0}^{S} \kappa_\nu(S')\rho(S')\mathrm{d}S'. \tag{2.3}$$

The frequency specific optical depth, τ_ν, of a volume of gas, can be thought of as the extent to which radiation is blocked by the material from the site of emission. Substitution of equation (2.3) into equation (2.1) results in:

$$\frac{\mathrm{d}I_\nu}{\mathrm{d}\tau_\nu} = -I_\nu + J_\nu, \tag{2.4}$$

where $J_\nu \equiv j_\nu/(\kappa_\nu \rho(S))$, is the source function (Rybicki & Lightman, 1985). J_ν represents how the intensity of radiation is influenced by the medium through which it propagates. For the case of free-free emission it is assumed to equal zero. The equations and discussion above are general to the propagation of radiation through a medium. I will now relate this to the environments of stellar atmospheres.

A photon leaving the photosphere of a star can be absorbed by a line transition of an element in the atmosphere. The width of the line transition is described by the profile function; incorporating turbulent and thermal motions in the wind, this equation has the following Gaussian form:

$$\phi(\Delta\nu) = \frac{1}{\sqrt{\pi}\Delta\nu_{\mathrm{G}}} \exp\left(-\left(\frac{\Delta\nu}{\Delta\nu_{\mathrm{G}}}\right)^2\right) \tag{2.5}$$

where $\Delta\nu = \nu - \nu_0$, with ν_0 being the frequency at which the ion can emit and absorb the photon in the ion's rest frame. The Gaussian width

$$\Delta\nu_{\mathrm{G}} = \frac{\nu_0}{c}\sqrt{\frac{2}{3}\left(\langle v_{\mathrm{th}}^2\rangle + \langle v_{\mathrm{turb}}^2\rangle\right)}. \tag{2.6}$$

Here, c is the speed of light, $\langle v_{\mathrm{th}}^2\rangle = 3k_{\mathrm{B}}T/m_{\mathrm{i}}$ the average thermal motion with T the temperature, k_{B} the Boltzmann constant, m_{i} the ion mass and $\langle v_{\mathrm{turb}}^2\rangle$ is the average turbulent motion. If the wind is expanding monotonically with velocity $v(r)$, the absorption coefficient of the wind is Doppler shifted (Castor, 1974; Castor et al., 1975). If an ion exists along the path of the photon in such a manner that the Doppler shift brings the line transition of the ion into the region of the photon frequency,

$$\nu_0 - 1.5\Delta\nu_{\mathrm{G}} \leq \nu_p\,(1 - v/c) \leq \nu_0 + 1.5\Delta\nu_{\mathrm{G}}, \tag{2.7}$$

where ν_p is the photon frequency, then the photon can interact with the ion and be absorbed. The physical space over which this occurs is known as the interaction region (Lamers & Cassinelli, 1999). The factor $1.5\Delta\nu_{\mathrm{G}}$ in equation (2.7) ensures that $\sim 90\%$ of the Gaussian profile is encompassed.

The solution to equation (2.1) involves the integration of density over the interaction region. The width of the interaction region is also dependent upon the width of the profile function (equation (2.5)) and the velocity gradient in the wind. These factors make calculating the solution to the equation of radiative transfer a cumbersome procedure. However, a thin profile function or a steep velocity gradient will necessarily lead to a narrow interaction region, a property that allows an important simplification to be made.

The Sobolev approximation (Sobolev, 1960) greatly simplifies the above treatment, by talking the width of the profile function to the limit of a delta function. This simplification has the benefit that only local quantities, at the point where the absorption takes place, need to be taken into account when calculating the equation of radiation transfer (equation (2.1)) in stellar atmospheres. In the path of the photon, the region in which absorption can occur is now a point known as the Sobolev point. The following theory makes use of this approximation in deriving both the acceleration and equation of motion for line driven winds.

2.1.2 CAK theory

The theory of line driven winds was first laid out by Castor et al. (1975, hereafter CAK75) building on the work of Sobolev (1960). Below is a review of this theory, illustrating the key concepts and equations relevant to the later chapters and specifically to the results in Chapter 5, in which the the theory is directly applied in simulations.

This section is not a complete explanation of line driven winds but covers the important theory necessary for understanding the acceleration experienced by wind material due to this physical mechanism. Despite this, the theoretical treatment below is sufficient to capture the key physics without the need for exhaustive digressions. Furthermore, the theory of line driven winds has been built on and developed over numerous decades, with the inclusion of stellar oblateness and gravity darkening (Cranmer & Owocki, 1995) and extended to incorporate non-radial components by Gayley & Owocki (2000). However, these additional properties are not used in producing the simulation result of Chapter 5 and therefore their treatment is not within the scope of this work.

The optical depth, given by equation (2.2), applies to the case of a static atmosphere. Sobolev's approximation allows for this expression to be written in a form which applies to an expanding atmosphere (CAK75). Therefore, following on from equation (2.2) and replacing the absorption coefficient, κ_ν, with the line absorption coefficient κ_l it can be shown that, for a photon of frequency ν along line S, the optical depth in the radial direction becomes:

$$\tau_\nu(r_S) = (\kappa_l \rho)_{r_S} v_{\mathrm{th}} \left(\frac{\mathrm{d}v}{\mathrm{d}r}\right)^{-1} . \tag{2.8}$$

The subscript r_s is the radial distance to the Sobolev point, indicating that the quantities ρ and κ_l are evaluated here. $v_{\mathrm{th}} = \sqrt{2k_{\mathrm{B}}T_{\mathrm{eff}}/m_i}$ is the thermal velocity of the ions in the atmosphere, with T_{eff} the effective temperature of the wind (which is assumed to be that of the star, within the isothermal approximation) (CAK75).

CAK75 began their treatment of line driven winds by redefining (2.8) to reflect the optical depth in terms of electron scattering. This is arrived at by replacing the line absorption coefficient, κ_l, with the electron scattering opacity, κ_{e} and is given by:

$$t = \kappa_{\mathrm{e}} v_{\mathrm{th}} \rho \left(\frac{\mathrm{d}r}{\mathrm{d}v}\right) , \tag{2.9}$$

where it is assumed that the evaluation is performed at the Sobolev point and correspondingly, the subscript used in equation (2.8) is dropped and the symbol τ is replaced with t to reflect the change. This treatment also brings the notation closer in line with that used by CAK75. The radiative force per unit mass exerted on the wind due to an ensemble of emission lines can now be written as a function of this optical depth:

$$f_{rad} = \frac{\kappa_{\mathrm{e}} F}{c} M(t), \tag{2.10}$$

where F is the total flux contained within the lines. $M(t)$ is known as the force multiplier. It represents the collective effect of multiple lines on the expanding atmosphere and is results the expression:

$$M(t) = kt^{-\alpha}, \tag{2.11}$$

in which the constants k and α are dimensionless parameters which describe the fit of the force multilayer $M(t)$, plotted as a function of t for an ensemble of lines for a range of temperatures.

Together equations (2.10 and 2.11) provide an expression for the force per unit mass on a packet of wind material due to an ensemble of absorption lines.

The constant $\kappa_{\mathrm{e}} F/c$ in equation (2.10) is the electron scattering force per unit mass, which we can write as

$$g_e = \frac{\kappa_{\mathrm{e}} F}{c} = \frac{\kappa_{\mathrm{e}} L_*}{4\pi r^2 c}. \tag{2.12}$$

This allows us to rewrite equation 2.10 as

$$f_{rad} = g_e M(t), \tag{2.13}$$

In equation (2.12), the flux F has been replaced by the luminosity of the star divided by the surface area of a sphere bounding the volume within the radius r, which follows from a consideration of flux conservation.

So far, we have covered the concepts of radiative transfer in an expanding atmosphere, which has enabled us to formulate an expression for the optical depth (equation (2.8)) under the Sobolev approximation for such an atmosphere. This in turn has lead to the expression for wind acceleration of material under the action of an ensemble of absorption lines (equation (2.13)). The remainder of this section will use these expressions, together with results from gas dynamics, to form an equation of motion for a wind from a star that is assumed to be acting as a point source of radiation.

This equation of motion takes the generic form according to Lamers & Cassinelli (1999) of:

$$v\frac{\mathrm{d}v}{\mathrm{d}r} = -\frac{GM_*}{r^2} + \frac{1}{\rho}\frac{\mathrm{d}p}{\mathrm{d}r} + g_\mathrm{e} + g_l. \tag{2.14}$$

where G is the gravitational constant, M_* the stellar mass, v the velocity of the wind, p the wind pressure, r the radial distance from the star and both g_e and g_l are defined above by equations (2.10 and 2.11). The first term on the right hand side of equation (2.14) is the acceleration due gravity. This term, together with g_e, is combined to give an effective gravitational acceleration, $GM_*(1-\Gamma_\mathrm{Edd})/r^2$, in which Γ_Edd is the Eddington factor which accounts for the reduction in the effective gravity due to the stellar continuum radiation pressure acting on the wind. The Eddington factor is a function of the stellar luminosity and has a value in the range $0 < \Gamma_\mathrm{Edd} < 1$, where $\Gamma_\mathrm{Edd} = 1$ represents a star whose surface gravity equals the outward radiation pressure and begins to blow off its outer layers. Such a scenario represents a star moving off the main sequence and not the behaviour of the stellar types investigated in this thesis.

The second term in equation (2.14) is the acceleration due to pressure gradients, which stems directly from considerations of fluid dynamic behaviour and is a general result for a gas undergoing momentum change (Liepmann & Roshko, 2002). The pressure is related to the gas density through the following equation of state:

$$p = \rho c_\mathrm{s}^2. \tag{2.15}$$

Where c_s^2 is the square of the isothermal sound speed and has the form $c_\mathrm{s}^2 = k_\mathrm{B}T/m_\mathrm{i}$. Under this isothermal approximation, the ratio of specific heats, otherwise known as the polytropic index, is equal to unity. The validity of this assumption relies on the star acting as the dominant input of energy into the wind and that no significant mechanisms for cooling of the wind takes place. However, in the case of magnetically channelled winds (and indeed rotationally confined disks (Owocki et al., 1994)) substantial shocks can develop in the equatorial regions where outflowing material from different parts of the stellar surface meet in a shock and hence both heating and cooling can occur (Ud-Doula et al., 2008, 2013). However, adiabatic treatments which account for cooling, require a formalism for the contribution to thermal energy from stellar radiation. In short, the isothermal approximation has the benefit of ensuring the effect of stellar radiation is incorporated into the energy balance in the wind, without the need to explicitly account for it. In Chapter 5, the full implications of this isothermal assumption will be detailed.

Together, the final two terms in equation (2.14) give the collective acceleration due to both electron continuum and line scattering. g_l provides the largest contribution to the net acceleration of the wind at all radii and is several orders of magnitude greater than g_{e}.

A more complete definition of the line acceleration is provided by combining equations (2.11, 2.13 and 2.12), leading to:

$$g_l = \frac{\kappa_{\mathrm{e}} L_*}{4\pi r^2 c} M(t) = \frac{\kappa_{\mathrm{e}} L_*}{4\pi r^2 c} k t^{-\alpha}. \tag{2.16}$$

Substituting t with equation (2.9) gives:

$$g_l = \frac{\kappa_{\mathrm{e}} L_*}{4\pi r^2 c} k \left(\kappa_{\mathrm{e}} v_{\mathrm{th}} \rho \frac{\mathrm{d}r}{\mathrm{d}v} \right)^{-\alpha}. \tag{2.17}$$

Rearrangement of the above equation yields:

$$g_l = \frac{\kappa_{\mathrm{e}} L_*}{4\pi r^2 c} k \left(\frac{\mathrm{d}v/\mathrm{d}r}{\kappa_{\mathrm{e}} v_{\mathrm{th}} \rho} \right)^{\alpha}. \tag{2.18}$$

Expression (2.18) still contains v_{th} and k, parameters which are not necessarily trivial to determine. Gayley (1995) formulated a notation in which these parameters can be expressed through what is called a total flux- and population-weighted "Q-value" that was first formulated to characterise the relative strength of the force due to the sum over all emission lines on a bound electron compared to the force on a free electron. This parameter is useful for our analysis as it incorporates both $v_{\rm th}$ and k in the following way:

$$k = \frac{1}{1-\alpha}\left(\frac{v_{\rm th}}{c}\right)^{\alpha}\frac{\overline{Q}}{\overline{Q}^{\alpha}}. \tag{2.19}$$

Substitution of equation (2.19) into equation (2.18) results in:

$$g_l = \frac{1}{1-\alpha}\frac{\kappa_{\rm e}L_*\overline{Q}}{4\pi r^2 c}\left(\frac{{\rm d}v/{\rm d}r}{\rho c\overline{Q}\kappa_{\rm e}}\right)^{\alpha}, \tag{2.20}$$

providing an expression whose terms are all stellar properties which can be derived from observation, with the exception of the radial velocity gradient and $\overline{Q}$. Gayley (1995) computes Q-values for a range of stars and determines that $\overline{Q} \sim 10^3$ across a wide range of stellar conditions.

Equation (2.20) represents the force per unit mass that an ensemble of emission lines exerts on material within the stellar atmosphere. However, as previously mentioned, the star is assumed to be acting as a point source of radiation. This approximation is valid at large radii, where the stellar diameter is small in comparison to the radial distance. Within the proximity of the star, this condition is no longer valid and the star presents itself as a finite disk. To correct for this, CAK75 developed a finite disk correction factor, $f_{\rm D}$, through the definition of a modified force multiplication factor as follows:

$$M(t)' \equiv M(t)f_{\rm D}, \tag{2.21}$$

The derivation of $f_{\rm D}$ is a lengthy exercise and will not be covered here. $f_{\rm D}$ has an analytic form for the simple case of a non-rotating, uniformly illuminated disk and according to CAK75 is given by:

$$f_{\rm D} = \frac{(1+\sigma)^{\alpha+1} - (1+\sigma\mu_*^2)^{\alpha+1}}{(1-\mu_*^2)(\alpha+1)\sigma(1+\sigma)^{\alpha}}. \tag{2.22}$$

In the above expression $\sigma = ((r/v){\rm d}v/{\rm d}r) - 1$ and $\mu_*^2 = 1 - (R_*/r)^2$. Rotation, gravity darkening and limb darkening (which reflects the tendency for photons to leave the photo-

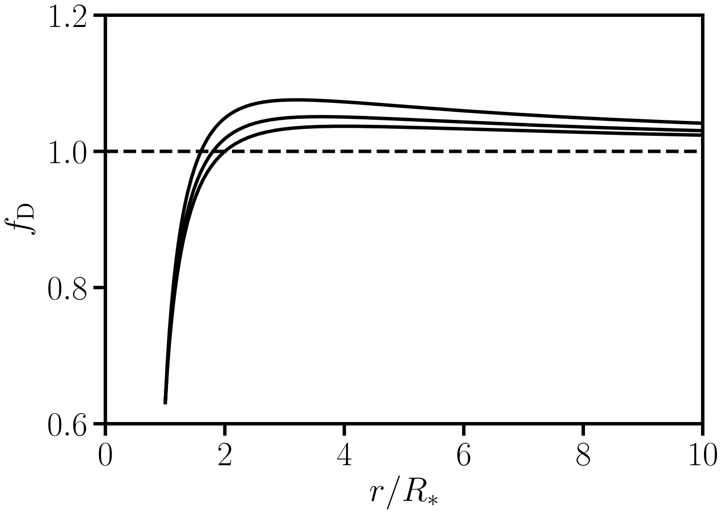

Figure 2.1: Finite disk correction factor for different velocity laws of increasing steepness. This steepness is described by equation (2.25) and varies from the lowest curve corresponding to $\beta = 1.0$, the middle $\beta = 0.8$ and top $\beta = 0.6$. Each separate curve originates at $f_{\mathrm{D}} = 1/(1+\alpha)$, where the force multiplier $\alpha = 0.6$ and all are asymptotic to $f_{\mathrm{D}} = 1$ at $r = \infty$.

sphere in a direction normal to the stellar surface) have been incorporated into versions of f_{D} (Cranmer & Owocki, 1995). However, equation (2.22) will be sufficient for the current discussion, as it captures the important property of the non-finite stellar disk.

A non-trivial function of radius, equation (2.22) never deviates from approximately unity over much of the possible range of values r can take. At the base of the stellar wind $f_{\mathrm{D}} = 1/(1+\alpha)$ and as $r \rightarrow \infty$, $f_{\mathrm{D}} \rightarrow 1$, recovering the condition for a point like star. The functional form of f_{D} is illustrated in Fig. 2.1 for a sample of velocity law parameters (see equation 2.25 below).

By noting that $g_l = g_{\mathrm{e}} M(t)$ and $M(t)' \equiv M(t) f_{\mathrm{D}}$ a finite disk corrected line acceleration, $g_l' = g_{\mathrm{e}} M(t)' = g_{\mathrm{e}} M(t) f_{\mathrm{D}}$, can be written as:

$$g_l = \frac{f_{\mathrm{D}}}{(1-\alpha)} \frac{\kappa_{\mathrm{e}} L_* \overline{Q}}{4\pi r^2 c} \left(\frac{\mathrm{d}\boldsymbol{v}/\mathrm{d}r}{\rho c \overline{Q} \kappa_{\mathrm{e}}} \right)^{\alpha}, \tag{2.23}$$

where the prime symbol has been dropped as this is the final form g_l will take. A distinctive property of g_l is that it is proportional to $(\mathrm{d}v/\mathrm{d}r)^{\alpha}$. Since typically $\alpha \sim 0.6$, there is a non-linear dependence of g_l on the velocity gradient. This implies that the winds of massive stars are highly unstable. The net effect of this is that a slight change in the velocity gradient at small radii is amplified as the wind flows out from the star and leads to the development of shocks at larger radii. This property has been investigated by Runacres & Owocki (2002), who found that these shocks lead to large temperature fluctuations in the wind, further calling into question the validity of the isothermal approximation for line driven winds.

The combination of equations (2.14 and 2.23) and incorporation of the reduction in effective gravity due to continuum scattering, provides the final form of the momentum equation for a steady state massive star wind with monotonically increasing velocity:

$$v\frac{\mathrm{d}v}{\mathrm{d}r} = -\frac{GM_*(1-\Gamma_\mathrm{e})}{r^2} + \frac{1}{\rho}\frac{\mathrm{d}p}{\mathrm{d}r} + \frac{f_\mathrm{D}}{(1-\alpha)}\frac{\kappa_e L_* \overline{Q}}{4\pi r^2 c}\left(\frac{\mathrm{d}\boldsymbol{v}/\mathrm{d}r}{\rho c \overline{Q}\kappa_\mathrm{e}}\right)^\alpha . \tag{2.24}$$

When solving equation (2.24) for the velocity of the wind, there are many mathematically allowed solutions. However the only physically valid solution is found when the velocity close to the star meets the velocity at large distances ($r > 10\ R_*$) in a smooth manner. This physical solution constrained by the condition that it should pass through a point known as the critical point (CAK75). This condition implies that, for a given set of stellar parameters, there is only one valid velocity profile, which is given by the simplified version of the result of equation (2.24) as follows:

$$v = v_\infty \left(1 - \frac{R_*}{r}\right)^\beta , \tag{2.25}$$

where v_∞ is the terminal velocity of the wind once it has reached an infinity large radial distance. The exponent β is a parameter which describes the steepness of the velocity profile. Small values of β correspond to steep velocity profiles and vice versa (Daley-Yates et al., 2016). Massive stars typically have β values which lie within the range $0.5 < \beta < 1.0$. The line acceleration, velocity profile and velocity gradient are plotted in Fig. 2.2 for $\beta = 0.8$ and $\alpha = 0.6$. The majority of the winds acceleration occurs within the range $1R_* < r < 3R_*$ and the line acceleration, g_l, peaks within the region

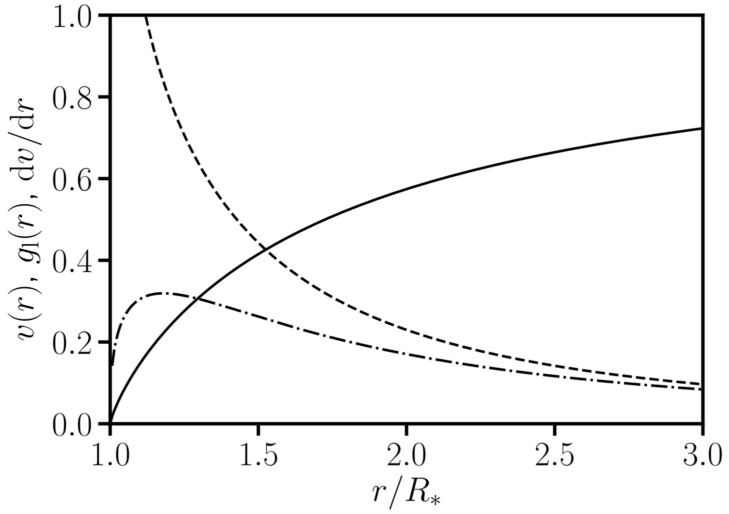

Figure 2.2: Normalised velocity (solid line), velocity gradient (dashed line) and line acceleration (dot-dashed) profiles as a function of radius for a massive star. Note that the wind has reached a substantial fraction of the terminal velocity within $1R_* < r < 3R_*$. The line acceleration g_l reasonable for the wind reaching the terminal velocity occurs in region $1R_* < r < 1.5R_*$, within the immediate vicinity of the star.

$1R_* < r < 1.5R_*$.

Equation (2.24) is in a static, time independent form. If time dependence is introduced then it takes the form of a momentum equation of a similar nature to the momentum equation contained within the set of equations which govern the dynamic motion of a fluid, otherwise known as the Hydrodynamics (HD) equations. These equations together with their extension to Magnetohydrodynamics (MHD) are presented in detail in Chapter 3. This is an important result as it allows the application of the above theory to the field of HD and provides a means to diagnose the dynamics of line driven winds.

Equation (2.23) represents the expression used in generating the results presented in Chapter 5. In the next section I will turn to the subject of thermally driven winds such as that of the Sun and other planet hosting stars.

2.2 Thermally driven winds

The winds of cool stars ($T_{\rm eff} < 6500$ K) are driven by thermal expansion, a consequence of the higher temperatures found in their corona ($T > 10^6$ K) (Lamers & Cassinelli, 1999). The exact heating mechanism responsible for such high temperatures is one of the great unsolved challenges of solar and stellar physics and astrophysics in general. Several mechanism have been put forward as an explanation, including heating by Alfvén waves, micro turbulence and magnetic reconnection (see Aschwanden et al. (2001) for a review of this topic).

The solution of this historical problem is not the topic of this section however and unlike my discussion of line driven winds above, in which the driving mechanism is define from first principles, here I shall take the coronal temperature as given. I will use as a starting point the concept of a thermodynamically expanding gas, deriving the equation of motion and the resulting velocity profile without knowledge of the underlying physical process responsible for the heating.

The theory below was first developed by Parker (1958) and was later built upon and adapted for magnetised winds by Weber & Davis (1967). This modification will not be covered here, as the wind model is chosen to provide an initial condition to a simulation in which the wind will self consistently adapt to the presence of the stellar magnetic field. Therefore, an isothermal wind model with a stationary velocity profile and a hydrostatically stratified density profile will suffice. The simulations for which the theory below will be applied are presented in Chapters 6 and 7.

I shall begin with the principles of mass conservation,

$$\frac{\partial \rho}{\partial t} + \nabla \cdot (\rho \boldsymbol{v}) = 0 \tag{2.26}$$

and momentum conservation,

$$\rho \frac{\partial \boldsymbol{v}}{\partial t} + \rho \left(\boldsymbol{v} \cdot \nabla\right) \boldsymbol{v} = -\nabla p + \rho g, \tag{2.27}$$

in which the symbols have the same meanings as in the previous section. However I will reiterate them here for clarity: v is the velocity, ρ the density, p the pressure and g the acceleration due to gravity. I will now make several assumptions that will allow equations (2.26 and 2.27) to be simplified. By assuming an isothermal expansion and working under a steady state situation, the time derivatives vanish and mass conservation becomes a momentum density divergence,

$$\nabla \cdot (\rho \boldsymbol{v}) = 0. \tag{2.28}$$

Momentum conservation then reduces to the following:

$$\rho \left(\boldsymbol{v} \cdot \nabla\right) \boldsymbol{v} = -\nabla p + \rho g. \tag{2.29}$$

At this point it is useful to cast the equations (2.28) and (2.29) into a spherical polar formalism. This is done by expressing the derivative operator, ∇, in spherical coordinates,

$$\nabla \cdot \boldsymbol{A} = \frac{1}{r^2}\frac{\partial}{\partial r}\left(r^2 A_r\right) + \frac{1}{r\sin(\theta)}\frac{\partial}{\partial \theta}\left(A_\theta \sin(\theta)\right) + \frac{1}{r\sin(\theta)}\frac{\partial}{\partial \phi}A_\phi, \tag{2.30}$$

where A_r, A_θ and A_ϕ represent the three spatial components of the vector field $\boldsymbol{A}$. Observing that we are only interested in radial quantities as our wind has no θ or ϕ dependence allows us to use only the first term of equation (2.30) and apply it to the mass continuity equation (2.28) such that:

$$\frac{1}{r^2}\frac{\mathrm{d}}{\mathrm{d}r}\left(r^2 \rho v_r\right) = 0. \tag{2.31}$$

From this it naturally follows that $r^2 \rho v_r =$ constant, where we have dropped the vector notation for the velocity as we are concerned with its radial component only. Combining these assumption and applying them to the momentum equation (2.29), we obtain:

$$\rho v_r \frac{\mathrm{d}v_r}{\mathrm{d}r} = -\frac{\mathrm{d}p}{\mathrm{d}r} - \frac{GM_*}{r^2}\rho, \tag{2.32}$$

where I have replaced the gravitational acceleration g with GM_*/r^2.

As we are working under the isothermal assumption, the pressure is replaced with the isothermal sound speed, $c_\mathrm{s}^2 = p/\rho$, leading to:

$$\rho v_r \frac{\mathrm{d}v_r}{\mathrm{d}r} = -c_\mathrm{s}^2 \frac{\mathrm{d}\rho}{\mathrm{d}r} - \frac{GM_*}{r^2}\rho \tag{2.33}$$

At this point we need to return to the spherical, steady state mass continuity expression, equation (2.31), and apply the product rule to get

$$\rho v_r \frac{\mathrm{d}r^2}{\mathrm{d}r} + r^2 \left[\rho \frac{\mathrm{d}v_r}{\mathrm{d}r} + v_r \frac{\mathrm{d}\rho}{\mathrm{d}r}\right] = 0 \tag{2.34}$$

We can now algebraically rearrange equation (2.33) for $\mathrm{d}\rho/\mathrm{d}r$, substitute into equation (2.33) and cancel terms. By doing so, we obtain:

$$\frac{\mathrm{d}v_r}{\mathrm{d}r} - \frac{v_r^2}{c_\mathrm{s}^2}\frac{\mathrm{d}v_r}{\mathrm{d}r} = \frac{v_r}{c_\mathrm{s}^2}\frac{GM_*}{r^2} - \frac{v_r}{r^2}\frac{\mathrm{d}r^2}{\mathrm{d}r} : \tag{2.35}$$

Then, by collecting like terms, we finally get the integrand:

$$\left(\frac{v_r^2}{c_\mathrm{s}^2} - 1\right)\frac{\mathrm{d}v_r}{v_r} = \left(2 - \frac{GM_*}{c_\mathrm{s}^2 r}\right)\frac{\mathrm{d}r}{r}. \tag{2.36}$$

To further develop this equation we need to introduce several dimensionless quantities, $\psi \equiv v^2/c_\mathrm{s}^2$, $\lambda \equiv v_\mathrm{esc}^2/(2c_\mathrm{s}^2)$ and $\xi \equiv r/R_*$ which allow for a cleaner representation. The delimiters in equation (2.36) are then $\mathrm{d}v_r = (c_\mathrm{s}^2/2v)\mathrm{d}\psi$ and $\mathrm{d}r = R_*\mathrm{d}\xi$. Upon substitution of these dimensionless variables, equation (2.36) becomes:

$$\frac{1}{2}\left(1 - \frac{1}{\psi}\right)\mathrm{d}\psi = \left(\frac{2}{\xi} - \frac{\lambda}{\xi^2}\right)\mathrm{d}\xi. \tag{2.37}$$

To integrate this expression we need to find the limits of both ψ and ξ. As ψ is functionally dependent upon v_r it varies from ψ_0 at the stellar surface to some value ψ in the extended wind. ξ is linearly a function of r and therefore varies from 1, the stellar surface, to some value r above the surface. These limits applied to equation (2.37) provide the integral,

$$\frac{1}{2}\int_{\psi_0}^{\psi}\left(1-\frac{1}{\psi}\right)\mathrm{d}\psi=\int_{1}^{\xi}\left(\frac{2}{\xi}-\frac{\lambda}{\xi^2}\right)\mathrm{d}\xi, \tag{2.38}$$

which upon integration and rearrangement leads to:

$$\psi-\ln(\psi)-\psi_0+\ln(\psi_0)=4\ln(\xi)+2\lambda\left(1-\frac{1}{\xi}\right). \tag{2.39}$$

To progress further and determine a physically meaningful value for ϕ_0, we turn to the exact argument used by Parker (1958). First we separate out the terms not dependent on ψ:

$$Y=4\ln(\xi)-2\lambda\left(1-\frac{1}{\xi}\right) \tag{2.40}$$

and

$$Z=\psi-\ln(\psi), \tag{2.41}$$

and we find that, both Y and Z decrease from there initial values as ξ increases and that Y is minimised when $\xi = \lambda/2$ and Z is minimised when $\psi = 1$, both increasing monotonically after these minima. Finally, for real values of v_r, the minima in Y and Z must coincide at the same ξ. Therefore, when $\xi = \lambda/2$, $\psi = 1$ allowing us to write:

$$\psi_0-\ln(\psi_0)=2\lambda-3-4\ln\left(\frac{\lambda}{2}\right). \tag{2.42}$$

Substituting this result in to equation (2.39) and cancelling terms gives the final expression known as Parker's equation for the Solar wind:

$$\psi-\ln(\psi)=-3-4\ln\left(\frac{\lambda}{2}\right)+4\ln(\xi)+2\frac{\lambda}{\xi} \tag{2.43}$$

Equation (2.43) is however transcendental and an analytic solution for the velocity profile is not possible. By taking a numerical approach, this situation is remedied. A suitable root finding algorithm such as the Newton-Raphson or Bisection methods can be applied iteratively to the solution of equation (2.43) at successive values of ξ. Thus a radial profile of ψ, and therefore the velocity profile v_r, can be constructed from $v_r = c_\mathrm{s}\sqrt{\psi}$.

In a similar manner to the equation of motion for line driven winds, equation (2.43) has many mathematically valid solutions but only one solution which satisfies physical reality. If the velocity profile is integrated both outwards from the stellar surface and inwards from the outer wind, then the physically valid solution occurs when the two integration directions meet in a smooth manner. The point where they coincide in this way is known as the critical point. As root finding routines such as those mentioned above require an initial guess for the roots position, care must be taken about the critical point. This solution of Parker's equation must be done separately either side of the critical point by choosing initial guesses to be above or below this point. The critical point radius itself is a function of the sound speed and can be calculated via:

$$r_\mathrm{c} = \frac{GM_*}{2c_\mathrm{s}^2}. \tag{2.44}$$

The critical point is reached for typical solar values within a few solar radii above the surface. Thus for the majority of the calculation of the velocity profile, a value larger than r_c is required.

The density profile can also be described via the dimensionless variables used in deriving equation (2.43) with the following exponential function giving this radial density profile:

$$\rho(r) = \rho_0 \exp\left[\lambda\left(\frac{1}{\xi} - 1\right) - \frac{\psi}{2}\right], \tag{2.45}$$

where ρ_0 is the surface density. This expression is a consequence of hydrostatic considerations and is derived by again making the isothermal assumption and applying it to the momentum conservation expression, equation (2.27).

Both the velocity and density profiles are plotted in Fig. 2.2, showing both the inner wind ($r < 3\ R_*$) and extended ($r > 8\ R_*$) wind regions. This solution and its description of an isothermal expanding atmosphere has proved highly successful at providing initial

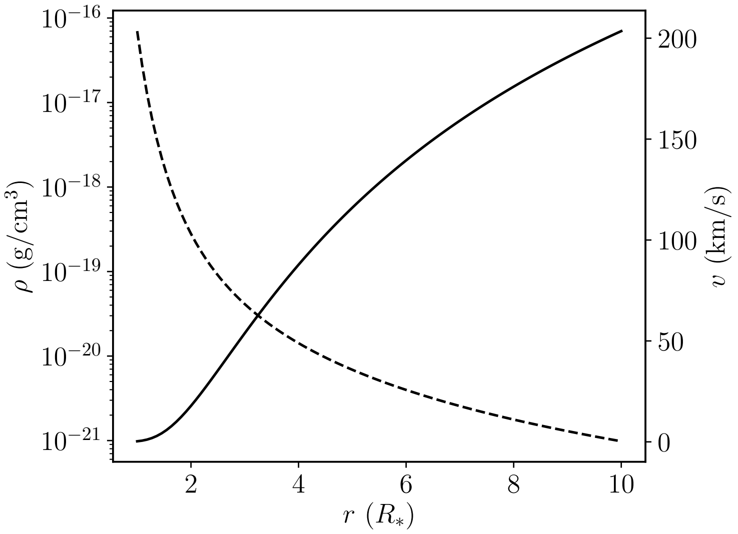

Figure 2.3: Velocity and density profiles calculated from Parker's solar wind equation using typical values of the solar corona. Close to the stellar surface ($r < 1.5\ R_*$), the velocity profile experiences slow growth which is then followed by a rapid increase in the range $1.5\ R_* < r < 4\ R_*$ before gradually easing to a flatter profile at larger radii $r > 10\ R_*$. The density profile follows an exponential decay at all radii, except at $r < 2\ R_*$ where the slow velocity growth results in a shallower decrease.

conditions for numerical simulations, and accurately recreates results of the fast Solar wind and is frequently used in both theoretical and numerical investigations of physical systems involving cool stars. Examples include studies of the angular momentum and magnetic breaking (Pantolmos & Matt, 2017) and the interactions of exoplanets with their hosts (Matsakos et al., 2015); both studies use the solution of Parker's equation to provide initial conditions for their simulations. As such this isothermal wind paradigm forms the basis for the simulation initial condition presented in chapters 6 and 7.

The following section details the planetary winds which develop in the atmospheres of planets hosted by low mass stars.

2.3 Planetary winds

Exoplanets which have undergone migration to orbital periods < 10 days receive considerable radiation from their stellar hosts. For gas giants, this radiation forms the basis for an energy budget capable of driving the thermal expansion of the planets outer atmosphere. This thermal expansion is similar in nature and, to first order approximation, obeys the same equation of motion as the coronal winds described above. The difference is that these short orbit gas giants do not posses a corona and the atmosphere remains $< 10^4$ K. This temperature is still considerably higher than the gas giants found in the solar system, which is the reason why, together with the typical mass and radii of these hot gas giants, they have become known as hot Jupiters (HJs).

There have been several recent theoretical studies that have argued for a hydrodynamic description of HJ winds. Murray-Clay et al. (2009), motivated by Lyman-α observations of HJ hosting star HD 209458, constructed a model for the escape of atomic hydrogen including heating, cooling, ionization balance, gravity and finally stellar wind ram pressure confinement; finding that mass-loss from the HJ in a Parker wind type solution best recreates the observed Lyman-α flux. A particle based approach by Bourrier & Lecavelier des Etangs (2013) also reached similar conclusions for both the manner and magnitude of planetary mass-loss

Further modelling by Guo (2011) involved parametrizing the planetary mass-loss by the stellar Ultraviolet (UV) flux and found either a linear or power law relationship between the mass-loss and incident flux depending on its magnitude, with the power law describing the high flux regime.

More recently Salz et al. (2016) produced a grid of 18 simulations for a range of HJs using a detailed photoionisation model coupled to a HD modelling code. This hybrid study accurately reproduced the sodium D lines observed for HD 189733b but had limited success reproducing observations of HD 209458b. They concluded that, depending on the extent of gravitation confinement, the HJ atmospheres are either hydrostatic or HD in nature. This approach has been successfully applied by Matsakos et al. (2015); Carroll-Nellenback et al. (2017); D'Angelo et al. (2018) to the study of HJ hosting systems.

I use these studies to justify the treatment of HJ atmospheres as behaving in a manner describable by the fluid approximation of an isothermally expanding atmosphere. As such the atmospheres of the HJ simulated in Chapters 6 and 7 are initialised in the same manner as the winds of the host stars they orbit, by applying Parker's solution to the solar wind, equation (2.43).

2.4 Other wind driving mechanisms

For completeness, to end this chapter I will give a short review of the other major wind driving mechanisms found across the HR diagram that are not directly related or used in the work presented in later chapters. The winds described below are from the works of Lamers & Cassinelli (1999) and Owocki (2004). For a more complete discussion the interested reader should refer to these publications.

Stars with convective zones just below the surface can produce oscillations resulting in waves in their atmospheres. These wave translate to pressure gradients and therefore a net acceleration of material outwards from the surface. These winds are know as sound driven wind (Lamers & Cassinelli, 1999) and are only apparent in low surface gravity stars and for the theory to be generally relevant, other driving mechanism must work in tandem to bring wind material to the critical point for the wave driving to be relevant, such as continuum radiation pressure.

Dust driven winds are powered by continuum radiation which is absorbed by dust grains formed in the extended stellar atmosphere. This driving mechanism is limited to luminous red supergiant stars and stars within a specific mass-loss rate range which, for typical Asymptotic Giant Branch (AGB) stars, occurs between 10^{-7} $M_\odot$/yr and 10^{-5} $M_\odot$/yr, according to Lamers & Cassinelli (1999), because the radiation-dust coupling is sensitive to both the gas properties as well as the absorption and emission properties of the dust grains. The velocity ranges experienced by dust driven winds are markably different form the other driving mechanisms covered in this chapter. Typical terminal velocities are of the order of 30 km/s, several orders of magnitude lower than those experienced by line driven or coronal winds.

Stars close to the Eddington luminosity limit posses winds driven primarily by continuum radiation electron scattering. The CAK line force saturates at this limit. In this process the outwards force balances and exceeds the force of gravity and material is lifted from the stellar surface. These stars are known as Luminous Blue Variables (LBV) stars. As their name suggests, these stellar types can experience non-steady mass-loss rates with rapid outbursts, which can exceed the steady line driven mass-loss by up to four orders of magnitude (Owocki, 2004).

The Eta Carinae system is a prime example of such stars. A binary system with an eccentricity of ~ 0.9, where the primary experiences disruptive events as the secondary passes periastron drastically increasing the mass-loss over short periods. Eta Carinae has undergone a *great eruption* between 1827 - 1857 and again a *lesser eruption* between 1887 - 1895. For a review of this system, the historical observations and the remaining challenges see Davidson & Humphreys (1997). Eta Carinae itself is thought to be comprised of a primary Wolf-Rayet type star and a secondary O-type star with a combined mass of $\sim 250\ M_\odot$ (Kashi & Soker, 2010). Such systems represent the extremes of the known massive star population and the properties of their winds are intimately linked to their nature as a binary system (Clementel et al., 2015a,b).

3

Magnetohydrodynamics

> *"Magnetohydrodynamics combines the intuitive nature of Maxwell's equations with the easy solvability of the Navier-Stokes equations. It's so straightforward physicists add "relativistic" or "quantum" just to keep it from getting boring."*
>
> – Randall Munroe, *xkcd*

Magnetohydrodynamics (MHD) has proved an invaluable tool for investigating many phenomena, generally throughout physics and the physical sciences. It is a field of study which aims to describe the behaviour of a fluid comprised of positively charged particle species according to a set of conservation laws (Kulsrud, 2004). In astrophysics, MHD has shown it is capable of providing physical insight into physical problems over a wide range of time and length scales. This generality is due to the equations which govern MHD being scale invariant and the quantities involved in the calculations being related through dimensionless ratios such as the Reynolds number, magnetic Reynolds number and the Lundquist number. This length and time invariance means that MHD, and more generally, Hydrodynamics (HD), can describe both tea in a cup and the gas flow in a nebula. Such generality is the power of fundamental theories.

The field of HD and MHD has been expanded to include physics such as special and general relativistic mechanics (White et al., 2016) and plasma effects such as resistivity and cooling (Mignone et al., 2007). The original equations and the extensions have found practical application thanks to numerical frameworks such as the finite volume or Godunov method (Godunov, 1959), in which space and time are discretised and evaluated on numerical grids. The details of these equations, their extensions, methods for solution and the codes available that implement them will be discussed in this chapter.

The next section will present the equations of MHD, introducing each equation separately and discuss its terms and their physical meaning and the assumptions they are derived under.

3.1 The equations of magnetohydrodynamics

The equations of ideal MHD are a set of conservation laws which describe a fluid through the primitive variables: density, ρ, velocity, $\boldsymbol{v}$, pressure, p, and magnetic field, $\boldsymbol{B}$ (Kulsrud, 2004). Each quantity requires its own conservation law, which advances the state both through time and space. The term "primitive" reflects the property of these variables not being divisible into more basic ones. An example of a non primitive variable is momentum density, $\boldsymbol{m} = \rho\boldsymbol{v}$, which can be broken down into density and velocity, which are primitive. There are numerous ways in which these equations can be written involving non-primitive quantities such as current density or electromotive force. However, the laws set out below are presented in such a way as to not introduce any additional variables (Mignone et al., 2007). The formulation of the MHD equations is done under two important assumptions: the first is that the length scales, over which the physical situation is being described, is larger than the length scale at which particle effects become apparent. The second is that the different particle species in the plasma can all be described as a single fluid and not a multi-fluid system (Kulsrud, 2004).

The first conservation law is mass conservation and is given by:

$$\frac{\partial \rho}{\partial t} + \boldsymbol{v} \cdot (\boldsymbol{\nabla} \rho) + \rho \left(\boldsymbol{\nabla} \cdot \boldsymbol{v}\right) = 0. \tag{3.1}$$

The first term is the time evolution of the density and the following two terms are the spatial change in mass distribution due to density and velocity gradients in the plasma. We have encountered this equation in Chapter 2 when constructing Parker's expression for the solar wind, equation (2.43).

The second equation describes the evolution of the momentum. We have encountered this equation in a slightly different form when considering the equation of motion for line driven winds in Chapter 2[1]. Hence the equation of motion for a fluid according to MHD is:

$$\frac{\partial \boldsymbol{v}}{\partial t} + \boldsymbol{v} \cdot (\boldsymbol{\nabla} \boldsymbol{v}) + \frac{1}{\rho} \boldsymbol{B} \times (\boldsymbol{\nabla} \times \boldsymbol{B}) + \frac{1}{\rho} \boldsymbol{\nabla} p = -\boldsymbol{\nabla} \Phi + \boldsymbol{g}. \tag{3.2}$$

The first two terms on the left hand side are the temporal and spatial change in velocity. The third term is the contribution to the momentum change from magnetic field gradients, which also incorporates contributions to the momentum change from current densities. The final term on the left hand side is the momentum change due to pressure gradients in the fluid. The two terms on the right hand side represent accelerations due to the gradient of a potential field acting on the fluid and acceleration due to gravity respectively.

The third equation gives the evolution of the magnetic field. This equation is an induction equation in which the first term on the left hand side is the temporal evolution of the magnetic field and the remaining terms on the left hand side are velocity and magnetic field gradients, which together can be thought of as the curl of the electric field; the equation is:

$$\frac{\partial \boldsymbol{B}}{\partial t} + \boldsymbol{B} \left(\boldsymbol{\nabla} \cdot \boldsymbol{v} \right) - \left(\boldsymbol{B} \cdot \boldsymbol{\nabla} \right) \boldsymbol{v} + \left(\boldsymbol{v} \cdot \boldsymbol{\nabla} \right) \boldsymbol{B} = \boldsymbol{v} \left(\boldsymbol{\nabla} \cdot \boldsymbol{B} \right). \tag{3.3}$$

The term on the right hand side is not physical and represents any deviation from the condition that $\boldsymbol{\nabla} \times \boldsymbol{B} = 0$. This term appears in the derivation of equation 3.3 through vector identities and is mathematically allowed, however, in reality, this term would be exactly zero conforming with the non-existence of magnetic mono-poles. When discretising the MHD equations, this condition is not always explicitly enforced and methods must be employed to correct for this. Therefore this source term is present for completeness (Mignone et al., 2007).

The final equation is that of the energy evolution. As with the previous equations, the first term is the temporal pressure change and the final two are the spatial change.

---

[1] This line-driven wind momentum equation differs from the MHD momentum equation, as it lacks time dependence.

The equation is given by:

$$\frac{\partial p}{\partial t} + \boldsymbol{v} \cdot (\boldsymbol{\nabla} p) + p c_{\mathrm{s}}^2 (\boldsymbol{\nabla} \cdot \boldsymbol{v}) = 0. \tag{3.4}$$

Equations (3.1-3.4) form a set of coupled hyperbolic equations which govern the behaviour of a magnetised fluid. However, each equation in turn introduces a new variable, which requires an additional partial differential equation to be solved. In order to close this set of equations the sound speed, c_{s}, has been introduced given by the equation of state,

$$c_{\mathrm{s}} = \sqrt{\frac{\gamma p}{\rho}} \tag{3.5}$$

which relates the pressure to the density via the adiabatic index, γ. Other equations of state can be used to close the set of equations; for example the adiabatic Equation of State (EOS). However the isothermal EOS is the simplest while still allowing me to illustrate the properties of the MHD equations.

These equations are known as the equations of Ideal MHD. The reason they are considered ideal is that there are no particle effects. Additional terms which introduce non-ideal behaviour, for example viscosity or resistivity, can also be incorporated as additional terms in the above expressions (Kulsrud, 2004).

Typically these additional terms represent dissipative effects and means for modifying the primitive variables in a manner not described by the MHD equations. For example plasma effects such as resistivity which acts to dissipate the magnetic field in a given region according to the ambient plasma conditions. Resistivity is included as additional source terms on the right hand side of both the induction and energy equations

Equations (3.1, 3.2, 3.3 and 3.4) can be expressed in slightly more compact form, by introducing the non primitive variables $\boldsymbol{m}$, $\mathcal{E}$ and e. $\boldsymbol{m}$ is the momentum density, $\mathcal{E}$ is the electric field and e is the specific energy. In this form they are known as the conservative form of the MHD equations. This is because they primarily involve the description of conserved quantities such as momentum density rather than separately, density and velocity. The above equations in this form and in the same order are:

$$\frac{\partial \rho}{\partial t} + \boldsymbol{\nabla} \cdot (\boldsymbol{m}) = 0, \tag{3.6}$$

$$\frac{\partial \boldsymbol{m}}{\partial t} + \boldsymbol{\nabla} \cdot (\boldsymbol{m}\boldsymbol{v} - \boldsymbol{B}\boldsymbol{B} + \boldsymbol{I}p) = -\rho\boldsymbol{\nabla}\Phi + \rho\boldsymbol{g}, \tag{3.7}$$

$$\frac{\partial \boldsymbol{B}}{\partial t} + \boldsymbol{\nabla} \times \boldsymbol{\mathcal{E}} = 0, \tag{3.8}$$

$$\frac{\partial}{\partial t}(E + \rho\Phi) + \boldsymbol{\nabla} \cdot ((E + p + \rho\Phi)\,\boldsymbol{v} + \boldsymbol{B}\,(\boldsymbol{v} \cdot \boldsymbol{B})) = \boldsymbol{m} \cdot \boldsymbol{g}, \tag{3.9}$$

and

$$E = \rho e + \frac{m^2}{2\rho} + \frac{B^2}{8\pi}. \tag{3.10}$$

Where $\boldsymbol{I}$ is the unit tensor and the other symbols have the same meaning as above (Mignone et al., 2007).

The motivation for expressing these equations in the two forms above becomes evident when these equations are implemented in numerical form for use in computer algorithms. The primitive formalism preserves positivity of quantities such as pressure as well as sub-luminal flow velocity. The conservative form preserves conservation of energy, momentum and magnetic flux (Mignone et al., 2007, 2012). Which formalism is best suited to the task at hand is dependent upon the calculation being performed. As an example, the reconstruct-average-solve strategy involves first converting conserved variables to primitive, then deriving both left and right hand states at the boundary of the adjacent grid sites. These states are then used to compute the net flux into the computational cell over the time step, Δt, (Mignone et al., 2007). This procedure will be covered in greater detail in Section 3.3.

There are many implementations of the MHD equations in publicly available computer codes (Kritsuk et al., 2011). These codes implement the MHD equations on grids in both static and adaptive modes for a range of coordinate systems such as Cartesian, Polar, Cylindrical and Spherical and in particle form which require no grids at all. They include both ideal and non-ideal terms for both classical and relativistic versions of the MHD equations. The following section presents the methods for numerical solution of the MHD equations and present a selection of publicly available codes that allow for the simulation of a wide range of astrophysical phenomena and behaviour.

3.2 Numerical magnetohydrodynamics

The practice of numerical fluid dynamics can be dated back to the very first attempt to predict the weather by F. L. Richardson through the solution of partial differential equations, by hand (Toro, 2009). This undertaking marked the beginning of computational fluid dynamics.

Since these early beginnings, methods and their implementation have developed to the point where fluid simulation have been applied to the solution of not only weather prediction but also the investigation of physical phenomena from the motion of blood through arteries in the human body to the formation of the cosmic web and galaxy clusters which form the observable and dark universe. Thankfully, such calculations are restricted to computers and no longer conducted by hand.

3.2.1 Discretisation methods

The application of the MHD equations to study physical phenomena requires their discretization and representation as a spatially discontinuous discrete structure. This can take the form of either a numerical regular, irregular or hierarchical grid, or an ensemble of particles. The distinction between these two methods is the frame in which the calculations are performed. For grid based methods it is the Eulerian frame and in particle approach it is the Lagrangian frame. Both approaches have their strengths and weaknesses.

An implementation of the Eulerian approach is the Godunov or Finite Volume (FV) method introduced by Godunov (1959) which proved highly successful at simulating a wide range of physical fluid phenomena due to its convergence properties, stability and conservative properties. However, the FV method has several limitations, including the lack of Galilean invariance and angular momentum conservation, as well as its inability to encompass large differences in length scales. For example, when performing MHD simulations of star forming regions, the length scales which need consideration cover many orders of magnitude (Dmitruk et al., 2004), from large scale dust clouds to protostellar cores. Traditional static grid based MHD either requires a highly refined grid and therefore excessive amounts of computational resources, or makes do with a coarse grid which is unable to resolve fine detail. There are techniques which attempt to address this limitation. Adaptive Mesh Refinement (AMR) is a technique in which if the gradient of a quantity at any given grid cell exceeds a specified limit, the grid cell is subdivided and the local resolution is increased to accommodate the reduced characteristic length scale (Mignone et al., 2012). This method has become increasingly popular, with most modern HD and MHD programs providing an implementation of AMR (Fryxell et al., 2000; Teyssier, 2002; Mignone et al., 2007).

The Lagrangian approach however circumvents the issue of incompatible length scales as the fluid equations are represented as an ensemble of particles and does not use a grid (Monaghan, 2005). One successful method is known as Smooth Particle Hydrodynamics (SPH) and was first introduced by Gingold & Monaghan (1977) and Lucy (1977). Instead of using a grid, SPH follows an approach similar to that of Molecular Dynamics (MD), where the coordinates of each particle are updated each time step, thus doing away with the need for a mesh. Each particle is treated as a smoothed out Gaussian kernel; however, this approach does come with its own drawbacks. For example, calculating the optical depth of a distribution of smooth particles becomes much more involved than in the case of a connected grid, in which values are assumed constant across a grid cell. This makes SPH unsuitable for simulating the winds detailed in Chapter 2. Monaghan (2005) has written a review of SPH and provides an in depth discussion of the theory underpinning the technique. SPH methods however have relative drawbacks in comparison to grid based codes and include a lack of convergence properties and the suppression of fluid instabilities Schaal et al. (2015).

Both the FV and SPH methods have a long history in the literature and have been applied since the 1960s and 1970s to problems of fluid dynamics in astrophysics and otherwise. The two approaches have seen advances which reduced their limitations and expanded their applicability.

More recently other methods have been developed which aim to overcome some of the limitations of both the grid and particle based approaches discussed above. Two examples include the family of so called moving mesh and meshless methods. In the case of moving meshes, the objective is to combine the advantages of FV and SPH via the use of irregular Voronoi diagrams (Voronoi, 1908) in which each cell centre is advected by the fluid flow in the same manner as SPH but fluid quantities in each cell are updated by calculating fluxes at cell interfaces according to Godunov's method (Springel, 2010). This approach has the advantage that it preservers Galilean invariance, conserves angular momentum, resolves fluid instabilities and is naturally adaptive. Meshless methods follow the same approach as moving meshes but the boundary between cells is not a sharp discontinuity but a smoothed transition and bears closer resemblance to SPH than it does FV (Hopkins, 2015). These novel moving mesh methods however suffer from the same lack of convergence which affects SPH (Springel, 2010), require large memory resources and are typically more computationally intensive than traditional FV or SPH (Springel, 2010; Schaal et al., 2015).

Another important method which is gaining considerable interest in the astrophysics community (Zanotti et al., 2015; Fambri et al., 2017; Manzanero et al., 2018; Guillet et al., 2018; Sánchez-Vizuet & Solano, 2018; Karakus et al., 2018; Velasco-Romero et al., 2018; Balsara & Kappeli, 2018) but can trace its origins back to the 1970s, is the Discontinuous Galerkin (DG) method, pioneered by Reed & Hill (1973); Baker (1977). The basic structure of this approach is essentially the same as the FV method, Eulerian and grid based, however the solution in a given computational cell K is represented as a linear combination of $N(k)$ orthonormal basis functions, ϕ_l^K. This formulation has the benefit of having a small memory footprint (when compared to moving mesh codes), is in principle of arbitrary order accuracy and angular momentum conserving[2].

Both the moving mesh and DG methods are new additions to the numerical astrophysics community and as such their limitations are not fully understood and their implementation in public codes is limited. For these reasons, I chose to use a traditional FV method to perform the simulations presented in this thesis. The following sections detail the mathematical steps of the FV method and list the common numerical codes available which implement this method, before introducing the specific code used to perform the simulations that are presented in Chapters 5, 6 and 7.

3.3 The finite volume method

In this section I will give an overview of the FV procedure. For simplicity I restrict the treatment to 1D and communicate the simplest form of each step of the calculation. Higher dimensions are achieved by simply conducting the same calculations in the additional directions and swapping variables where appropriate. I will also only treat the HD case for conciseness, dropping the magnetic field variables from equations (3.6-3.9).

I begin the description by rewriting the equations of HD in the compact form:

$$\frac{\partial \boldsymbol{U}}{\partial t} + \nabla \cdot \boldsymbol{F}(\boldsymbol{U}) = \boldsymbol{S}(\boldsymbol{U}), \tag{3.11}$$

where $\boldsymbol{U}$ is a 1D vector of conservative variables, $\boldsymbol{F}(\boldsymbol{U})$ is the flux tensor, where the rows are the fluxes of the components of the vector $\boldsymbol{U}$. $\boldsymbol{S}(\boldsymbol{U})$ is the combination of all source

---

[2] Traditional finite volume codes are limited to overall 2nd order of accuracy despite the individual components of the algorithm having an accuracy of greater than 2nd order.

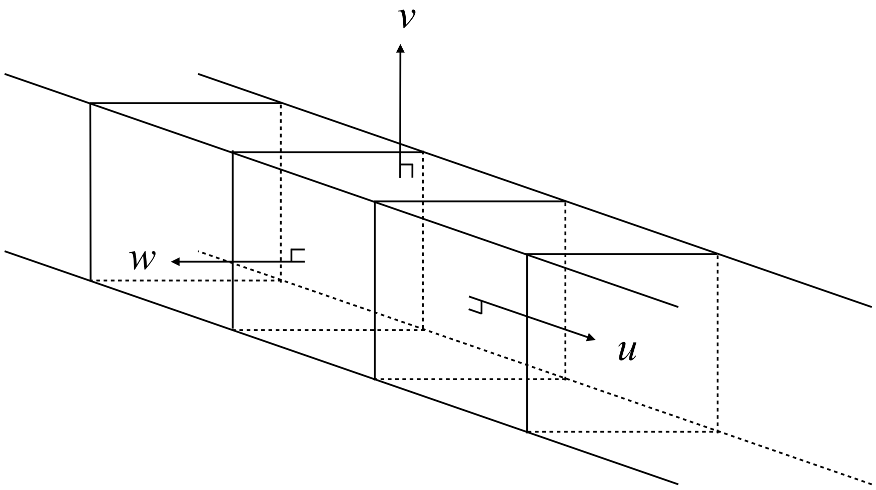

Figure 3.1: The cell layout in a 1D numerical problem. Indicated are the components of the fluid velocity with u the velocity normal to the 1D line direction and v and w the tangential components.

terms. $\boldsymbol{U}$ and $\boldsymbol{F}(\boldsymbol{U})$ take the forms:

$$\boldsymbol{U} = \begin{pmatrix} \rho \\ \rho u \\ \rho v \\ \rho w \\ E \end{pmatrix}, \qquad \boldsymbol{V} = \begin{pmatrix} \rho \\ u \\ v \\ w \\ p \end{pmatrix}, \qquad \boldsymbol{F}(\boldsymbol{U}) = \begin{pmatrix} \rho u \\ \rho u^2 + p \\ \rho uv \\ \rho uw \\ u(E+p) \end{pmatrix}. \tag{3.12}$$

I have also added the vector of primitive variables, $\boldsymbol{V}$, for completeness. In the above vectors, u, v and w represent the normal and two tangential components of the fluid velocity. In this context normal means, in the case of a 1D problem, the velocity component along the 1D line and the tangential components are the velocities tangential to the 1D line. These components along with the 1D numerical cell layout is shown in Fig. 3.1.

In numerical notation equation (3.12) gives the state at the next timestep, U^{n+1} as a function of the state at the current timestep, U^n, and the net flux into the cell from the upper and lower cell interfaces:

$$\boldsymbol{U}_i^{n+1} = \boldsymbol{U}_i^n + \frac{\Delta t}{\Delta x_i}\left(\boldsymbol{F}_{i-1/2} - \boldsymbol{F}_{i+1/2}\right) + \boldsymbol{S}_i(\boldsymbol{U}_i^n). \tag{3.13}$$

The superscripts n and $n+1$ denote states at the current time t and the next time $t+\Delta t$, and the subscript i indicates the cell under consideration. The flux functions, $\boldsymbol{F}_{i-1/2}$ and $\boldsymbol{F}_{i+1/2}$, are fluxes through the faces of cell i at $i-1/2$ and $i+1/2$ respectively and determined via solution of the Riemann problem:

$$\boldsymbol{F}_{i-1/2} = \mathcal{R}\left(\boldsymbol{V}_{L,i-1/2}^n, \boldsymbol{V}_{R,i-1/2}^n\right) \qquad \boldsymbol{F}_{i+1/2} = \mathcal{R}\left(\boldsymbol{V}_{L,i+1/2}^n, \boldsymbol{V}_{R,i+1/2}^n\right). \tag{3.14}$$

The primitive states $\boldsymbol{V}_{L,i-1/2}^n$, $\boldsymbol{V}_{R,i-1/2}^n$, $\boldsymbol{V}_{L,i+1/2}^n$ and $\boldsymbol{V}_{R,i+1/2}^n$ are those on the left (L) and right (R) sides of the cell interfaces at $i-1/2$ and $i+1/2$ and are illustrated in the diagram of Fig. 3.2. These states are reconstructed by extrapolating from the cell centred values, $\boldsymbol{V}_i^n$, to the cell interfaces at $i-1/2$ and $i+1/2$. The reconstruction can be one of several types of ascending order accuracy: flat (1st order), linear (2nd order) and parabolic (3rd order) or another higher order method[3] (Mignone et al., 2007). Fig. 3.2 shows the reconstruction for the linear case, where the gradient in each cell is calculated using a central difference method.

The cell face states are then passed to the Riemann solver, equations (3.14), for evaluation. This operation can take many forms and there is extensive literature and ongoing work to develop new accurate but computationally efficient methods (Miyoshi & Kusano, 2005; Toro, 2009; Balsara & Kappeli, 2018). The exact solution to the Riemann problem was supplied by Godunov (1959) as part of the method named after him. The anatomy of the Riemann problem is illustrated in Fig. 3.3.

The spacetime diagram in Fig. 3.3 of the Riemann problem is divided between distinct regions with differing physical conditions. The division between these regions is defined

---

[3] There are several other higher order methods such as the WENO and MP5 methods however I shall only mention up to 3rd order here

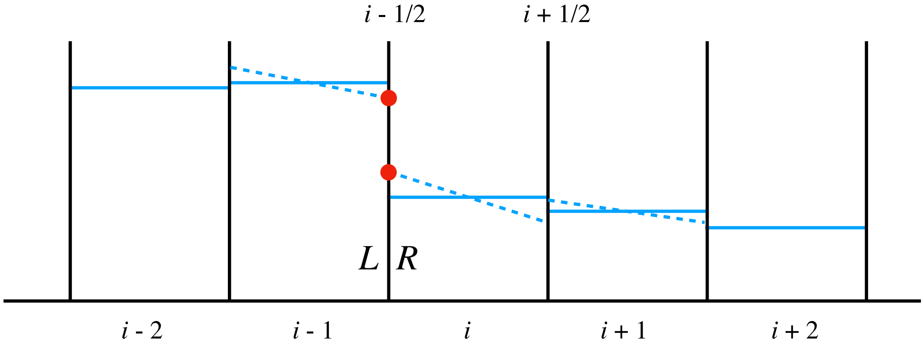

Figure 3.2: Diagram of the flux determination between cell $i-1$ and i. The blue solid lines represent any variable in V and each value of i represents a separate numerical cell. The dashed blue lines are the linear gradients determined through a central difference approximation. The five cells shown make up the stencil needed for the linear reconstruction method where the gradients in the central three cells are computed from the cell $i-2$ through $i+2$. The red dots indicate the states $\boldsymbol{V}^n_{L,i-1/2}$ and $\boldsymbol{V}^n_{R,i-1/2}$ on the left (L) and right (R) side of the interface at $i-1/2$ respectively, which the Riemann solver uses to calculate the flux function between the two cells.

by a series of waves and rarefactions which decay away from the inter cell boundary from $t = 0$ and $x = 0$. The exact shape of these waves/rarefactions and their position relative to both the boundary and each other determines the solution to the Riemann problem and the resultant flux of fluid quantities across the cell boundary.

The exact mathematical solution to the Riemann problem is however computationally cumbersome and rarely applied to practical situations, with many codes utilising approximate Riemann solvers (Mignone et al., 2007). Exact Riemann solvers have also been shown to result in spurious numerical effects such as the carbuncle and odd-even decoupling phenomena, which are consequences of low numerical dissipation in the regions of grid aligned flow (Quirk, 1994). A popular family of Riemann solvers which has proved robust and efficient is that of the Harten, Lax and van Leer (HLL) type (Harten et al., 1983). The reason I describe this solver rather than any other, is that this class of solver is used to perform the simulations in Chapters 5, 6 and 7. The interested reader is directed to the book by Toro (2009) for an in depth review of the various Riemann solvers available and their mathematical basis.

The HLL approximation divides the spacetime diagram of Fig. 3.3 into three region: left state, right state and a central state bounded by the right and left going characteristics at $u - c_{\rm s}$ and $u + c_{\rm s}$. This intermediate state is known as the HLL state. Which of these

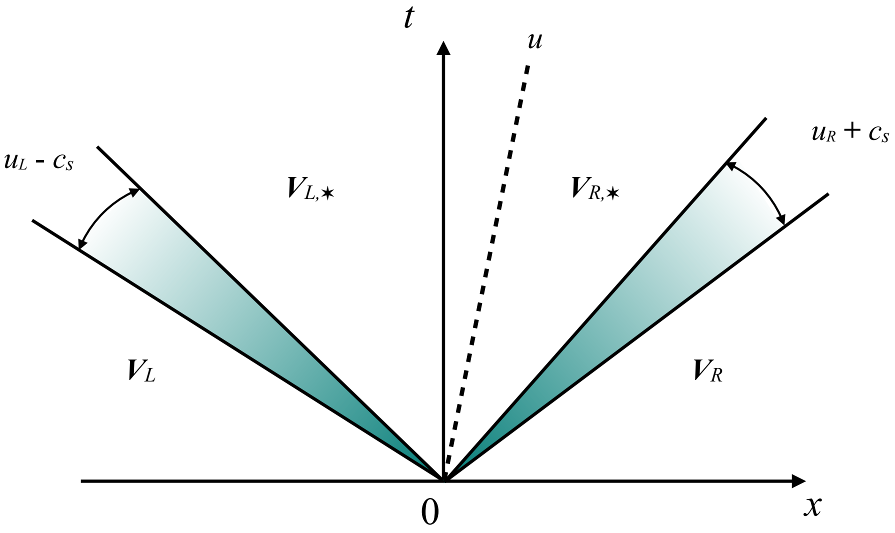

Figure 3.3: Spacetime diagram for the Riemann problem. Here $x = 0$ indicates the physical location of the boundary between computational cells. The dashed line and the two teal coloured fans represent the three waves which decay away from the initial boundary at $t = 0$ whose speeds are $u - c_\mathrm{s}$, u and $u + c_\mathrm{s}$. The dashed lines denote the contact discontinuity between the states in the two cells separated by the boundary. The teal fans are waves that can either be rarefactions or shocks, with the width of the fan indicating the rarefaction/shock strength; a shock exists for a fan with width zero. The starred and non-starred regions comprise the values required to solve the Riemann problem.

three states is returned as the cell face flux, $F_{i\pm1/2}$, is determined by the condition

$$\boldsymbol{F}^{\mathrm{HLL}}_{i\pm1/2} = \begin{cases} \boldsymbol{F}_L & \text{if } 0 \le C_L \\ \dfrac{C_R\boldsymbol{F}_L - C_L\boldsymbol{F}_r + C_L C_R\left(\boldsymbol{U}_R - \boldsymbol{U}_L\right)}{C_R - C_L} & \text{if } C_L \le 0 \le C_R \\ \boldsymbol{F}_R & \text{if } 0 \ge C_R \end{cases} \tag{3.15}$$

where $\boldsymbol{U}_L$ and $\boldsymbol{U}_R$ are the conservative states on the left and right of the cell boundary and C_L and C_R are the left and right going wave speeds, given by, in their simplest form:

$$C_L = \min\left(u_L - c_\mathrm{s}, u_R - c_\mathrm{s}\right), \qquad C_R = \min\left(u_L + c_\mathrm{s}, u_R + c_\mathrm{s}\right), \tag{3.16}$$

where c_s is the sound speed and u_L and u_R are the left and right going rarefaction/shock speeds, indicated in Fig. 3.3. In the above equations, the ± symbol indicates that the Riemann problem is performed independently for the interfaces at both $i-1/2$ and $i+1/2$. Extensions to the HLL solver are the HLLC solver of Toro et al. (1994) which restores the contact discontinuity (see Fig. 3.3) and the HLLD solver of Miyoshi & Kusano (2005) which extends the approach to MHD.

Once $\boldsymbol{F}_{i-1/2}$ and $\boldsymbol{F}_{i+1/2}$ are determined from the Riemann problem, they can then be used, along with any source terms from $\boldsymbol{S}_i(\boldsymbol{U}_i^n)$, to evaluate equation (3.13). As the reconstruction is done on the primitive variables, one must convert from conservative to primitive before the reconstruction stage. The example method above is comprised of a single Euler-like time integration step, linear interpolation and the HLL Riemann solver. Many other combinations are possible, comprising different order accuracies for the reconstruction, time stepping and Riemann problem stages of the FV method. However, all these combinations share the same basic steps of: reconstruct, Riemann solve, time advance and average and is illustrated in the flowchart in Fig. 3.4

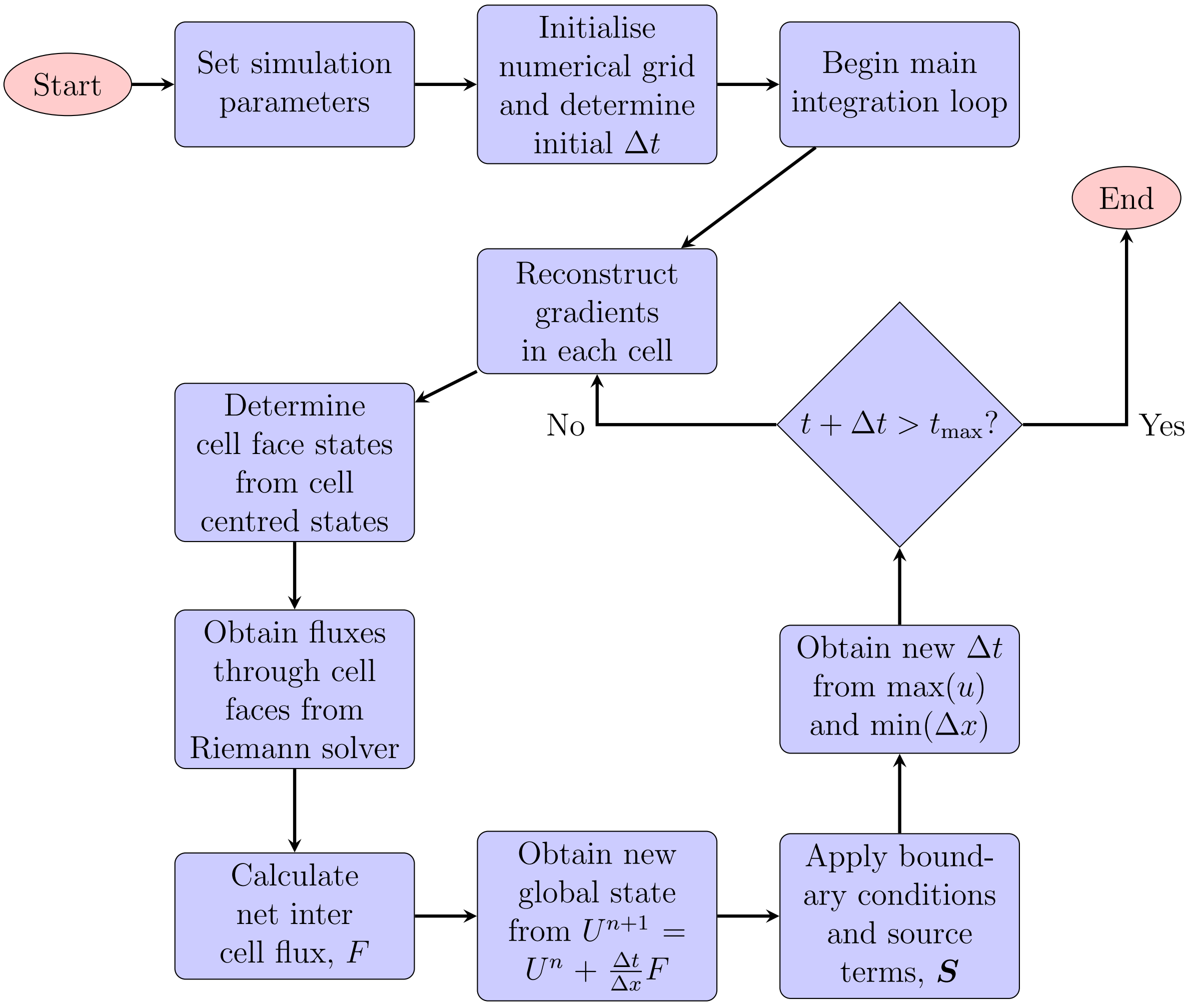

Figure 3.4: Flowchart representing the major stages and calculations performed during the FV method.

All FV codes implement a variation on this reconstruct-solve-average approach (Mignone et al., 2007) and their differences reduce to the implementation, grid structure and optional extra physical source terms. The following sections present a brief review of the common FV codes in the astrophysics community, and gives a justification for use of the code chosen for conducting the work presented in this thesis.

3.4 Finite volume public codes

There are many codes which exist which allow users to simulate astrophysical behaviour by applying the equations set out in Section 3.1, using a variety of techniques. However the are many traits which they all share; for example they all have parallel implementations using the Message Passing Interface (MPI). As such, what is briefly detailed in this section are the defining differences amongst the codes, the situations for which they are most suited and any distinctive features.

The codes that will be briefly described here are: FLASH (Fryxell et al., 2000), RAMSES (Teyssier, 2002), PLUTO (Mignone et al., 2007), Athena (together with its more recent incarnation Athena++) (Stone et al., 2008; White et al., 2016) and MPI-AMRVAC (Xia et al., 2018). These codes have been chosen as they span almost two decades in development and active use, thereby represent the developments which have taken place over that time frame in the field of numerical astrophysical MHD. Comparisons between some of these codes and their individual performance under various test situations is described in a review paper by Kritsuk et al. (2011) which compares the ability of some of the codes listed above (and others) to reproduce isothermal magnetised supersonic turbulence. A brief description of each code is given below in roughly the order of code age.

The first code FLASH was initially designed to simulate the thermonuclear flashes (hence the name) observed on the surface of neutron stars and white dwarfs (Fryxell et al., 2000) through the use of nuclear reaction network. FLASH has however been applied to a range of other physical situations including purely HD and MHD simulations. Written in Fortran, FLASH makes use of both static and AMR grids and the piecewise parabolic method (PPM) to solve the equations of MHD (Fryxell et al., 2000).

The next code to be considered is RAMSES which was written to be an N-body and MHD code for the treatment of structure formation in the universe with high spatial resolution by Teyssier (2002). The code is well suited to studying galaxy and star formation in which self-gravitation and high resolution at contrasting length scales are important. RAMSES accomplishes this by making use of an AMR technique, with a tree-based data structure allowing recursive grid refinements on a cell-by-cell basis (Teyssier, 2002). The code is second order accurate in both space and time.

PLUTO is designed to be a code for the solution of hypersonic flows in 1, 2 and 3 spatial dimensions (Mignone et al., 2007). The code is not designed with any one particular astrophysical phenomena in mind. As such, the authors have provided a range of numerical techniques for the solutions of the HD and MHD equations in both classical and relativistic forms. The code allows for second, third or higher order accuracy in both time and space on Cartesian, Polar, Cylindrical or Spherical grids with AMR (Mignone et al., 2012). The design philosophy behind PLUTO is a modular approach to allow for the inclusion or exclusion of a range of physical behaviour including viscosity, cooling, thermal transport, resistivity and a rotating frame (Mignone et al., 2007). These attributes make PLUTO a general purpose code.

Athena is the successor to the long-standing, widely used MHD code known as ZEUS. Athena is described as being designed as a highly extendible code allowing for future increases in its abilities (Stone et al., 2008). The original implementation of the code includes second and third order accuracy in both time and space, Cartesian and Cylindrical and static grid refinement (a variant of AMR in which the user pre-specifies the area which is to have higher resolution). Physics capabilities include cooling, Hall effect, ambipolar diffusion, Ohmic heating, viscosity and thermal conduction (Stone et al., 2008). The original Athena code did not see wide spread adoption in the literature. However, recently it has seen a complete rewrite where the grid structures has been extended, general as well as special relativistic MHD have been implemented along side an octree based AMR grid structure. These changes are communicated in White et al. (2016) and the new code is known as Athena++ to reflect its rewrite in the c++ programming language.

MPI-AMRVAC or the MPI parallelised AMR versatile advection code is similar to the recent Athena++ code as it uses an octree based AMR approach which allows for Cartesian, cylindrical polar and spherical grids. There are a number of source terms for non-ideal MHD, a notable one being the ability to simulate dust. The code is written in Fortran with a novel preprocessor aimed at allowing the user to write dimension independent problems that can then be run under different conditions (Xia et al., 2018).

3.4.1 Which code to use?

Given the similarities between the codes described above and the conclusions of Kritsuk et al. (2011), one may be forgiven for struggling to decide on which code to use. In the absence of a code designed around the simulation of either line driven winds of massive stars or the enviroments of exoplanets, the most sensible choice is a code which covers the widest range of numerical techniques, and provides physics beyond simply the solution of the ideal MHD equation. This is to allow for the widest possible scope for future investigations. FLASH and RAMSES are specific in their design (either supernovae or cosmological settings) and not specifically suited to studying stellar winds or exoplanets. Athena, PLUTO and MPI-AMRVAC are general purpose in their design and highly modular. However the PLUTO code has the largest number of additional physics modules, geometries and capabilities. At the beginning of the work presented in this thesis, PLUTO was also the most regularly updated, and has the largest range and flexibility when concerning numerical algorithms, allowing the user to easily switch reconstruction, timestepping method and Riemann solver independently. This flexible approach to code design was the reason that PLUTO was chosen.

In the following section the performance of PLUTO on multiple Central Processing Unit (CPU) systems will be tested to determine if the code is limited either by available

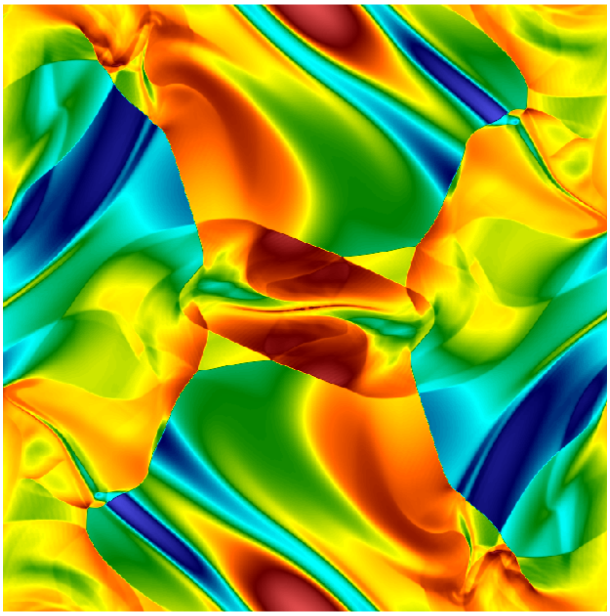

Figure 3.5: Mid-simulation snapshot of the 2D Orszag-Tang vortex MHD test simulation. The simulation was conducted with a resolution of 768 × 768 grid points. The snapshot illustrates the number of shocks generated in the summation, shown as sudden discontinuous change in colour.

computational resources or by the efficiency of the program itself.

3.4.2 Scaling of PLUTO on multi-CPU systems

To test the scalability of the PLUTO code and determine the return in speedup gained when the code is run on multi-core machines, a limited strong scaling study of PLUTO was conducted. The machine available on which to test PLUTO was the University of Birmingham's BlueBear computing system. At the time of testing, BlueBear was comprised of 128 compute nodes; each node has 2 dual-processor 8-core (16 cores/node) 64-bit 2.2 GHz Intel Sandy Bridge E5-2660 CPUs, giving a total of 2048 cores across all nodes. However, the user has access to a limited supply of these resources as BlueBear is a shared resource. Each user has access to a maximum of 10 compute nodes providing 160 cores in total for a maximum of 48 hours (at the time of testing).

The MHD problem used as a test was the Orszag-Tang vortex. This test was first introduced by Orszag & Tang (1979) and is often used to test the validity of MHD algorithms implemented in codes. The model tests the ability of a code to simulate the transition from subsonic to supersonic MHD turbulence, the formation of MHD shocks

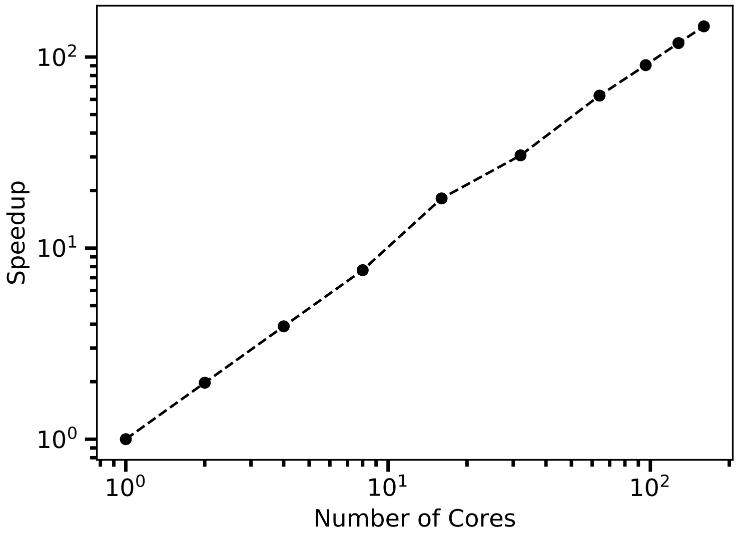

Figure 3.6: Strong scaling of the astrophysical MHD code PLUTO for the standard 2D Orszag-Tang vortex test problem. The test was run on a two dimensional grid with a resolution of 768×768 grid points. Parallalisation is provided by the MPI library. Decomposition of the grid was done onto 1, 2, 4, 8, 16, 32, 64, 96, 128 and finally 160 cores.

and shock-shock interactions as well as test the $\boldsymbol{\nabla} \cdot \boldsymbol{B} = 0$ condition. The Orszag-Tang vortex has become a widely used test in numerical MHD, making it a useful tool for code comparison. A snapshot, mid-simulation, is presented in Fig. 3.5. However, for the purposes of this test it serves to simply illustrate PLUTO's ability to scale with parallel decomposition in 2D.

The results in Fig. 3.6 show the speedup of PLUTO running the Orszag-Tang vortex problem on a 2D Cartesian grid with 768×768 grid points. The problem was run on an increasing number of CPU cores from a single core through to 160 cores distributed over 10 nodes. The logarithmic plot shows an almost linear increase in the speedup as the number of cores increase. A final speedup of ~ 160 corresponds to approximately a one for one gain as the number of CPU cores increase.

This scaling however, is unlikely to increase indefinitely. As the core count increases so too does the cost of sending communication between cores. This occurs because as the grid is decomposed into smaller and smaller regions, the ratio of boundary grid cells (which are communicated between cores) to internal grid cells increases, and therefore so too does the amount of information passed between cores at each time step. The net effect is that with an increase in CPU cores, there is a corresponding decrease in run time which is offset by the increase in communications. This implies that there is some theoretical peak speedup as a function of CPU core count, with the implication that any practical use of PLUTO is not restricted by the number of CPU cores available for a given calculation. However, this limit is not reached by the number of CPU cores used in this test and the scaling is approximately linear.

4

Sub-mm free-free emission from the winds of massive stars in the age of ALMA

This chapter is a reformatted copy of the paper Daley-Yates et al. (2016): “Sub-mm free-free emission from the winds of massive stars in the age of ALMA” and is my own work, aside from Sections 4.3.4 and 4.3.5 which contain text and calculations form co-authors.

4.1 Introduction

The stellar winds of massive stars are driven primarily by absorption in spectral lines and are therefore known as line-driven winds. The theoretical basis for the description of these winds was set out by Castor et al. (1975, hereafter CAK), building on the work by Lucy & Solomon (1970). These winds are distinctive due to a non-linear dependence of the wind acceleration on the local density and velocity gradient. As a result, the wind structure is highly unstable and dynamic in nature (Runacres & Owocki, 2002). These effects make diagnosing the wind structure challenging and their theoretical treatment is an active area of research.

Observations of massive stellar winds are a principal means for diagnosing their properties (Barlow & Cohen, 1977; Prinja & Howarth, 1988; Castor & Lamers, 1979). Both thermal and non-thermal emission is detectable from these stellar winds, but thermal emission provides a large spectral window for characterising the wind properties (Wright & Barlow, 1975; De Becker, 2007). Radio emission from massive stars has historically been the subject of considerable interest, (Braes et al., 1972; Wright et al., 1974; Cohen et al., 1975) and in particular Wright & Barlow (1975, hereafter WB75). Thermal emission from massive stars is not due to processes at the optical photosphere, but free-free interactions between charged species in the ionised wind material (De Becker, 2007). Therefore, any predictions of thermal emission assumes that the stellar surface is radio quiet. This work will explore the region where radio and sub-mm emission is due to multiple factors including the stellar blackbody spectrum and wind acceleration region.

Analytical modelling of the symbiotic nova V1016 Cyg was accomplished by Seaquist & Gregory (1973). This work provided the first early steps towards characterising the radio thermal spectral flux from stellar objects. Seaquist & Gregory (1973) assumed a uniform, spherically symmetric, time-independent, isothermal flow. The resulting spectral flux density as a function of frequency takes the form $S_\nu \propto \nu^\alpha$, where $-0.1 \leq \alpha \leq +2$. This model was built upon in the seminal work conducted by WB75. This highly successful model for the prediction of thermal emission from stellar winds is frequently quoted to explain observational results and justify theoretical conclusions (Blomme et al., 2003; Leitherer & Robert, 1991; Montes et al., 2011). Refinement of the Seaquist & Gregory (1973) model by WB75 leads to a spectral index $\alpha = 0.6$.

WB75 describe how their model agrees well with observation of a selection of massive stars at GHz radio frequencies. Their model is based upon the assumption that the flux originates from the outer reaches of the wind (but still sufficiently close to the star to be considered isothermal) where the velocity can be approximated at all radii, by the wind terminal velocity. Beyond this region, the temperature of the wind is insufficient for full ionisation of the wind and recombination begins to occur (Drew, 1989). At this point, the free-free interactions cease and thermal emission is extinguished.

As the observational frequency increases, emission from the accelerating wind begins to contribute to S_ν. WB75 discuss this and state that an analytic solution which accounts for the acceleration region is not possible. In their paper, WB75 compare the model predictions to both radio and infrared observations of the star P Cygni. They find that the slopes of both data sets independently agree with their predictions. However, it is not until the model is extrapolated from low to high frequencies, that there is a higher level of flux at infrared wavelengths than the model predicts. This implies a steepening in the spectral index.

Several observations conducted at frequencies up to 250 GHz for number of different stellar objects have been carried out. For example, observations of Wolf-Rayet binaries by Montes et al. (2015), however, the focus of the study is the wind-wind collision region and not the initialisation of the wind. Observations of single massive stars conducted at 230 GHz were carried out by Leitherer & Robert (1991). Acceleration and deceleration regions are considered but in the context of the extended wind and not the initialisation region. One study at sub-mm and infrared frequencies of the Wolf-Rayet star γ Velorum by Williams et al. (1990) shows clear deviation from $\alpha = 0.6$ at high frequencies. Nugis et al. (1998) see a steepening in the spectra with $\alpha = 0.77$ and 0.75 for the winds of a sample of WN and WC stars respectively, with the deviation from $\alpha = 0.6$ attributed to clumping of the wind material. Their data is very sparse in the sub-mm range however.

A number of infrared observations of early type stars have been conducted by both Castor & Simon (1983) and Abbott et al. (1984). Castor & Simon (1983) deduced that their observations could not determine the stellar wind velocity laws, leading to large uncertainties in the mass-loss rates of the stars they studied. Abbott et al. (1984) found that the velocity law varies dramatically from star to star, again leading to the large variations in the mass-loss rates. The above examples highlight the importance of the acceleration region as an avenue of exploration into the properties of early type stars and the importance of future observations.

Pittard (2010) briefly discuss the presence of the acceleration region and its impact on the spectral flux, as a preamble to a study of binary O stars. Consequently the calculations are limited to a single set of stellar parameters. However, the frequency range covered in this calculation is extensive and includes the acceleration region.

Telescope technology as been the main limitation to this exploration. With the advent the Atacama large Millimeter/sub-mm Array (ALMA), this situation has changed. ALMA has both simultaneously the spectral window and sensitivity to allow for observations of massive stars which test the full spectrum of their wind. ALMA has several bands covering the range from 84 GHz to 950 GHz. As an example of ALMAs sensitivity, at an observing frequency of 630 GHz (Band 9), with a bandwidth of 7.5 GHz and dual polarisation, a rms sensitivity of $\sim$ 0.25 mJy is achieved with an integration time of 3600 s. These calculations were performed assuming optimal observing conditions, for example lowest water vapor column density and were conducted using the ALMA Sensitivity Calculator available on the ALMA website.

Presented in this work are numerical calculations of the thermal free-free emission from the stellar winds of an ensemble of massive stars. Both accelerating and terminal velocity regions of the wind are accounted for together with a consideration of non-smooth clumped winds. The results are placed into the context of what is observable by ALMA. Comparisons are drawn between the numerical results and the WB75 model. The following section will give a brief overview of the stellar parameters which have been used in this study.

4.2 Stellar parameters

The following stellar parameters are taken from Krtička & Kubát (2012) in the case of the main sequence O-type stars and from Krtička (2014) in the case of the main sequence B-type stars. The values of these parameters are plotted as a function of mass-loss rate, $\dot{M}$, in Fig. 4.1. The stellar parameters of the B-type stars are not displayed as, while they were used to place constraints on the process described below, they are outside the range of stellar parameters used in the calculations. Krtička (2014) and Krtička & Kubát

(2012) derive these stellar parameters from a model non-local thermodynamic equilibrium (NLTE) stellar wind, which they use to derive values of $\dot{M}$. Their values for the stellar effective temperature, T_{eff}, stellar radius, R_* and stellar mass, M_*, are interpolated from formulas derived by Harmanec (1988).

Krtička & Kubát (2012) Considered three groups of stars in their analysis; main sequence, Giants and Supergiants. In our study we only consider their main sequence stars and direct the interested reader to the above paper for details of the models.

Values for the terminal velocity are arrived at by assuming that $v_\infty \approx 3v_{\text{esc}}$, where v_{esc} is the stellar escape velocity, with $v_{\text{esc}} = \sqrt{2GM_*(1-\Gamma_{\text{e}})/R_*}$. Γ_{e} is the Eddington parameter of the star which is derived in turn from the stellar luminosity; $\Gamma_{\text{e}} = \sigma_{\text{e}}L_*/(4\pi \text{G}M_*)$ where it is assumed that $L_* = 4\pi R_*^2\sigma T_{\text{eff}}^4$ with σ the Stefan-Boltzmann constant. σ_{e} is the electron scattering opacity and G is the gravitational constant. Throughout this study the distance between the star and the observer will be kept constant for all stellar models at $D = 0.5$ kpc.

By plotting each of these stellar parameters as a function of $\dot{M}$, a series of polynomials can be optimised via the least squares method to give a functional relationship between $\dot{M}$ and T_{eff}, R_* and M_*. The polynomial fitted is 2^{nd} order in $\log_{10}(\dot{M})$ and takes the form

$$f(\dot{M}) = a + b\log_{10}(\dot{M}) + c\left(\log_{10}(\dot{M})\right)^2, \tag{4.1}$$

where $f(\dot{M})$ is the stellar parameter that is being calculated and a, b and c are fit parameters which undergo optimisation. Equation (4.1) is also shown in Fig. 4.1 as the black line in each graph.

Equation (4.1) assumes an oversimplified relationship between $\dot{M}$ and the stellar parameters. For example, the model only accounts for main sequence B-type and O-type stars and not Giants or Supergiants. However, it has captured the essential scaling between $\dot{M}$ and the other parameters over the range of $\dot{M}$ values considered in this work.

Some care is required when considering the range of $\dot{M}$ values to use during the calculations. A star with a high mass and correspondingly high $\dot{M}$ together with an

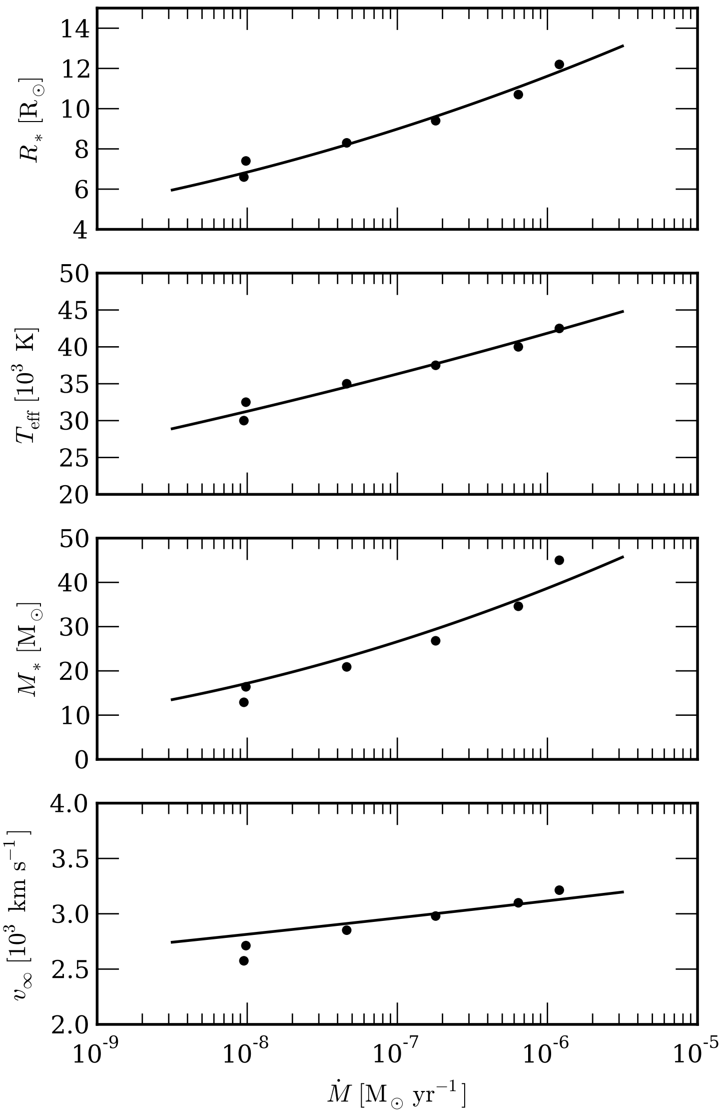

Figure 4.1: Stellar parameters used by both the WB75 analytic model and numerical model presented in this work, to calculate the spectral flux density for a series of massive stars with mass-loss rate in the range $10^{-8.5}$ M$_\odot$ yr^{-1} $< \dot{M} < 10^{-5.5}$ M$_\odot$ yr^{-1}. The data are taken from Krtička & Kubát (2012).

Table 4.1: The assumed stellar parameters for the calculated models.

Model	$\dot{M}$	R_*	T_{eff}	M_*	v_∞	v_{esc}	$\log_{10}(\frac{L_*}{L_\odot})$	Γ_{e}
Units	[$M_\odot$/yr]	[$R_\odot$]	[10^3 K]	[$M_\odot$]	[10^3 km/s]	[10^3 km/s]		
S0	$10^{-5.5}$	13.1	44.7	45.7	3.20	1.07	5.75	0.31
S1	$10^{-6.0}$	11.6	41.9	38.8	3.12	1.04	5.53	0.22
S2	$10^{-6.5}$	10.2	39.0	32.3	3.04	1.01	5.30	0.15
S3	$10^{-7.0}$	9.0	36.3	26.6	2.96	0.99	5.06	0.11
S4	$10^{-7.5}$	7.9	33.7	21.6	2.89	0.96	4.82	0.08
S5	$10^{-8.0}$	6.8	31.3	17.2	2.81	0.94	4.56	0.05

intense luminosity, will have a large effective radius at radio wavelengths (which will be discussed in Section 4.3.1) even at high radio frequencies and the opposite is true for a low mass star. As such, the influence of the acceleration region, may not be within the observable frequencies of the current generation of radio telescopes. To account for this, a suitable range for $\dot{M}$ was chosen and found to be 10^{-8} $M_\odot$ yr^{-1} $< \dot{M} <$ $10^{-5.5}$ $M_\odot$ yr^{-1}, with six models designated S0 - S5, where "S" refers to "smooth", with mass-loss rates evenly spaced by 0.5 dex. Table 4.1 displays the final parameters that were used to perform the calculations set out below. For all models the mean ion charge $Z = 1.128$ and the ratio of electron and ion number densities $\gamma = 1.09$, were kept constant.

By investigating the above range of possible $\dot{M}$ values, it can be determined whether any deviation from a constant spectral index is observed when a non-terminal velocity flow is taken into account and within the range of current observatories.

4.3 Emission Models

This section will review the theoretical basis of both terminal velocity and accelerating winds, followed by a discussion of the concept of a frequency dependent effective stellar radius. The Gaunt factor plays an important role in these concepts and as such a review of recent high precision calculation of this factor is given. The effect of clumping on the spectral flux is also considered and a limited set of calculations presented. Finally, the numerical setup of the calculations are communicated.

4.3.1 Terminal velocity stellar wind

The model developed by WB75 assumes the winds has both spherical symmetry as well as terminal velocity. The principle results of this theory are outlined below.

The spectral flux density, S_ν, at a distance D from the star is given by the integral of the intensity of radiation, $I(\nu, T)$, along a line of sight from an observer to the star:

$$S_\nu = \int_0^\infty \frac{I(\nu, T)}{D^2} 2\pi q \mathrm{d}q. \tag{4.2}$$

Here the impact parameter q gives the radial distance from the star, perpendicular to the line of sight of the observer in a cylindrical geometry. A rigorous treatment of the solution to this integral is given in WB75. For the purpose of this work it is sufficient to simply state the result:

$$S_\nu = 23.2 \left(\frac{\dot{M}}{\mu v_\infty} \right)^{4/3} \frac{\nu^{2/3}}{D^2} \left(\gamma g_{\mathrm{ff}} \overline{Z^2} \right)^{2/3} . \tag{4.3}$$

Here μ is the mean atomic weight of the gas, v_∞ is the terminal velocity of the outflowing stellar material in km s^{-1}, ν is the frequency of emitted radiation in Hz, D is the distance of the object from the observer in kpc, g_{ff} is the free-free Gaunt factor (see Section 4.3.2), γ is the ratio of the electron and ion number densities, $\overline{Z^2}$ is the mean squared ion charge and the flux, S_ν, is measured in Jy. Equation (4.3) is valid in the region of the spectrum in which $h\nu \ll k_{\mathrm{B}} T_{\mathrm{eff}}$, limiting its applicability to infrared and radio frequencies.

The above analysis leads to the spectral index $\alpha = 2/3$, and therefore $S_\nu \propto \nu^{2/3}$. However, the Gaunt factor, g_{ff}, has a slight frequency dependence (see Section 4.3.4). With this additional consideration, $S_\nu \propto \nu^{0.6}$, at GHz frequencies.

Rearrangement of equation (4.3) allows for the definition of an effective radius, R_ν (WB75), which represents the inner limit from which emission can propagate through the wind to the observer. Therefore, at a given frequency the total flux emitted is due to the material exterior to R_ν. Equation (4.4) gives this radius in terms of the wind parameters discussed above:

$$R_\nu = 2.8 \times 10^{28} \left(\gamma g \overline{Z^2}\right)^{1/3} T^{-1/2} \left(\frac{\dot{M}}{\mu v_\infty \nu}\right)^{2/3}, \tag{4.4}$$

where all the symbols have the same units as above and R_ν is measured in cm. As has already been mentioned, the model constructed by WB75 makes a number of assumptions about the geometry, composition and homogeneity of the circumstellar material, such as spherical symmetry and terminal wind velocity. See Section 4.3.3 for an in-depth discussion of the effective radius, R_ν.

A numerical approach allows for these assumptions to be relaxed and for the acceleration region to be included in the calculations. For this to be accomplished, the wind density profile must be specified according to the velocity profile given by the results of CAK theory. The following section describes this process.

4.3.2 Accelerating stellar wind

The theory set out below follows closely the method used by Stevens (1995). The formulation of the problem that is presented here begins in a 3D Cartesian geometry. Refinement of the model then reduces it to cylindrically geometry. This is accomplished by first generating a 3D grid and assigning a value of density to each grid point. For the simple case of a spherically symmetric, monotonically increasing velocity wind, the density is given by:

$$n_\mathrm{i} = \frac{\dot{M}}{4\pi \mu_i m_\mathrm{H} r^2 v(r)} = \frac{A}{r^2} \tag{4.5}$$

where μ_i is the mean mass per ion in (amu), m_H is the proton mass and n_i is the wind ion density. This density profile comes directly from mass conservation and is a general result for a stellar wind. What makes the density profile specific to a particular star is the form which $v(r)$ takes. In the case of a massive star with a CAK wind, $v(r)$ can be represented by:

$$v(r) = v_\infty \left(1 - R_*/r\right)^\beta, \tag{4.6}$$

where β determines the steepness of the velocity profile. A large β value leads to a more gradual acceleration and vice versa. Hence, larger values of β allow the acceleration region of the star to protrude further into the wind.

We have assumed this velocity law, however there are numerous other velocity laws which could have been employed, see Müller & Vink (2008) for an in depth comparison of alternatives to equation (4.6). In addition, it is now thought that massive stars have a small sub-surface convection zone (Cantiello, 2009) and this region may well be responsible for generating the perturbations that give rise to clumping in the wind (see Section 4.3.5).

Equation (4.6) assumes spherical symmetry, deviations from this would affect the resulting radio flux, however the effect is not usually large. For simplicity we ignore non-spherical symmetry in this work (see Schmid-Burgk 1982 for a discussion of non-spherical symmetry for terminal velocity wind models and simple geometries).

Defining the Cartesian coordinates x, y and z, where x is the direction of the line of sight of the observer (where the observer is situated at $x = +\infty$). The total intensity $I_\nu(y, z)$ in terms of the Planck function $B_\nu\left[T(x, y, z)\right]$ and the optical depth $\tau(x, y, z)$ is:

$$I_\nu(y, z) = \int_{-\infty}^{+\infty} B_\nu\left[T(x, y, z)\right] \exp(-\tau(x, y, z)) \kappa_{\mathrm{ff}}(x, y, z) \mathrm{d}x, \tag{4.7}$$

in which $\kappa_{\mathrm{ff}}(x, y, z)$ is the free-free absorption coefficient given by $\kappa_{\mathrm{ff}} = \kappa_{\mathrm{e}}\rho$ where κ_{e} is the electron scattering opacity.

The infinitesimal optical depth of the wind material across the distance $\mathrm{d}x$ can be defined as $\mathrm{d}\tau = -\kappa_{\mathrm{ff}}(x, y, z)\,\mathrm{d}x$, where the negative symbol indicates that τ decreases from the observer to the point of emission (Stevens, 1995). Substitution of this expression into equation (4.7) allows for it to be recast in terms of the maximum optical depth, $\tau_{\max}$, along the observers line of sight, which results in the line of sight intensity

$$I_\nu(y, z) = B_\nu\left(T\right) \int_0^{\tau_{\max}(y,z)} \exp(-\tau(x, y, z)) \mathrm{d}\tau, \tag{4.8}$$

where the isothermal assumption has been applied to allow the Planck function to be removed from the integrand. Integration of equation (4.8) leads to

$$I_\nu(y,z) = B_\nu\left(T\right)\left[1 - \exp(-\tau_{\mathrm{max}}(y,z))\right], \tag{4.9}$$

therefore $I_\nu(y,z)$ is only a spacial function of $\tau_{\mathrm{max}}(y,z)$, along each column in x. At radio and sub-mm frequencies $hv \ll k_{\mathrm{B}}T$, leading to $B_\nu(T) \sim 2k_{\mathrm{B}}T_{\mathrm{eff}}\nu^2/c^2$. where h is Planck's constant. At this point the wind temperature, T, has been replaced by the stellar effective temperature, T_{eff}, an assumption we make for the remainder of this work.

Under the same condition which allows the Planck function to be simplified, $\kappa_{\mathrm{ff}}(x,y,z)$ can be re-expressed as a function of frequency and temperature such that

$$\kappa_\nu(T_{\mathrm{eff}}) = 0.0178\frac{Z^2 g_{\mathrm{ff}}}{T_{\mathrm{eff}}^{3/2}\nu^2}n_{\mathrm{e}}n_{\mathrm{i}} = K_\nu(T_{\mathrm{eff}})n_{\mathrm{e}}n_{\mathrm{i}}. \tag{4.10}$$

This expression retains its spacial dependence due to n_{e} and n_{i}, which are the local electron and ion number densities respectively. g_{ff} is the free-free Gaunt factor (see Section 4.3.4) given by:

$$g_{\mathrm{ff}} = 9.77 + 1.27\log_{10}\left(\frac{T_{\mathrm{eff}}^{3/2}}{\nu Z}\right) \tag{4.11}$$

(Stevens, 1995).

The number densities n_{e} and n_{i} are related through the ratio $\gamma = n_{\mathrm{e}}/n_{\mathrm{i}} \sim 1$, allowing the electron number density to be removed from the expression and replaced by $n_{\mathrm{e}} = \gamma n_{\mathrm{i}}$. The value of γ is dependent upon the wind metallicity (which is assumed to be solar). For solar abundances γ will be approximately independent of radius as long as H is fully ionised. Following from equation (4.10), $\mathrm{d}\tau = K(\nu,T)\gamma n_{\mathrm{i}}^2\mathrm{d}x$, allowing τ_{max} in equation (4.9) to be written as:

$$\tau_{\mathrm{max}}(y,z) = \int_{-\infty}^{+\infty}\gamma K_\nu(T_{\mathrm{eff}})n_{\mathrm{i}}^2(x,y,z)\mathrm{d}x. \tag{4.12}$$

Bringing together equations (4.2) and (4.9) gives the total flux,

$$S_\nu = \frac{B_\nu\,(T_{\rm eff})}{D^2}\int_0^\infty \left[1-\exp(-\tau_{\rm max}(y,z))\right]{\rm d}y{\rm d}z, \tag{4.13}$$

from the wind.

We have assumed $T = T_{\rm eff}$, the flux $S_\nu \propto B_\nu K_\nu^{2/3}$. Here $B_\nu \propto \nu^2 T_{\rm eff}$ and $K_\nu \propto \frac{g_{\rm ff}}{\nu^2 T_{\rm eff}^{3/2}}$, so that $S_\nu \propto \nu^{2/3} g_{\rm ff}^{2/3}$, which is the same result as in WB75. Consequently, S_ν is largely independent of the assumed value of T (assuming that the wind remains largely ionised), or rather only has a small T dependence through the Gaunt factor (Schmid-Burgk, 1982). Therefore, models with an assumed temperature gradient will yield rather similar results to those presented here.

Together, equations (4.12 and 4.13) allow for the calculation of free-free thermal radio emission from a density distribution, $\rho(r)$. However, these equations are still continuous and in order for them to be applied to a discrete density grid, they need to be discretized. This is a trivial step and involves simply replacing the integrals over the three Cartesian coordinates, x, y and z, with summations.

Moving from Cartesian to cylindrical geometry reduces the computational demand of the calculation. This is done by dropping the dependence upon y, and the summation over that coordinate and then multiplying by $2\pi z$, where $0 < z < z_{\rm max}$. Both the maximum optical depth and total flux are then written in cylindrically symmetric, numerical form as:

$$\tau_{\rm max}(z) = \gamma K_\nu(T_{\rm eff})\sum_x n_{\rm i}^2(x,z) \tag{4.14}$$

and

$$S_\nu = \frac{2\pi B_\nu\,(T_{\rm eff})}{D^2}\sum_z \left[1-\exp(-\tau_{\rm max}(z))\right] z. \tag{4.15}$$

These two equations form the final expressions that were used to generate the results presented in Section 4.4.

4.3.3 Effective radius and acceleration

WB75 defined the characteristic radius by taking the point at which the free-free optical depth $\tau_{ff} = 0.244$. The physical meaning of this characteristic radius (discussed in Section 4.3.1) is rather vague (and has often been over-interpreted) and other characteristic radii can be defined. For example Panagia & Felli (1975) define their characteristic radius as that radius from within which half the free-free flux originates.

The WB75 characteristic radius is defined as the radius where, for all radii greater than this, the wind material is optically thin and contributes to the total emission. The flux of optically thin free-free emission from radii in this range ($R_\nu < r < \infty$) is:

$$F_\nu = \frac{1}{D^2} \int_{R_\nu}^{\infty} 4\pi r^2 j_{ff}(r) dr \tag{4.16}$$

with

$$j_{ff} = 1.4 \times 10^{-27} T_{\text{eff}}^{1/2} n_e n_i g_{ff}. \tag{4.17}$$

A more useful definition, suggested by Van Loo et al. (2004), is to define a characteristic radius as that radius where $\tau_{ff} = 1$ (integrating from infinity down to a radius R_ν). For a terminal velocity, spherically symmetric wind this is easy to calculate. Therefore, the free-free optical depth from ∞ to an effective radius R_ν is

$$\tau_{ff} = \gamma K_\nu(T_{\text{eff}}) A^2 \int_{R_\nu}^{\infty} \frac{1}{r^4} dr = \frac{\gamma K_\nu(T_{\text{eff}}) A^2}{3 R_\nu^3}. \tag{4.18}$$

Rearranging for R_ν:

$$R_\nu = \left[\frac{\gamma K_\nu(T_{\text{eff}}) A^2}{3\tau_{ff}} \right]^{1/3}. \tag{4.19}$$

The radius ratio between models with $\tau_{ff} = 1.0$ and $\tau_{ff} = 0.244$ (i.e. the WB75 characteristic radius) is then $R_\nu(\tau_{ff} = 1)/R_\nu(\tau_{ff} = 0.244) = 0.62$, Bringing R_ν closer to R_* for $\tau_{ff} = 1$. Expressing this in convenient units we have that

$$R_\nu(\tau_{ff} = 1) = 1.75 \times 10^{28} Z^{2/3} g_{ff}^{2/3} T^{-1/2} \left(\frac{\dot{M}}{\mu v_\infty \nu} \right)^{2/3} \tag{4.20}$$

with $\dot{M}$ in $M_\odot$ yr^{-1} and v_∞ in km s^{-1}.

Using model S1 as a representable set of stellar parameters, at an observing frequency of, 600 GHz, we have $R_\nu(\tau_{ff} = 1) = 1.7\ R_*$ and at 900 GHz, $R_\nu(\tau_{ff} = 1) = 1.3\ R_*$. For a $\beta = 0.8$ wind acceleration model, we are already clearly deep in the wind acceleration zone. At this frequency, for models with lower mass-loss rates, a terminal velocity wind may lead to a characteristic radius smaller than the stellar radius. Meaning that wind acceleration must be accounted for within the ALMA bands. However, this is only true for a constant velocity model, $R_\nu(\tau_{ff} = 1)$ is a general quantity and can easily be calculate in the case of an accelerating wind. There are analytic solutions for the free-free optical depth for some β wind velocity models (equation (4.6)). We can find solutions for $\beta = 1/2$, $\beta = 1$, $\beta = 3/2$, $\beta = 2$ and so on. In this case we have the nucleon density

$$n_{\rm i} = \frac{A}{r^2(1 - R_*/r)^\beta} \tag{4.21}$$

and the free-free optical depth from infinity to a radius R_ν given by

$$\tau_{ff} = \gamma K_\nu(T_{\rm eff}) \int_{R_\nu}^{\infty} n_{\rm i} dr = (\gamma K_\nu(T_{\rm eff}) A^2) I(\beta) \tag{4.22}$$

where $I(\beta)$ is an integral whose solution specifically depends on the velocity law. When $\beta = 0$ we have $I(0) = 1/(3R_\nu^3)$, giving the earlier expression of equation (4.19).

For $\beta = 2$ we have the following integral

$$I(\beta = 2) = \int_{R_\nu}^{\infty} \frac{dr}{r^2(1 - R_*/r)^2} = \frac{1}{3} \left[\frac{1}{(R_\nu - R_*)} \right]^3 \tag{4.23}$$

which reduces to the constant velocity result when $R_\nu \gg R_*$ (which is obviously the

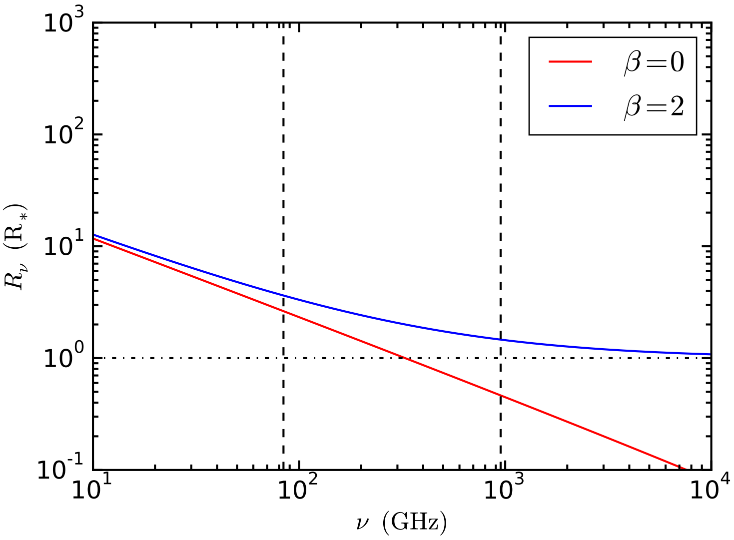

Figure 4.2: Effective radio photosphere radius as a function of frequency for velocity laws with $\beta = 0$ and $\beta = 2$. $\beta = 0$ corresponds to the WB75 model where $S_\nu \propto \nu^{0.6}$. As β increases there is deviation from this linear model as in the case of $\beta = 2$. All non zero values of β are asymptotic to $R_\nu = 1$, only for a velocity law where $\beta = 0$ does R_ν value less than R_*. The vertical dashed lines indicate the ALMA frequency range for bands 3 - 9.

case). Substituting equation (4.23) into equation (4.22);

$$\tau_{ff} = (\gamma K_\nu(T_{\text{eff}})A^2)\frac{1}{3}\left[\frac{1}{(R_\nu - R_*)}\right]^3 \tag{4.24}$$

and rearranging gives

$$R_\nu = \left[\frac{\gamma K_\nu(T_{\text{eff}})A^2}{3\tau_{ff}}\right]^{1/3} + R_*. \tag{4.25}$$

Equation (4.25) is identical to equation (4.19) with the addition of an extra term on the right hand side, R_*. This accounts for the characteristic radius being asymptotic to R_* at higher frequencies ($\nu > 100$ GHz). Fig. 4.2 shows R_ν for both $\beta = 0$ and $\beta = 2$ with $\tau_{ff} = 1$.

For model S1, at an observing frequency of $\nu \approx 900$ GHz, the WB75 model results in $R_\nu \approx 0.5R_*$ which is obviously non-physical, however the accelerating wind model results in $R_\nu \approx 1.7R_*$, which has physical meaning. This difference shows the importance in accounting for the wind acceleration region at high radio and sub-mm wavelengths.

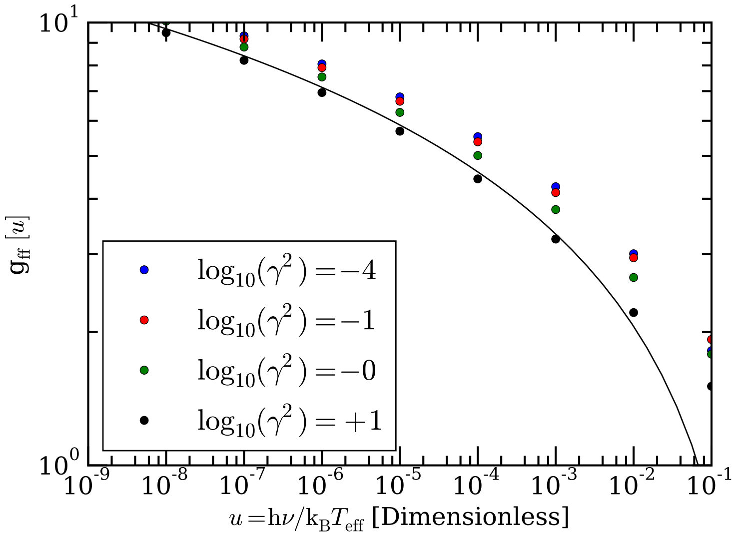

Figure 4.3: The free-free Gaunt factor, g_{ff}, as a function of the parameter $u = h\nu/k_{\mathrm{B}}T_{\mathrm{e}}$ for several values of γ. The solid line represents equation (4.11) and the data are from Van Hoof et al. (2014).

4.3.4 Gaunt factor

A recent study by Van Hoof et al. (2014) has improved the understanding of g_{ff}, by performing calculations at unprecedented accuracy and across a larger parameter space than has thus far been attempted. Van Hoof et al. (2014) communicate an extensive data set, allowing testing of the equation (4.11). Van Hoof et al. (2014) provide values of the Gaunt factor as a function of $u = h\nu/k_{\mathrm{B}}T_{\mathrm{e}}$ and $\gamma = Z^2\mathrm{Ry}/k_B T_{\mathrm{e}}$. Here T_{e} is the electron temperature and Ry is the infinite-mass Rydberg unit of energy (13.606 eV). Under the isothermal assumption $T_{\mathrm{e}} = T_{\mathrm{eff}}$, for $T_{\mathrm{eff}} = 40 \times 10^3$ K, u falls within the range $10^{-5} < u < 10^{-2}$.

Fig. 4.3 plots a selection of results from Van Hoof et al. (2014) along with equation (4.11). Due to the good agreement between the data and equation (4.11) (with only a slight deviation at higher values of u) and the relatively weak dependence of S_ν on $g_{\ \mathrm{ff}}$, equation (4.11) was deemed to be sufficiently accurate for the temperature and frequency ranges that were investigated.

4.3.5 Wind clumping and the clumping factor

Due to the instabilities inherent in line-driven stellar winds (Owocki et al., 1988) we expect the winds of massive stars to be clumped and it is highly likely that the degree of clumping will vary strongly with radius. Such a radially varying clumping will have an impact on the spectral shape of the radio/sub-mm emission from massive stars. Clumping has been discussed in the literature already, for example, WB75, Abbott et al. (1981) and Van Loo et al. (2004, 2006) amongst others.

If the clumping is constant throughout the wind, for a specific mass-loss rate, the flux will be raised uniformly across all wavelengths. This means that there will be an over estimate of the mass-loss rate. If the clumping is not constant then the effect will be different at different wavelengths, allowing the possibility of a more detailed investigation of how clumping varies radially.

Clumping has also been included in spectral modelling of the optical/IR part of the spectrum, for example Hillier & Miller (1999) and Oskinova et al. (2007).

Oskinova et al. (2007) discussed the difference between microclumping and macroclumping. The basic assumption of microclumping is that the wind clumps are small compared to the mean free path of photons (i.e. optically thin). In spectral lines this may not be true (where the line centre can have a large optical depth). Where clumps are optically thick (or optically thick at some frequencies) this is generally referred to as "macroclumping" and here concepts of porosity in the wind come into play (see Owocki & Cohen, 2006 for a discussion of the possible impact of macroclumping and porosity on the X-ray line profiles of massive stars).

Ignace (2016) has discussed the consequences of different forms of macroclumping on the expected radio/sub-mm spectra of the winds of massive stars. Here we focus on microclumping and specifically radially varying microclumping.

For the continuum free-free processes it is likely to be the case that we are dealing with microclumping for much of the wind. Remember though that the free-free opacity is a strong function of frequency and density ($\propto (n_i n_e)/\nu^2$) and so a clump that is optically thin at high frequencies will become optically thick at low frequencies.

For the clumped wind calculations presented here, we assume that the wind consists of small, optically thin clumps. These clumps fill a volume f_V and an inter clump medium that is essentially a void. This is clearly a major assumption and we would expect a range of clump densities at all radii. Following on from Runacres & Owocki (2002), the clumping factor f_{cl} is defined as

$$f_{cl} = \frac{<\rho^2>}{<\rho>^2} = \frac{1}{f_V}\,. \tag{4.26}$$

Where ρ is the wind density and the symbol $<>$ is the time average of the quantity. In this case $f_{cl} > 1$ and $f_V < 1$. Optical analyses have suggested quite large values of $f_{cl} \sim 10-50$ in the inner wind, where the optical lines are formed (Crowther et al., 2002; Bouret et al., 2005). However, clumping factors of 50 would have a very large effect on the results and it is unlikely that such large clumping factors are correct, see Oskinova et al. (2007), as such we have not used factors of this magnitude in this work. The maximum clumping factor used here is $f_{cl} = 2$.

In general, for the case were f_{cl} is constant throughout the wind, then the flux S_ν from a clumped wind scales as $S_\nu \propto (\dot{M}^2 f_{cl})^{2/3}$, so that the presence of clumping reduces the mass-loss required to give the same level of emission.

There are several different versions for the assumed form of clumping. Hillier & Miller (1999); Bouret et al. (2005) used this form for the *volume filling* clumping factor in calculations using the CMFGEN code:

$$f_V(r) = f_{V,\infty} + (1 - f_{V,\infty})e^{-v(r)/v_{cl}} \tag{4.27}$$

where $v(r)$ is the wind velocity as a function of radius r (For all clumped wind models present here, $v(r)$ is assumed to have the form of equation (4.6) with $\beta = 0.8$) and v_{cl} is the velocity at which clumping starts. The parameter $f_{V,\infty}$ is effectively the volume filling clumping factor at large radii.

Typical values discussed in terms of fitting optical line profiles are $f_{V,\infty} = 0.1$ and $v_{cl} = 30$ km s^{-1} Bouret et al. (2005), i.e. clumping starts very close to the star and there is a very significant degree of clumping. Also, in this model the wind stays clumped out to large radii, once clumped the wind does not become unclumped. It is worth noting that optical line profiles do not seem to be that sensitive to clumping and are formed closer to the star, as compared to the bulk of the radio/sub-mm emission.

Related to this, Schnurr & Crowther (2008) have suggested another prescription for the clumping, namely

$$f_V(r) = f_{V,max} + (1 - f_{V,max}) \left[e^{-v(r)/v_1} + e^{(v(r)-v_\infty)/v_2}\right] \tag{4.28}$$

where v_1 and v_2 are constants and $f_{V,max}$ sets the minimum value of the volume filling clumping factor (i.e. maximum clumping). In contrast to the previous case, $f_V(r) \to 1$ as $r \to \infty$. We adopt this clumping law here and note that it resembles (in very broad outline only) the results from the theoretical calculations of Runacres & Owocki (2002). We have not attempted to adjust the clumping parameters (v_1, v_2, $f_{V,max}$) to reproduce their results. We note that the clumping in the Runacres & Owocki (2002) results is rather more pronounced, with a peak clumping parameter $f_{cl} > 10$, and with the peak clumping occurring at around $10 - 20R_*$ (at rather larger radii than assumed here). The radially varying volume filling clumping factors are shown in Fig. 4.4, excluding the constant clumping models for sake of clarity. Table 4.2 shows the clumped wind models C0 - C3 used in this study, which all have an underlying smooth wind model given by model S2.

With this parameterisation of clumping we can recalculate the expected radio/sub-mm emission, using the prescription described earlier, using the clumped values of the density in each cell, with $\rho_{cl} = \rho_{sm}/f_V$, with ρ_{cl} the clumped density at a given radius, ρ_{sm} the smooth density at a given radius and f_V as above. In addition, in each cell the clumps comprise only a fraction f_V of the path, the rest being a void.

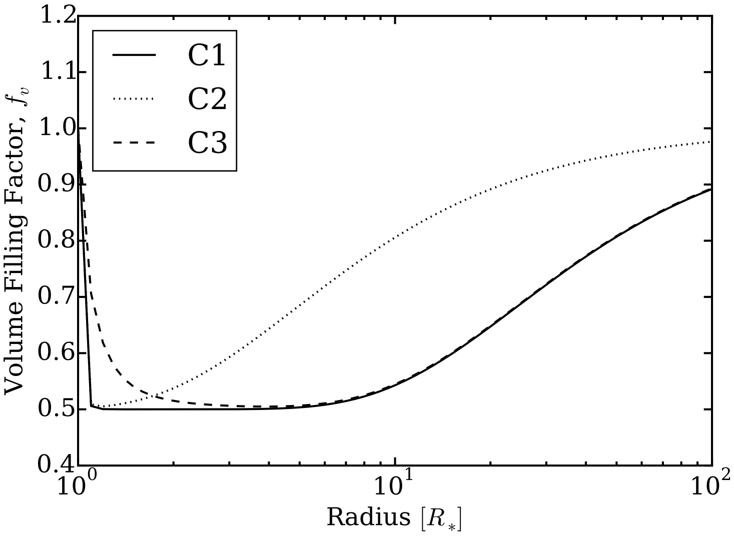

Figure 4.4: The radially dependent volume filling clumping parameter for the models set out in Table 4.2. The uniform clumping models have $f_V = 1$ for the smooth model (Model S2) and $f_V = 0.5$ for the uniform clumping model (Model C0). neither of these lines are shown for purposes of clarity.

Table 4.2: The parameters used for the clumping model.

Model	f_{max}	v_1	v_2	Comment
S2	1.0	0	0	No clumping
C0	0.5	0	0	Uniform clumping
C1	0.5	100	100	Radially dependent clumping
C2	0.5	100	500	Less clumping at large r
C3	0.5	500	100	Less clumping at small r

4.3.6 Numerical setup

A grid was initialised for $\{x_i, z_j\}$ with $x_{i_{\max}} = 2 \times 10^5$, approximately covering the range $-1800\ R_* < x < 1800\ R_*$, and $z_{j_{\max}} = 1 \times 10^5$, approximately covering the range $0 < z < 1800\ R_*$. This gives and inter-grid spacing $\Delta x = \Delta z = 0.018\ R_*$. This grid covers a 2D spatial extent, which encompasses the outer regions of the stellar wind while still having the necessary resolution to resolve the flux from close to the stellar surface. The star is located at the origin of the coordinate system, at the centre of the lower edge of the domain. Using equations (4.5) and (4.6), the grid is populated with ion number densities.

The calculations are performed according to the theory defined in Section 4.3.2; the maximum optical depth, $\tau_{\max}(z)$, for each column in x (along the line of sight) is calculated using equation (4.14). Then summing all values of $\tau_{\max}$ with equation (4.15) gives the total flux S_ν. The region where $r < R_*$ was set to an arbitrarily large value, such that it appears as an optically thick medium. Finally, S_ν is calculated according to the WB75 method (i.e assuming a terminal velocity wind) using equation (4.3), which we shall refer to as $S_{\nu,WB75}$. The next section will present, compare and discuss the results of these calculations.

4.4 Results and discussion

Fig. 4.5 presents S_ν for models S0 - S5 calculated using equations (4.14) and (4.15). For each $\dot{M}$ there is clear deviation from the S_ν predicted by WB75. The numerical calculations initially agree with the analytic theory for $\nu < 10^2$ GHz. Beyond this, the gradient increases and eventually merges with the Rayleigh-Jeans (RJ) part of the stellar blackbody spectrum for $\nu > 10^3$ GHz. This can be seen clearly in the upper right panel of Fig. 4.6 which shows α as a function of ν. Initially $\alpha = 0.6$, corresponding to the WB75 prediction. As the observing frequency increases, α increases ever more rapidly before levelling off with $\alpha \to 2$ for $\nu > 3 \times 10^3$ GHz. The transition between these two values encompasses both the effect of the acceleration region and the point at which the RJ tail

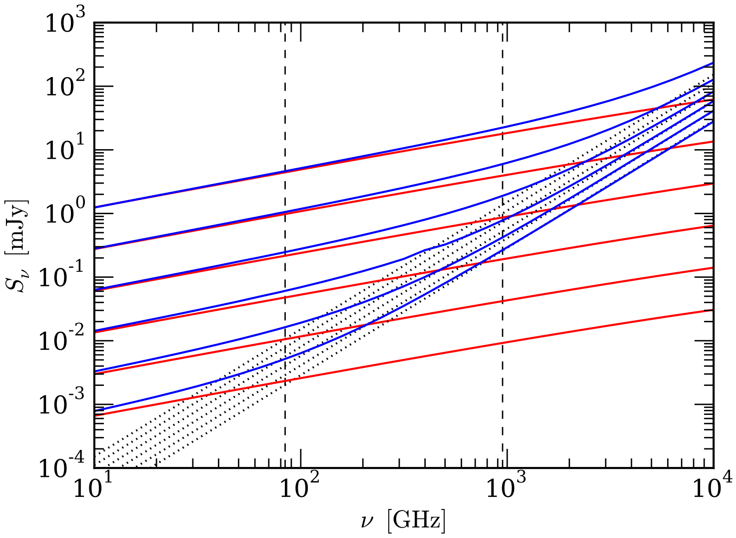

Figure 4.5: The predicted radio flux, S_ν, from our ensemble of stellar models, assuming a distance of 0.5 kpc and wind velocity parameter $\beta = 0.8$. The results are shown as a function of ν for stellar models S0 - S5. The thermal radio emission results from the terminal velocity WB75 model are shown as the red lines. The numerical results from the new accelerating wind models are the blue lines. The black dotted lines are the RJ curves of the emission from the stellar surface. Each separate set of lines corresponds to a different value of $\dot{M}$, increasing from bottom to top as the mass-loss rate increases. The vertical dashed lines indicate the ALMA frequency range for bands 3 - 9.

begins to contribute significantly to the total spectral flux.

The observing frequency at which the acceleration region begins to contribute is sensitively dependent upon $\dot{M}$. A sufficiently low $\dot{M}$ leads to the acceleration region contributing to S_ν at a flux level which is unobservable by ALMA (if the star is at approximately 0.5 kpc). This is the case for the lower end of the $\dot{M}$ range, for example the bottom curve of Fig. 4.5. For these curves, the RJ contribution to the spectral flux is completely dominant in the ALMA frequency range.

In contrast, if an $\dot{M}$ is too high, the acceleration region will contribute to S_ν at a frequency which is higher than the spectral window of ALMA. This does not occur for the $\dot{M}$ range used during this study. The model with largest value of $\dot{M}$, model S0, which corresponds to the top curve in Fig. 4.5, shows a clear divergence from the WB75 prediction and is sufficiently separate from the RJ tail in frequency space to not be effected by its presence. As such, the deviation predicted by the numerical model for the largest value of $\dot{M}$ in this study is due to the acceleration region and is within ALMA's spectral

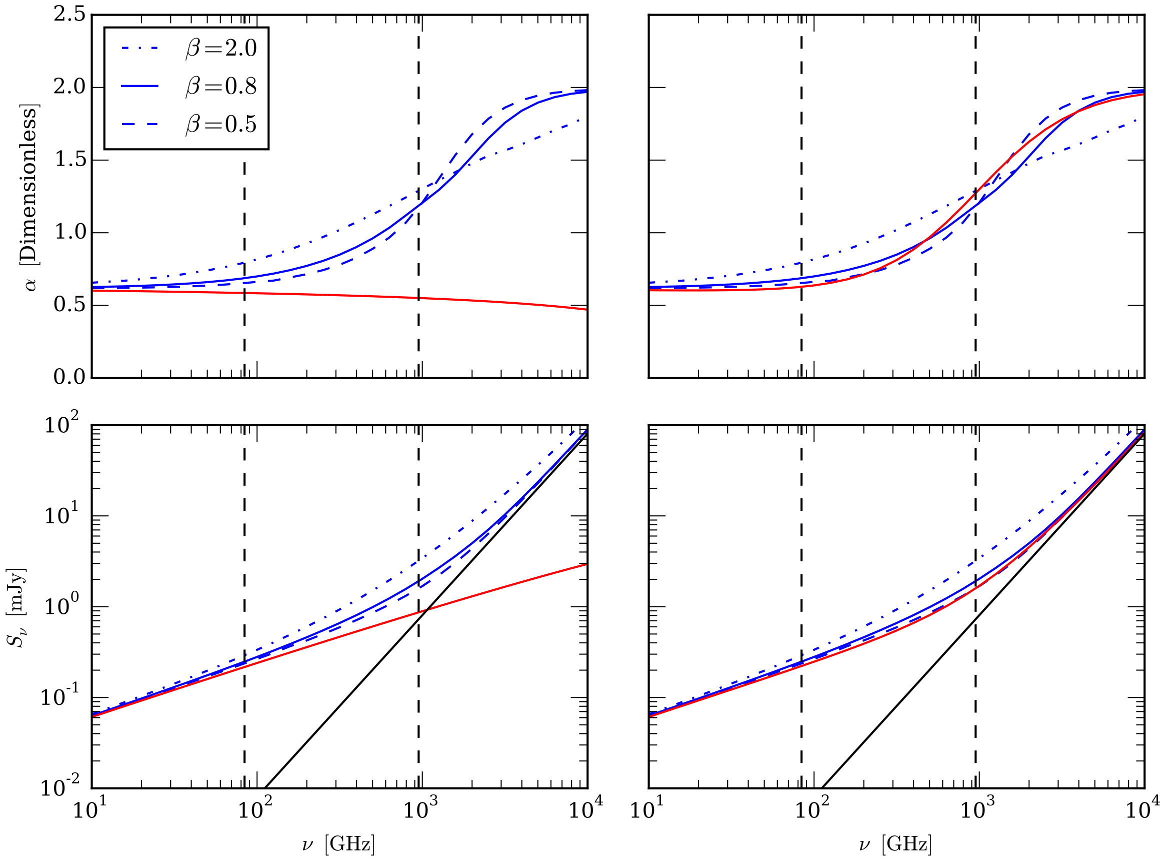

Figure 4.6: The predicted radio flux, S_ν (bottom row of diagrams), and spectral index, α (top row of diagrams), for wind model S2. The red lines indicate the result from the WB75 model and the blue lines indicate the results for the numerical model. There are three separate values for the velocity law parameter: $\beta = 0.5$, $\beta = 0.8$ and $\beta = 2.0$, indicated by the dashed line, the solid line and the dot-dashed line respectively. The straight black lines indicate the RJ curve of the stellar surface. The right hand column is distinct from the left due to the RJ curve having been added to the WB75 result. The vertical dashed lines approximately indicate the ALMA frequency range. The vertical dashed lines indicate the ALMA frequency range for bands 3 - 9.

window. This is non obvious in Fig. 4.5 due to the logarithmic scale.

The point at which the gradient begins to change occurs at an increased observing frequency for each increase in $\dot{M}$. The reason for this is that a higher value of $\dot{M}$ leads to larger R_ν, requiring a higher observing frequency to see through the wind to the same location. Conversely, at a fixed $\dot{M}$, increasing the observing frequency decreases R_ν until it reaches R_*. However, there is an upper limit on the observing frequency, given by ALMA's spectral window, $\nu < 10^3$ GHz. The balance between $\dot{M}$ and observing frequency is key for determining whether the acceleration region of a star's wind is detectable by ALMA.

The physical reasoning behind the increase in S_ν when the acceleration region is taken into account, is that the wind material must undergo acceleration from rest to the terminal velocity. This acceleration leads to a wind density which is greater than would be present if the wind were initial travelling at terminal velocity. Since $\tau_{\max} \propto n_{\mathrm{i}}^2 \propto \rho^2$ and $S_\nu \propto [1 - \exp(-\tau_{\max})]$, there is a non-linear response from S_ν to a change in the density profile away from the r^{-2} given by the terminal velocity model. This results in the change to α seen in Fig. 4.6.

The radio flux, S_ν, along with the spectral index, α, for model S2 are depicted in the bottom two and top two panels of Fig. 4.6 respectively, The left-hand column shows S_ν and α for both the numerical model and the WB75 model, while the right-hand column shows the same, however the RJ part of the stellar blackbody has been added to the WB75 model. This has been done such that the acceleration region is the sole difference between the two methods, allowing for a more direct comparison.

Both the WB75 model and the numerical model show very similar behaviour across the frequency spectrum investigated, with several important distinctions. The plots on the left show the transition between the terminal velocity wind to the stellar blackbody for the numerical model, where by the spectral index, $\alpha = 0.6 \rightarrow 2.0$. The WB75 model experiences no such transition. In fact there is a gradual decrease in α, due to the frequency dependence of g_{ff}. In the right hand column the WB75 model is forced to transit to $\alpha = 2.0$ due to the RJ curve. Here the behaviour of the two models is

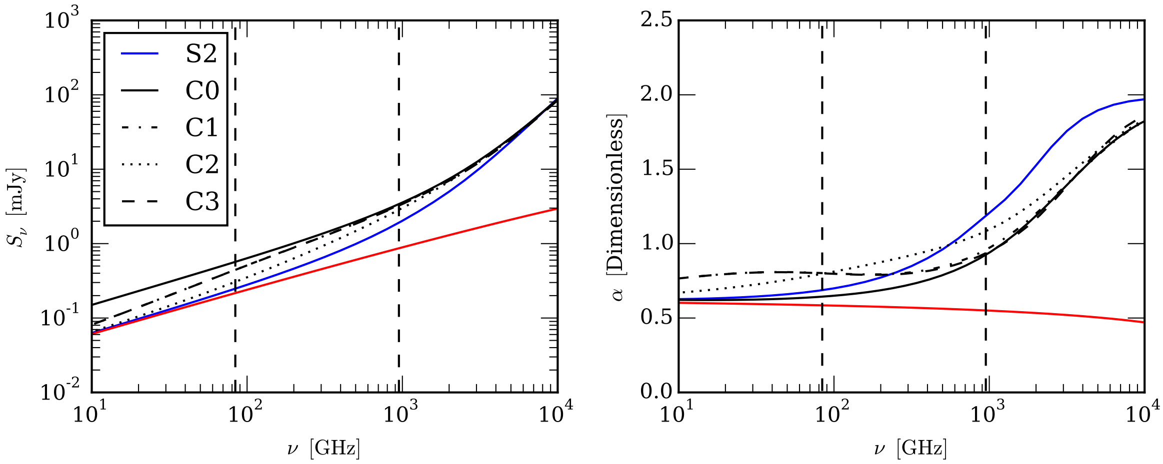

Figure 4.7: Comparison between clumped wind models C0 - C3 and unclumped wind model S2 (see Tabel 4.2). Both clumped and unclumped models result in an increase in spectral flux for low frequencies ($\nu \lesssim 500$ GHz). At frequencies higher than this, all models converge to a spectral flux with an index $\alpha = 2$, which is consistent with the RJ blackbody curve. The behaviour of the spectral index α is more nuanced, with the unclumped wind model providing the smoothest transition for $0.6 < \alpha < 2$. The clumped wind models take a range of values in the ALMA range (dashed vertical lines). It is notable that clumped wind models C1 and C3 display considerable degeneracy at all frequencies studied, showing only slight divergence at $\nu > 900$ GHz. The vertical dashed lines indicate the ALMA frequency range for bands 3 - 9.

qualitatively similar. The difference is made apparent by varying β. As the value of β increases, the density profile becomes steeper, this results in a greater deviation from the WB75 α as the value of β increases. The net effect is to smooth out the acceleration region, leading to the wind passing through a more gradual acceleration, which extends further from the star. Conversely, a smaller β leads to a more rapid acceleration which occurs closer to the stellar surface. In the limit of $\beta \to 0$ the acceleration is instantaneous and the WB75 model is recovered. The value of β is therefore an important consideration when predicting S_ν. As such, observations of the S_ν across ALMA's spectral window will provide further constraints on the precise value of β for a given set of stellar parameters. Leading in turn to a better understanding of $\dot{M}$.

In their analysis, WB75 describe the breakdown of their model at high observing frequencies (or low $\dot{M}$), where sharp temperature gradients and the acceleration region require the solution of the equation of radiative transfer. By using the acceleration law from CAK theory (equation 4.6) together with a numerical approach, these complications are avoided.

A recent paper by Manousakis & Walter (2015) investigates the velocity profile of the X-ray binary Vela X-1. A velocity law with $\beta \sim 0.5$ is found to favour the data. However, the influence of the pulsars radiation field on the dynamics of the donor stars wind are not well understood Manousakis & Walter (2015) make reference to work done by Stevens (1993) who investigated different wind velocity laws and the effect on S_ν. The treatment of other velocity laws than equation (4.6) is however, beyond the scope of this study. Thum et al. (2013) present millimeter observations of the massive stellar object LkHα101. By analysing high-n line transitions they deduce a slow moving wind whose spectral flux corresponds to a non-constant wind velocity. In contrast with the previous analysis, Blomme et al. (2002) attribute observed flux excess from the wind of the early-type star η Ori to wind clumping rather than the wind acceleration region. The following section will present the effects of clumping on the results of the spectral flux calculations.

4.4.1 Spectral flux due to clumping

We have calculated the radio/sub-mm spectral flux for several different clumping models, which are summarised in Table 4.2. All models presented, have wind parameters according to the smooth wind model S2 (see Table 4.1). Models C0 - C3 investigate the effects of varying clumping in both the inner and outer wind, as compared to a standard, uniform, clumping model.

For the case of uniform clumping (Model C0), the radio flux is increased by a factor $f_V^{-2/3}$ as expected, and for $f_V(r) = 0.5$, the flux is increased by a factor 1.59. The spectral results are shown in Fig. 4.7, where the flux and the spectral index α are shown.

The clumped models (C0-C3) illustrate how radially varying clumping affects the predicted radio/sub-mm emission from massive stars. As expected, the presence of clumping generally pushes up the expected emission. If the clumping is more pronounced at smaller radii, then the effect on the expected flux is more pronounced at higher frequencies and vice versa (Fig. 4.7. The changes in the spectral index α are also shown in Fig. 4.7 and these show that substantial changes in α are predicted across the ALMA bands for these clumping models and it will be possible to observe these changes for several nearby O-stars (see below).

4.4.2 ALMA detectability

ALMA has frequency bands which roughly cover the range 80 GHz $< \nu <$ 950 GHz. While previous observations have covered parts of this frequency range, none have so far had comparable sensitivity to ALMA. This sensitivity allows for the detection of sub-mJy flux from an unresolved point source such as the massive stars which are being considered in this work. Therefore, observations which can determine the contribution to S_ν from the acceleration regions of massive stars will be possible providing a further avenue for diagnosis of massive star winds.

To determine the enhancement of S_ν due to the acceleration region we introduce the following quantity:

$$\Delta S_\nu = S_{\nu,\mathrm{accel}} - S_{\nu,\mathrm{WB75}}, \tag{4.29}$$

where $S_{\nu,\mathrm{accel}}$ is the spectral flux due to the acceleration region and $S_{\nu,\mathrm{WB75}}$ is the spectral flux due to the WB75 model including the RJ flux. ΔS_ν is therefore the difference in predicted flux between the two models. The larger ΔS_ν is the greater the inaccuracy of any prediction based on the WB75 model.

Fig. 4.8 plots ΔS_ν at $\nu = 630$ GHz (ALMA Band 9) for all mass-loss rates in the study. As has already been discussed, ALMA's sensitivity is $S_\nu \geqslant 0.25$ mJy for an integration time of 1 hour. Mass-loss rates which result in $\Delta S_\nu < 0.25$ mJy are therefore not detectable. This point occurs for $\dot{M} > 10^{-7.5}$ M$_\odot$ yr^{-1}. Thus a star with $\dot{M}$ larger than this is required for the acceleration region to make an observable contribution to S_ν. The largest $\dot{M}$ of this study provides the largest difference in flux: $\Delta S_\nu \sim 3.3$ mJy. A spectral flux of this size is detectable by ALMA.

The calculations performed during this work have assumed a distance $D = 0.5$ kpc for each stellar model. Since $S_\nu \propto 1/D^2$, a more distant object with $\dot{M} = 10^{-7.5}$ M$_\odot$ yr^{-1}

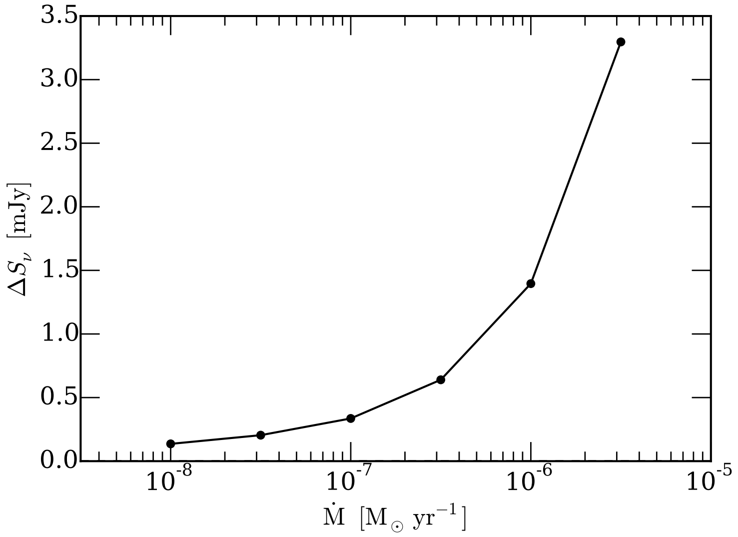

Figure 4.8: The difference, ΔS_ν, between the accelerating and WB75 models, at a frequency of $\sim$ 630 GHz. The effect of the RJ curve has been added to the analytic calculation such that ΔS_ν is solely due to the contribution to the emission from the acceleration region.

will result in a flux lower than the ALMA detectable threshold (at an integration time of 1 hour). Therefore the calculations are most relevant to the study of O type stars with $D < 0.5$ kpc, for example ζ Pup with $D \sim 0.33$ kpc or ζ Oph with $D \sim 0.15$ kpc (Maiz-Apellaniz et al., 2004).

4.5 Conclusions

Early theoretical work carried out by WB75 on the radio emission from stellar winds of massive stars showed that $S_\nu \propto \nu^{0.6}$. This dependence is based on the assumption of a terminal velocity stellar wind. This study has built upon this early work by applying a generalised numerical form of the equations which WB75 began with, to a discrete density grid with a profile that corresponds to the results of CAK theory. As such, this study has been able to investigate the region in the immediate surroundings of a series of stars undergoing mass-loss in the range 10^{-8} $\mathrm{M}_\odot$ yr^{-1} $< \dot{M} < 10^{-5.5}$ $\mathrm{M}_\odot$ yr^{-1}.

Due to a mixture of differing physical regimes within the stellar atmosphere close to the base of the wind, the wind acceleration region is a challenging subject which until recently has received little treatment both theoretically and observationally. This situation is changing due to ALMA and the wind acceleration region has begun to receive attention for example in the context of pre-main sequence stars (see Thum et al. 2013).

It has been shown that the spectral index α is strongly non-linear in the ALMA frequency range due to the effect of the wind acceleration region and the gradient strongly depends on the velocity law parameter β. The excess flux associated with the acceleration region ΔS_ν increases with $\dot{M}$ and should be detectable with ALMA. Therefore, if wind acceleration is not accounted for, miss-identification of the stellar mass-loss rate may occur.

The picture is further complicated by the addition of wind clumping. The effect of clumping on S_ν both at radio and ALMA wavelengths has considerable degeneracy with the smooth wind models. The spectral flux due to a smooth wind model and a specific β velocity law may be very similar to a clumped wind model with a different value of β. Both types of models raise the density with respect to a terminal velocity model, with the precise details varying from model to model. However, we know winds must accelerate, regardless of the details of the clumping posses. Recognising this basic physical property leads directly to acceleration as the baseline for the description of massive star winds at sub-mm frequencies.

The degeneracy between models results in a fundamental ambiguity between the velocity law, β, and the clumping factor, f_{cl}. To lift this degeneracy more observational data from within the ALMA range is required.

5

3D MHD simulation of a oblique rotating magnetic massive star and synthetic thermal radio emission

This chapter is a reformatted copy of the paper Daley-Yates et al. in preparation: "3D MHD simulation of a oblique rotating magnetic massive star and synthetic thermal radio emission" and is my own work.

5.1 Introduction

Magnetism in massive stars has gained significant attention in recent decades due to the unexpected number of these stars that display global, dynamically significant, magnetic fields (Petit et al., 2013; Wade et al., 2013, 2015, 2016). They are unexpected since massive stars have their convective zones beneath a radiative outer envelope; inhibiting the dynamo action thought responsible for generating stellar magnetic fields (see Walder et al. (2012) for a recent review). Cantiello et al. (2009) report theoretical results which indicate the coupling of subsurface convection with wind clumping and emergence of magnetic field on the surface of O and B-type stars. This picture has proved too simplistic for explaining the approximately 10% of Galactic O-type and B-type stars with detectable magnetic fields (Wade et al., 2013). The MiMeS project (Magnetism in Massive Stars) has done considerable work advancing our understanding of these stars both from an observational and theoretical stand point (Wade et al., 2016). Now the Magnetism in Massive Stars and Binarity and Magnetic Interactions project (BinaMIcs) is illustrating that massive star magnetism occurs in binary systems as well, with ε Lupi the first discovered magnetic massive binary where both the primary and secondary possess detectable magnetic fields (Shultz et al., 2015). Theoretical and numerical studies are required to help understand the wealth of observational data coming from these projects.

Analytic and semi-analytic modelling of the inner magentospheres of massive stars have been conducted by Townsend & Owocki (2005) and Townsend et al. (2007) producing the Rigidly Rotating Magnetosphere model (RRM) and Owocki et al. (2016) producing the Analytic Dynamical Magnetosphere model (ADM). Both models are designed to overcome the limitations of direct numerical simulations and to provide insight without the computationally intensive treatment of full MHD. These analytic models capture the suspension of material on magnetospheric field lines and while successful at reproducing observable emission in X-rays and H_α are unable to describe the free streaming wind or magnetically perturbed material at large radii. As such they are unsuitable for predicting radio/sub-mm emission.

ud-Doula & Owocki (2002) first studied the role of large scale cylindrically symmetric magnetic fields in shaping the dynamics and structure of massive star winds using 2D isothermal Magnetohydrodynamic (MHD) simulations. Results showed coherent disk structures forming in the magnetic equator as outflowing wind material is channelled by the magnetic field lines forming a standing shock. This model was improved upon with adiabatic physics by ud-Doula et al. (2008) and ud-Doula et al. (2009) and ultimately 3D simulations of the star θ^1 Ori C, incorporating optically thin cooling by ud-Doula et al. (2013). More recently 2D simulations investigating the incompatibility of large scale stellar magnetic fields and the circumstellar disk found around classical Be stars have been conducted by ud-Doula et al. (2018) demonstrating the that large scale fields of the order

~ 100 G will disrupt any Keplerian disk close to the star.

The work presented here builds on this earlier work by extending the studied wind region out beyond the stellar magnetosphere to regions where the dynamic influence of the magnetic field has diminished. More crucially we also allow magnetic obliquity of the dipole, resulting in non-spherical and non-cylindrical symmetric wind evolution. We achieve this though the use of direct numerical MHD simulations. We analyse the resulting wind structure in the context of diagnosis methods developed by ud-Doula & Owocki (2002); ud-Doula et al. (2008, 2009, 2013); Petit et al. (2013), quantify the departure from spherical symmetry over time and radial distance and finally calculate the synthetic radio lightcurves and continuum spectra; placing the results into what is observably possible with current technologies such as the JVLA and ALMA.

5.1.1 O-Star thermal radio emission

Radio emission from massive stars has historically been the subject of considerable interest (Braes et al., 1972; Wright et al., 1974; Wright & Barlow, 1975; Cohen et al., 1975) as the observed emission from Plank curve calculations deviate from what is expected (Wright & Barlow, 1975). This additional emission is due to free-free interactions between the charged species in the stellar wind and hence the emission is know as thermal.

Early analytical modelling of the winds of massive stars and the calculation of radio emission from the symbiotic nova V1016 Cyg was accomplished by Seaquist & Gregory (1973). The model they developed was based on the assumptions of a uniform, spherically symmetric outflow at constant temperature. The resulting spectral flux density as a function of frequency takes the form $S_\nu \propto \nu^\alpha$, where the spectral index, α, lies between $-0.1 \leq \alpha \leq +2$.

Refinement of the model by Wright & Barlow (1975) leads to a spectral index of $\alpha = 2/3$ at radio and infrared wavelengths. The relationship between S_ν and α arises due to the optical depth of the circumstellar material possessing a different value depending on the frequency of the emission; hence for higher frequencies, emission originates form deeper within the gas and therefore a greater extent of gas contributes to the emission at that frequency, leading to this positive gradient. This concept will be covered in subsequent sections.

The precise dependence of the spectral flux on ν allows for calculating the rate at which the star is losing mass through its wind. As such thermal radio observations provide an important window onto stellar evolution and the impact which the star has on the interstellar medium.

In Daley-Yates et al. (2016) we conducted a theoretical study of the thermal radio/sub-mm emission from a range of non-magnetised O-star parameters; with an emphasis on modulation of the continuum spectra by wind acceleration close to the stellar surface, observably accessible thanks to the sub-mm bands of ALMA. We continue this theme by applying the same analysis to the winds of magnetic massive stars.

5.2 Modelling

The model outlined here follows closely the methods used by ud-Doula & Owocki (2002) and specifically ud-Doula et al. (2013) who performed the first 3D numerical modelling of magnetised O-star winds by simulating the star θ Ori C under the adiabatic regime with optically thin radiative cooling. We deviate from this treatment by restricting our models to isothermal behaviour. The additional complication of the oblique magnetic dipole warrants this simplification as the numerical influence of the polar axis singularity becomes non-negligible (this issue will be discussed in Section 5.2.5.3). The following section details the calculations and numerical schemes used to perform this simulation.

5.2.1 Magnetohydrodynamics

The winds of massive stars are accelerated to supersonic speeds within a fraction of a stellar radius, making them ideally suited to modelling via the equations of Magnetohydrodynamics (MHD):

$$\frac{\partial \rho}{\partial t} + \boldsymbol{\nabla} \cdot (\rho \boldsymbol{v}) = 0 \tag{5.1}$$

$$\frac{\partial \boldsymbol{v}}{\partial t} + (\boldsymbol{v} \cdot \boldsymbol{\nabla})\, \boldsymbol{v} + \frac{1}{4\pi\rho} \boldsymbol{B} \times (\nabla \times \boldsymbol{B}) + \frac{1}{\rho} \nabla p = \boldsymbol{g} + \boldsymbol{g}_{\mathrm{L}} + \boldsymbol{F}_{\mathrm{co}} \tag{5.2}$$

$$\frac{\partial \boldsymbol{B}}{\partial t} + \nabla \times (\boldsymbol{B} \times \boldsymbol{v}) = 0. \tag{5.3}$$

Where ρ, $\boldsymbol{v}$, $\boldsymbol{B}$, p, $\boldsymbol{g}$ and $\boldsymbol{F}_{\mathrm{co}}$ are, the density, velocity, magnetic field, pressure, acceleration due to gravity and acceleration due to the co-moving frame respectively. The additional acceleration term, g_{L}, describes the acceleration due to line absorption (see Section 5.2.1.1). $\boldsymbol{F}_{\mathrm{co}}$ is the sum of both the centrifugal and Coriolis forces: $\boldsymbol{F}_{\mathrm{co}} = \boldsymbol{F}_{\mathrm{centrifugal}} + \boldsymbol{F}_{\mathrm{coriolis}}$ which are;

$$\boldsymbol{F}_{\mathrm{centrifugal}} = -\left[\boldsymbol{\Omega}_{\mathrm{fr}} \times (\boldsymbol{\Omega}_{\mathrm{fr}} \times \boldsymbol{R})\right] = \boldsymbol{\Omega}_{\mathrm{fr}}^2 \left(x\hat{x} + y\hat{y}\right) \tag{5.4}$$

and

$$\boldsymbol{F}_{\mathrm{coriolis}} = -2\left(\boldsymbol{\Omega}_{\mathrm{fr}} \times \boldsymbol{v}\right) = 2\Omega_{\mathrm{fr}} \left(v_x\hat{x} + v_y\hat{y}\right). \tag{5.5}$$

Here $\boldsymbol{\Omega}_{\mathrm{fr}}$ is the angular frequency of the rotating frame with $\boldsymbol{r}$ the radial distance vector.

As the simulation is isothermal, we close equations (5.1 - 5.3) using the relation:

$$p = \rho c_{\mathrm{iso}}^2, \tag{5.6}$$

in which c_{iso} is the isothermal sound speed, given by $c_{\mathrm{iso}}^2 = 2k_{\mathrm{B}}T/m_{\mathrm{p}}$, where k_{B} is the Boltzmann constant, T_{eff} the stellar surface effective temperature and m_{p} the proton mass.

5.2.1.1 Radiative driving

The winds of massive stars are accelerated by scattering of the stellar radiation in absorption lines of elements within the wind; as such they are known as line driven winds. The theory of line driving was first established in a seminal paper by Castor et al. (1975). The principle result is the description of an expanding wind whose acceleration is governed by the local density and, under the approximation made by Sobolev (1960), the velocity gradient and is given by:

$$g_L = \frac{f_\mathrm{D}}{(1-\alpha)} \frac{\kappa_e L_* \overline{Q}}{4\pi r^2 c} \left(\frac{\mathrm{d}\boldsymbol{v}/\mathrm{d}r}{\rho c \overline{Q} \kappa_\mathrm{e}} \right)^\alpha . \tag{5.7}$$

Where L_* is the stellar luminosity, c the speed of light, κ_e the electron scattering opacity, α the CAK exponent and $\boldsymbol{v}$ and ρ have the above meanings. All the parameters of equation (5.7) are derivable from observations except for $\overline{Q}$ for which Gayley (1995) computed a value of $\sim 10^3$ for a range of stellar parameters. The above variables are detailed in Table 5.1.

Finally f_D is the finite disk correction factor, which accounts for the finite size of the stellar disk close to the star and is given by:

$$f_\mathrm{D} = 1 - \frac{\alpha}{2r^2} \left(1 - \frac{v_r}{\frac{\mathrm{d}v_r}{\mathrm{d}r} r} \right) \left(1 + \frac{1-\alpha}{2r^2} \left(1 - \frac{v_r}{\frac{\mathrm{d}v_r}{\mathrm{d}r} r} \right) \right) \tag{5.8}$$

(private communication Owocki & ud-Doula). Where $\mathrm{d}v_r/\mathrm{d}r$ is the gradient of the radial component of velocity in the radial direction.

Equation (5.7) is derived and used under the assumption that non-radial components of the line driving either perfectly cancel or are negligible. Gayley & Owocki (2000) showed that this assumption is not strictly true for rotating stars and found that there exists a net non-zero azimuthal line force which acts counter to the rotation of the star. While this can lead to increases in the equatorial angular momentum loss, they also claim there is no major impact on the large scale wind dynamics and for this reason we restrict our work to the 1D radial line acceleration given above. However, it is worth noting that equation (5.7) is not strictly speaking complete.

For a rigorous treatment of line driving with non-radial components, see works by Pittard (2009) for the case of binary O-stars and Kee et al. (2016) for line driven ablation of circumstellar disk of classical Oe/Be stars. There have also been recent studies of the line-deshadowing instability conducted in 2D with hydrodynamic simulation incorporating both radial and lateral line acceleration by Sundqvist et al. (2018) and Owocki

& Sundqvist (2018). While not fully 3D, these studies show the development of wind clumping which arises as a consequence of the non-1D treatment of the line driving.

Equation (5.7) is applied on the right hand side of equation (5.2) as a source term along side gravitational and rotational source terms.

5.2.2 Stellar parameters

For the simulated star, we take parameters from Daley-Yates et al. (2016), whose stellar models are derived from the data of Krtička (2014). We use model S3 from the former work and summarise the parameters in Table 5.1.

The mass-loss rate, $\dot{M}_{B=0}$ refers the mass-loss of a star with the same parameters but with no magnetic field and is calculated, according to Owocki & ud Doula (2004), in the following manner:

$$\dot{M}_{B=0} = \frac{L_*}{c^2}\left(\frac{\alpha}{1-\alpha}\right)\left(\frac{\overline{Q}\Gamma_{\rm e}}{1-\Gamma_{\rm e}}\right)^{\frac{1-\alpha}{\alpha}}(1+\alpha)^{-1/\alpha}\,. \tag{5.9}$$

Where L_*, c, α and $\overline{Q}$ have their previous meanings and $\Gamma_{\rm e}$ is the Eddington parameter.

We use $\dot{M}_{B=0}$ to specify the initial conditions of the density profile via the expression

$$\rho = \frac{\dot{M}_{B=0}}{4\pi r^2 v(r)} \tag{5.10}$$

where the velocity profile is

$$v(r) = v_\infty(1 - R_*/r)^\beta, \tag{5.11}$$

with β determining the steepness of the velocity profile. The mass-loss from the star in the simulation deviates from this idealised value due to confinement by the magnetic field, the actual mass-loss rate is measured from the simulation results.

Instead of specifying the equatorial field strength directly, we specify the dimensionless magnetic field confinement parameter to have a value $\eta_* = 50$, resulting in a equatorial magnetic field, $B_{\rm eq} = 324$ G (see equation (5.12), of the following section). This value was chosen as a balance between what is numerically feasible and physically representative, based on data from the MIMES project (Petit et al., 2013; Wade et al., 2016). the value is similar in magnitude to the O8 f?p-type star HD 108 and the B-type stars NU Ori, HD 66665 and σ Lup.

Larger equatorial magnetic field strengths lead to more restrictive numerical time steps. As such, $\eta_* = 50$, produces the desired behaviour, in perturbing the stellar wind to form an excretion disk but allows for the simulation to be run in a feasible time span.

The angle of magnetic field obliquity, ζ, is constrained by the presence of the polar boundaries at $\theta = 0$ and $\theta = \pi$. This issue will be discussed in more depth in Section 5.2.5.3, however it is necessary to state here that the boundary restricts the obliquity of the dipole and that greater obliquity leads to enhanced numerical effects at the aforementioned boundaries. The chosen value of $\zeta = 30°$ reflects this issue and was deemed a significant enough obliquity to promote the desired perturbation to the stellar wind, yet small such that numerical effects are kept to a negligible level.

The remaining parameters in Table 5.1 are used to calculate equation (5.7) and to parametrise the simulation code units. For example, in the results in Section 5.3, distances are given in stellar radii.

5.2.3 Magnetosphere characterisation

Petit et al. (2013) presents a scheme which characterises the global behaviour of a massive star magnetosphere as a function of several dimensional quantities developed by ud-Doula & Owocki (2002) and ud-Doula et al. (2008). These quantities are the wind magnetic confinement parameter,

$$\eta_* \equiv \frac{B_{\rm eq}^2 R_*^2}{\dot{M}_{B=0} v_\infty} \tag{5.12}$$

and the ratio of the rotational speed $v_{\rm rot}$ to the orbital speed $v_{\rm orb}$,

$$W \equiv \frac{v_{\rm rot}}{v_{\rm orb}} = \frac{\omega R_*}{\sqrt{GM_*/R_*}}. \tag{5.13}$$

Table 5.1: Stellar parameters for the study.

Name	Parameter	Value
Initial mass-loss	$\dot{M}_{B=0}$	$10^{-7}\ M_\odot yr^{-1}$
Stellar radius	R_*	$9\ R_\odot$
Stellar mass	M_*	$26\ M_\odot$
Effective temperature	$T_{\rm eff}$	36300K
Luminosity	$\log_{10}(L_*/L_\odot)$	5.06
Eddington factor	Γ_{Edd}	0.11
Q-factor	$\overline{Q}$	700
Terminal velocity	v_∞	$3\ V_{\rm esc}$
Escape velocity	$v_{\rm esc}$	$1000\ kms^{-1}$
Rotational rate	ω	$0.2\ \omega_{\rm crit}$
CAK exponent	α	0.6
Velocity law	β	0.8
Magnetic field inclination	ζ	30°
Rotation parameter	W	0.11
Confinement parameter	η_*	50.0
Kepler radius	$R_{\rm K}$	$4.39\ R_*$
Alfvén radius	$R_{\rm A}$	$2.96\ R_*$

In the above expressions, $B_{\rm eq}$ is the equatorial magnetic field strength, R_* is the stellar radius, $\dot{M}_{B=0}$ is the stellar mass-loss rate in the presence of no magnetic field and v_∞ is the wind terminal velocity. ω, G and M_* are the angular rotational frequency, gravitational constant and stellar mass respectively. The Kepler and Alfvén radii are then calculated from

$$R_{\rm K} = W^{-2/3} R_* \tag{5.14}$$

and

$$R_{\rm A} = 0.3 + (\eta_* + 0.25)^{1/4} R_*. \tag{5.15}$$

See Petit et al. (2013) for a detailed discussion of these expressions.

The case when $\eta_* >> 1$ represents a strongly confined wind where the magnetic pressure dominates and conversely when $\eta_* << 1$ the field is weak and the wind ram pressure dominates. For the rotational parameter, $W = 1$ represents the critical stellar breakup rotational speed, where the gravitational acceleration equals the rotational acceleration at the stellar equator. Together the above two parameters characterise the dynamics of material suspended in the stellar magnetosphere.

Petit et al. (2013) divided massive star magnetospheres into two distinct categories; dynamical and centrifugal. The division is determined by the relative values of the Kepler and Alfvén radii. For a star with $R_{\mathrm{K}} > R_{\mathrm{A}}$, it's magnetosphere is defined as dynamical and wind material confined on closed magnetic field lines experiences an unstable equilibrium and consequently there is continuous motion of material as field lines are loaded and emptied. However, for a star with $R_{\mathrm{K}} < R_{\mathrm{A}}$, there exists a region between the two radii in which material experiences a stable equilibrium between gravity, magnetic tension and centrifugal acceleration, below R_{K} behaviour is still dynamical. Under this framework, the star in our simulation has a dynamical magnetosphere. See Table 5.1 for the values of η_*, W, R_{K} and R_{A}.

Out beyond both R_{K} and R_{A} material undergoes a net outward acceleration as g_{L} exceeds all other inward acceleration. As this material has already undergone confinement and perturbation away from its initial spherical surface velocity, a disk structure develops whose outward path intersects with the apex of the closed magnetic field lines. The net effect is to produce a standing disk shaped shock structure with a topology intimately linked to the magnetic field topology. Fig. 5.1 illustrates this interplay between outward flow of the wind and its confinement by the dipole magnetosphere. As can be seen in profile in Fig. 5.1, for an oblique dipole, the shock structure forms a contorted disk.

The following section explains the procedure for calculating the synthetic thermal radio emission from the structure described above.

5.2.4 Synthetic radio/sub-mm emission

The numerical procedure for calculating synthetic radio emission follows the one developed in Daley-Yates et al. (2016). For the details of the calculation see Chapter 4, Section 4.3.2. For the present study it will suffice to cover the equations directly used in the calculation. The intensity of radio emission for each column along the line of sight from the observer

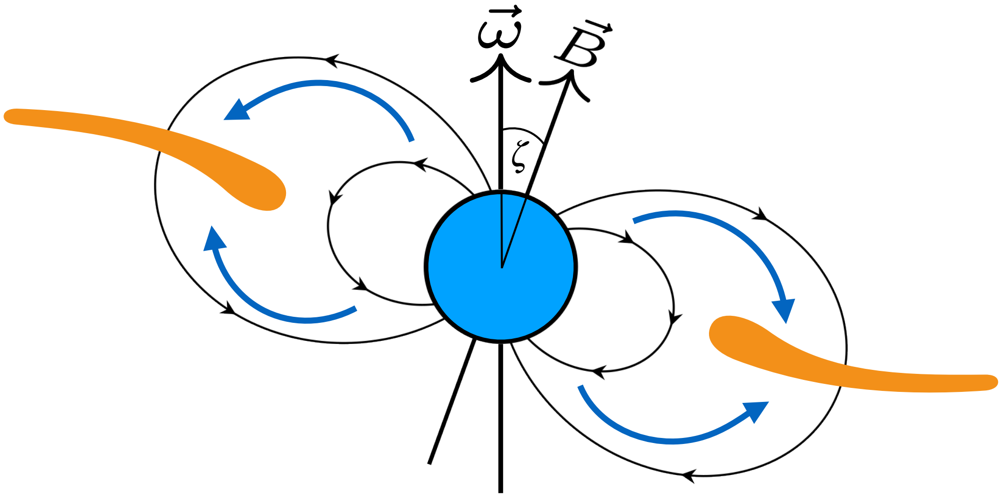

Figure 5.1: Cartoon diagram illustrating the magnetic field topology and confinement of the stellar wind. The blue circle at the centre is the star, annotated are the magnetic field lines with their vector direction and the dipole obliquity, $\zeta = 30°$. The blue arrows indicate the path material travels along as the wind interacts with the magnetic field. The orange tear-drop like shapes represent the shocked wind material.

through the simulation domain is given by:

$$I_\nu(y,z) = B_\nu\left(T\right) \int_0^{\tau_{\rm max}(y,z)} \exp(-\tau(x,y,z)){\rm d}\tau, \tag{5.16}$$

where $B_\nu(T)$ is the Planck function at frequency ν, T the temperature, τ the optical depth and $\tau_{\rm max}$ is the maximum optical depth along the observers line of sight. Equation (5.16) is integrated to give

$$I_\nu(y,z) = B_\nu\left(T\right)\left[1 - \exp(-\tau_{\rm max}(y,z))\right]. \tag{5.17}$$

Where

$$\tau_{\rm max}(y,z) = \int_{-\infty}^{+\infty} \gamma K_\nu(T_{\rm eff}) n_{\rm i}^2(x,y,z){\rm d}x. \tag{5.18}$$

$n_{\rm i}$ is the ion number density and γ is the ratio of the electron and ion number densities, $\gamma = 1.01$, under the assumption of solar metallicity. The final variable in equation (5.18) is

$$K_\nu(T_{\text{eff}}) = 0.0178\frac{Z^2 g_{\text{ff}}}{T_{\text{eff}}^{3/2}\nu^2}, \tag{5.19}$$

which relates the temperature, T_{eff}, metallicity, Z, observing frequency, ν and g_{ff}, which is the free-free Gaunt factor, given by:

$$g_{\text{ff}} = 9.77 + 1.27\log_{10}\left(\frac{T_{\text{eff}}^{3/2}}{\nu Z}\right), \tag{5.20}$$

in which the symbols have their above meaning. Finally, the total spectral flux emitted at a frequency, ν, is then the integral of the intensity I_ν over the yz-plane:

$$S_\nu = \frac{1}{D^2}\int_0^\infty\int_0^\infty I_\nu(y,z)\mathrm{d}y\mathrm{d}z, \tag{5.21}$$

with D the distance between the observer and the star and I_ν given by equation (5.17).

Equations (5.17, 5.18 and 5.21) are the primary expressions used for calculating the synthetic radio emission, the results of which are presented in Section 5.3.3

It is possible to determine the mass-loss rate, $\dot{M}_*$, from the free-free radio emission of massive stars. In a seminal paper, Wright & Barlow (1975) construct a framework for predicting the spectral flux, S_ν as a function of $\dot{M}_*$. Their equation (equation (8) of Wright & Barlow (1975)) can therefore be algebraically manipulated to give $\dot{M}_*$ in terms of the stellar properties, listed in Table 5.1, and S_ν. The exact expression is given by Bieging et al. (1989) as:

$$\dot{M}_{\text{obs}} = \frac{3.01\times 10^{-6}\mu}{Z(\gamma g_{\text{ff}}\nu)^{1/2}}v_\infty S_\nu^{3/4}D^{3/2}M_\odot yr^{-1}. \tag{5.22}$$

Where μ is the mean atomic weight, v_∞ is in km/s and D is in kpc. The remaining variables are in cgs units.

A recent JVLA survey by Kurapati et al. (2016) used equation (5.22) to predict the mass-loss rates of a sample of B- and O-type stars. We shall use equation (5.22) here and attempt to recover the input simulation mass-loss rate from the synthetic radio prediction.

5.2.5 Simulation

The MHD equations (5.1 - 5.3) were solved using the publicly available code PLUTO (version 4.2) (Mignone et al., 2007).

The chosen algorithm was fully unsplit and 2nd order accurate in space and time, using linear reconstruction, Runge-Kutta time stepping and employed the HLL Riemann solver. The extended GLM divergence cleaning algorithm was used to ensure the $\nabla \cdot \boldsymbol{B} = 0$ condition.

5.2.5.1 Numerical grid

The numerical grid in our simulation covered a physical extent of $r \in \{1, 40\}\ R_*$, $\theta \in \{0, \pi\}$ radians and $\phi \in \{0, 2\pi\}$ radians. This provided a computational region extending from the stellar surface to the outer wind, far beyond the magnetospheric radius, thus facilitating the capture of low frequency radio emission generated by the extended wind.

The simulations were performed using a stretched rectilinear spherical polar grid in which the physical volume was discretised with 300 cells in r, 120 cells in θ and 240 cells in ϕ. This leads to a cell size in the r direction which stretched from $\Delta r_1 \approx 0.0007\ R_*$ to $\Delta r_{300} \approx 0.93\ R_*$ with a constant stretching factor of 1.0243. Both the θ and ϕ directions have equal spacing of $\Delta\theta_j = \Delta\phi_k \approx 0.026$ radians.

5.2.5.2 Initial conditions

The initial conditions of the simulations were specified using the density and velocity profile equations (5.10) and (5.11).

The magnetic field was initialised as a perfect dipole centred at the origin and is rotated about the y-axis, in the xz-plane. This configuration then relaxes into quasi-steady state as the simulation evolves.

5.2.5.3 Boundary conditions

The outer radial boundary of the simulation is set to outflow. The inner radial boundary is set such that the the star is continually feeding material to the wind and therefore replenishing material in the simulation. As the wind is accelerated to supersonic radial speeds within a fraction of a stellar radii, and as the line driving is dependent on the velocity gradient (equation (5.7)), the evolution of the entire simulation is an boundary value problem which is sensitively dependant on the lower radial boundary condition. To account for this sensitivity we used the boundary conditions of ud-Doula & Owocki (2002) and ud-Doula et al. (2013). The density is specified via equation (5.11), replacing the velocity profile with a ratio linked to the sound speed; $\rho = \dot{M}/4\pi R_*^2(c_{\rm iso}/\xi)$ where ξ is a factor parametrised to give a stable material inflow at the boundary and is typically $5 < \xi < 30$. Values of ξ outside this range can result in oscillations of the solution at the boundary.

The velocity in the lower radial boundary is specified by linearly extrapolating back from the first 2 computational cells above the boundary, allowing the flow into the computational active zone to adjust to the conditions of the wind and permitting material to also re-enter the stellar surface as magnetically confined material follows field lines back to the stellar surface. Specifying the boundary in this manner also allows the mass loading of the wind to self consistently adapt to the rotation of the star. Large rotational frequencies can lead to the modulation of mass-loss of a star, because the effective gravity at the rotational equator is reduce relative to the poles and material is lifted from the surface more easily.

The boundary of the lower and upper azimuthal direction is made reciprocal such that material can move freely around the star. The upper and lower boundary of the polar direction was set to reflective so as not to act as a sink for material. This final boundary condition is non-physical and a reflective polar boundary can lead to spurious heating along the polar axis. There are several methods design to overcome this numerical difficulty. One such method is known as π-boundary conditions in which the fluid quantities are translated π around the axis and vector values transformed such that material effectively passes over the pole. This method is implemented in the public codes Athena++ (White et al., 2016) and MPI-AMRVAC (Xia et al., 2018). PLUTO does not provide this functionality however. Another means of avoiding the spurious heating is to average fluid quantities over the poles and effectively smooth over the anomalies.

As the current study aim is to quantify the thermal radio emission, and as this is effectively independent of the gas temperature, we have chosen to run the simulation under an isothermal equation of state. This effectively side steps the issue of polar boundary heating, as the temperature is constant at T_{eff} and not evolved with time. The extent to which the boundary impacts the density, velocity and magnetic profiles is discussed in Section 5.3.1.

The isothermal assumption forces us to neglect behaviour due to both shock heating and radiative cooling. Both of which have been shown to play a role in the wind dynamics (ud-Doula et al., 2008, 2013). As such, this is a limitation of the present study and fully adiabatic simulations with cooling physics are the aim of future studies.

5.2.5.4 Steady state criteria

The simulation were deemed to have reached steady state after a simulation time of 1 Ms or approximately 20 stellar rotations. This time frames allows material to relax from the initial spherical symmetry to the confined configuration. Any excess material is also blown off to the outer boundary within this time frame.

Once the 1 Ms had been reached, we ran the simulation for a further 2 rotations with fine time spaced sampling. This allowed for high temporal resolution for the synthetic radio light curve calculations in Section 5.3.3.2.

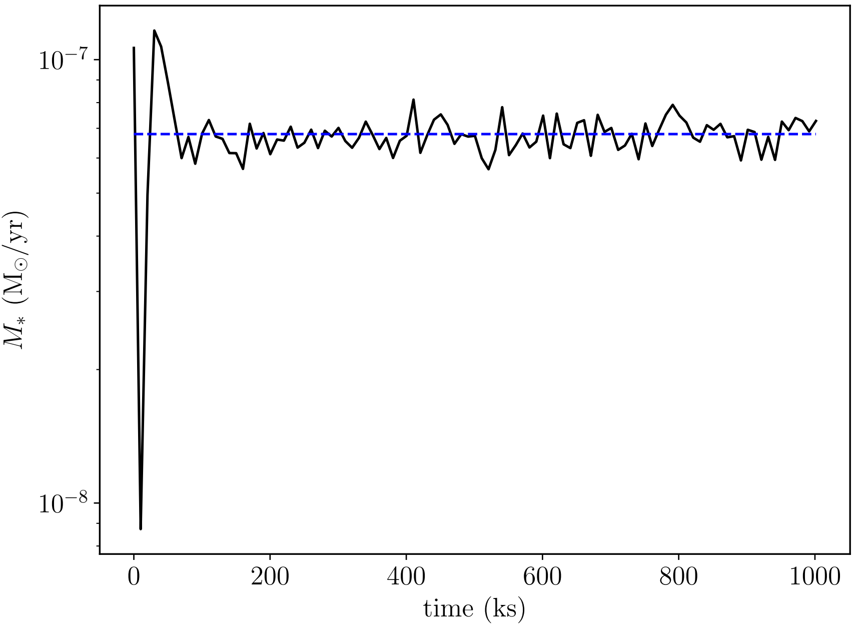

Figure 5.2: Evolution of the mass-loss over the course of the simulation. The mass flux from the star is initially ~ 10^{-7} M$_\odot$/yr and relaxes to an average value of 6.8 × 10^{-8} M$_\odot$/yr (indicated by the blue dashed line) after ~ 100 ks where it remains for the rest of the simulation.

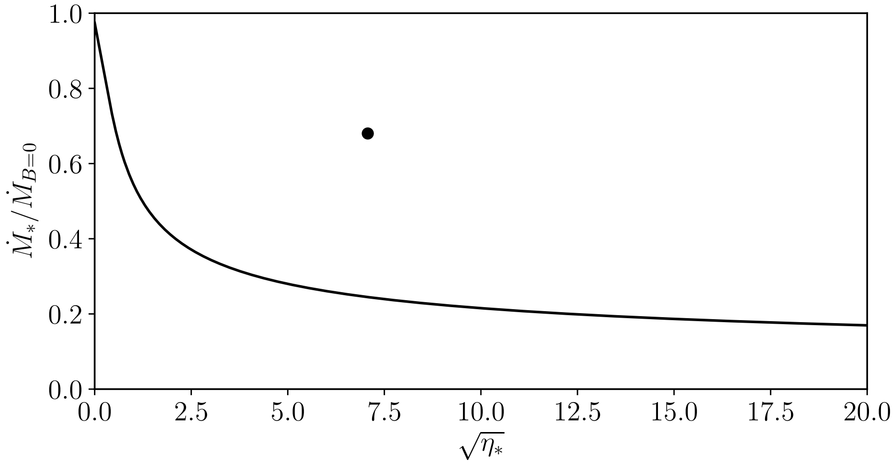

Figure 5.3: Dependence of the mass-loss $\dot{M}_*$ on the confinement parameter η_* for $W = 0.11$. The black dot indicates the measured mass-loss reduction from the simulations as the ratio of the initial and averaged quasi-steady state mass-losses and has a value $\dot{M}_*/\dot{M}_{*,B=0} = 0.68$.

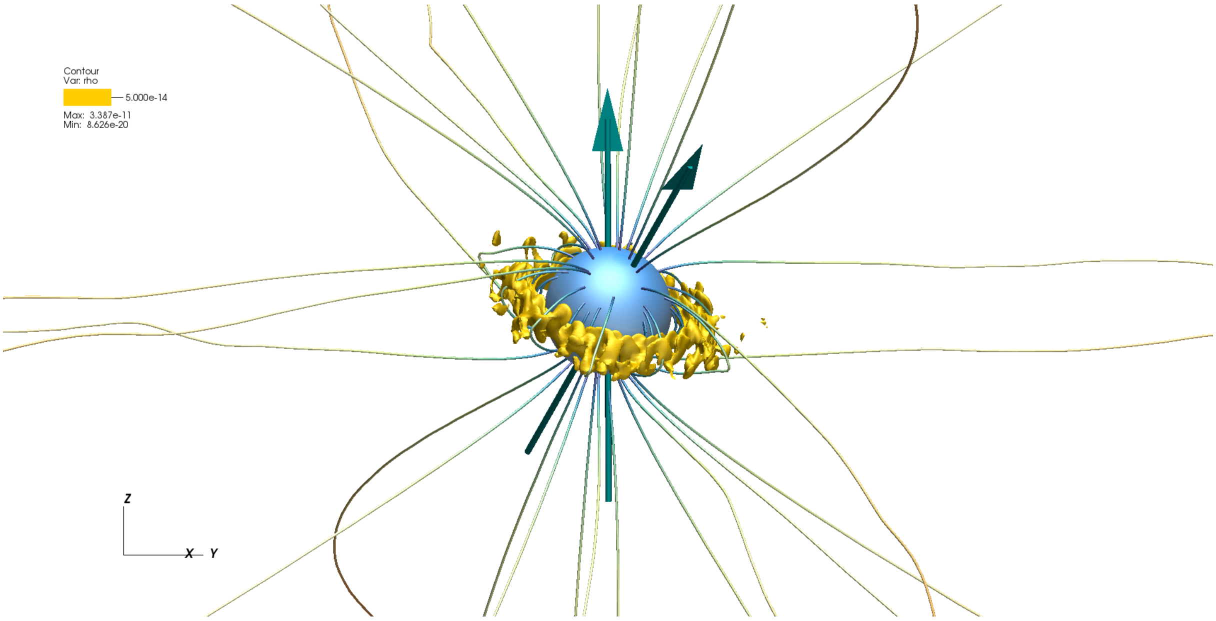

Figure 5.4: 3D representation of the simulation domain for the immediate surroundings of the star. The blue sphere at the centre indicates the stellar surface, the streamlines are the magnetic field, coloured by the log of magnitude and the yellow contour is an isodensity surface of 5×10^{-14} g/cm^3. While the value of this contour is some what arbitrary, it aids in illustrating the confinement of the stellar wind and the departure from spherical symmetry due to the magnetic field. The two arrows indicate the rotational axis (vertical arrow) and the magnetic dipole vector (oblique arrow).

5.3 Results and discussion

The following subsections layout the simulation results; staring with the profiles for the three primary fluid quantities: ρ, $|\boldsymbol{v}|$ and $|\boldsymbol{B}|$. We will then quantity the extent to which the wind has deviated from spherical symmetry and finally examine both the synthetic radio lightcurves and the radio/sub-mm spectrum.

First we will cover the issue of convergence and ascertain whether quasi-steady state has been reached. Fig. 5.2 shows the evolution of the mass-loss, $\dot{M}_*$. The initial mass-loss, $\sim 10^{-7}$ $\mathrm{M}_\odot$/yr undergoes a drastic reduction and oscillation as the spherical wind reacts to the presence of the magnetic field. This initial phase then stabilises to an average mass-loss of 6.8×10^{-8} $\mathrm{M}_\odot$/yr after $\sim$ 100 ks. This simulation average mass-loss will be referred to from here on as $\dot{M}_{\mathrm{sim}}$.

There is still an oscillation amplitude of $\sim$ 1.5% about $\dot{M}_{\mathrm{sim}}$ due to motion of material suspended on closed field lines within the inner magnetosphere. As magnetic tension, gravity, centrifugal and radiative acceleration balance in unstable equilibrium, material can either leave or re-enter the stellar surface, resulting in the oscillations.

ud-Doula et al. (2008) derived an expression describing the manner in which $\dot{M}_{B=0}$ is modulated by η_* and W (see equation (24) and Fig. 8 of the aforementioned paper). We plot this function for the stellar parameters in Table 5.1 and a range of η_* values in Fig. 5.3. The curve in this figure represents the prediction of ud-Doula et al. (2008) and the black dot, the value we measure directly from our simulation and has a value of $\dot{M}_{\mathrm{sim}}/\dot{M}_{*,B=0} = 0.68$. This result is in contrast to the predicted value of $\dot{M}_*/\dot{M}_{*,B=0} = 0.24$ and approximately 3 times larger. This means that the mass-loss of our simulated star is larger than current theory predicts.

As the magnetic confinement of the wind is not aligned with the equator as it is in the zero obliquity dipole case, this could lead to a reversal in the effect of mass-loss reduction. As this simulation is effectively a single data point, we leave further speculation for a full parameter study of the effect of dipole obliquity on stellar mass-loss. The larger $\dot{M}_{\mathrm{sim}}/\dot{M}_{*,B=0}$ may also be a consequence of running the simulation under the isothermal

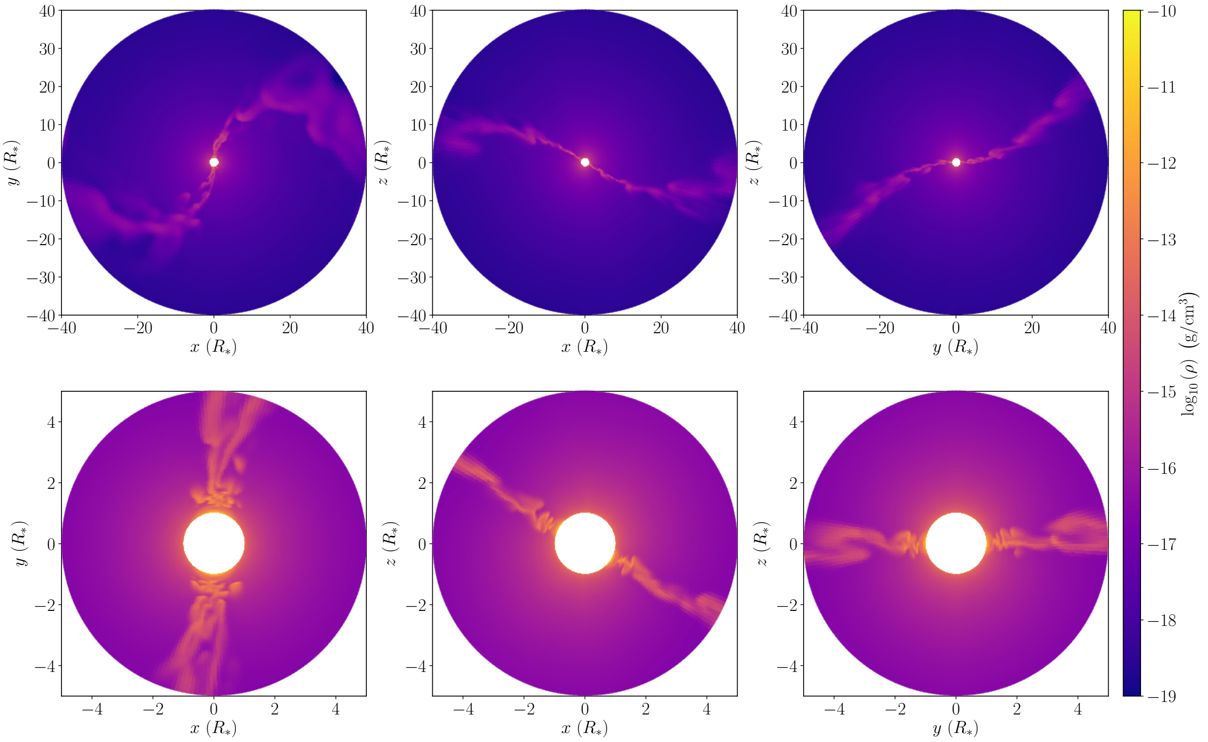

Figure 5.5: Slice plots of the global quasi-steady state density structure at 1 Ms. The star is situated in the centre with the confined material appearing as a curved "S" shape. Each plot shows a slice in a different coordinate plane, from left to right is the; xy-, xz- and yz-plane. All three columns exhibit the contortion of the expanding excretion disk due to the action of rotation. Top: the full simulation domain. Bottom: close-up of the density structure of the inner 5 R_* of the simulation. The density structure clearly shows the confinement of material in the magnetic equator, off-set from the rotational equator.

assumption as shock heating and cooling play a role in shaping the motion of material close to the surface. A final possible explanation for the larger mass-loss may also be a result of the velocity profile which exhibits a departure from analytic theory, with a magnitude approximately 3 time larger. This velocity profile is discussed in detail in Section 5.3.1.2.

As the mass-loss rate evolution in Fig. 5.2 attests, the simulation has reached quasi-steady state by $t = 1$ Ms, the profiles in the following section are therefore taken at this time point.

5.3.1 Wind structure

A 3D representation of the star and inner magnetosphere showing the stellar surface, magnetic field lines and isodensity surface is given in Fig. 5.4. Two arrows indicate the

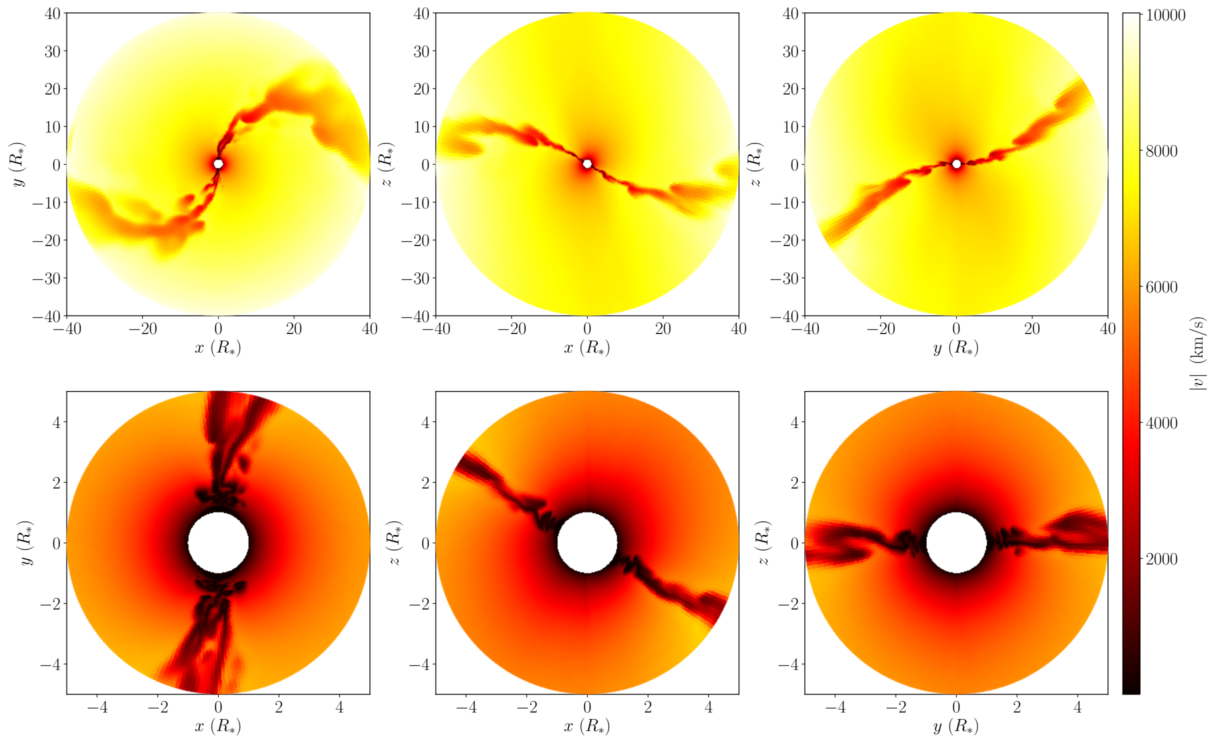

Figure 5.6: Same as Fig. 5.5 but for the velocity magnitude profile. The top row shows the extended wind with a clear contrast between the free streaming and the slower moving disk material. The bottom row shows the inner wind velocity. The sonic point is reached within a fraction of a stellar radus. The polar axis is visible as a discontinuity in values in the central panel of the bottom row. This jump has however had a negligible impact on the extended wind, as can be see in the cosponsoring panel of the top row. Beyond the $\sim 5\ R_*$, the wind has reached the terminal velocity. The profile in all three panel exhibits values for the terminal velocity several time greater than is predicted by the standard CAK model. The prediction of $v_\infty\ =\ 3000$ ks is exceeded and a terminal velocity of $v_\infty\ =\ 10000$ ks has been reached in the outer wind. Such wind speeds are non-physical and are a failing of the model.

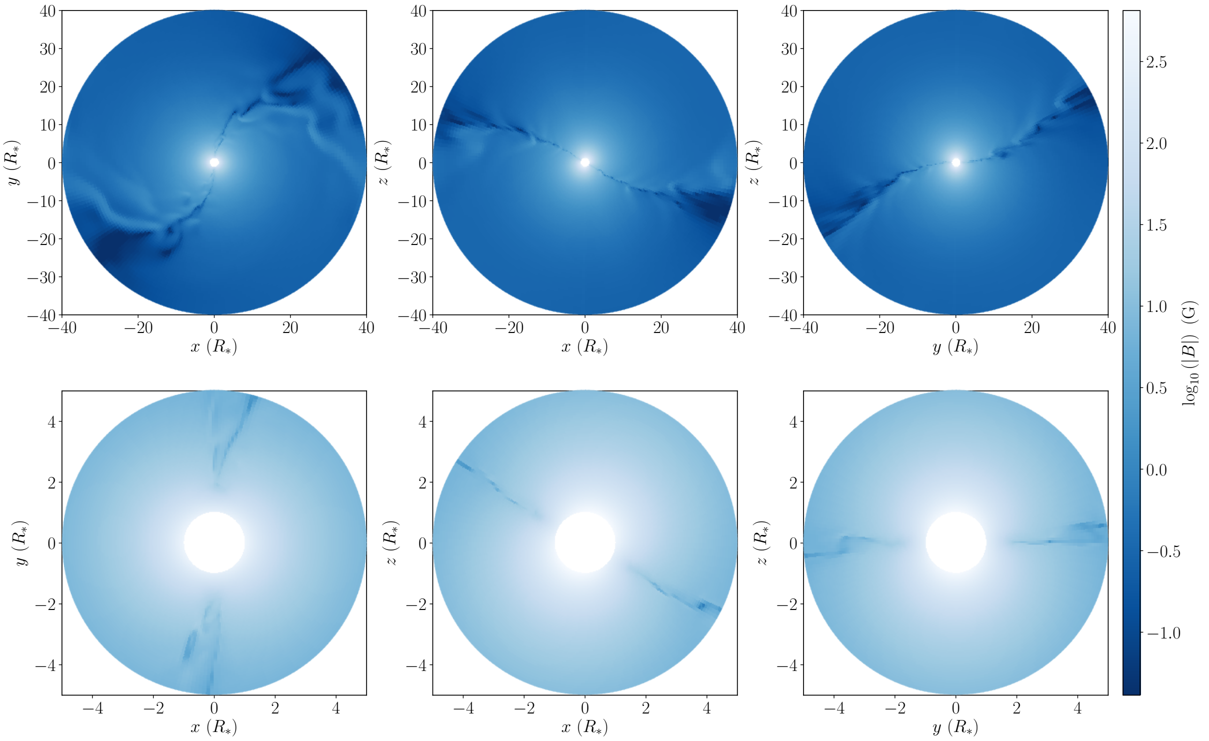

Figure 5.7: Same as Fig. 5.5 but for the $\log_{10}(|\boldsymbol{B}|)$. The central column shows a slice looking down the y-axis which is the axis about which the dipole field is rotated; the maximum field magnitude is located on the stellar surface at both magnetic poles. This value is 648 G, twice the equatorial value. Examining the top row, it can be seen that the magnetic field decays smoothly from the surface to the extended wind everywhere except for the excretion disk, where the current sheet is and is several orders of magnitude lower than in the free streaming wind.

rotation axis (vertical arrow) and the magnetic axis (oblique arrow). The yellow isodensity contour illustrates the confinement of material in the closed field region.

The radial extent of this region and the closure latitude are related through the following equation:

$$\sin(\theta_{\mathrm{c}}) = \sqrt{R_{*}/R_{\mathrm{c}}}. \tag{5.23}$$

Where R_{c} is the radial distance from the centre of the star to the apex of the longest closed field line and θ_{c} the co-latitudinal coordinate at which the field line makes contact with the stellar surface. the subscript c stands for closure (ud-Doula et al., 2008). Vidotto et al. (2011) use a similar expression to estimate the latitude of cyclotron emission from an exoplanetary atmosphere using the notation R_{M} indicating the radius of the magnetosphere. As massive stars are the topic of the present study we use the notation of ud-Doula et al. (2008). As an estimate for R_{c}, we use the Alfvén radius given by equation (5.15), which leads to a closure latitude $\theta_{\mathrm{c}} = \pm 35.5°$. This analysis neglects deformation of the closed field lines by either rotation or wind ram-pressure. By visual inspection of Fig. 5.4, there is qualitative agreement between the prediction of $R_{\mathrm{c}} \sim 3\ R_{*}$ and $\theta_{\mathrm{c}} \sim \pm 35°$ and our simulation results.

Another feature shown in Fig. 5.4 is the braking of symmetry about the rotational axis due to the obliquity of the dipole. ud-Doula et al. (2013) observed symmetry breaking in the excretion disk, however as their simulation included no dipole obliquity, this breakdown of symmetry is due to the interplay between rotation and optically thin radiative losses. This final effect is not present in the current study and any rotational asymmetry is therefore due to the magnetic field topology.

Fig. 5.5, 5.6 and 5.7 show multiple slices through the computational domain in the xy-, xz- and yz-planes for ρ, $|\boldsymbol{v}|$ and $|\boldsymbol{B}|$ respectively for both the extended and inner wind regions. In each plot the star is centred at the origin and the wind extends from the surface at $r = 1\ R_{*}$ to $r = 40\ R_{*}$ where it leaves the simulation domain.

5.3.1.1 Density

The 2D density profiles in Fig. 5.5 further emphasise the sharp departure from both the initial spherical wind and the cylindrical symmetry seen in the aligned dipole case. In the central column, in which we look down the y-axis, the magnetic field obliquity is clearly visible as the arms of the excretion disk are off-set from the equatorial plane by 30°, the same off-set as the magnetic field dipole vector. The panel on the left looks down the rotational axis and shows a slice along the rotational equator. As the magnetic equator is off-set from this, the slice cuts through the excretion disk, which appears as a contorted ”S” shape. All panels clearly show the confinement of material in the magnetic equator, off-set from the rotational equator which expands radially to form an extended excretion disk, as the rotation of the star precesses, this disk is then contorted.

5.3.1.2 Velocity field

For the velocity profile in Fig. 5.5, there is a clear contrast between the free streaming and the slower moving disk material with a difference in velocity magnitude of the order $\sim$ 2000 km/s. However, the entire simulation is supersonic, with the sonic point virtually indistinguishable from the stellar surface.

An important numerical feature visible in the central column on the velocity profiles is the discontinuity of the polar axes. Both show a non-physical jump in values. However, this jump has not propagated into the extended wind, as such we assume there is negligible impact on the wind evolution.

Preliminary adiabatic simulations showed this polar axis discontinuity to result in spurious heating along the pole. As the simulation evolved, this numerical thermal perturbation begins to impact not only the pressure profile but all other fluid quantities, for this reason, we chose an isothermal model, with constant temperature.

The velocity profile, according to the prediction of CAK theory, should reach a terminal velocity of approximately $v_\infty = 3000$ km/s. This is not however what is observed in the simulation; with the extended velocity profile reaching a non-physical value of

$v_\infty \approx 10000$ km/s. This several times greater result than the prediction demonstrates that the present model is incomplete regarding the wind acceleration. The isothermal nature of the model imposes several restrictions on the physics involved in the radiative driving. Line acceleration is quenched in regions where the gas temperature exceeds $\sim 10^6$ K as the line transitions in which the stellar flux is scattered are no longer available due to virtually full ionisation (Pittard, 2009). Temperatures of this magnitude are seen in 3D simulation of O-star wind magnetic confinement as gas is shock heated in the disk ud-Doula et al. (2013). The isothermal condition prevents this as the gas temperature remains at the stellar effective temperature, well below the ionisation cut-off. Such wind speeds seen here are non-physical and a failing of the current model. However, as the radio/sub-mm emission is primarily a function of the density field and not of the velocity field, we conclude that this departure of the velocity field from what is expected has a negligible impact on the results.

5.3.1.3 Magnetic field

The final set of profiles, displayed in Fig. 5.7, depict the magnetic field in the three axes planes. The central plane clearly shown the obliquity of the dipole with the largest field value, indicating the two magnetic poles, off set from the rotational poles by 30°. This value is 648 G, twice the equatorial value. The magnetic field decays smoothly from the surface to the extended wind everywhere except for the excretion disk, where the current sheet has formed. Within the Alfvén radius, lose to the star, magnetic pressure controls the flow dynamics, however for the vast majority of the extended wind gas pressure dominates.

5.3.2 Spherical nature of the wind

At this point we shall discuss the extent to which the wind has deviated from its initial spherical symmetry.

As the calculation of thermal radio emission is a function of the maximum optical

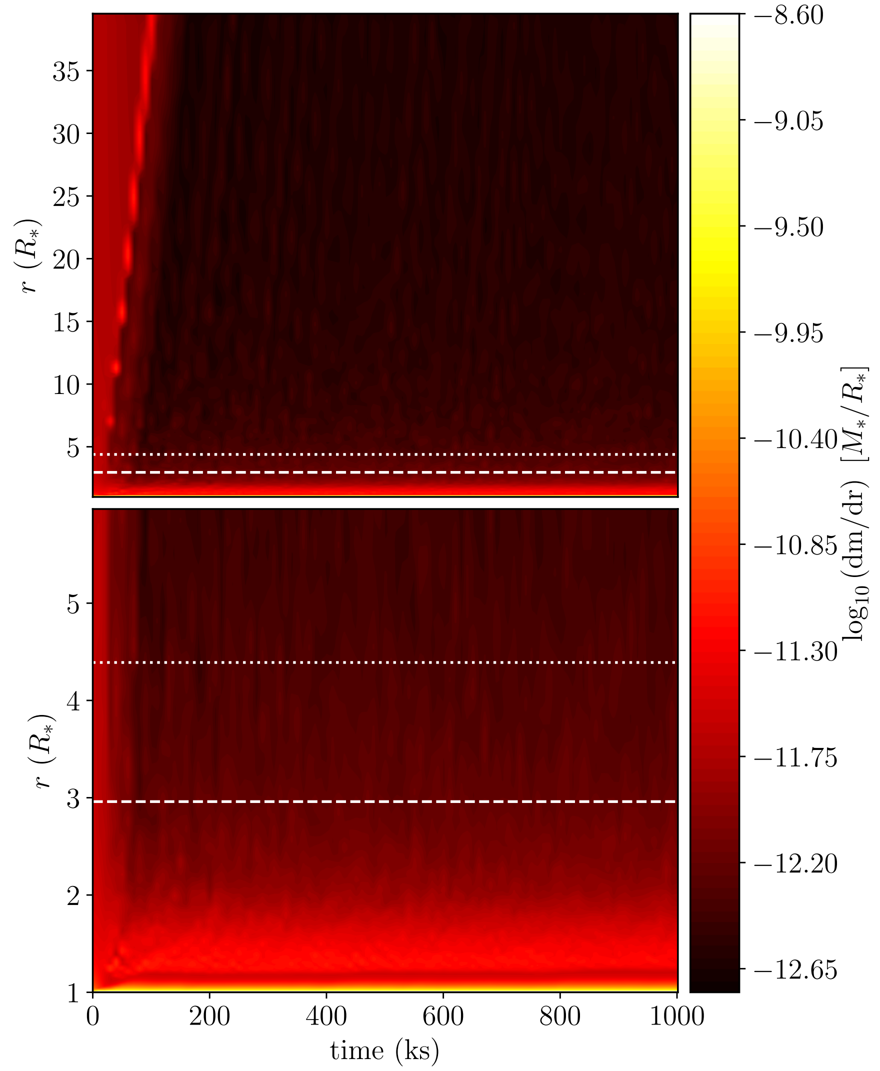

Figure 5.8: Radial mass distribution for the total simulation (top panel) and the inner 6 R_* (bottom panel). The blow-off of the initial conditions can be seen in the left of the top panel, where a fan of material tracks outwards in the first $\sim$ 200 s. Beyond this point the global radial motion of material is approximately constant with small perturbations resulting in lines tracking outward from the stellar surface coursed by clumps which form in the inner magnetosphere. In both panels the Alfévn (dashed line) and Kepler (dotted line) radii are marked.

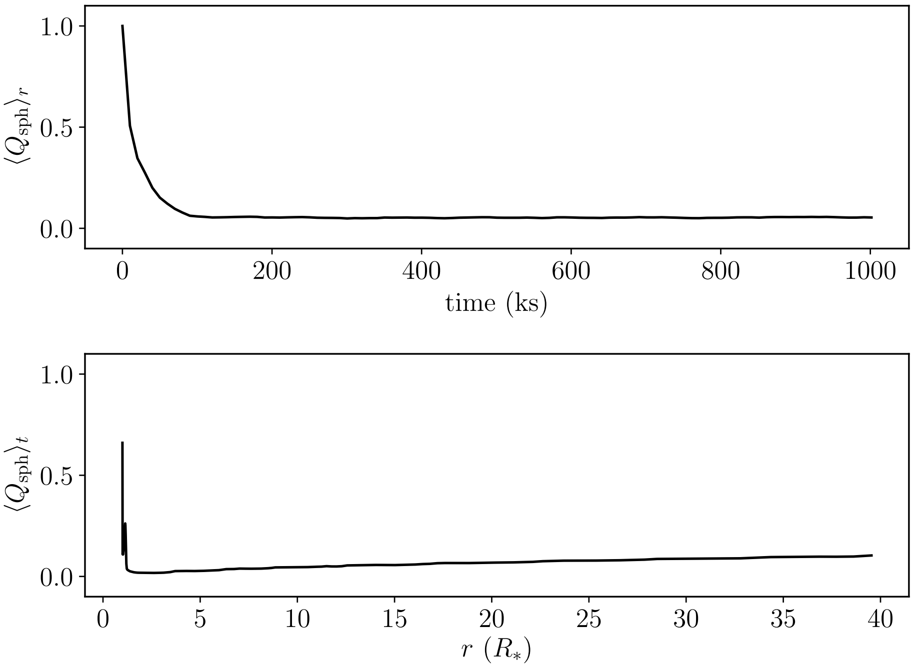

Figure 5.9: Average spherical quality factor, $\langle Q_{\rm sph}\rangle$, averaged over both time (top) and space (bottom). Both plots show a rapid departure from spherical symmetry within the first 100 s. While the time average falls to 0.055 and remains approximately constant, the spatial average initially decreases then linearly increases out to 40 R_* where it reaches a value of 0.104, meaning that the inner wind is less spherical than the outer.

depth and this in turn is a function of the column density, the wind structure entirely determines both the magnitude and rotational modulation of the observed spectral flux. Wind clumping, collimation and disk structures will all impact the degree to which emission can escape the system and reach the observer.

In the case of a purely spherical wind, there is an effective minimum radius around the star at which emission from the wind at larger radii can escape to the observer; emission from within the effective radius cannot. The optical depths dependence on the density, means that emission from the inner wind is effectively (from the point of view of the observer) obscured by the extended wind at larger radii. This effective radius is thus the radio photosphere of the star. For a clumped, magnetically confined or otherwise non-spherical wind, this photosphere is not spherical and emission escapes from varying radii. As such, quantifying the winds departure from spherical symmetry is an important step in placing the radio emission in context.

This is accomplished by following the approach of ud-Doula et al. (2008), who devised an expression to quantify the radial distribution of material in the magnetosphere. By integrating the product $r^2\rho\left(r,\theta,\phi,t\right)\sin(\theta)$ over the two angular coordinates, θ and ϕ one is left with the global density structure stratified in the radial direction. This radial mass distribution is given by the following expression:

$$\frac{\mathrm{d}m\left(r,t\right)}{\mathrm{d}r} = r^2 \int_0^{2\pi}\int_0^{\pi} \rho\left(r,\theta,\phi,t\right)\sin(\theta)\mathrm{d}\theta\mathrm{d}\phi. \tag{5.24}$$

Motivated by the need to capture the behaviour of material in the case of an aligned dipole, ud-Doula et al. (2008) chose to limit the integration over θ to a small angular region centred about the equator. In this study, the behaviour is not constrained to the rotational equator so we integrate over the full range of θ.

Equation (5.24) is plotted in Fig. 5.8 over the entire radial range of the simulation and for a limited region of the inner 6 R_*. The first $\sim$ 100 ks of the evolution of $\mathrm{d}m\left(r,t\right)/\mathrm{d}r$ is a striking illustration of the blow-off of the initial conditions, where a fan of higher density material tracks outwards from the surface to the boundary. For t $>$ 100 ks the global radial motion of material is approximately constant with only small perturbations, as clumps of material concentrate in the closed magnetosphere, breakout and track outwards leading to radial lines in $\mathrm{d}m/\mathrm{d}r$.

Both the Kepler and Alfvén surfaces are indicated in the figure and show little change in $\mathrm{d}m/\mathrm{d}r$ across them. This is consistent with the dynamical magnetospheric behaviour described in Section 5.2.3.

As a consequence of the magnetic confinement and the reduction in the mass-loss rate, the stellar wind is overall much less dense than for a corresponding non-magnetised stellar wind and emission from deeper in the wind, closer to the stellar surface will be able to escape. However, as the total wind material is reduced, the total spectral flux, S_ν will also be reduced, resulting in a fainter signal reaching the observer. Additional free-free absorption along the line of sight may also contribute to the reduction in observable emission.

To further quantify the departure from spherical symmetry, we now detail the formalism of a dimensionless measure to be used as an indicator for the overall spherical nature of the wind.

For a given radius there exists a spherical shell, S, of width $\mathrm{d}r$. To quantify the spherical distribution of material within this shell we adopt the following procedure. Each density value within the shell, $\rho\left(\theta, \phi\right)$, is normalised by the maximum density, $\rho_{\mathrm{max}}\left(\theta, \phi\right)$, in the shell, these normalised density values are then integrated over the entire shell. Finally this integral is divided by the total number of sample points within the shell. The final expression,

$$Q_{\mathrm{sph}}\left(r, t\right) = \frac{1}{N_S} \int_S \frac{\rho\left(\theta, \phi\right)}{\rho_{\mathrm{max}}\left(\theta, \phi\right)} \mathrm{d}S, \tag{5.25}$$

gives the spherical quality factor, Q_{sph}, within the range $0 < Q_{\mathrm{sph}} < 1$ and is a measure of the departure of the density distribution from a spherical wind within shell S at radius r and time t. A value of 1 indicates a spherically symmetric wind while a value of 0 indicates a complete departure from spherical symmetry.

By computing Q_{sph} for every radial shell and for every time point, it is then possible to calculate both the time average, $\langle Q_{\mathrm{sph}} \rangle_t$, for every radial point and the radial averaged, $\langle Q_{\mathrm{sph}} \rangle_r$, for every time point. These two quantities are plotted in Fig. 5.9. Each data point in the top plot represents the $\langle Q_{\mathrm{sph}} \rangle_r$ for the entire simulation volume as a function of time and every data point in the bottom plot represents the $\langle Q_{\mathrm{sph}} \rangle_t$ across every time point in the simulation as a function of radius.

From Fig. 5.9, we can see that, for all time after the initial $\sim$ 100 ks, $\langle Q_{\mathrm{sph}} \rangle_r$ remains constant at 0.055. However, the radial profile of the time average indicates an increase in $\langle Q_{\mathrm{sph}} \rangle_t$ towards larger radii to a value of 0.104. This is consistent with a broadening out of the excretion disk as it expands radially.

Temperature is constant in the simulation, however as the disk is denser than its surroundings there is still a pressure gradient leading to an expansion, this together with rotation and diverging magnetic field lines spreads material out at larger radii. For an

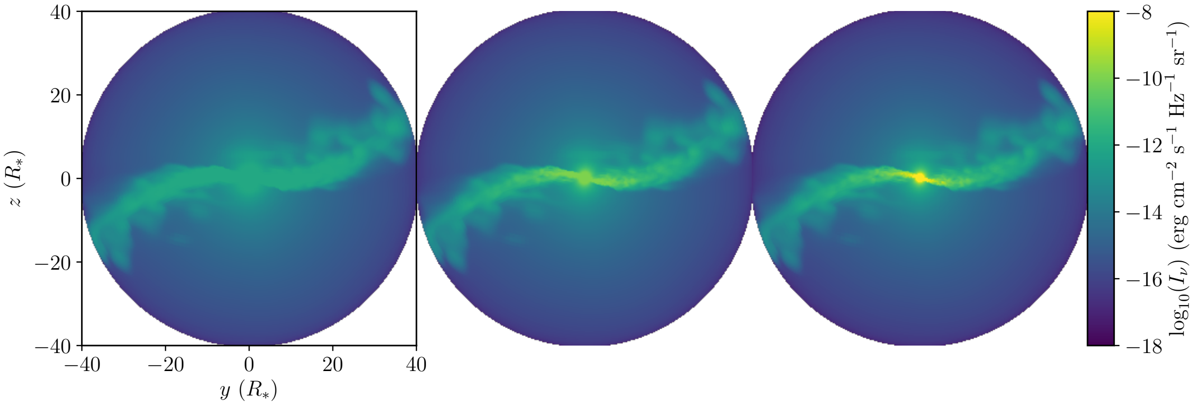

Figure 5.10: Intensity of radio emission for an observing inclination of 30°, phase 216° and observing frequencies of 10 GHz (left), 100 GHz (middle) and 1000 GHz (right). The figure illustrates the additional resolution gained by observing at higher frequencies, as the panel, from left to right shows a progressively sharper central star.

adiabatic model, this expansion will be made more acute as a temperature would also enhance the broadening and lead to a greater $\langle Q_{\text{sph}} \rangle_t$ at larger radii than seen here.

The results for both $\mathrm{d}m\,(r,t)\,/\mathrm{d}r$ and $\langle Q_{\text{sph}} \rangle$ indicate a wind which has undergone rapid departure from spherical symmetry, with a decrease in the overall wind mass from the initial condition leading to lowered column density along the observers view compared to the same wind without the action of a magnetic field. With this in mind, we now turn to the results of the synthetic radio emission.

5.3.3 Radio/sub-mm emission

We divide the radio emission results into first a discussion of the structure of the emission volume as it appears from the radio intensity calculation of equation (5.17) together with its dependence on the observing frequency, inclination and rotational phase. Secondly, the total spectral flux density, S_ν is calculated to give both a radio light curve for two rotations, at three discreet frequencies over a range of phases and inclinations of the star and a spectral frequency range of 10 GHz $< \nu <$ 10^4 GHz at constant inclination and phase. This range is chosen as it spans the observing bands of the instrument ALMA. For both the rotational modulation and continuum spectra, we calculate $\dot{M}_{\text{obs}}/\dot{M}_{\text{sim}}$.

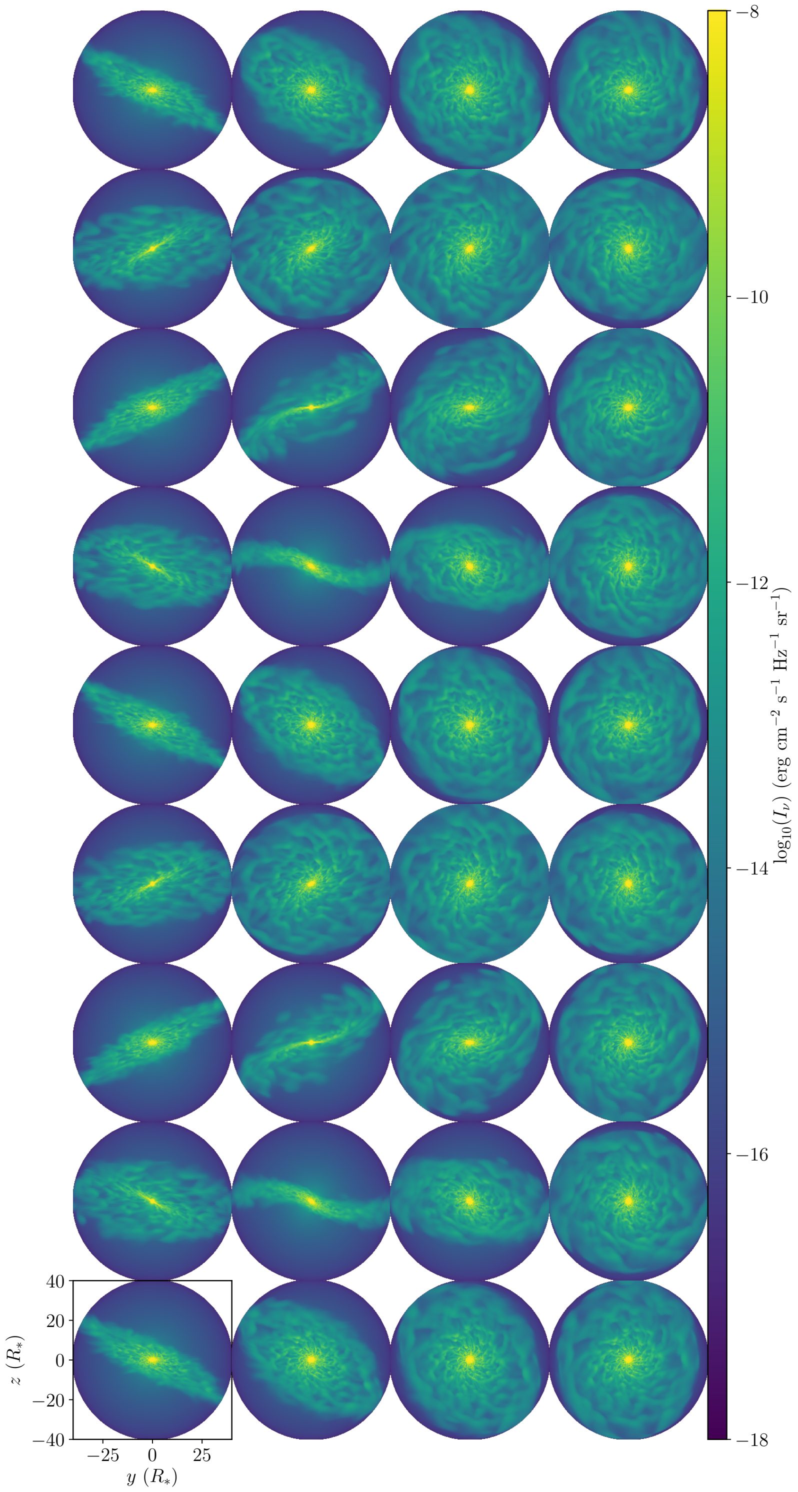

Figure 5.11: Intensity of radio emission for rotational phase and observing inclination, all plots are generated at 900 GHz. Each column represents observing inclinations of 0° (viewing along equator), 30°, 60° and 90° (viewing down the polar axes) from left to right respectively. Each row are snap shots of the radio intensity for increasing phase from 0 radians to 4π radians (two full rotations), equally spaced by $4\pi/9$ radians. The second column on the left experiences the greatest degree of variability in the disk while the right most column experiences the least, presenting the same disk surface area to the observer over the 2 complete rotations.

5.3.3.1 Wind structure in emission

To illustrate the concept of optical depth and dependence of observational results on the chosen observing frequency, we plot in Fig. 5.10 the intensity of radio emission, I_ν, at the same specific phase and inclination of 30° and 216° for three dex in observing frequency, ν, of: 10 GHz, 100 GHz and 1000 GHz. Form left to right, the figure shows increasing fidelity in the inner region close to the star, where the density profile has its largest values. Higher frequencies thus penetrate further into the wind. Only the highest observing frequency of 1000 GHz is able to penetrate the wind down to approximately the stellar surface. If ν is increased beyond 1000 GHz, emission from the stellar surface black body radiation will begin to dominate, we will discuss this further in Section 5.3.3.3

To gain an appreciation of the rotational modulation and dependence on observer inclination of the intensity map, I_ν, we limit the parameter space to a single observing frequency of 900 GHz; chosen as it lies within ALMA frequency band 9. Fig. 5.11 shows time series snapshots for I_ν. Rows 1 - 9 show the rotational phase at equidistant intervals of $4\pi/9$ across the full two rotations and the four columns show, from left to right, inclination values of 0°, 30°, 60° and 90°.

The second column, inclination of 30°, shows the greatest degree of variability with the disk presenting both its edge and face to the observer. Looking down the rotational axis, inclination of 90°, the disk exhibits the smallest degree of variability, always showing the same disk extent. However, a face on disk presents the largest ratio of visible surface area to volume for an observer; resulting in the greatest total emission.

For all phases and inclinations, the central star is clearly visible, in contrast to the left image of Fig. 5.10, calculated at 10 GHz, where the star is obscured by the extended wind and emission from the centre is of the same order of the surrounding disk. As Fig. 5.11 is calculated at 900 GHz, we can conclude that this frequency is sufficient to probe the range of densities, and therefore optical depths, occurring in the simulation.

A final noteworthy result of the rotation and inclination calculation, is the apparent difference of the rotational period between the first column of Fig. 5.11 and the other three. For this first column, rows 1, 5 and 9 show the same image, while rows 3 and 7 show the same image but inverted about the z-axis. This inversion is evident form the simulation results, as the intensity map effectively shows a resolved source. However, an earth bound observer sees the total flux, S_ν, which is the integration of I_ν over both y and z. Such inversions of the source are not captured by the total flux and may lead to false predictions of the rotational period, as shown in the following section.

5.3.3.2 Radio lightcurves

We now turn to the time dependence of S_ν. Fig. 5.12 shows this dependency for the rotational phases and inclination of Fig. 5.11 for observing frequencies of 250 GHz and 650 GHz in addition to 900 GHz.

As already apparent in the intensity maps, $I_\nu(y, z)$, of the previous section; for an inclination of 90° there is virtually no variability. This is in marked contrast to the curves of the three other inclination which all show rotational modulation between factors of approximately 1.5 and 2.

One would expect the greatest degree of modulation for the 30° inclination, as this equals the obliquity of the dipole field and therefore the normal to the disk should coincide with the observers line of sight periodically through the rotation. This is indeed what we see in Fig. 5.12. However, it is the 60° inclination which results in the largest maximum emission. this is the result of a combination of magnetic tension and disk warping leading to the largest observed surface area for the disk at this inclination for phases of 0, 1 and 2.

For an inclination of 0°, the light curve exhibits 4 distinct minima and maxima, in contrast to 30° and 60° inclinations which only show 2 distinct minima and maxima. Therefore, the top row does indeed show a rotation rate for the star with is twice the actual, as predicted in the previous section.

The different behaviour of all lightcurves across all inclination and phases illustrates the sensitive dependence upon the magnetic field that the radio emission from the in-

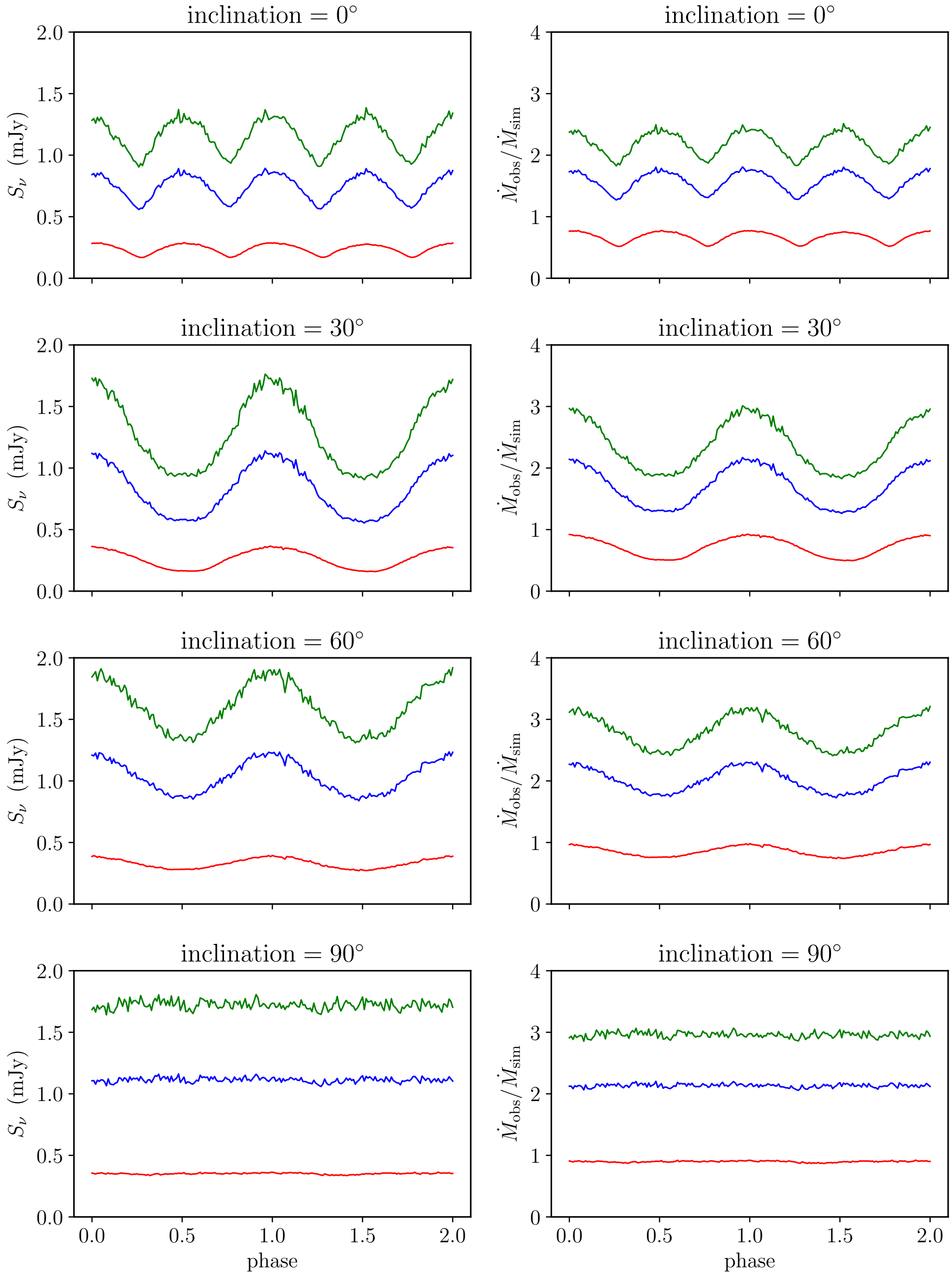

Figure 5.12: Left column: radio lightcurves over two rotations for the 4 observing inclinations, top to bottom: 0° (viewing along equator), 30°, 60° and 90° (viewing down the polar axes). Each inclination shows the result for the 3 observing frequencies; 250 GHz (red), 650 GHz (blue) and 900 GHz (green). What is immediately apparent is the lack of variability for all three frequencies in the 90° inclination plot. This is due to the excretion disk presenting the same surface area to the observer over the 2 complete rotations. For an inclination of 0°, the light curve exhibits 4 distinct minima and maxima, in contrast to 30° and 60° inclinations which only show 2 distinct minima and maxima. Right column: rotational modulation of the inferred mass-loss from the synthetic radio lightcurves. All frequencies and observing inclinations show modulation of the predicted mass-loss except observations at 90° which shows flat predictions at all phases and frequencies. Rotation at 900 GHz and inclination of 30° shows the largest degree of modulation. Each observing frequency results in a different inferred mass-loss due to the dependence of mass-loss on the spectral flux.

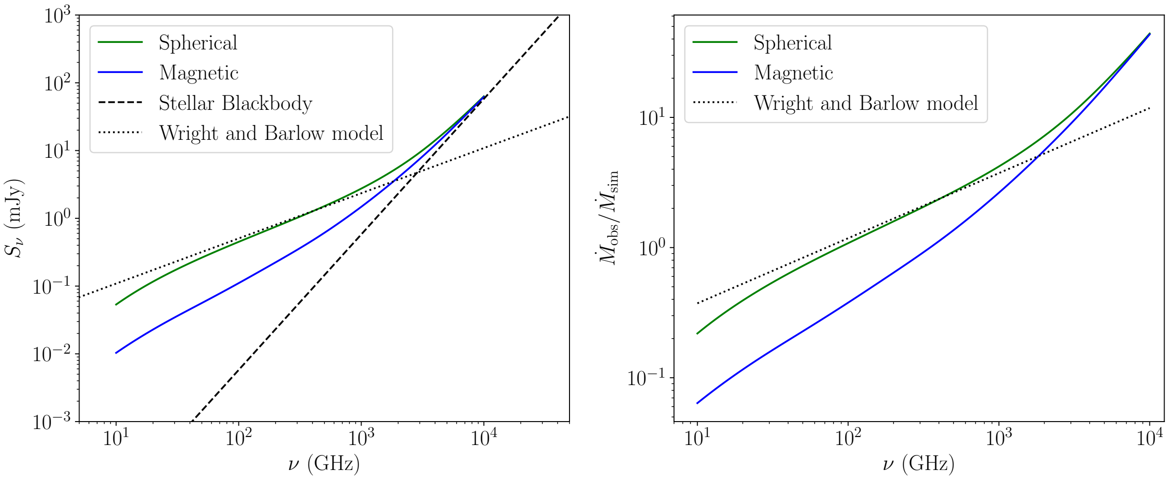

Figure 5.13: Left: radio/sub-mm spectrum for 3 models of emission; numerical spherically symmetric (green curve), numerical magnetic (blue curve) and analytic Wright & Barlow (1975) model (black dotted line). The stellar surface black-body curve is also shown (black dashed line). Both numerical models converge with the surface black-body at $\nu > 10^4$ GHz while the Wright & Barlow (1975) model does not. Right: Corresponding mass-loss predictions for the three emission models using equation (5.22).

ner and extended wind has. Understanding observing inclination, rotational phase and obliquity is therefore critical for placing observed S_ν in context.

In Section 5.2.4 we detailed the method for estimating stellar wind mass-loss rates from the observed spectral flux, S_ν. The left column of Fig. 5.12 shows the mass-loss rate inferred from the synthetic radio observations via equation (5.22), $\dot{M}_{\rm obs}$, normalised to the average simulation mass-loss rate, $\dot{M}_{\rm sim}$. As $\dot{M}_{\rm sim}$ is measured directly in our simulation, the resulting reduction in the wind mass and spherical nature due to magnetic confinement should be apparent and allow us to self-consistently assess the discrepancy between $\dot{M}_{\rm sim}$ and the inferred mass-loss from the synthetic radio emission, $\dot{M}_{\rm obs}$. Thus $\dot{M}_{\rm obs}/\dot{M}_{\rm sim} = 1$ corresponds to the situation where the inferred observed mass-loss is equal to the simulated mass-loss.

All frequencies and observing inclinations show modulation of $\dot{M}_{\rm obs}$ except for the 90° inclination which shows flat predictions at all phases and frequencies consistent with the flat radio curves. These flat predictions still depart from $\dot{M}_{\rm sim}$ however, with higher frequencies overestimating the mass-loss rate. This becomes more acute as the observing frequency increases, with 900 GHz leading to the largest overestimate. Rotation at

900 GHz and inclination of 30° shows the largest degree of modulation, constant with the corresponding S_ν. As the mass-loss calculation, equation (5.22), has a functional dependence on the spectral flux of $\dot{M}_* \propto S_\nu^{3/4}$, we can expect for a doubling of S_ν to result in a 1.68 times increase in $\dot{M}_*$, which is approximately what we see for the lightcurves in the right-hand column.

For the signature of magnetic confinement on the rotational modulation and therefore the radio emission and predicted mass-loss to diminish, the wind would have to return to a spherical expansion. For our simulation, this will happen at large radii (and therefore at low observing frequencies). From the lower plot of Fig. 5.9, we can see that $\langle Q_{\rm sph} \rangle_t$ has increased to 0.1 between the initial confinement, close to the star, and the outer simulation boundary. The physical distance required for $\langle Q_{\rm sph} \rangle_t \rightarrow 1$ is not covered in this work, however, it seams likely that this would happen at radii where the contribution to the spectral flux occurs at frequencies $<<$ 1GHz. Once $\langle Q_{\rm sph} \rangle_t = 1$, modulation of the radio emission would no longer happen. However, at these radii, the density of the wind would be so low that free-free absorption would not be sufficient to prevent rotationally modulated emission from closer to the star escaping to the observer. At these radii, recombination may also have occurred for the majority of the wind.

The noise seen in both the radio lightcurves and the corresponding mass-loss curves, is due to the numerical details of the radio calculation, which involves interpolation from spherical to Cartesian coordinate systems. By doing so, resolution is reduced close to the stellar surface where high frequency ($\sim 10^3$ GHz) emission originates from. Lower frequency (~ 10 GHz) emission originates from the outer wind where resolution is not reduced (for a spherical grid, the cell size increases with radius). This explains the lack of numerical noise in the 250 GHz curves.

5.3.3.3 Continuum spectrum

The radio continuum for our simulated star, along with two comparative models, is plotted in the left panel of Fig. 5.13. These comparative models are the Wright & Barlow (1975) model (black dots, referred to as WB75 from here on) discussed in Section 6.1 and 5.2.4 and the numerical results of the theory laid out in Section 5.2.4, applied to the spherically symmetric initial conditions of the simulation (green curve, referred to as SPSY from here on). The stellar black-body radiation is also indicated (black dashes). The magnetically confined wind result (blue curve, referred to as MC from here on) shows a clear departure from both the SPSY and WB75 models for $\nu < 10^3$ GHz. At $\nu > 10^3$ GHz, both SPSY and MC curves converge to the black body radiation indicative of the optically think regime of the stellar surface. This limit is not observed by the WB75 model as its theoretical basis ignores the presence of the stellar surface and the acceleration region where the density profile departs from a $1/r^2$ dependence (see Daley-Yates et al. (2016) for an in-depth discussion). This highlights the WB75 models applicability to the extended wind region, where a spherical wind will have a flat velocity profile (equal to v_∞) and also its inability to capture the emission behaviour at high frequency. The WB75 model is the basis for the mass-loss prediction of equation (5.22), its limitations will therefore effect any mass-loss predictions based on the spectral flux.

The corresponding normalised mass-loss prediction $\dot{M}_{\rm obs}/\dot{M}_{\rm sim}$ for the continuum spectra are displayed in the right panel of Fig. 5.13. All models show a dependence on ν with a two orders of magnitude variance. The numerical spherical prediction agrees with the WB75 model in the mid frequency range 10^2 GHz $< \nu < 10^4$ GHz, which corresponds to a constant gradient for the spectral flux (a spectral index of $\alpha = 0.6$), but departs either side of this range. For the magnetically confined wind, except for agreement with the numerical spherical wind at high frequency $\nu > 10^3$ GHz, there is approximately an order of magnitude reduction in $\dot{M}_{\rm obs}/\dot{M}_{\rm sim}$ across all frequencies.

Recently Ramiaramanantsoa et al. (2017) communicated observations of the O4I(n)fp star ζ Puppis with the BRITE-Constellation nanosatellies. They detected one single periodic, non-sinusoidal component of the emission, which they attributed to the presence of bright surface features. Separate simultaneous spectroscopic observations led them to infer the action of corotating interaction regions (CIRs). While no surface spots are present in our simulation, the modelling of ζ Puppis by Ramiaramanantsoa et al. (2017) to explain the BRITE-Constellation observations, results in spiral structures of a similar nature to those in Fig. 5.5. We do not make direct comparisons to the models of Ramiaramanantsoa et al. (2017), since ζ Puppis and our model star are very different. However, we highlight the similarity in the features and that, following further analysis of the synthetic observables at BRITE-Constellation frequencies, magnetically activity may provide a compelling explanation for the origin of CIRs in the magnetic massive star population.

JVLA observations by Kurapati et al. (2016) of seven O-type and eleven B-type stars resulted in the detection of two O-type and two B-type stars. While all four stars were detected at 10 GHz only one was detected at 23 GHz. The lack of detection at this higher frequency is attributed to thermal free-free absorption in the extended wind. In the context of our results, this free-free absorption would need to occur at radii not captured by our simulation or the winds of the observed stars would need to be much denser. Mass-loss rates and therefore wind densities may also be lower than that used in our simulation, resulting in lower fluxes. Another possible explanation for the lack of detection is that the magnetic confinement of the stellar wind has, in the manner of our synthetic radio results, reduced the spectral flux possibly below the sensitivity of the JVLA.

Kurapati et al. (2016) report that their theoretical, $\dot{M}_{\rm th}$, and observationally inferred, $\dot{M}_{\rm ob}$, mass-loss rates may vary by a factor of 3, as the $\dot{M}_{\rm th}$ are based on the models of Vink et al. (2000) which assume smooth spherical symmetry and no magnetic confinement. This is indeed the order of variability seen in our synthetic lightcurves and continuum emission, where we see deviation by a factor of 3 for the magnetic wind compared to the spherical wind.

Our results agree with the results of Kurapati et al. (2016) to within the uncertainty stated for their $\dot{M}_{\rm th}$. However, we draw attention to the fact that magnetic confinement of the wind introduces a dependency of the emission on not only the density profile but also the observing inclination and phase; as both spherical and cylindrical symmetry of the wind has been broken.

5.4 Conclusions

We have performed 3D isothermal MHD simulations of a magnetic rotating massive star with a non-zero dipole obliquity and predicted the synthetic radio/sub-mm observable lightcurves and continuum spectra for a frequency range compatible with ALMA. From these results we also compare the simulation mass-loss rate to the inferred observed mass-loss rate calculated from the synthetic spectral flux.

Despite the lack of shock heating and cooling physics imposed by the isothermal assumption, spherical and cylindrical symmetry is broken due to the obliquity of the stellar magnetic dipole resulting in an inclination and phase dependence of both the synthetic spectral flux and corresponding inferred mass-loss rate. Both quantities vary by factors between 2 and 3 over a full rotational period of the star, illustrating the divergence from a symmetric wind.

We also show that a constant spectral index, α, model agrees well with our numerical prediction for a spherical wind for $\nu < 10^3$ GHz, however it is unable to capture the behaviour of emission at $\nu > 10^3$ GHz. As such we caution the use of such constant α models for predicting emission from non-spherical winds such as those which form around magnetic massive stars.

As this is the first 3D simulation of a massive star wind incorporating an oblique dipole, there is a large parameter and physical space left to study. Future work will extend the current model to adiabatic physics, allowing for shock heating and optically thin cooling of the gas. Both of these physical mechanisms are important for the generation of higher energy emission such as X-ray and H_α.

6

Inhibition of the electron cyclotron maser instability in the dense magnetosphere of a hot Jupiter

This chapter is a reformatted copy of the paper Daley-Yates & Stevens (2018): “Inhibition of the electron cyclotron maser instability in the dense magnetosphere of a hot Jupiter” and is my own work, aside from Section 6.1.4 contains text form the co-author.

6.1 Introduction

Understanding the evolution of giant exoplanets is important as they give us insights into the long term evolution of the planetary systems in which they reside. The reason for this is that giant planet formation is inhibited close to the parent star (Murray-Clay et al., 2009), and they must undergo migration across many orders of magnitude of radius to be found in short–period orbits (< 10 d). Such planetary migration has implications for the evolution of their entire host system (Fogg & Nelson, 2005; Petrovich & Tremaine, 2016; Alvarado-Montes et al., 2017).

Giant planets in such close orbits are known as hot Jupiters (HJs). As a consequence of their close orbits, the planets atmosphere receives large amounts of UV radiation, leading to atmospheric blow off or the establishment of a hydrodynamic planetary wind (Matsakos et al., 2015) which can reach temperatures of 10^4 K (Shaikhislamov et al., 2014).

Recent studies have monitored increased emission in X-ray as well as metal lines of HJ hosting stars (Shkolnik et al., 2008; Miller et al., 2015; Pillitteri et al., 2015). Gurdemir et al. (2012) conclude that enhanced emission in Ca II H and K lines of HD 179949 is due to planetary material accreting onto the stellar surface, inducing enhanced chromospheric emission.

Many of the dynamic behaviour and observable signatures of extrasolar planetary systems can be characterized through the paradigm of star–planet interaction (SPI). Traditional planet detection techniques including the transit and radial velocity methods (see Wright & Gaudi (2012) for a review of the various methods), rely centrally on observing the interplay between the planet and the host star. At many wavelengths, such as infrared or visible, the planet is simply too dim compared to the luminosity of its host star, making direct detection rare.

Radio wavelengths provide an alternative method for exoplanet observation to those described above, with the possibility of direct planet detection (Stevens, 2005; Zarka, 2007). Planet hosting stars are typically radio quiet; therefore, SPI processes that result in significant, detectable radio emission will be observed despite the presence of the host star. Star–planet magnetic interaction (SPMI) is a prime candidate for generating such observable radio emission. Examples of this type of interaction include magnetic reconnection between polar magnetic field lines of the star and planet as well as reconnection in the magneto tail of the planet. Another mechanism for SPMI is the amplification of the electron cyclotron maser instability (ECMI). Emission via this mechanism is due to incident solar wind power, both ram and magnetic, on the planetary magnetic field. The efficiency of the ECMI for producing radio emission is the main topic of this paper.

6.1.1 Electron cyclotron maser instability: a means for detecting hot Jupiters

ECMI is a process where electrons emit radiation due to confinement by magnetic field lines along which they travel, gyrate and accelerate around (Melrose & Dulk, 1982; Dulk, 1985). The emission is almost 100 % circularly polarized and directionally beamed. The environment around exoplanets such as HJs is thought to be well suited for producing this form of emission, due to high magnetic field strengths and strong incident stellar wind power.

Many studies have investigated the conversion of incident stellar wind power to ECMI emission (Kivelson et al., 1997; Stevens, 2005; Zarka, 2007; Hess & Zarka, 2011). Conversion efficiencies up to 0.2 % of the incident stellar wind power has been proposed by Zarka (2007) as a consequence of a *radio-magnetic Bode's Law* (see the aforementioned paper for details). Such high power conversion rates would lead to emission of the order of 1 - 10 mJy of detectable emission (from a candidate system at 10 pc; Stevens (2005)). Such high fluxes indicate that, for a full understanding of the observable radio signatures of SPMI, the host star must be considered explicitly in any model as its dynamic behaviour influences the evolution and observable properties of short–period HJs.

ECMI emission is also seen at radio wavelengths from a number of other stellar sources. Examples include the following:

- Low-mass dwarf stars, sometimes referred to as ultracool dwarfs. The observed radio emission is characterized by bright, circularly polarized bursts at GHz frequencies that are of short duration (1–100 min). Williams (2017) provides a summary of recent results on this class of object.

- Magnetic early–type stars can also show highly polarized, rotationally modulated bursts, consistent with ECMI emission (Trigilio et al., 2011). See also Das et al. (2017) for results on the magnetic Bp star HD 1333880 (HR Lup) and the main–sequence B2.5V star HR 5907 (Leto et al., 2018).

- RS CVn type systems, which can also show highly circularly polarized burst like emission in the binary system. See Slee et al. (2008) for observations of the RS CVn system HR 1099.

6.1.2 Radio emission from hot Jupiter exoplanets

Infra-red, visible and UV emission from exoplanets are difficult to detect from Earth due to the high luminosity of the host star (Zarka, 2007). Main sequence solar type stars are however quiet in the low frequency radio spectrum, making the detection of radio emission from the planet feasible (Grießmeier et al., 2007).

As discussed in the previous section, radio ECMI emission is directly related to the magnetic field strength of the planet. Therefore observations of this type of emission can provide an indirect means of measuring and classifying the planetary magnetic field. This quantification of the magnetic filed gives us constraints on internal structure models and planetary rotation, informing us about the evolutionary history of the planet and host system (Hess & Zarka, 2011).

HJs present the best opportunity for studying extra solar planetary radio emission. This is due to their close proximity to their host stars and their potentially strong magnetic fields.

The SPMI origin of non-thermal radio emission is by nature transient. If the planet orbits within the Alfvén surface of the star, reconnection events between the stellar and planetary magnetospheres will occur (Strugarek et al., 2014), depending on the dynamic behaviour of the stellar surface. In addition, the amplification of ECMI emission by the incident stellar wind is inherently dependent upon the wind conditions along the trajectory of material from the stellar surface to the planet. Transient stellar surface events such as coronal mass ejections (CME) and flares, will modify the ram pressure and magnetic energy density of the wind, leading to higher intensity EMCI emission (Llama et al., 2013; Vidotto et al., 2015). The transient nature of these phenomenon makes detection challenging.

A recent study by Weber et al. (2017) explored analytically the ECMI process in the magnetospheres of HJs. The study concludes that enhanced particle density, due to the planetary wind, inhibits the ECMI process for magnetic field strengths < 50G. Our study aims to build on this result by conducting self–consistent numerical magnetohydrodynamic (MHD) simulations of a HJ system, including the host star. Simulations produce dynamic features that are not captured in analytic calculations.

6.1.3 Analogies in the solar system

Justification for the expectation of bright ECMI emission is found via analogy to the solar system planets and the Jovian moons. For example, the Jovian auroral radio emission, at MHz frequencies, is dominated by ECMI processes from keV electrons in the auroral regions of the planet (George & Stevens, 2007). At higher frequencies ($\sim$ GHz), the emission from electrons in the planets radiation belts dominate, however at orders of magnitude lower intensity than EMCI emission (Zarka, 2007). There is a cut–off at lower frequencies due to the Earth's ionosphere (see Section 6.1.4). ECMI emission has also been detected from Saturn, Uranus and Neptune by space–based missions (Zarka, 1998).

Zarka (2007) theoretically investigated HJ radio emission via extrapolation from the solar system planets and the Jovian moons. By considering the incident solar wind power and the effective obstacle area of each body (magnetispheric radius), the emitted radio power can be estimated. Using this approach, Zarka (2007) developed a generalised 'radio Bode law', where there is almost a one–to–one relationship between the incident power and the emitted radio power, given an efficiency factor of $\sim\ 2 \times 10^{-3}$. This leads to an estimate of emitted radio power for an HJ in the region of $10^{14} - 10^{16}$ W (see fig. 6 of Zarka (2007)). Radio power at this magnitude results in detectable emission of the order of a few mJy (Stevens, 2005). This flux is easily detectable by the current generation of telescopes.

6.1.4 Prospects for detectability

The possible detection of exoplanet radio emission is hampered by the presence of the Earths ionosphere. The ionosphere is a partially ionized layer of the atmosphere, with a typical altitude of 50–1000 km. It is very dynamic, with the electron density varying dramatically as a function of space and time, being mainly affected by UV and X-ray solar emission and by charged particles from the solar wind. The ionospheric plasma frequency (see Section 6.2.3.1) typically ranges between 1 and 10 MHz, but sometimes (e.g during sporadic E-layer events) can reach as high as 200 MHz. Cosmic radio waves with a frequency below the ionospheric plasma frequency will be reflected by the ionosphere and, thus, not reach an Earth-bound telescope. Understanding and accounting for the ionosphere is a major concern for low–frequency radio telescopes (operating at $<$ 300 MHz), such as the GMRT, LOFAR, LWA and Murchison Widefield Array (MWA) and SKA-Low in future (Intema et al., 2009).

Thus far, there have been several observational studies that have attempted to detect exoplanet radio emission including LOFAR/VLT observation by Knapp et al. (2016) and LOFAR observations by Turner et al. (2017). Both report no detections. Murphy et al. (2014) have placed limits on low-frequency radio emission from 17 known exoplanetary systems with the MWA. They detected no radio emission at 154 MHz, and put 3σ upper limits in the range $15.2--112.5$ mJy. The only reported detection thus far is of 150 MHz emission from HAT-P-11b by Lecavelier des Etangs et al. (2013) with a flux of 3.87 mJy. This signal, however, was not detected by repeat observations and is, thus, not conclusive.

This study aims to further investigate this conclusion by performing high–resolution simulations of both the exoplanetary magnetosphere and global evolution of the stellar wind in which the exoplanet is embedded. This is done using MHD, adaptive mesh refinement numerical simulations. The following section will detail the governing conservation equations and the specific setup used to simulate the stellar and exoplanetary bodies and the mechanism and conditions needed for ECMI emission to be produced.

6.1.5 Simulations

Numerous numerical studies have been carried out in recent years, which have simulated many aspects of SPI, examples range from detailed studies of the close in atmospheres of HJs (Strugarek et al., 2014; Khodachenko et al., 2015; Vidotto et al., 2015), the atmospheres of their host stars (Alvarado-Gómez et al., 2016; Fares et al., 2017), to the global structure of the planetary-stellar wind interaction (Bourrier & Lecavelier des Etangs, 2013; Owen & Adams, 2014; Alexander et al., 2015; Bourrier et al., 2016). The study presented here builds on this work, specifically on the simulations conducted by Matsakos et al. (2015), extending it to investigate ECMI emission in the context of SPMI.

6.2 Modelling

The models constructed here follow the approach used by Matsakos et al. (2015); however, instead of using a static numerical grid in which the MHD equations are solved, we employ the method of adaptive mesh refinement (AMR). The advantage of using a static mesh is that the resolution and, therefore, the memory usage are kept constant throughout the simulation. This is not the case with AMR, whose advantage is that evolution of material not in the vicinity of either the star or the planet can be actively traced. This allows for a high–resolution study of the large–scale structure of material evaporated from the planet to be studied. This is an important consideration if observable effects such as asymmetric transit depths (Llama et al., 2013) are to be investigated.

Chadney et al. (2015) argue that the atmosphere of an HJ is either in a hydrostatic or hydrodynamic state depending on its distance from its host star. The transition between these to regimes is an orbital distance of ~ 0.5 au, for a solar type star. Since the orbital distance in this work is set to 0.047 au, we make the assumption that the planetary atmosphere is purely hydrodynamic in nature. This assumption is further reinforced by work carried out by Murray-Clay et al. (2009), who model heating and cooling, ionization balance, tidal gravity and pressure confinement by the host star wind when studying the nature of the mass-loss from UV evaporated HJs. They found that the resulting planetary wind takes the form of a Parker wind emitted from the planets day side. For this reason, both the stellar and planetary winds in this study take the form of that described by Parker (1958) and evolve according to the equations of MHD. The following section details these equations.

6.2.1 Magnetohydrodynamics

The equations of MHD are solved in a frame co-rotating with the orbital motion of the planet. These equations are as follows:

$$\frac{\partial \rho}{\partial t} + \boldsymbol{\nabla} \cdot (\rho \boldsymbol{v}) = 0 \tag{6.1}$$

$$\frac{\partial \boldsymbol{v}}{\partial t} + (\boldsymbol{v} \cdot \boldsymbol{\nabla}) \boldsymbol{v} + \frac{1}{4\pi\rho} \boldsymbol{B} \times (\nabla \times \boldsymbol{B}) + \frac{1}{\rho} \nabla p = \boldsymbol{g} + \boldsymbol{F}_{\mathrm{co}} \tag{6.2}$$

$$\frac{\partial p}{\partial t} + \boldsymbol{v} \cdot \boldsymbol{\nabla} p + \gamma p \nabla \cdot \boldsymbol{v} = 0 \tag{6.3}$$

$$\frac{\partial \boldsymbol{B}}{\partial t} + \nabla \times (\boldsymbol{B} \times \boldsymbol{v}) = 0. \tag{6.4}$$

Where ρ, $\boldsymbol{v}$, $\boldsymbol{B}$, p, $\boldsymbol{g}$ and $\boldsymbol{F}_{\mathrm{co}}$ are, respectively, the density, velocity, magnetic field, pressure, acceleration due to gravity and acceleration due to the co-moving frame. $\boldsymbol{F}_{\mathrm{co}}$ is the sum of the centrifugal and Coriolis forces: $\boldsymbol{F}_{\mathrm{co}} = \boldsymbol{F}_{\mathrm{centrifugal}} + \boldsymbol{F}_{\mathrm{coriolus}}$, which are given by

$$\boldsymbol{F}_{\mathrm{centrifugal}} = -\left[\boldsymbol{\Omega}_{\mathrm{fr}} \times (\boldsymbol{\Omega}_{\mathrm{fr}} \times \boldsymbol{R})\right] = \boldsymbol{\Omega}_{\mathrm{fr}}^2 \left(x\hat{x} + y\hat{y}\right) \tag{6.5}$$

and

$$\boldsymbol{F}_{\mathrm{coriolus}} = -2\left(\boldsymbol{\Omega}_{\mathrm{fr}} \times \boldsymbol{v}\right) = 2\Omega_{\mathrm{fr}}\left(v_x\hat{x} + v_y\hat{y}\right), \tag{6.6}$$

where $\boldsymbol{\Omega}_{\mathrm{fr}}$ is the angular frequency of the frame in which the calculations are being conducted and R is the radial distance from the origin.

An adiabatic equation of state is used to close the MHD equations. Both the stellar and planetary winds are assumed to be quasi-isothermal, to approximate this behaviour while still operating under an adiabatic framework, we set $\gamma = 1.05$ in equation (6.3). This results in quasi-isothermal behaviour, in which the degrees of freedom of the system are slightly larger than would be available to a monotonic ionised gas. As there are no active heating or cooling sources in our simulation, this quasi-isothermal approximation mimics the ionisation of the stellar wind by radiation and coronal heating.

In the following sections, the equations that govern the stellar and planetary winds as well as the their interiors, magnetic fields and orbital parameters are presented.

6.2.2 Stellar and planetary models

Since both the stellar and planetary winds and magnetic fields are initialised using the exact same equations, they are presented here in their most basic form. When distinguishing between equations that are specific to or contributions specifically from one of the individual bodies, a subscript either $_*$ or $_\circ$ is used to indicate that it applies to the star or planet respectively. For example, when referring to the radial distance, there is the radius from the stellar centre $r_* = \sqrt{x_*^2 + y_*^2 + z_*^2}$ and the radius from the planet centre $r_\circ = \sqrt{(x_* - a)^2 + y_*^2 + z_*^2}$, where a is the orbital separation (in our models the star is centred on the origin such that $r_* = r$). Hence, when referring to the radius, r, it is assumed that the reader will understand that r_* is implied when in the context of the star and $r_\circ$ in the context of the planet. Therefore, when an equation is comprised solely of variables relating to the star or planet, the subscripts are dropped.

6.2.2.1 Wind model and initial conditions

The models for both the stellar and planetary winds are initialized according to the isothermal Parker wind model (Parker, 1958). The governing equation is

$$\psi - \ln(\psi) = -3 - 4\ln\left(\frac{\lambda}{2}\right) + 4\ln(\xi) + 2\frac{\lambda}{\xi}, \tag{6.7}$$

where the three dimensionless parameters ψ, λ and ξ are defined as

$$\psi \equiv \left(\frac{v_{\mathrm{W}}^{\mathrm{init}}(r)}{c_{\mathrm{s}}} \right)^2, \tag{6.8}$$

$$\lambda \equiv \frac{1}{2} \left(\frac{v_{esc}}{c_{\mathrm{s}}} \right)^2, \tag{6.9}$$

$$\xi \equiv \frac{r}{R}, \tag{6.10}$$

where $v_{\mathrm{W}}^{\mathrm{init}}(r)$ is the initial radial wind velocity, at the start of the simulation, $v_{esc} = \sqrt{2GM/R}$ is the escape velocity and the isothermal sound speed is given by $c_{\mathrm{s}} = \sqrt{k_{\mathrm{B}}T/\mu_{\mathrm{mol}}m_{\mathrm{p}}}$, with k_{B} the Boltzmann constant, T the temperature, $\mu_{\mathrm{mol}} = 0.5$ is the mean molecular weight, and m_{p} the proton mass. ξ gives the distance from centre of the body, in units of the bodies radii. R is the radius of either body. See Section 6.3.3, Fig. 6.9 for the analytic and simulation result for equation (6.7).

Equation (6.7) is transcendental and must be solved numerically. Using an appropriate root finding algorithm, such as the Newton–Raphson method, allows equation (6.7) to be solved for $v_{\mathrm{W}}^{\mathrm{init}}(r)$ for all values of r. The final step is to account for the rotation of the frame by assigning non-radial components to the wind velocity. This is done differently for the star than for the planet, as the star is located at the rotational axis of the frame. In the case of the star, the components are

$$v_{*x}^{\mathrm{init}} = \sin(\theta_*) \left[\, \cos(\phi_*) v_{*\mathrm{W}}^{\mathrm{init}}(r_*) + \sin(\phi_*) r_* \left(\Omega_{\mathrm{fr}} + \Omega_* \right) \right], \tag{6.11}$$

$$v_{*y}^{\mathrm{init}} = \sin(\theta_*) \left[\, \sin(\phi_*) v_{*\mathrm{W}}^{\mathrm{init}}(r_*) + \sin(\phi_*) r_* \left(\Omega_{\mathrm{fr}} + \Omega_* \right) \right], \tag{6.12}$$

$$v_{*z}^{\mathrm{init}} = \cos(\theta_*) v_{*\mathrm{W}}^{\mathrm{init}}(r_*). \tag{6.13}$$

For the planet they are

$$v_{\circ x}^{\mathrm{init}} = \sin(\theta_\circ) \left[\, \cos(\phi_\circ) v_{\circ\mathrm{W}}^{\mathrm{init}}(r_\circ) + \sin(\phi_*) r_* \Omega_{\mathrm{fr}} - a\Omega_{\mathrm{orb}} \sin(\mathcal{M}) - \sin(\phi_\circ) r_\circ \Omega_\circ \, \right], \tag{6.14}$$

$$v_{\circ y}^{\rm init} = \sin(\theta_\circ)\,[\,\sin(\phi_\circ) v_{\circ \rm W}^{\rm init}(r_\circ) - \cos(\phi_*) r_* \Omega_{\rm fr} + a\Omega_{\rm orb}\cos(\mathcal{M}) + \cos(\phi_\circ) r_\circ \Omega_\circ\,]\,, \tag{6.15}$$

$$v_{\circ z}^{\rm init} = \cos(\theta_\circ) v_{\circ \rm W}^{\rm init}(r_\circ). \tag{6.16}$$

Where $r_{*,\circ}$, $\theta_{*,\circ}$ and $\phi_{*,\circ}$ are calculated from $x_{*,\circ}$, $y_{*,\circ}$ and $z_{*,\circ}$ by coordinate transformation. $\mathcal{M}$ is the mean anomaly, which accounts for the motion of the planet around the star. As the calculations are conducted in the frame of the orbiting planet, $\mathcal{M} = 0$ at all times. The parameters $\Omega_{\rm orb}$, Ω_* and $\Omega_\circ$ are the orbital, stellar and planetary rotational frequencies respectively. Our models assume that the planet is tidally bound to the star and that the star simply rotates at the same rate as the planetary orbit. This, together with the fact that the simulations are conducted in the rotating frame of the orbit, means that $\Omega_* = \Omega_\circ = \Omega_{\rm orb}$, with $\Omega_{\rm orb} = \sqrt{GM/R_{\rm orb}}$.

This frame-work greatly simplifies the simulations, as the planets position is kept constant with time. However, as pointed out by Matsakos et al. (2015), equations (6.11–6.16) are general and can accommodate the frame, star and planet having different rotational frequencies. To achieve this, Kepler's equation should be solved to advance the position of the planet as a function of time (this would also allow for eccentric orbits). In addition, the model assumes that the centre of mass of the system is located at the centre of the star. If this assumption is relaxed, then the position of the star would also have to be updated in a similar manner.

At all points in the wind, material is subject to acceleration due to gravity, this is applied as an acceleration vector according to

$$\boldsymbol{g}(x, y, z) = -\frac{GM}{r^3}\boldsymbol{r}, \tag{6.17}$$

from both the star and the planet. The total gravitational acceleration is then the sum of the contributions from both bodies $\boldsymbol{g}_{\rm tot}(\boldsymbol{r}) = \boldsymbol{g}_*(\boldsymbol{r}_*) + \boldsymbol{g}_\circ(\boldsymbol{r}_\circ)$. The initial pressure in the wind is found by solving

$$P^{\rm init}(x,y,z) = P\exp\left[\lambda\left(\frac{1}{\xi}-1\right)-\frac{\psi}{2}\right]. \tag{6.18}$$

P is the pressure at the stellar or planetary surface, found by solving

$$P = \frac{k_{\rm B}T\rho}{\mu_{\rm mol}m_{\rm p}}, \tag{6.19}$$

from the isothermal equation of state. Where ρ and T are the density and temperature at the stellar or planetary surface, given in Table 6.1. The initial wind density profile is then

$$\rho^{\rm init}(x,y,z) = \frac{\rho}{P}P^{\rm init}(x,y,z). \tag{6.20}$$

6.2.2.2 Magnetic fields

The magnetic field of both the star and planet are initialized as dipoles according to the following equation:

$$\boldsymbol{B}^{init}(x,y,z) = \frac{B_{\rm eq}R^3}{r^5}\left[3xz\hat{x}+3yz\hat{y}+\left(3z^2+r^2\right)\hat{z}\right] \tag{6.21}$$

where $B_{\rm eq}$ is the equatorial magnetic field of the body. The magnetic field external to the stellar and planetary surfaces is initialized as the sum of the stellar and planetary fields, $\boldsymbol{B}_{\rm tot} = \boldsymbol{B}_* + \boldsymbol{B}_\circ$. This ensures that the initial field has no discontinuities. This field is initially independent of the fluid dynamics. As the simulation evolves, the magnetic field reacts to and relaxes into the wind. This process leads to a magnetosphere that is largely dipolar in the inner regions. Larger radii field lines are dragged with the flow forming an open magnetosphere. These open magnetic field lines correspond to a line of latitude on the surface of the bodies whose hight above the equator is a function of the strength of the magnetic field. A stronger field corresponds to a higher latitude (see Section 6.2.3.2).

6.2.2.3 Stellar and planetary interiors

The stellar and planetary surfaces are treated as internal boundaries to the simulation. Within the stellar or planetary surfaces, all quantities are held constant with time such that they are uniformly dense spheres. This simplifies the treatment of gravity within the bodies, allowing us to write the internal gravity as

$$\boldsymbol{g}^{\text{intern}}(x, y, z) = \frac{4}{3}\pi G\rho\boldsymbol{r}. \tag{6.22}$$

From this, the hydrostatic condition leads to the following expression for the internal pressure;

$$P^{\text{intern}}(x, y, z) = P + \frac{2}{3}\pi G\rho^2\left(R^2 - r^2\right), \tag{6.23}$$

where the density, ρ, is given in Table 6.1.

Equations (6.22) and (6.23) are not, strictly speaking consistent with the mass of the star or planet, as $M \neq \frac{4}{3}\pi G\rho R^3$, with ρ the surface density, and lead to a discontinuity in the gravitational field at the stellar and planetary surfaces. However, as this region is not in the computational active region, it will have zero influence on the solution.

The internal magnetic field is specified as a series of three concentric shells. The inner region, where $0\ R < r < 0.5\ R$, has a constant magnetic field of $16B_{\text{eq}}\hat{z}$. This is done so that the field magnitude in this region meets the magnitude of the dipole field in the second layer, $0.5\ R < r < 1\ R$, in a smooth manner. Beyond this radius, the field is still dipolar but time dependent and allowed to be modified by the outflowing wind. This configuration avoids the singularity at $r = 0$ in equation (6.21). In the region $1\ R < r < 1.5\ R$, the density, pressure and velocity are set and held constant in time according to equations (6.11–6.16) and equations (6.18) and (6.20) in Section 6.2.2.1, to reflect the initial wind region. The magnetic field is free to evolve in this region and relax into the flow. All three regions, which both the star and planet are divided into, are illustrated in Fig. 6.1.

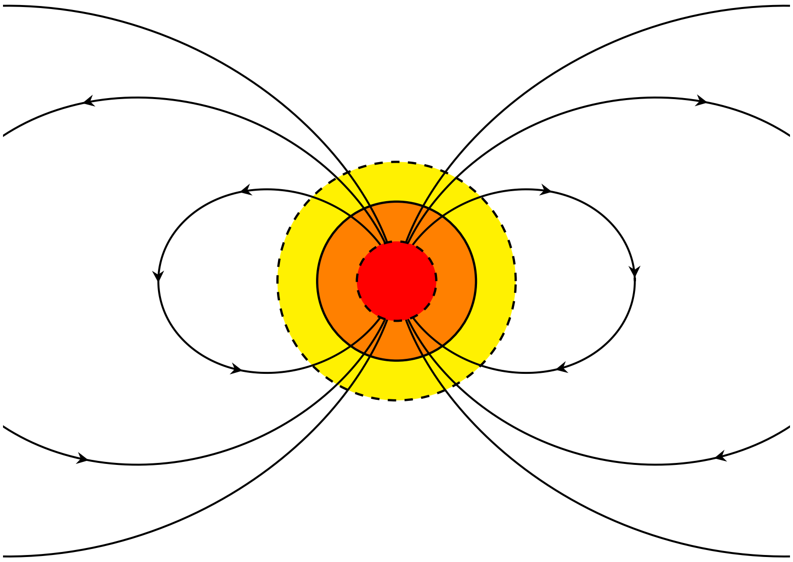

Figure 6.1: Diagram illustrating the three layers used to initialize and hold constant the star or planet. Red indicates the central region of the body, within which all fluid quantities are held constant with time at their initial values with the magnetic field $16B_{\rm eq}\hat{z}$. The orange shell is identical to the red region except that the magnetic field has a dipole configuration. Yellow indicates the outer atmosphere of the body in which all quantities except the magnetic field are held constant with time. The solid black circle indicates the surface of the body.

6.2.2.4 Stellar and planetary surface parameters

Throughout this study, stellar parameters such as radius, mass and coronal temperature are set to solar values and are summarized in Table 6.1. Parameters for the planet are the same as those used by Matsakos et al. (2015), who parametrised the values for base density and pressure using high resolution 2D simulations of stellar outflows originally conducted by Matt & Pudritz (2008). The base values are adapted such that mass-loss rates ($\dot{M}$) and wind values in the 3D simulations match those of the 2D models.

In this study, to verify the above approach, $\dot{M}$ from both the star and planet was measured directly from the simulation results. This was done by specifying a surface of constant radius around the star and planet of $2R_*$ and $2R_\circ$, respectively, and calculating the flux of material across this surface. The mass-loss rates are shown in Fig. 6.2. The values at the start of the simulation are due to the winds being initialized as non–magnetized outflows. As the winds respond to the presence of the stellar and planetary magnetospheres, $\dot{M}$ readjust as the radial velocity decreases according to mass conservation: $\dot{M} = 4\pi\rho r^2 v(r)$. In the stellar case, $\dot{M}$ reaches a stable value at 2.14×10^{12} g/s. This value is consistent with the solar $\dot{M}$. The planetary mass-loss reaches equilibrium at $\sim 8 \times 10^9$ g/s, which is constant with simulations by Salz et al. (2016) for HJs such as WASP-12 b (Hebb et al., 2009) and GJ 3470 b (Bonfils et al., 2012). Both of these exoplanets have semi-major axes that are smaller to the value used in this work but have comparable surface temperatures.

The topic of asymmetric mass-loss between a planets day- and night-side is an active area of research. Tripathi et al. (2015) study this difference and determine a steady state mass-loss of $\sim 2 \times 10^{10}$ g/s for an HJ with similar parameters to those used in this study. This mass-loss is comparable, within an order of magnitude, to that obtained in the simulation presented here, which assumes spherical mass-loss according to a Parker wind solution. Tripathi et al. (2015) employ a sophisticated treatment of the ionization balance and the dynamics of neutral plasma species and do not include magnetic fields and focus solely on the region within the direct vicinity of the HJ. For these reasons and because we wish to investigate the global evolution of the evaporated material throughout the star-planet system, we chose to adopt the more simplistic approach described at the start of Section 6.2.

As both the star and the planet serve as sources of magnetised flow in the simulation, a correct $\dot{M}$ ensures that the correct amount of material is replenished in the computational domain, in order to keep the simulation in quasi–steady-state, once the initial conditions have advected to the outer boundaries. This does not, however, guarantee that flow dynamics in the vicinity of the star or planet are correctly reproduced in 3D simulations. Magnetic field geometry plays a large, if not dominant, role and will be discussed in Section 6.3.3.

The choice of equatorial magnetic field strength, B_{eq}, for the star was based on approximate values for the solar magnetic field, $2G$ (see Table 6.1). In the case of the HJ, we assume that the field is driven by dynamo action due to the rotation of the planet (Stevenson, 2003; Strugarek et al., 2014). Since the HJ is tidally locked (Grießmeier et al.,

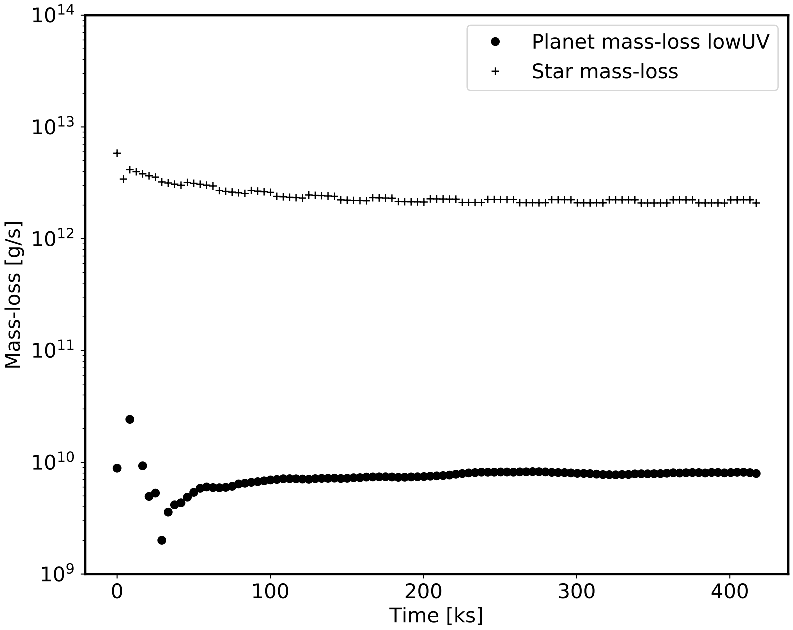

Figure 6.2: Mass-loss rates for the bodies in the simulation. The star has a steady–state mass-loss of 2.14×10^{12}g/s, and the planet has a steady–state mass-loss of 7.9×10^{9}g/s. The simulation was run for a total time of 417.2ks to reach steady state.

2004), its rotation is much slower than that of Jupiter, which has an $B_{\rm eq} \approx 15$ G. As such, a $B_{\rm eq} = 1$ G was chosen. This value is consistent with those found in the literature (Pillitteri et al., 2015; Strugarek et al., 2015a; Nichols & Milan, 2016).

For simplicity, the magnetic field topology of both the star and planet was set to dipolar, with the dipole moment aligned with the rotation axis, which, in turn, is perpendicular to the plain of the ecliptic. This configuration produces a planetary magnetosphere that corresponds to the anti-aligned case of Strugarek et al. (2015a), anti-aligned with respect to the *local* magnetic field of the stellar wind at the planets position.

6.2.3 Electron cyclotron maser instability

6.2.3.1 Governing equations

The history and applications of this theory of emission of electromagnetic radiation via the ECMI process is summarized in a recent review by Treumann (2006). The frequency

Table 6.1: Stellar and planetary parameters used in the simulations.

Parameter	Symbol	Star	Planet
Mass	$M_{*,\circ}$	1 $\mathrm{M}_\odot$	0.5 $\mathrm{M_J}$
Radius	$R_{*,\circ}$	1 $\mathrm{R}_\odot$	1.5 $\mathrm{R_J}$
Temperature	$T_{*,\circ}$	1×10^6 K	6×10^3 K
Equatorial magnetic field strength	$B_{eq*,\circ}$	2 G	1 G
Surface density	$\rho_{*,\circ}$	5×10^{-15} g/cm^3	7×10^{-17} g/cm^3
Orbital radius	a	–	0.047 au
Orbital period	p_{orb}	–	3.7 days
Rotational period	$p_{\mathrm{rot}*,\circ}$	3.7 days	3.7 days

at which emission due to the ECMI process propagates at is given by the frequency of gyration of electrons about magnetic field lines, known as the cyclotron frequency:

$$\nu_{\mathrm{ce}}(\mathrm{MHz}) = \left(\frac{eB}{2\pi m_{\mathrm{e}}c}\right) = 2.80B \tag{6.24}$$

(Stevens, 2005). As described by Treumann (2006), the ECMI is a plasma instability that, given a background non-thermal electron population, pumps directly the free-space electromagnetic modes. These modes are the result of a dispersion relation for the propagating electromagnetic radiation and lead to several conditions on efficient generation. The relevant modes for this study is the RX-mode and LO-mode, whose lower cut-off references are

$$\nu_{\mathrm{X}} = \frac{1}{2}\left[\nu_{\mathrm{ce}} + \left(\nu_{\mathrm{ce}}^2 + 4\nu_{\mathrm{pe}}^2\right)^{1/2}\right] \tag{6.25}$$

and

$$\nu_{\mathrm{pe}}(\mathrm{MHz}) = \left(\frac{n_{\mathrm{e}}e^2}{\pi m_{\mathrm{e}}}\right)^{1/2} = 8.98 \times 10^{-3} n_{\mathrm{e}}^{1/2}. \tag{6.26}$$

respectively. Finally, electrons contributing to the ECMI process must also follow a loss-cone distribution function, which is the case for magnetospheric cusp configurations such as the one discussed here.

If the two frequencies, equations (6.25) and (6.26) are exceeded and

$$\frac{\nu_{\mathrm{ce}}}{\nu_{\mathrm{pe}}} > 1, \tag{6.27}$$

then there is non-negligible emission due to the ECMI process. In practice, equation (6.27) needs to be $\gtrsim 2.5$ for the emission to be efficient (Weber et al., 2017). Equation (6.27) will form the diagnostic for measuring cyclotron emission from our simulation results.

In this study, radio ECMI emission is assumed to follow a straight line from the source of emission to the observer. A rigorous treatment of emission propagation requires the consideration of the changing refractive index of the stellar wind due to density fluctuations and the $1/r^2$ dependence of equation (6.20) along the line of emission, modifying its path, as it travels through the stellar wind. However, this influence on the emission trajectory is assumed to be small and the emission takes a straight line from its origin to the observer.

Equation (6.24) is a linear function of the local magnetic field strength, B. Therefore, if the planetary $B_{\rm eq}$ were to increase, so too would $\nu_{\rm ce}$. For a fixed mass-loss rate, increasing $B_{\rm eq}$ would result in a change of the density field at the point in space where $\nu_{\rm ce}$ is calculated, through the channelling of planetary and stellar wind material. If we consider the case where increasing $B_{\rm eq}$ leads to linear increase in $n_{\rm i}$ then we account for a worst case scenario for the generation of ECMI emission. As equation (6.26) is a weak function of $n_{\rm i}$, $\nu_{\rm pe}$ would also see an increase but to a lesser degree than $\nu_{\rm ce}$. Therefore, $\nu_{\rm ce}$ and $\nu_{\rm pe}$ both scale with $B_{\rm eq}$. For example, if $B_{\rm eq} \rightarrow 2B_{\rm eq}$, then $\nu_{\rm ce} \rightarrow 2\nu_{\rm ce}$ while $\nu_{\rm pe} \rightarrow \sqrt{2}\nu_{\rm pe}$, but only if doubling $B_{\rm eq}$ resulted in twice the number of confined ions. This simplified theoretical scaling of $\nu_{\rm ce}$ and $\nu_{\rm pe}$ with $B_{\rm eq}$ is shown in Fig. 6.3. Making the assumption that doubling $B_{\rm eq}$ leads to twice the number of confined ions, therefore doubling $n_{\rm i}$, we can see that as $B_{\rm eq}$ increases, both $\nu_{\rm ce}$ and $\nu_{\rm pe}$ (via $\nu_{\rm pe} \propto \sqrt{n_{\rm i}}$) do also increase and there is a value of $B_{\rm eq}$ where equation (6.27) exceeds unity and ECMI emission is produced.

6.2.3.2 Emission generation

ECMI emission is highly directional. Fig. 6.4 shows a diagram of the magnetosphere of an exoplanet embedded in a stellar wind. The image illustrates active regions where magnetic field lines form either a closed or open magnetosphere. The red highlighting shows the

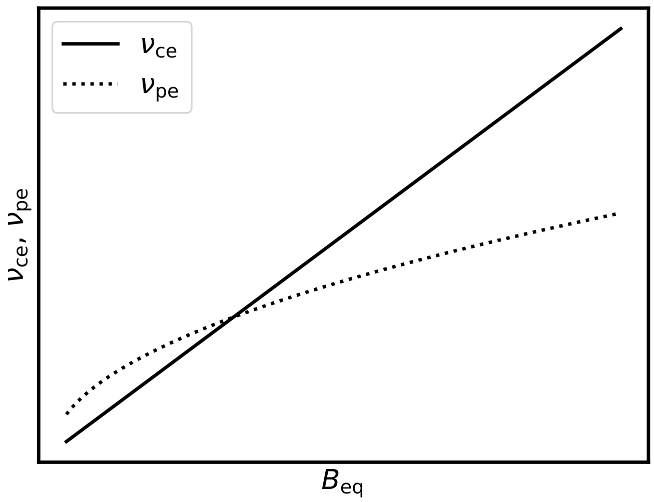

Figure 6.3: Schematic diagram of the scaling for both ν_{ce} and ν_{pe} with B_{eq} at an arbitrary point in space. Assuming that n_i increases linearly with B_{eq} then the relation $\nu_{pe} \propto \sqrt{n_i}$ means that, at a given magnetic field strength, ν_{ce} will exceed ν_{pe} and ECMI will be efficient at producing radio emission.

longest closed field lines that form exoplanetary analogies with the Van Allan radiation belts in the Earth's magnetosphere. Magnetic field lines between these two closed regions form the open part of the magnetosphere, allowing electrons from the stellar wind to enter. Again, in analogy with Earth, these regions are known as the polar cusps. Electrons enter the cusps process in a helical path whose frequency of gyration is directly proportional to the magnetic field strength (see equation 6.24). Any emission produced by this motion is directed into a hollow conical opening pointing in the direction of electron motion. This results in highly directional emission (Dulk, 1985). Vidotto et al. (2011) calculated the ν_{ce} using the opening angle, α, corresponding to the latitude of the closed magnetic field lines marked in red in Fig. 6.4, giving an estimate of the shape of the emitting region. The field strength at this latitude gives ν_{ce} and α can be approximated by

$$\alpha = \arcsin\left[(R_\circ/R_\mathrm{M})^{1/2}\right]. \tag{6.28}$$

R_M is the radius corresponding to the largest closed field line and is inferred from simulation results in Section 6.3.5. This together with equation (6.24) gives ν_{ce}.

Tilley et al. (2016) calculate the directional dependence of the ECMI flux emitted from the poles of a simulated HJ, as projected onto a celestial sphere centred on the exoplanet. Directional dependence was found to be highly influenced by the stellar wind ram pressure and planet magnetosphere topology. However, they do not calculate absolute flux levels, only showing normalized fluxes. We do not calculate the direction of the emission here as this study is principally concerned with the plasma environment in the stellar and planetary wind and whether and where the ECMI emission is produced in the first place.

While ν_{ce} is dependent on the magnetic field strength and geometry, the intensity of emission is a function of the power available to the electrons trapped in the magnetosphere. This power is estimated by Zarka (1998), and later used by Stevens (2005) as

$$P_{\mathrm{r}} = \delta \frac{\dot{M}_* u_{\mathrm{W}}^2 R_{\mathrm{eff}}^2}{4a^2}. \tag{6.29}$$

Here, δ is an efficiency parameter ($\sim 7 \times 10^{-6}$), $\dot{M}_*$ is the stellar mass-loss rate, u_{W} is the stellar wind at the orbital radius, a, and R_{eff} is the effective radius of the magnetosphere as seen by the stellar wind and the only factor in equation (6.29), which is a property of the exoplanet. The star plays the central role in supplying power in the form of incident kinetic and magnetic energy. For a typical HJ, $P_{\mathrm{r}} \sim 10^{15}$ W (Stevens, 2005; Zarka, 2007)

Equation (6.29) assumes that the result of equation (6.27) is greater than the threshold for efficient production of radio emission. In Section 6.3, it will be shown that this simple model is insufficient to accurately describe the ECMI process in HJs.

6.2.4 Numerical modelling

The computational mesh is initialized everywhere according to the equations presented in Section 6.2.2 for the stellar wind. A region of $10R_{\circ}$ around the planet is initialized for the planetary wind in the same manner. The MHD equations (equations 6.1–6.4) were solved numerically using the publicly available MHD code PLUTO (version 4.2; Mignone et al. (2007, 2012)). This was done using a second order scheme with linear spatial recon-

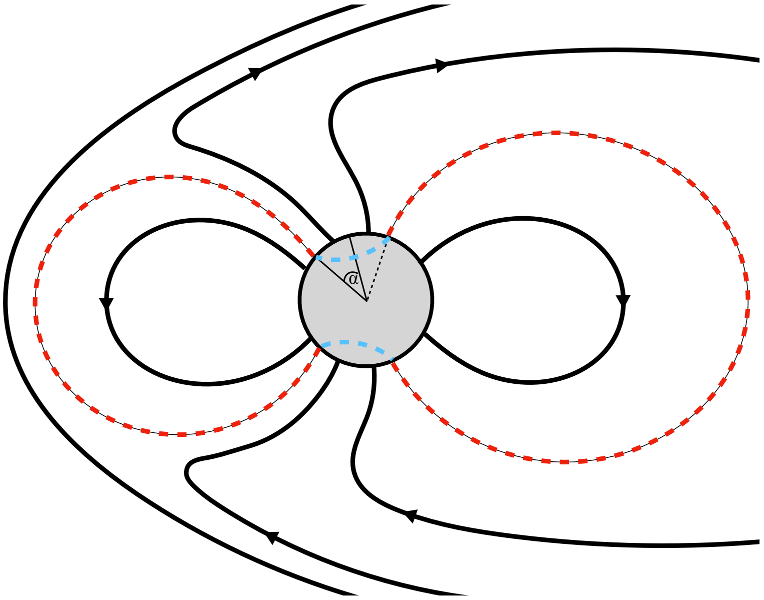

Figure 6.4: Schematic diagram of the magnetic field geometry for an HJ embedded in a stellar wind. To the left, the solid black line with no arrows indicates the bow shock. The longest closed field lines are highlighted in red. Field lines at higher latitudes are effectively open to the stellar wind. The angle α indicates the lowest latitude above which the field lines are open. The dashed blue lines are the regions from which the ECMI emission is expected.

struction (Van Lear limiter) and second order Runga–Kutta for the time stepping. This was paired with the Harten Lax & van Leer discontinuous (HLLD) Riemann solver. The magnetic field zero divergence condition was enforced using the generalized Lagrangian multiplier (GLM) formalism of Dedner et al. (2002), see also Mignone et al. (2010) and Mignone & Tzeferacos (2010) for its implementation in PLUTO.

The outer boundary conditions to the computational domain are set to zero gradient (outflow). As the velocity everywhere just inside the boundary is directed outwards, these boundary conditions insure that the finite computational domain does not influence the solution.

The vicinity of the planet is characterized by a high magnetic field strength and a high density but low velocity outflow. This results in a plasma-$\beta \ll 1$. Therefore, the magnetic field dominates the evolution of the flow in this region. These conditions can prove challenging to the numerical scheme and lead to the development of unphysical structure within the planetary magnetosphere. This issue is alleviated by using the technique of background field splitting in which equations (6.1)–(6.4) are rewritten with the magnetic field $\boldsymbol{B}_{\rm tot} \rightarrow \boldsymbol{B}_0 + \boldsymbol{B}_1$, where the total magnetic field, $\boldsymbol{B}_{\rm tot}$, is split into an initial field, $\boldsymbol{B}_0$, which is static with respect to time, and a perturbation to this initial field, $\boldsymbol{B}_1$, which is evolved with the simulation. This allows for the planetary outflow to smoothly interact with the magnetosphere as it expands from the planet surface, reducing grid aligned flow artefacts. Using this technique results in a stable time–step, remaining constant throughout the simulation.

To ensure that the simulation reaches quasi-steady state, the simulation is evolved through × 10 the time for a fluid particle to be advected from the surface of the star to the outer boundary. This flow time is approximately 10 h; therefore, the simulation is evolved through 100 h or 360 ks.

The following sections detail the specifics of the numerical mesh used in the simulation and the dynamically adaptive refined mesh used. In the following, x, y and z are relative to the origin of the coordinate system.

6.2.4.1 Simulation mesh

The physical extent of the mesh employed in our simulation was $-32\ R_* < x, y < 32\ R_*$ and $-16\ R_* < z < 16\ R_*$. This region was discretized into a mesh with an initial resolution of 128^2 cells in the xy plane and 64 cells in the z direction. This gives a resolution of two cells per stellar radius. This initial mesh was successively refined with a maximum five AMR levels to an effective resolution of $4096^2 \times 2048$ or 64 cells per stellar radius.

The mesh refinement is carried out by checking the gradient of the density in each cell at every second time–step. If the density gradient fulfils a threshold criterion, then the cell is marked for refinement, see Mignone et al. (2012) for details. This allows the mesh to track the evolution of the planetary material as it interacts with the stellar wind. An example of the refined mesh is shown in Fig. 6.5. Each nested patch indicates an additional AMR level that is twice as refined as its parent patch.

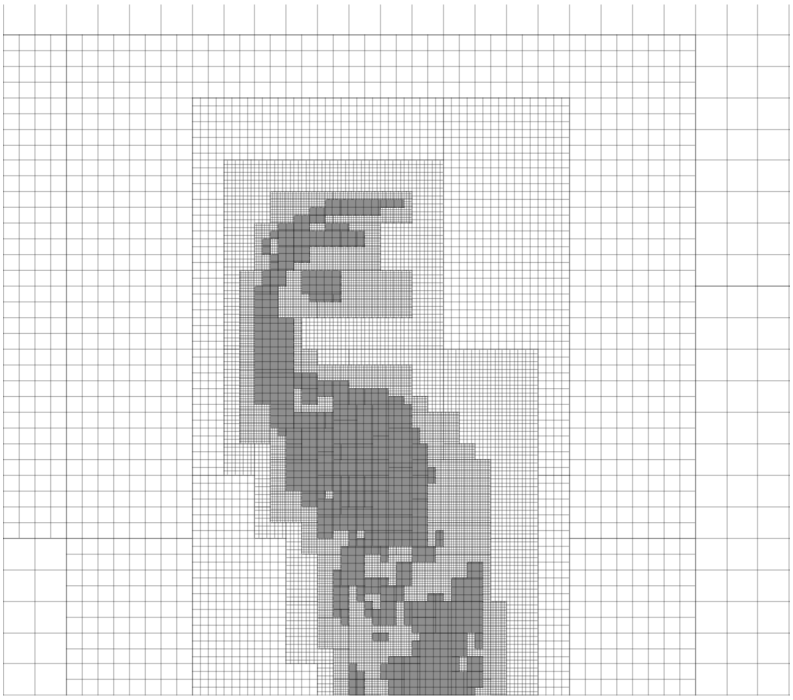

Figure 6.5: Example of the mesh refinement employed in the simulation. The patch regions denote different refinement levels. Each additional refinement level represents a two times increase in the resolution from the previous. The most coarse level can be seen on the left and right of the image and is the base resolution and the highest refined region, centred on the planet and bow shock.

6.2.4.2 Assumptions and limitations

The base of the stellar and planetary winds is held constant out to 1.5 R_* and 1.5 $R_\circ$ respectively. This is done to allow the stellar and planetary outflows to initialize properly and not stall in the presence of the magnetic field of either body. This introduces the limitation that any material, either form the star or planet, can only come within 1.5 $R_*(R_\circ)$ of the star(planet) surface. This limits the ability to use the simulation results presented here for studying accretion of material onto either body. It is left to future studies to relax this condition and to study accretion in greater detail.

A central consideration in numerical MHD simulation is insuring the $\nabla \cdot \boldsymbol{B} = 0$ condition. The configuration in Section 6.2.2.3 for the internal magnetic field presents a challenge. As the solution is over written at each time–step, mono-poles are introduced at the interface between the constant field (internal) and the evolving field (external). The extent to which this influences the evolution of the simulation can to some extent be measured using the approach of Hopkins (2016), where a measure of the divergence is given by $\Delta x|\nabla \cdot \boldsymbol{B}|/|\boldsymbol{B}|$, with Δx the cell width. To assess the impact of the static planetary core (and by extension the static stellar core), this quantity is plotted in Fig. 6.6 for a slice plot of the steady state solution, aligned with the z-direction, intersecting the centre of the planet. $\Delta x|\nabla \cdot \boldsymbol{B}|/|\boldsymbol{B}| < 10^{-2}$ in all regions exterior to the planet. Higher values are contained to the interior, static core of the body, allowing us to draw the conclusion that the divergence cleaning method, together with the static planetary interior, does not introduce systematic errors into the solution.

An alternative method is to assign a large enough density value to the planet such that the magnetic field diffusion time–scale is much greater than the simulation time–scale. Since the planetary wind is defined by the inflow density, fixed on the surface, we are not free to used this method.

One further major assumption is that the entire star and planetary wind material is fully ionized and, therefore, optically thin to the UV radiation from the star, incident on the planet and providing the source of the atmosphere's photoevaporation. This assumption could only be relaxed if the planetary outflow was not fixed at its base and the photoevaporation was calculated based on radiation transfer. Such a calculation is beyond the scope of this study.

Simulation results including initial conditions, global and circumplanetary evolution and ECMI efficiency calculations are presented in the following sections.

6.3 Results and discussion

The results are laid out in the following manner: global simulation initial conditions, evolution and steady–state solution, description of the magnetised stellar wind, description of the circumplantary environment, quantification of the ECMI radio power and frequency of emission and, finally, calculation of $\nu_{\mathrm{ce}}/\nu_{\mathrm{pe}}$ with the determination of the efficiency for the generation of radio emission via the ECMI process.

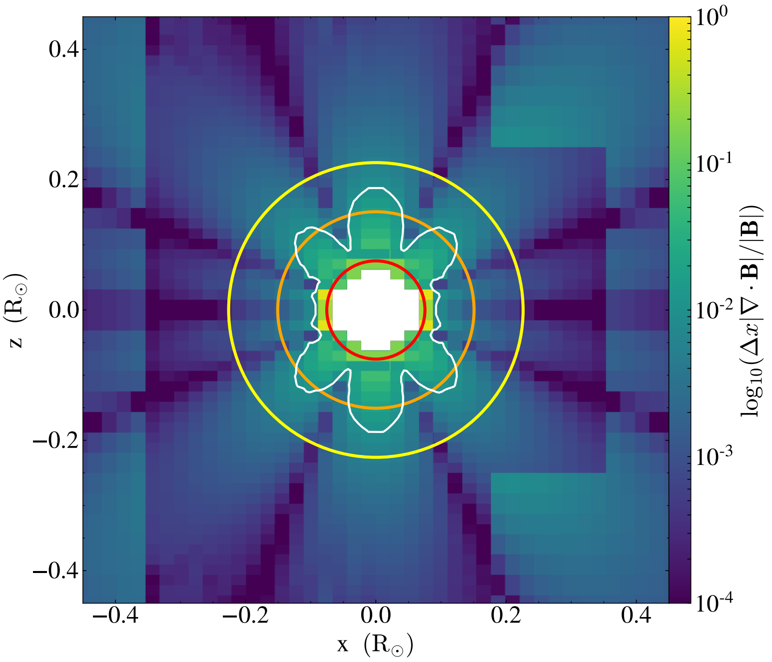

Figure 6.6: Plot of the magnetic field divergence measure $\log_{10}(\Delta x|\nabla\cdot\boldsymbol{B}|/|\boldsymbol{B}|)$. The three circles and their colouring indicate the layers of the planet as described in Section 6.2.2.3. A single white contour indicates the surface within which $\log_{10}(\Delta x|\nabla\cdot\boldsymbol{B}|/|\boldsymbol{B}|) > 10^{-2}$. At all points, this region is contained within the region where the solution is held constant with time, as such the deviation from $\nabla\cdot\boldsymbol{B} = 0$ has no influence here. Outside the planet $\log_{10}(\Delta x|\nabla\cdot\boldsymbol{B}|/|\boldsymbol{B}|) < 10^{-2}$, a value considered to have minimal effect of the solution.

6.3.1 Initial conditions

The entire simulation domain, star at the centre and planet situated to the right, is shown in Fig. 6.7. Across the entire simulation domain, the wind initial conditions are set according to the stellar properties only, except for a cavity of radius 10 $R_\circ$ around the planet, which is initialized solely with the planetary wind parameters. This allows the planetary wind to initialize properly and not stall due to the ram pressure of the stellar wind. These initial conditions are designed such that the planetary wind is at approximately terminal velocity and will expand radially in a smooth manner in the first time–step, allowing quasi–steady state to be reached in the shortest time possible. As mentioned in Section 6.2.4, the magnetic field is evolved using the method of background field splitting. As the static background field is required to be force–free, it is initialized as the sum of the stellar and planetary fields, under the assumption that the sum of two force-free fields is itself force-free.

6.3.2 Global evolution

Fig. 6.8 shows the final quasi-steady state solution. The top image shows a side–on view, looking down the y-axis with overlaid magnetic field lines. The bottom image shows a top down view, looking down the z-axis, of the system with overlaid velocity flow lines. Care must be taken when interpreting the magnetic field lines in the top image, as the field lines shown are constructed using the magnetic vectors in the plane of the slice used to produce the image only. As such, the warping of the field lines by the stellar wind is not fully captured and can lead to artificial structures in the magnetic topology. Therefore, the field lines in Fig. 6.8 should be interpreted as illustrative rather than literal.

At the orbital radius, the stellar wind has drawn open the stellar magnetic field lines to present an open magnetosphere to the planet. The planetary material itself is swept back to form a cometary tail.This material gradually dissipates and is eventually advected into the lower y-boundary of the simulation. The majority of the simulation domain remains dominated by the stellar wind.

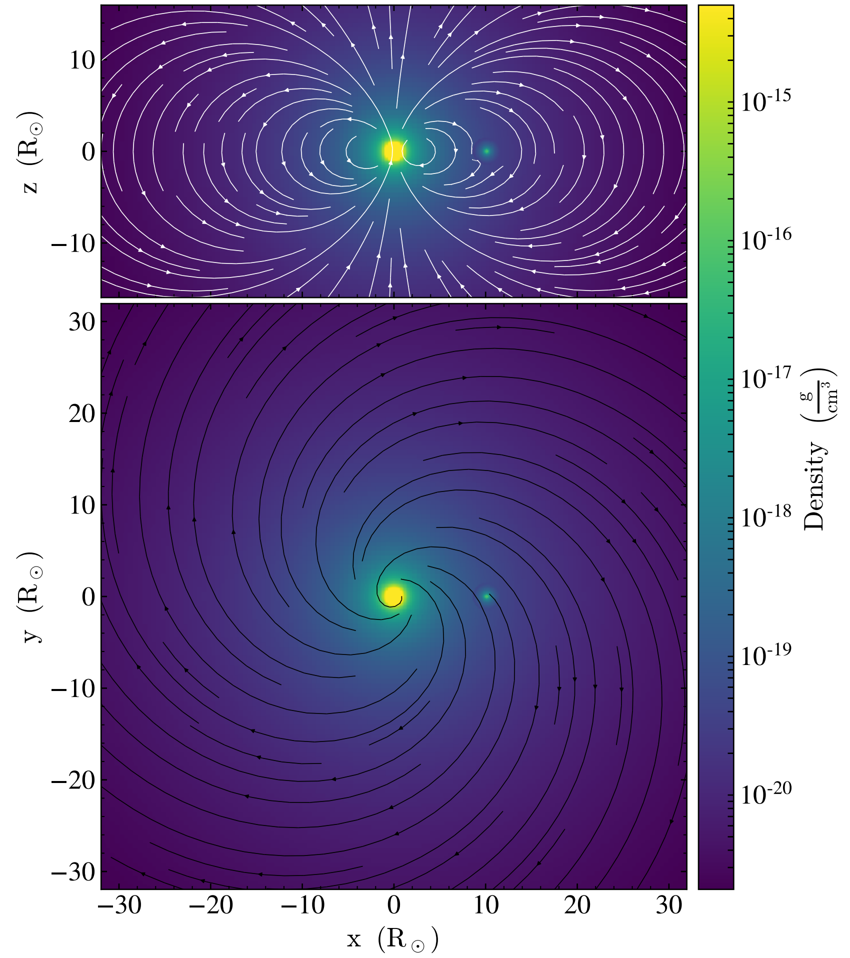

Figure 6.7: Initial conditions for the stellar and planetary bodies and the extended wind. Top panel: view along the y-axis showing the star, planet and total magnetic field that is dominated by the stellar magnetosphere. Bottom panel: similar to the top image but looking down the z-axis onto the orbital plane, and the velocity flow lines of the initial Parker wind model are shown as black lines.

Cometary tail structures are also found in the work of Bourrier & Lecavelier des Etangs (2013), Bourrier et al. (2016) and Schneiter et al. (2016). The former uses a particle model together with a theoretical Lyman-α absorption line to track the motion of the UV photoevaporated planetary material. They find that for HD209458b the synthetic and observational absorption profiles agree, leading to a theoretical mass-loss rate between 10^9 and 10^{11} g/s, with the host star producing 3–4 times the solar value for ionising flux. This mass-loss rate range corresponds well to the mass-loss determined for the model planet presented here.

The large temperature difference between the stellar wind and the planetary material between 10^6K and 6×10^3K suggests that additional physics not incorporated into the simulations presented here could play a substantial role in the evolution of the cometary tail, for example inclusion of thermal conduction or sub-grid turbulence may lead to a higher degree of dissipation. Behaviour of the tail does not play an important role in the ECMI emission, especially in comparison to the planetary polar regions, where the magnetic field is strongest. As such, these additional physics are left to future investigations.

6.3.3 Circumstellar evolution

The magnetic field lines from the stellar surface fall into two categories: either field lines that form closed loops back to the opposite hemisphere or field lines that are open and would in reality connect with the interplanetary/interstellar magnetic field, with a cutoff between these open and closed field lines at a specific line of latitude on the stellar surface.

To test the validity of the numerical stellar wind results, analytic solutions to Parker's equation (equation 6.7) along side numerical results of the velocity and density profiles from the simulation are shown in Fig. 6.9. Both of the simulated profiles are reduced with respect to the analytic results. This can be seen in the evolution of the stellar mass-loss, discussed in Section 6.2.2.4, showing initially $\dot{M}_* = \dot{M}_\odot$, which then decreases and approaches $2 \times 10^{12}\mathrm{g/cm}^3$, a decrease of approximately 30%. Closed field lines in the equatorial region of the stellar wind constrain the expanding wind, reducing the velocity

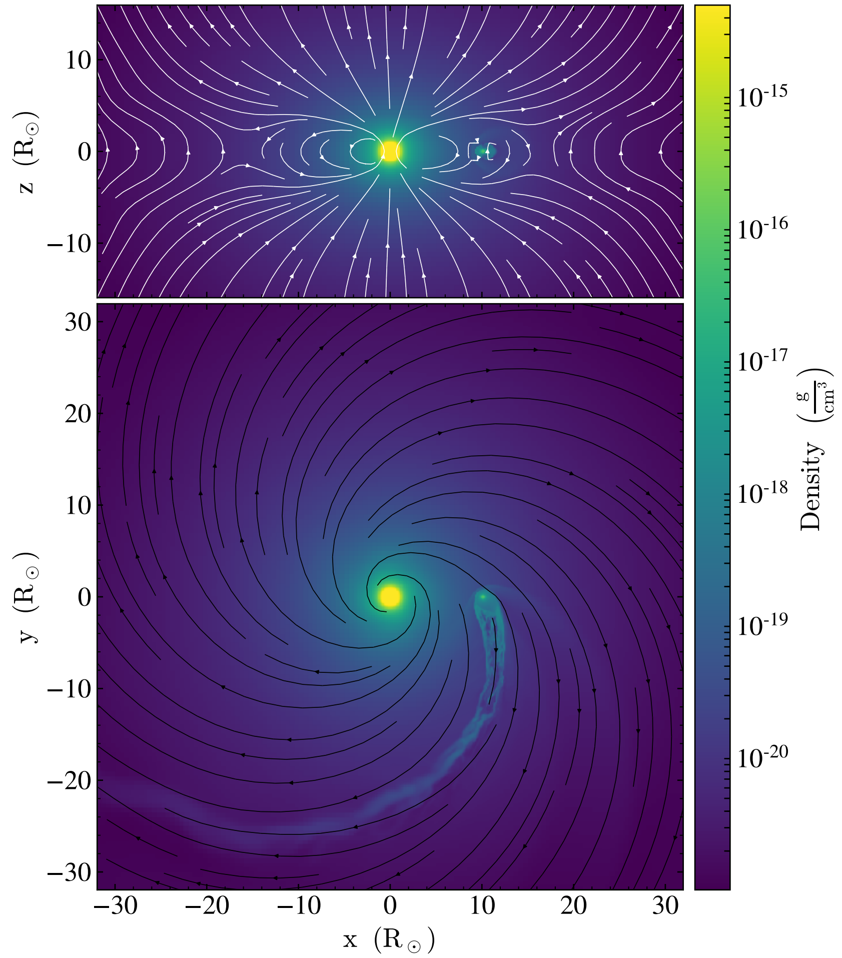

Figure 6.8: Global quasi–steady–state solution, large–scale structure of the flow will not change, only short, small–scale changes will continue. Top panel: side–on view, looking down the y-axis with overlaid magnetic field lines. Bottom panel: top down image, looking down the z-axis, of the system with overlaid velocity flow lines.

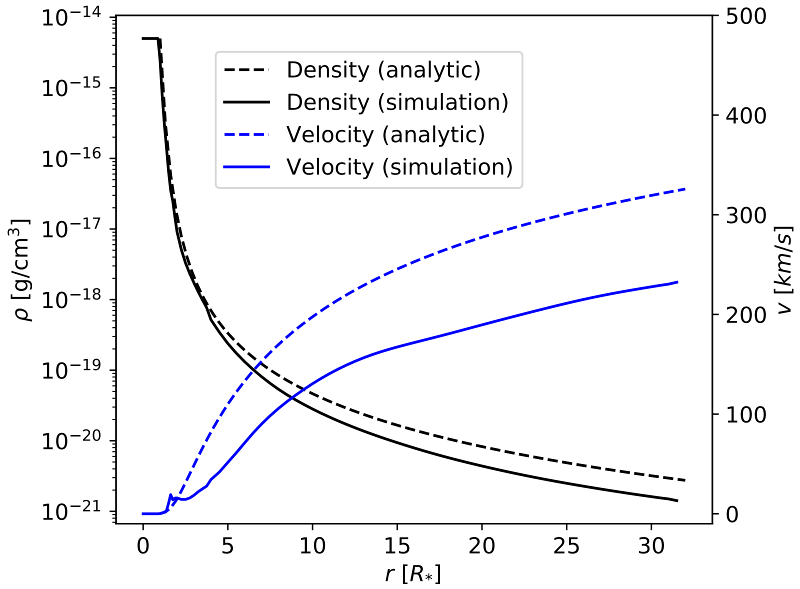

Figure 6.9: Density and velocity of the simulated stellar wind. Shown are the profiles in the orbital plane, characterizing the conditions encountered by HJ as it precesses on its orbit. Outside of this region, the stellar wind will be different due to the dipolar nature of the magnetic field. Dashed lines indicate the analytic solution, as calculated from Parker's equation (equation 6.7), and solid lines are taken from the steady–state simulation results. Both quantities exhibit a decrease with respect to their analytic counterparts, which becomes more pronounced with radial distance form the stellar surface.

and thus the amount of material that can escape the stellar surface. This material then accumulates in the magnetosphere. Matsakos et al. (2015) characterized this accumulation region as the *stellar dead zone* within which the wind can not overcome the combination of stellar gravity and magnetic tension. This region can be seen for $v(r < 4R_*)$ in Fig. 6.9. This deviation from the Parker solution is accounted for by the fact that $\gamma = 1.05$ which will reduce the density and velocity profiles, also the resolution of the star may contribute via numerical dissipation. However, these results agree with the expected behaviour for a magnetized stellar wind (Matt & Pudritz, 2008; Matsakos et al., 2015).

6.3.4 Circumplanetary evolution

To classify the extended atmospheres of HJs, Matsakos et al. (2015) divided simulated behaviour into four categories, which are as follows:

- type-1, bow shock and thin tail;

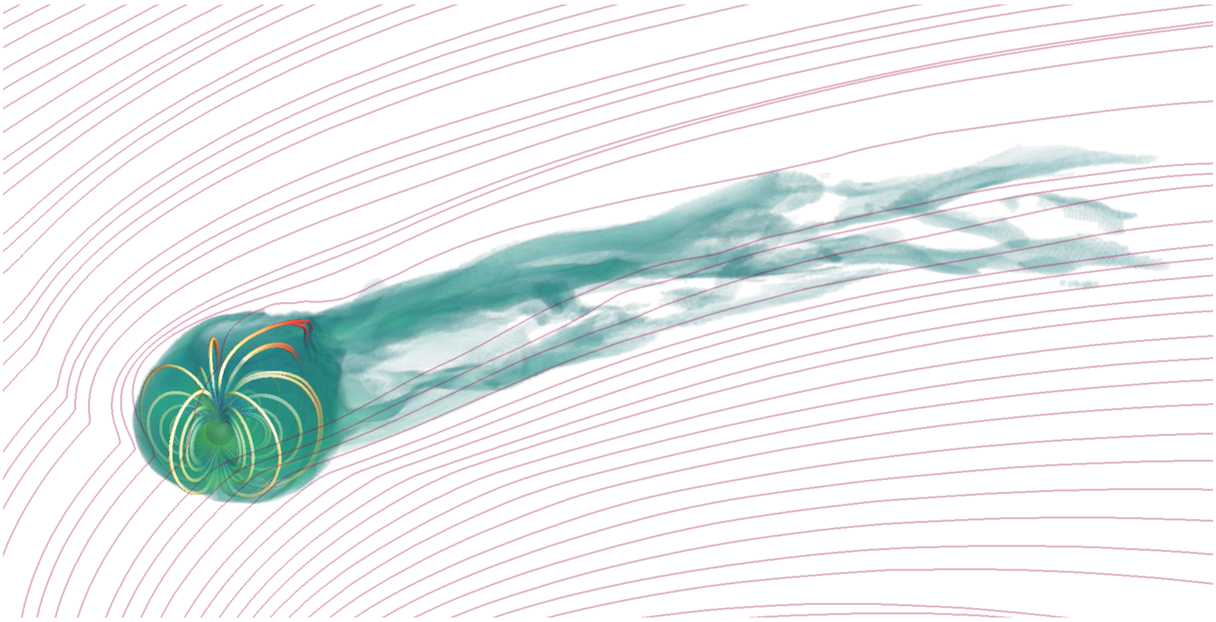

Figure 6.10: Volume rendering of the planet. The diffuse green cloud represents density for values greater than 3×10^{-18} g/cm^3.This material forms a cloud that has thermally expanded to fill the planetary magnetosphere and then begun to overflow and mix with the oncoming stellar wind (illustrated here by the red flow lines). The magnetic field lines of the planetary magnetosphere are show with a blue to red colour scheme depicting the field strength.

- type-2, colliding winds and tail;
- type-3, strong planetary-wind, accretion and tail; and
- type-4, Roche-lobe overflow, accretion and tail.

The behaviour of the HJ atmosphere simulated in this study falls into classification type-1.

A 3D rendering of the planet is shown in Fig. 6.10. The green volume represents density values greater than 3×10^{-18} g/cm^3. This material surrounds the HJ, fills the magnetosphere by following field lines (blue to red colour scheme depicting the field strength) and thermally expands until it overflows from the aft part magnetosphere and mixes with the downstream stellar wind.

The bow shock and thin cometary tail is shown in greater detail in Fig. 6.11, where (from the top row to bottom row) density, velocity magnitude, magnetic field magnitude and temperature are plotted for both a top down (left–hand column) and side on (right–hand column) views. Each of these quantities will be detailed in the following sections.

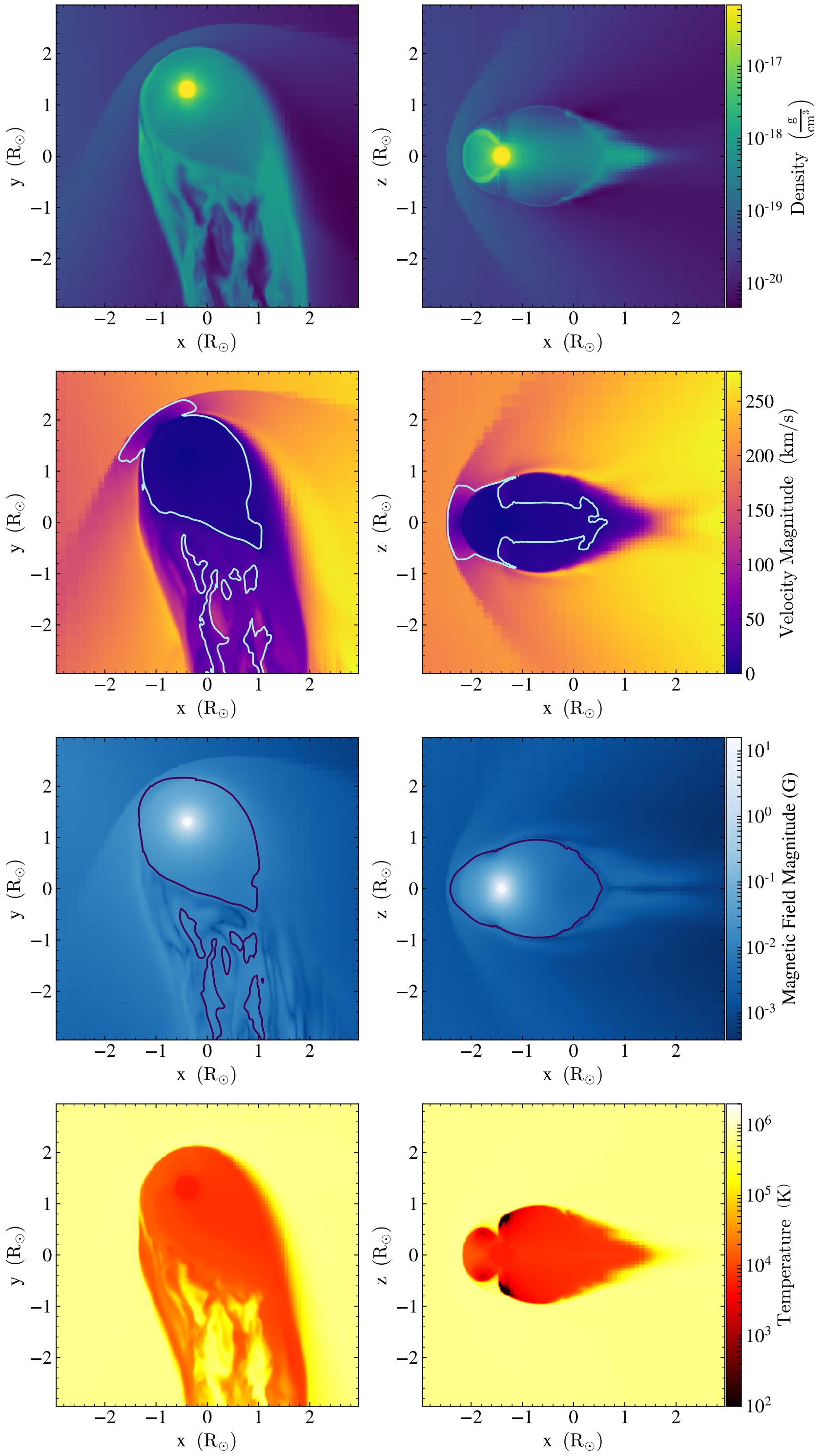

Figure 6.11: Density, velocity magnitude (with sonic surface contour), magnetic field magnitude (with Alfvénic Mach surface contour) and temperature plots of the magnetosphere. Left–hand column: top down view showing the planet, bow shock and start of cometary tail. Right–hand column: same as left–hand column but for a plane parallel to the z-axis. The plane intersects the centre of the planet and the apex of the bow shock. Mass-loss from the planet has filled the magnetosphere with material from the planet's atmosphere, confined by the planetary magnetic field. This material overflow from the downstream part of the magnetosphere to form the cometary tail.

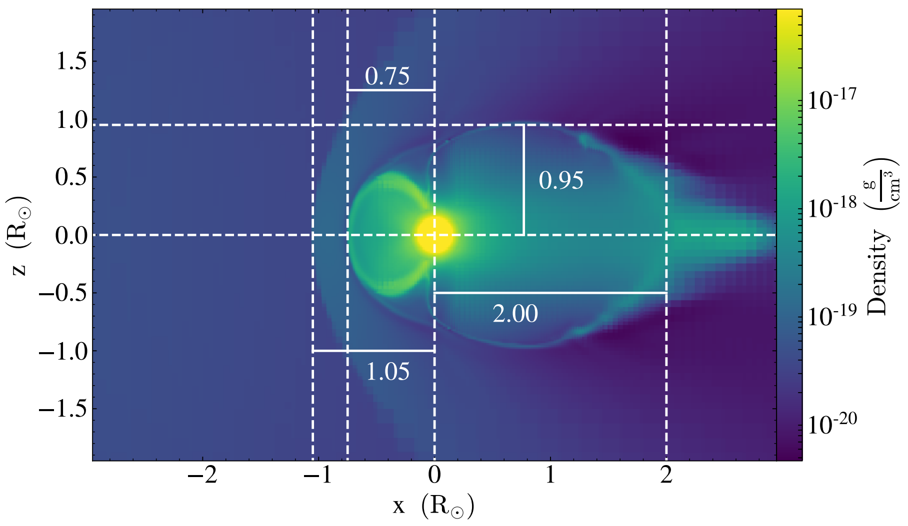

Figure 6.12: Diagram illustrating the position and extent of the separate parts of the magnetosphere. Dotted lines highlight the planets center as well as the edges of the magnetosphere. Solid lines show the width of each feature. The total length of the magnetosphere is given by $D_{\mathrm{M}} = 0.75 + 2 = 2.75$ R$_*$. The magnetospheric radius, used in equation (6.28) to determine the frequency of ECMI emission, is $R_{\mathrm{M}} = 0.75$ R$_*$. The effective radius seen by the stellar wind and used in equation 6.29 to calculate the power available to the ECMI process is $R_{\mathrm{eff}} = 0.95$ R$_*$. The stand-off distance of the bow shock, $R_{\mathrm{SO}} = 1.05$ R$_*$, is also shown.

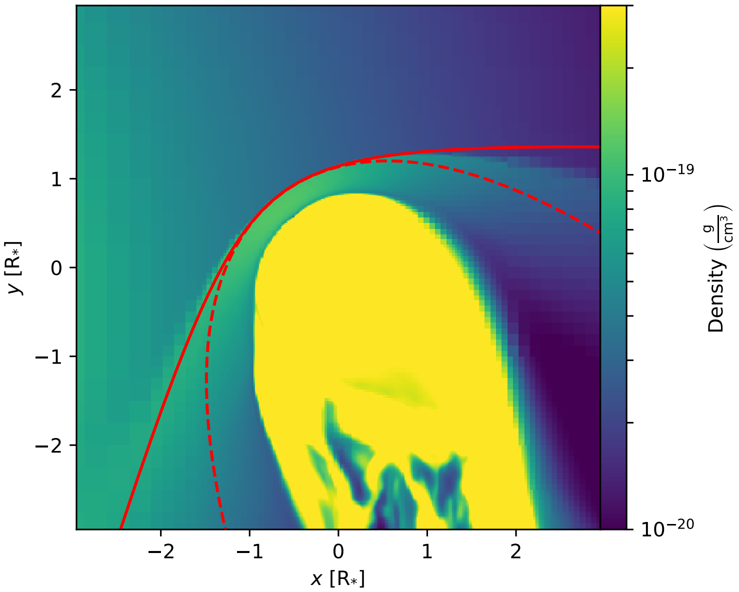

Figure 6.13: Comparison between predictions for the bow shock shapes. The solid red line indicates the prediction according to the work of Tarango-Yong & Henney (2018), and the dashed red line shows the prediction of Wilkin (1996). The underlaying simulated bow shock can be seen as the over–dense region upstream of the magnetosphere, with the colour map range chosen to highlight the shape of the bow shock for ease of comparison. Both simulated and analytic results agree well near the apex of the shock. Out to the sides, the agreement begins to break down with both curves diverging from the simulation results. The prediction of Tarango-Yong & Henney (2018) is the closest to the simulation results.

6.3.4.1 Density structure and bow shock

The planetary wind has expanded into the magnetosphere up to the magnetopause where it accumulates until it reaches equilibrium and overflows, escaping from the aft part of the magnetosphere forming a cometary tail. Material following open field lines that protrude from both poles can escape from the magnetosphere and mix with the stellar wind. This happens in at the polar cusps and is most apparent in the right–hand column.

For simplicity, Llama et al. (2013) state that the radius of the magnetosphere, R_M, is also the distance from the exoplanets center to the bow shock apex. This is not strictly true as can be seen in Fig. 6.12, which illustrates the various positions of the magnetospheric features relative to the exoplanets center and shows that the stand-off distance is 1.05 R_* and $R_\mathrm{M} = 0.75\ \mathrm{R}_*$, a value $\sim 30\%$ smaller. This difference between R_M and the stand-off distance is expected and it is observed for the Earth where the region between R_M and the stand-off distance is known as the magnetosheath. For the interest of clarity, in the following section, the distance to the apex will be referred to as the stand-off distance or R_SO.

The relative velocity of the exoplanet to the oncoming stellar wind is supersonic, $|u_\mathrm{K} - u_\phi| > c_\mathrm{s}$, leading to the formation of a bow shock ahead of the exoplanet and its magnetosphere. The angle made by the bow shock to the direction of orbital motion is given by $\theta_0 = \arctan(u_\mathrm{w}/|u_\mathrm{K} - u_\phi|)$ (Vidotto et al., 2010; Llama et al., 2013), where u_ϕ is the azimuthal wind velocity at the orbial radius and u_K is the Kepler orbital velocity. For large orbital radii $\theta_0 \rightarrow 90°$ (side on to the orbital motion), for small orbital radii $\theta_0 \rightarrow 0°$ (directly in the path of the exoplanet). In practice, $0° < \theta_0 < 90°$ and for this simulation $\theta_0 = 35.4°$. Wilkin (1996) derived an expression for the shape of the bow shock, giving the distance from the planets centre to the shock, r_shock, as a function of θ_0:

$$r_\mathrm{shock} = \frac{R_\mathrm{SO}}{\sin(\theta - \theta_0)} \left[3 \left(1 - \frac{\theta - \theta_0}{\tan(\theta - \theta_0)} \right) \right]^{1/2} . \tag{6.30}$$

The coordinate θ forms the angle between the orbital direction and the the apex of the shock. u_{K} is determined from $(GM_*/a)^{1/2}$ and u_{w} is sampled directly from the simulated stellar wind immediately a head of the planet. The stand-off distance of the bow shock is $1.05\ R_* = 6.97\ R_\circ$, which is taken from Fig. 6.12 as the distance between the apex of the bow shock and the exoplanets center. Bow shocks described by equation (6.30) are known as *wilkinoids* (Cox et al., 2012; Tarango-Yong & Henney, 2018) and assume a plane parallel incident wind. For the case of a colliding wind, they are known as *cantoids* (Tarango-Yong & Henney, 2018).

Good agreement is found between the parabola described by equation (6.30) and the simulation close to the apex of the bow shock: As θ increases the agreement begins to break down. The wings of the simulated bow shock are supported further upstream compared to the prediction of equation (6.30), which does not account for the presence of the magnetosphere, which leads to the conclusion that the bow shock in this work is not *wilkinoid* in nature. The two curves and their deviation are shown in Fig. 6.13. To account for the over supported wings of the bow shock in the *wilkinoid* prediction, a model based on the work of Tarango-Yong & Henney (2018) in which bow shock morphology is based upon a sophisticated treatment of parametric equations. Inputs to this model are dimensionless parameters allowing the model to be fitted to data or simulation results. These parameters are

$$Q = -\frac{b^2}{a^2},\ \Pi = \frac{aQ}{a - x_0},\ \Lambda = \sqrt{Q\left(\frac{a + x_0}{a - x_0}\right)}. \tag{6.31}$$

A by eye fit for this simulation gives values of $Q = -4.6$, $\Pi = 2.7$ and $\Lambda = 1.4$. By substitution and algebraic manipulation of equations (6.31), a and b are found. The Cartesian coordinates of the curve are then given by

$$x = x_0 + a\cosh(t),\ y = b\sinh(t), \tag{6.32}$$

with parametric variable $t \in [0, \pi]$. The interested reader is directed to Tarango-Yong & Henney (2018) for a full description of the procedure. $r_{\mathrm{shock}}(\theta)$ and θ are recovered from

Cartesian to polar coordinates via $\theta = \tan^{-1}(y/x)$ and $r_{\text{shock}} = \sqrt{x^2 + y^2}$. This model will be referred to as *thoid* model (after the authors of the afore mentioned paper) for the remainder of the is paper. The *thoid* curve is plotted in Fig. 6.13 as the solid red line and more closely matches the wings of the shock than the *wilkinoid* curve.

The *thoid* model is derived based on the notion of a colliding wind system where the object around which the bow shock forms and the source of the wind in which it resides are point-like sources. This is precisely the situation that is found in the simulation presented here, a result that leads to the conclusion that the bow shock of a HJ needs to be modelled as a *thoid* type bow shock.

Symmetry is often invoked in the characterization of bow shocks; however, this symmetry is broken when the bodies around which the shocks form are in orbital motion (Stevens et al., 1992; Gayley, 2009). Such symmetry breaking is present in Fig. 6.13, with the left wing of the shock undergoing greater compression than the right. This is due to the relative differences in density and velocity either side of the planet. At the orbital radius, the velocity and density gradients are high relative to the extended wind, this is apparent in Fig. 6.9. This leads to the asymmetry seen in the figure and accounts for the deviation from the model bow shock described by equation (6.32). For HJs orbiting at larger radii, the gradients will be shallower leading to a more symmetric bow shock.

A proper treatment of the morphology of the bow shock would require an expression that gives the distance to the bow shock as $r_{\text{shock}}(\theta) \rightarrow r_{\text{shock}}(\theta, \phi)$, i.e. a 3D representation that captures the non-spherical nature of the magnetosphere, an endeavour beyond the scope of this study.

6.3.4.2 Velocity field

The bow shock, magnetosphere and tail are all apparent in the velocity maps of Fig. 6.11. The bow shock exhibits a distinctive jump corresponding to the jump in density seen in the panel above with the apex of the shock undergoing the greatest change in velocity. Within the magnetosphere, the velocity is approximately constant and < 50 km/s, indicating either that the terminal velocity of the planetary wind is reached before the stand off distance of the magnetopause or that the magnetosphere is saturated with material that is then pressure supported leading to a corresponding reduction in velocity. The later conclusion is supported by inspection of the sonic surface position (see contour in the second row of Fig. 6.11), covering approximately the width of the magnetosphere in the equatorial plane. This is not the case for the initial conditions, where the sonic surface forms a sphere centred on the planet with a radius of 0.5 R_*, about half the width of the steady–state solution. As the simulation evolves, the planetary wind expands into the magnetosphere while undergoing compression by the incident stellar wind, the magnetically confined material increases and with it the radius of the sonic surface, out to the magnetopause.

Large velocity gradients exist between the planetary and stellar winds of the order of 150 km/s, leading to a high degree of velocity shear and a Kelvin–Helmholtz (KH) unstable boundary. As the results show, there is no such instability present. A number of factors can act to inhibit this type of instability. A magnetic field parallel to the direction of the velocity field can suppress the instability if the Alfvénic Mach number, M_{Alf}, is of the order of unity in the shear layer (Frank et al., 1996; Ryu et al., 2000), the contour in the magnetic field plot (row three of Fig. 6.11), i.e. $M_{\mathrm{Alf}} = 1$ in the region of the velocity shear and thus suppresses KH instabilities. Non-magnetized HJs may exhibit KH behaviour.

Numerical dissipation can also lead to a suppression of KH instabilities, Riemann solvers less conservative than the HLLC solver lead to diffusion at the velocity interface, resulting in a smooth transition with no instability. The simulations presented here were conducted using algorithms known to be capable of producing KH behaviour, leading to the conclusion that either the resolution employed is insufficient to resolve these features or that the magnetic suppression described above is responsible for the absence of the KH instability.

Comparing the sonic surface and Alfvénic Mach surface in the second and third rows of the right–hand column of Fig. 6.11, one can see that the sonic surface almost reaches the poles of the planet, while the Alfvénic Mach surface remains at the magnetopause, and therefore material out of the equatorial plane is primarily supported by magnetic tension rather than ram or thermal pressure from the planetary wind.

6.3.4.3 Magnetic field topology

The planetary magnetic field remains largely dipolar apart from an antisymmetric perturbation aft and fore of the planet. The asymmetric shape of the magnetosphere is due to the ram pressure of the stellar wind on the field lines, compressing upstream and elongating downstream, where the planets magnetosphere is stretched out to form a magnetotail and plasma sheet. The 3D representation of the field lines in Fig. 6.10 also shows this asymmetry. From the third row in Fig. 6.11, it can be seen that the magnetosphere downstream of the exoplanet is approximately twice the radius of the upstream magnetosphere. This makes estimating the magnetospheric radius, R_{eff}, challenging as the closed field line region described in Section 6.2.3.2 can no longer be guaranteed to reflect the effective width of the magnetosphere, as seen by the oncoming stellar wind. As such, the R_{eff} will be estimated from the the extent magnetosphere cross section, this is shown in more detail in Fig. 6.12, see Section 6.3.5.

As mentioned in the previous section, Fig. 6.11 indicates the $M_{\text{Alf}} = 1$ surface, within which the exoplanetary wind is sub Alfvénic and perturbations to the magnetic field can travel back to the exoplanets surface. Outside this surface, the wind is super Alfvénic, meaning that the velocity is faster than the speed at which magnetic perturbations travel and is undisturbed by activity outside this surface unless the flow undergoes rapid change. This can be the result of, for example, a CME. The present simulation is conducted with a steady stellar wind, so this form of perturbation is absent. For a sufficiently active stellar host, which exhibits CME or other forms of rotational or time dependent events, the stability of the magnetosphere of an HJ will become a time–dependent problem.

6.3.4.4 Temperature distribution

The temperature profiles vividly illustrate the extent to which the exoplanetary wind expands from the surface. In both the left– and right–hand columns, the ambient stellar wind is constant at the stellar surface temperature apart from the exoplanetary material confined to the magnetosphere and the cometary tail. The bow shock is not apparent in the temperature maps, and the polar cusps are the same temperature as the stellar wind. This indicates that the stellar wind has penetrated the magnetosphere and can provide a supply of energetic electrons to the poles of the HJ for the ECMI process.

Another feature exhibited by both the northern and southern polar cusps is two dramatically lower temperature regions on the downstream side of the magnetosphere, these can be seen as the black regions in the bottom right–hand plot of Fig. 6.11. The temperature in these region is ~ 100 K despite being directly adjacent to the stellar wind (10^6 K). The presence of these features may indicate the limit of the isothermal assumptions made in the construction of the model described in Section 6.2.2.1. The inclusion of thermal conduction, cooling and a non-unity γ in equation (6.3) would be necessary to test this limit. It should be noted that the lack of temperature gradients within the magnetosphere is in agreement with the isothermal-like nature of the simulations. Together with this and in the absence of a comparable non-isothermal study, it is assumed that these features are purely artificial numerical artefacts and of negligible importance to the structure of the planets magnetosphere.

6.3.5 Radio power and frequency

A determining factor in the intensity, and therefore, detectability of radio emission from HJs is the power available to the ECMI process. Incident kinetic and magnetic energy from the stellar wind on the magnetosphere is translated into radio power. Section 6.2.3.2 describes this process, with equation (6.29) giving the theoretical radio power.

Fig. 6.12 highlights the separate parts of the magnetosphere including the effective radius, $R_{\rm eff} = 0.95\ R_*$. This value together with the stellar mass-loss rate $\dot{M}_* = 2.14 \times$

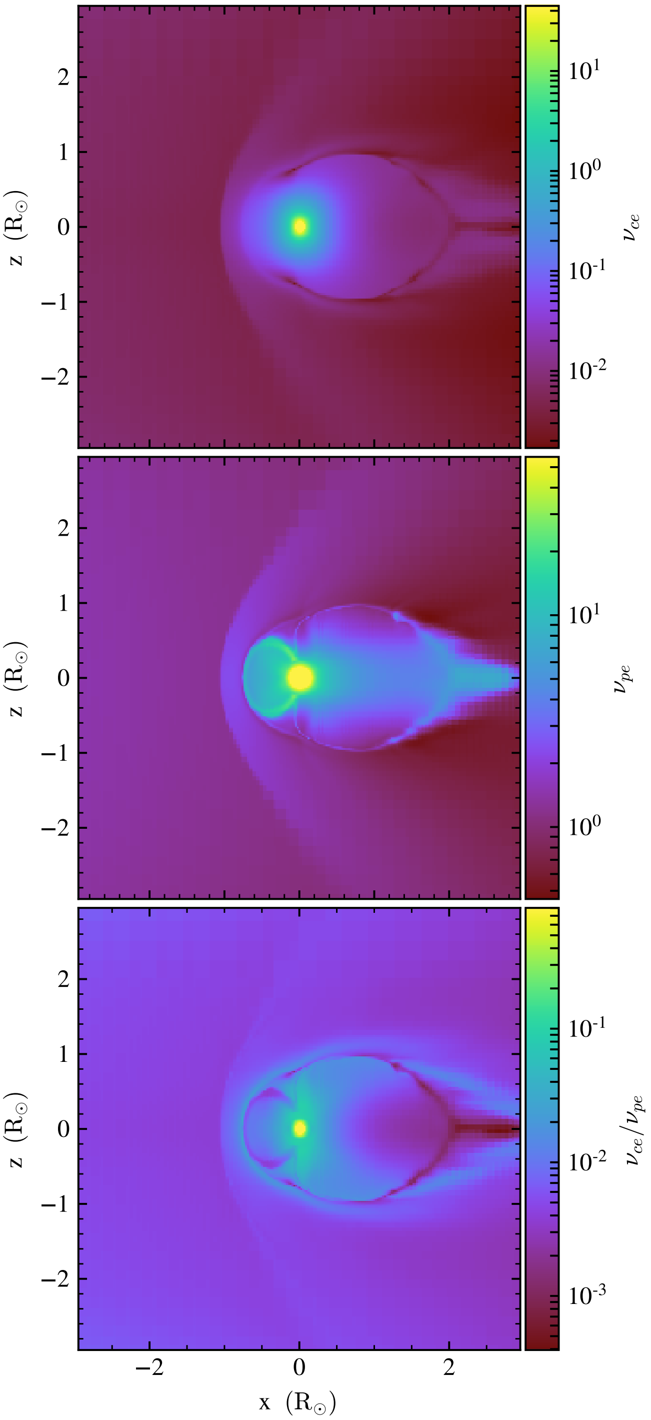

Figure 6.14: The immediate vicinity of the exoplanet with $\nu_{\rm ce}$ (top), $\nu_{\rm pe}$ (middle) and $\nu_{\rm ce}/\nu_{\rm pe}$ (Bottom). Features such as the bow shock, radiation belts and magnetopause are visible in each. The maximum of $\nu_{\rm ce}/\nu_{\rm pe} \sim 0.1$, an order of magnitude below the value necessary for the ECMI process to lead to radio cyclotron emission. This value is also 25 times lower than the efficiency criterion stated in Section 6.2.3.1. The expanding atmosphere of the exoplanet raises the plasma frequency in the magnetosphere, lowering the ratio $\nu_{\rm ce}/\nu_{\rm pe}$ and inhibiting the ECMI process.

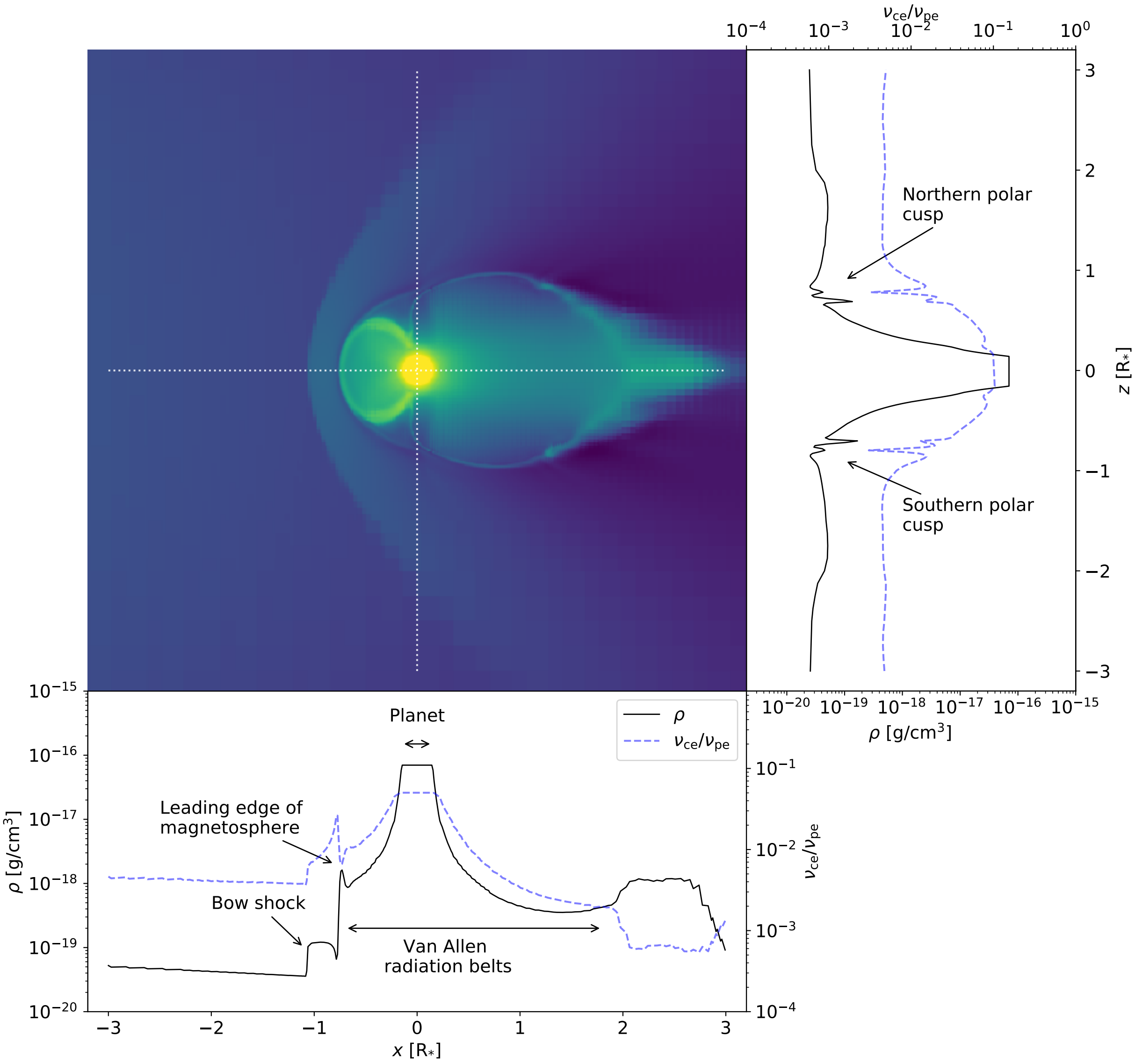

Figure 6.15: Top left–hand panel: density slice plot showing the exoplanet, magnetosphere and bow shock. The dotted white lines indicate the sampling used for the profiles shown below and to the right. Bellow panel: ρ and $\nu_{\mathrm{ce}}/\nu_{\mathrm{pe}}$ profiles for the sample line parallel to the x-axis, indicating the location of the planet, bow shock, leading edge of the magnetosphere and the equivalent Van Allen radiation belts. Right–hand panel: Same as below but for the sample line parallel to the z-axis. Indicated are the the northern and southern polar cusps that form entry points to the planets magnetosphere for stellar electrons.

10^{12} g/s, stellar wind velocity as seen by the planet, $u_{\mathrm{w}} = 207$ km/s and the parameters from Table 6.1, equation (6.29) is used to determine a radio power $P_{\mathrm{r}} = 1.42 \times 10^{19}$ erg/s available to the ECMI. Assuming a typical distance of 10 pc between the exoplanet system and the observer, the resultant radio flux is 0.069 mJy.

This flux is emitted at a range of frequencies between $\nu(B(\alpha))$, as described in Section 6.2.3.2, and ν_{peak}. The oncoming stellar wind has compressed the magnetosphere to such a degree that determining α via the transition from open to closed to field lines is not possible. The approximation, equation (6.28), is used with $R_{\mathrm{M}} = 0.75$ from Fig. 6.12 instead to give $\alpha = 23.5°$ and $B(\alpha) = B_{\mathrm{eq}} \left(1 + 3\cos^2(\alpha)\right)^{1/2} = 1.38$ G and therefore $\nu(B(\alpha)) = 3.88$ MHz which will serve as a lower bound for ν_{ce}. The upper limit, ν_{peak}, is assumed to be a function of the polar field strength, $B_{\mathrm{pole}} = 2B_{\mathrm{eq}} = 2$ G and therefore, using equation (6.24), $\nu_{\mathrm{peak}} = 5.60$ MHz. This leads to the range 3.88 MHz $< \nu_{\mathrm{ce}} <$ 5.60 MHz for the ECMI radio emission. As stated in Section 6.1.4, the ionospheric cut–off is 1–10 MHz, placing ν_{ce} at best in the lower end of what is detectable and at worst below the detectable threshold. A result that alone makes detecting radio emission from HJs with magnetic fields of the order used in this study a challenge. However, this range will be different for each HJ as it is a direct function of the magnetic field strength. Field strengths of $B_{\mathrm{eq}} \sim 5$ G will have an upper limit of 28 MHz, placing it above the 10 MHz cutoff.

6.3.6 Cyclotron emission

The frequency calculated in the previous section does not necessarily lead to detectable emission. The ECMI process is dependent upon two factors, as discussed in Section 6.2.3.1, the conditions must favour both a high ν_{ce} and a low ν_{pe}. These two frequencies are evaluated for the region around the planet and plotted in Fig. 6.14. In this figure, both ν_{ce} (top) and ν_{pe} (middle) are plotted along with their ratio $\nu_{\mathrm{ce}}/\nu_{\mathrm{pe}}$ (bottom). From equation (6.27), the ratio needs to be greater than ~ 2.5 for the ECMI process to be efficient at generating radio emission. As can be seen in the bottom plot of Fig. 6.14, this condition is not met at any point within the vicinity of the HJ, with the largest ratio of $\nu_{\rm ce}/\nu_{\rm pe} \sim 0.1$ in the polar region. This value is 25 times lower than the efficiency criterion stated in Section 6.2.3.1. The expanding atmosphere of the planet has raised $\nu_{\rm pe}$ to such a degree that it inhibits any emission from electrons undergoing the ECMI process. With the implication that, for an exoplanet such as the one simulated here, the ECMI process is inefficient at generating radio emission.

This result is in agreement with Weber et al. (2017), who, through analytic modelling, found very similar results for a range of exoplanet parameters including magnetic field strengths of the order 50 G. With the conclusion that, for efficient emission generation, a HJs magnetic field would need to be > 50 G, recent work by Yadav & Thorngren (2017) has investigated the energy available to the planetary dynamo in the form of absorbed radiation from HJ hosts. Their work found that the majority of HJs should have magnetic fields in the range $50 \text{ G} < B_{\rm pole} < 150 \text{ G}$ (see Fig. 2(b) of afore–mentioned paper). However, due to the work of Weber et al. (2017), one would conclude that such HJs should have been detected, casting doubt on the high magnetic field strength model. Other factors must also be considered, such as the intermittent nature of emission, beaming direction and the sparse number of observations. All factors play a role when considering the lack of radio detections of HJs.

Early results of the simulations presented here were communicated in Daley-Yates & Stevens (2017), in which two regions above and below the HJ poles were found to have $\nu_{\rm ce}/\nu_{\rm pe} > 1$. These simulations have been refined and now use a more sophisticated treatment of the magnetic field, handling the low plasma-β environment near the HJs surface, resulting in a more stable simulation. As such, the simulation in this work builds upon those presented in Daley-Yates & Stevens (2017).

To further investigate the relation between flow features, the HJ's magnetosphere and the ECMI efficiency ratio $\nu_{\rm ce}/\nu_{\rm pe}$, Fig. 6.15 displays a density slice through the HJ, showing both poles, bow shock and extended magnetosphere. Two lines intersecting at the planets centre, indicating the sample lines of the plots shown to the right and bottom of the figure. $\nu_{\mathrm{ce}}/\nu_{\mathrm{pe}}$ is sensitive to all features present in the density structure. In the case of the x-axis aligned profile, the bow shock, edge of the magnetosphere and the planet itself give rise to increases in $\nu_{\mathrm{ce}}/\nu_{\mathrm{pe}}$. For the z-axis aligned profile, the main features are the polar cusps with $\nu_{\mathrm{ce}}/\nu_{\mathrm{pe}}$ fluctuating across them. In both profiles, the highest ratio is found at the planets surface, in agreement with the previous section.

6.4 Conclusions

Radio emission due to the ECMI process in HJ exoplanets is expected to be considerable; however, to the contrary of numerous theoretical works, no repeatable detections have been made to date. This work provides an explanation for this through the use of MHD simulations. Global evolution and the circumplanetary environment of an HJ–hosting system have been investigated via rigorous treatment of both the stellar and planetary winds and magnetic field in order to determine the efficiency of the ECMI process for producing detectable radio emission.

The frequency of emission has been calculated using the model of Vidotto et al. (2011) as a lower limit for the emission and the polar magnetic field strength as an upper limit. This gives the range $3.88\ \mathrm{MHz} < \nu_{\mathrm{ce}} < 5.60\ \mathrm{MHz}$ for the emission frequency. This is below or close to the Earth's ionospheric cutoff frequency and detection limits of current instruments. HJs with field strength greater than used here may result in emission frequencies above this cut–off point.

For the simulated HJ, the ECMI process is completely inhibited by the expanding atmosphere, due to the UV radiation from the host star. This result is in close agreement with the analytic work of Weber et al. (2017). For such an exoplanet to produce detectable emission, the magnetic field is required to be considerably greater than that used here. As no such detections exist, credence is given to a weak magnetic field model that is used in this work and powered by slow rotation at the orbital frequency (tidal locking), over the strong magnetic field, radiation powered model of Yadav & Thorngren (2017).

So far the discussion of the possibility of ECMI emission has been dominated by considerations of the magnetic field strength. For a complete discussion we need to mention the mass-loss rate of the HJ. As the ECMI process is inhibited by the expanding atmosphere, the rate of this expansion is a critical quantity. However, the mass-loss of our simulated HJ is at the lower end of what is predicted (Salz et al., 2016). Larger mass-loss rates represent less favourable conditions for the ECMI process as this would lead to a higher density, and therefore larger ν_{pe} in the magnetosphere. Given that our simulated HJ represents a configuration favourable for the ECMI process and that the largest value of $\nu_{\mathrm{ce}}/\nu_{\mathrm{pe}}$ is still ~ 25 times too small for efficient generation of emission, we conclude that for the vast majority of HJ mass-loss rates the ECMI process is inhibited. This does not rule out ECMI emission from HJs with mass-loss rates less than that used in this study.

Analysis of the bow shock has also been conducted showing that the model of Tarango-Yong & Henney (2018) (*thoid*) better recreates the shock produced by an HJ than the more traditional Wilkin (1996) (*wilkinoid*) model.

Results presented in this work do not rule out the possibility for radio frequency detection of HJs that experience energetic or transient events such as CME, which act to compress and deform the exoplanetary magnetosphere. These transient events are left for future study.

7

It's raining hot Jupiters: 3D MHD simulations of star-planet wind interaction

This chapter is a reformatted copy of the paper Daley-Yates & Stevens submitted: "It's raining hot Jupiters: 3D MHD simulations of star-planet wind interaction" and is my own work.

7.1 Introduction

Hot Jupiter (HJ) type exoplanets reside in short orbits, having undergone migration from the orbital distances at which they form, these planets are subject to intense radiation from their host stars (Fogg & Nelson, 2005; Murray-Clay et al., 2009; Petrovich & Tremaine, 2016; Alvarado-Montes et al., 2017). As their radii and masses are similar to the solar system planet Jupiter, they are the largest and most readily detectable class of exoplanets. Indeed the first exoplanet to be discovered, 51 Peg b by Mayor & Queloz (1995) falls into this category. Due to the short periods of their orbits ($\sim$ 4 days), HJ are very suitable to detection via the transit and radial velocity methods, see Wright & Gaudi (2012) for a comprehensive review of detection methods. Despite this observational bias, many questions about the nature of HJ systems still remain unanswered and unpredicted observations unexplained. An example is the so called HJ *pile-up*, a phenomenon where the orbital period of HJs clusters between 2 - 6 Earth days and trails off to longer periods, giving rise to the term *pile-up*, see Chang et al. (2012) for possible responsible mechanisms and more resent theoretical work by Wise & Dodson-Robinson (2018); O'Connor & Hansen (2018). Such unexpected statistical features hint at the limit of our understanding and of the future challenges to theorists and observers who study HJ systems.

The migration of giant planets through to the HJ phase influences the evolution of planetary systems from initial planet formation to the final stages of the systems life. This stage, when a gas-giant becomes a HJ, is when the planet leaves its final mark on its host. Mass and angular momentum (AM) exchange as well as magnetic interactions between the HJ and its host impact on the long term evolution of both bodies, acting to either reduce or enhance the rate of spin down and orbital decay. Such effects have been investigated theoretically by Strugarek et al. (2015a) who found that the torque experienced by HJs can vary over an order of magnitude depending on the magnetic field of both HJ and host star; reporting migration timescales of 100 Myr. Such results show that star-planet magnetic interaction (SPMI) must be considered if a rigorous theory of the final stages of giant planet migration is to be developed.

Our aim with the present study is to further explore the paradigm of star-planet interaction by focusing on a HJ undergoing hydrodynamic mass-loss of its atmosphere and to place the results in the context of observable signatures left on the surface of it host star via accretion flows.

7.1.1 Planetary FUV evaporation

Mass-loss in HJs occurs predominately due to absorption of energy via incident (Far Ultraviolet) FUV and X-ray flux from the host star (Lammer et al., 2003; Pillitteri et al., 2015). Mass is then lost either through Jeans escape, which is a function of the planet's effective temperature, or by thermal expansion driven by the aforementioned incident radiation.

For HJs it has been shown that Jeans escape vastly underestimates their mass-loss. Indeed, the first exoplanet discovered, 51 Peg b, has an effective temperature similar to that of Jupiter's upper atmosphere ($\sim 700 - 1000$ K) (Smith & Hunten, 1990). It is the FUV and X-ray heating of the upper exosphere that results in temperatures an order of magnitude higher (Lammer et al., 2003) than the effective temperature. This enhancement of the exosphere temperature is directly responsible for the hydrodynamic atmospheric expansion seen in multiple HJs (Lammer et al., 2003; Weber et al., 2017; Sairam et al., 2018). Enhanced mass-loss is not the only a consequence of absorbed stellar radiation, many HJs exhibit lower mass while simultaneously a larger radii with respect to Jupiter (Tremblin et al., 2017) and hence a lower density, a result consistent with an increased internal energy. This increased energy via FUV absorption is though to contribute to atmospheric circulation, leading to a redistribution and possible equalisation of day- and night-side temperatures (see Schwartz et al. (2017); Dang et al. (2018); Zhang et al. (2018) for observations of temperature offsets from the sub-stellar point). FUV absorption possibly contributes to enhancement of the planetary dynamo and hence magnetic field. Values of the order 50 G are predicted by Yadav & Thorngren (2017), an order of magnitude larger than Jupiter's magnetic field. However, such field strengths would be detectable due to MHz radio emission via the Electron Cyclotron Maser Instability (ECMI) (Weber et al., 2017; Daley-Yates & Stevens, 2017, 2018).

The estimated mass-loss for HJs is typically in the region of 10^9 g/s $< \dot{M}_{\rm HJ} < 10^{12}$ g/s (Salz et al., 2016). The dynamics and spread of the evaporated HJ atmosphere in the interplanetary medium behaves differently depending on the rate of mass-loss. At lower $\dot{M}_{\rm HJ}$, the evaporating HJ atmosphere fails to reach the stellar surface and is swept back forming a cometary tail (Matsakos et al., 2015; Daley-Yates & Stevens, 2018). For comparatively large values of $\dot{M}_{\rm HJ}$, the atmosphere can undergo Roche lobe overflow and form strong accretion streams connecting with the stellar surface (Matsakos et al., 2015; Pillitteri et al., 2015). This form of interaction is the topic of the present work.

7.1.2 Star planet wind interaction

Recent observations of HJ hosting systems conducted with both the Cosmic Origins Spectrograph on board the Hubble Space Telescope (COS-HST) (Pillitteri et al., 2015) and the Echelle Spectro Polarimetric Device for the Observation of Stars instrument at the Canada-France-Hawaii Telescope (ESPaDOnS-CFHT) (Shkolnik et al., 2008) indicate that stellar emission is synchronised with the orbit of the HJ. It has been proposed that this is due to an intermittent accretion stream making foot-fall on the stellar surface, leading the HJ orbit by $\sim 90^\circ$. These two studies have also reported enhanced chromospheric activity for a number of stars hosting hot Jupiters, including HD 179949 and HD 189733 (Shkolnik et al., 2008; Pillitteri et al., 2015). Star-planet interaction via mass transfer, from planet to star, and thus the accretion of the planet by its host, is thought to be responsible. Thus far, there has been limited simulation work investigating this wind mediated type of star-planet accretion. Star-Planet Interaction (SPI) and Star-Planet Magnetic Interaction (SPMI) has been studied using Hydrodynamics (HD) and Magnetohydrodynamics (MHD) for a number of years (see below).

Physical systems in which multiple accelerated gaseous outflows form collisions are numerous in astrophysics; from AGN jets to massive star colliding wind binaries. These interactions are responsible for a range of detectable emission from synchrotron and X-ray to the acceleration of cosmic rays. In the context of exoplanetary systems and specifically those hosting HJs, there are two types of interaction depending on whether the HJ orbits inside or outside the stellar Alfvén surface. Inside, the HJ can interact via direct magnetic field line connection between the stellar and planetary magnetospheres, this situation has been modelled by Strugarek et al. (2014); Khodachenko et al. (2015); Vidotto et al. (2015); Strugarek et al. (2015b); Strugarek (2016). Outside the Alfvén surface direct magnetic connection of field lines is not possible as the flow is super-Alfvénic. Instead the mode of interaction is via magnetised flow of material from the HJ atmosphere to the stellar surface via an accretion stream (provided the HJ is undergoing rapid mass-loss), a type of interaction which will be referred to from here on as Star-Planet Wind Interaction

(SPWI) and has been modelled previously by Bourrier & Lecavelier des Etangs (2013); Bourrier et al. (2016); Owen & Adams (2014); Alexander et al. (2015); Matsakos et al. (2015); Carroll-Nellenback et al. (2017). Understanding the stellar wind dynamics is in itself an important aspect when considering SPI and there have been several separate studies that have investigated solely the properties of stellar winds of exoplanet hosting stars (Alvarado-Gómez et al., 2016; Fares et al., 2017).

Another form of SPWI is the formation of planetary bow shocks around HJs which lead to observable effects such as ingress features in transit observations, where the bow shock obscures some of the stellar light before the main transit of the planet across the stellar disk (Llama et al., 2013). Bow shocks are features which form due to incident kinetic and magnetic energy in the stellar wind on the planetary magnetosphere. This energy input has been proposed as a means to amplify the ECMI process and has been previously thought to result in detectable emission (Stevens, 2005; Zarka, 2007). This has however recently been brought into doubt by Weber et al. (2017); Daley-Yates & Stevens (2018).

These two categories of interaction, SPMI and SPWI, are complimentary; one does not preclude the other. Indeed, SPMI can occur at the same time as SPWI, however SPMI cannot occur if the orbit is outside the Alfvén surface, where SPWI can as it is, in principle, independent of the planets position relative to the Alfvén surface. The prerequisite for SPWI is that the HJ atmosphere be undergoing hydrodynamic escape and a planetary wind has established, a situation independent of the stellar Alfvén surface position. Hydrodynamic escape is however conditional upon the absorption of stellar FUV radiation in the HJ upper atmosphere and is different for each HJ system. As a rule of thumb, a hydrodynamic wind will establish if the HJ orbital radius is $a < 0.5$ au, according to Weber et al. (2017). The precise wind properties, mass-loss and day-side night-side outflows and temperature are a function of the stellar, planetary and orbital parameters, as briefly discussed in the previous section.

The focus of the present study is the quantification of the evolution of the stellar surface of a star which is undergoing accretion, via SPWI interaction, from the expanding atmosphere of a hosted HJ. Exploring non-magnetised and dipole-dipole interactions, we aim to distinguish between different regimes of magnetised interaction and quantify the mass accretion rate, accretion stream stability and AM transfer between planet and host star.

7.2 Modelling

The models used here are derived from the work of Matsakos et al. (2015) and are identical to those we present in Daley-Yates & Stevens (2018), with the exception of the planetary parameters for temperature and mass-loss (see Table 7.1). The reader is directed to this paper for a full description of the model used. Below, we give a short overview of the key equations.

7.2.1 Magnetohydrodynamics

To account for the orbital motion of the planet, the MHD equations are solved in the co-rotating frame of the planet and are given by:

$$\frac{\partial \rho}{\partial t} + \boldsymbol{\nabla} \cdot (\rho \boldsymbol{v}) = 0 \tag{7.1}$$

$$\frac{\partial \boldsymbol{v}}{\partial t} + (\boldsymbol{v} \cdot \boldsymbol{\nabla}) \boldsymbol{v} + \frac{1}{4\pi\rho} \boldsymbol{B} \times (\nabla \times \boldsymbol{B}) + \frac{1}{\rho} \nabla p = \boldsymbol{g} + \boldsymbol{F}_{\mathrm{co}} \tag{7.2}$$

$$\frac{\partial p}{\partial t} + \boldsymbol{v} \cdot \boldsymbol{\nabla} p + \gamma p \nabla \cdot \boldsymbol{v} = 0 \tag{7.3}$$

$$\frac{\partial \boldsymbol{B}}{\partial t} + \nabla \times (\boldsymbol{B} \times \boldsymbol{v}) = 0. \tag{7.4}$$

Where ρ, $\boldsymbol{v}$, $\boldsymbol{B}$, p, $\boldsymbol{g}$ and $\boldsymbol{F}_{\mathrm{co}}$ are, density, velocity, magnetic field, pressure, gravitational acceleration and Coriolis and centrifugal acceleration. $\boldsymbol{F}_{\mathrm{co}}$ is the sum of the centrifugal and Coriolis forces: $\boldsymbol{F}_{\rm co} = \boldsymbol{F}_{\rm centrifugal} + \boldsymbol{F}_{\rm coriolus}$ and are:

$$\boldsymbol{F}_{\rm centrifugal} = -\left[\boldsymbol{\Omega}_{\rm fr} \times (\boldsymbol{\Omega}_{\rm fr} \times \boldsymbol{r})\right] = \boldsymbol{\Omega}_{\rm fr}^2 \left(x\hat{x} + y\hat{y}\right) \tag{7.5}$$

and

$$\boldsymbol{F}_{\rm coriolus} = -2\left(\boldsymbol{\Omega}_{\rm fr} \times \boldsymbol{v}\right) = 2\Omega_{\rm fr}\left(x\hat{x} + y\hat{y}\right), \tag{7.6}$$

where $\boldsymbol{\Omega}_{\rm fr}$ is the angular frequency of the rotating frame and $\boldsymbol{r}$ is the radial distance.

To close the MHD equations, we employ an adiabatic equation of state. To mimic the isothermal nature of the stellar and planetary winds, we set $\gamma = 1.05$.

7.2.2 Stellar and planetary models

The initial conditions for the stellar wind and planetary mass-loss are based on the non-magnetic Parker wind model (Parker, 1958), the governing equation of which is

$$\psi - \ln\left(\psi\right) = -3 - 4\ln\left(\frac{\lambda}{2}\right) + 4\ln\left(\xi\right) + 2\frac{\lambda}{\xi} \tag{7.7}$$

with ψ, λ and ξ being three dimensionless parameters which are defined as:

$$\psi \equiv \left(\frac{v_{\rm W}^{\rm init}(r)}{c_{\rm s}}\right)^2 \tag{7.8}$$

$$\lambda \equiv \frac{1}{2}\left(\frac{v_{esc}}{c_{\rm s}}\right)^2 \tag{7.9}$$

$$\xi \equiv \frac{r}{R}. \tag{7.10}$$

$v_{\rm W}^{\rm init}(r)$ is the radial wind velocity profile at $t = 0$. The escape velocity is given by $v_{esc} = \sqrt{2GM/R}$ and $c_{\rm s} = \sqrt{2k_{\rm B}T/m_{\rm p}}$ is the isothermal sound speed. $k_{\rm B}$ is the Boltzmann constant, T the temperature and $m_{\rm p}$ the mass of the proton. ξ is the radial distance from either the centre of the star or planet, in units of stellar or planetary radii and R is the radius of either body.

7.2.2.1 Stellar and planetary surface parameters

The parameters for our model star and planet are presented in Table 7.1 and are directly based on those used by Matsakos et al. (2015), which in turn are parameterised values based on 1D simulations conducted by Matt & Pudritz (2008) for base density and pressure. These values are modified so that mass-loss rates and wind properties in the 3D simulations agree with the 1D models.

To investigate different magnetic regimes, we conducted several simulation, each with a different combination of magnetic fields

S0P0 Non-magnetised interaction: the simulation is conducted in the HD regime, both the star and the planet have no magnetisation.

S2P1 Dipole-dipole interaction: the magnetic fields of both bodies are dipolar and aligned with the rotational axis of the system. Two simulations of this model were run, one Cartesian and one spherical polar, see Section 7.2.6 for details.

S2P0 Dipole-non-magnetised interaction: a combination of the first two topologies, the stellar magnetic field is dipolar and the planet has no magnetisation.

These regimes cover three different types of interaction and together they are designed to determine whether the stellar or planetary magnetic fields influences the planetary accretion. The names of each model indicates the magnetisation of each body, **S** stands for the star and **P** stands for the planet. The number following the letters are the strengths of the magnetic field of each body. So **S2P0** states that the star has a dipole equatorial magnetic field strength of 2 G and the planet is not magnetised.

7.2.3 Roche potential

The physics of accretion occurs at all length scales in astrophysics from planetesimal formation on the shortest scales through massive star formation and black hole growth to the harts of galaxies where Active Galactic Nuclei (AGN) form tori and accretion disks

Table 7.1: Stellar and planetary parameters used in the simulations.

Parameter	Symbol	Star	Planet
Mass	$M_{*,\circ}$	1 $M_\odot$	0.5 M_J
Radius	$R_{*,\circ}$	1 $R_\odot$	1.5 R_J
Temperature	$T_{*,\circ}$	10^6 K	10^4 K
Equatorial magnetic field strength	$B_{eq*,\circ}$	0 G, 2 G	0 G, 1 G
Surface density	$\rho_{*,\circ}$	$5 \times 10^{-15}\ g/cm^3$	$7 \times 10^{-16}\ g/cm^3$
Orbital radius	a	–	0.047 au
Orbital period	$p_{\rm orb}$	–	3.7 days
Rotational period	$p_{{\rm rot}*,\circ}$	3.7 days	3.7 days

whose radiation and jets influence star formation and the evolution of the host galaxy it's self. While black hole and AGN accretion physics exist in the high energy accretion regime, stellar-HJ accretion occurs at much lower energy.

In the context of exoplanetary physics, accretion is most commonly explored when concerning the planets initial formation. In the present study we are concerned with accretion in the final stages of a planets life. For HJs, this means the flow, dynamics, physical quantities and transfer mechanics of photoevaporated atmospheric material from low mass object (planet) to high mass object (star). This is in contrast to stellar wind and stellar Roche lobe overflow accretion, where material is transferred from the physically larger object to the smaller, for example black hole or neutron star in the case of X-ray binaries.

To gain an insight into the gravitational topology of the HJ system, the Roche equipotential is plotted in Fig. 7.1. The L_1 point is only 2.48 $R_\circ$ from the planetary surface and if we assume material leaving the planetary surface is travelling at at least the planetary escape velocity, $v_{\rm escp,\circ} = 34.85$ km/s, material leaving the planetary surface will reach the L_1 point in at most 2.07 hours or 0.023 orbits. This tells us that mass lost from the day-side of the planet will enter under the dominant influence of the stellar gravitational field almost immediately. Material from the night-side will reach the L_2 point, situated at 2.75 $R_\circ$ from the planets surface, in at most 2.30 hours or 0.026 orbits, again leaving the planets gravitational influence in a fraction of an orbit and moving out beyond the orbital radius where it experiences a net outwards force, described by the gradient of the Roche

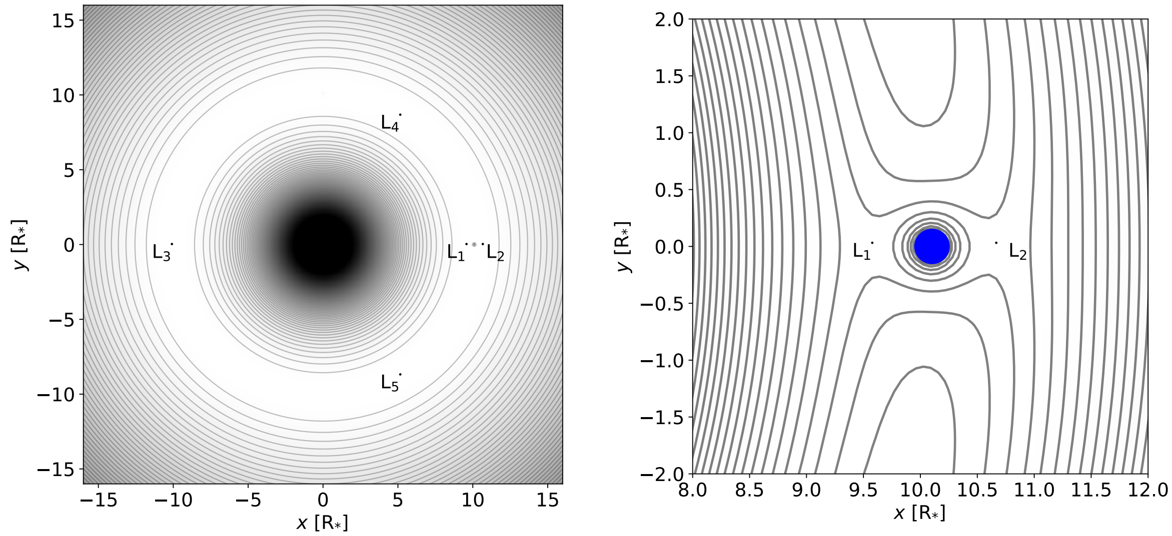

Figure 7.1: Left: Roche equipotential for the inner portion of the system. At the centre is the star and to the right the planet, with Lagrange points 1 - 5 indicated. Right: close up view of the Roche equipotential for the circumplanetary environment with the blue circle indicating the radius of the HJ. Lagrange points L_1 and L_2 are shown to the left and right and their distances from the planetary surface are 2.48 $R_\circ$ and 2.75 $R_\circ$ respectively.

potential and eventually leaves the simulation domain carrying away mass and AM from the system.

As the mass-loss from the HJ is isotropic, one can assume that material with a velocity vector preferentially directed towards one of the to Lagrange points will fall into one of the two regimes described above, either accreted onto the star or lost from the system. Based on this, one could assume that 50% of the planetary mass-loss should reach the stellar surface. However, this simple picture is based purely on gravitational considerations and does not account for dynamic, time-dependent behaviour such as interactions via wind-wind collisions which necessarily lead to fluid instabilities and also the presence of magnetic fields which can act to channel material. MHD simulations such as the ones presented in this work capture such behaviour and give both qualitative and quantitative insight into these systems.

7.2.4 Latitude and longitude of accretion

As the planetary wind material approaches the inner stellar magnetosphere it begins to interact with the stellar magnetic field. The spread of and position of the material, as it makes contact with the surface, will determine any enhancement of chromospheric activity and hence the observable signatures of SPWI.

There is nothing intrinsic in these single-fluid MHD simulations which tracks the trajectory and origin of mass as the simulations evolve. As such, there is no way to differentiate between material from the star or the planet.

To determine the exact position of material as it is deposited on the stellar surface, passive scalars are used to track the motion and advection of the planetary wind. Passive scalars exert no influence on the fluid dynamics but are advected by the fluid flow and can be used as a proxy for the motion of mass across the numerical grid. This allows for the position of the accreting quantities on the stellar surface to be defined.

At $t = 0$, the passive scalars are set at the planetary surface and are continuously renewed as $t > 0$. As the simulation evolves, the passive scalars are advected into the computational active region. The initial planetary surface concentration of passive scalars is set to 1 $n_{\rm pass}$ per unit volume (where n_{pass} is the passive scalar concentration) and as they are advected, this concentration decreases due to mixing of the stellar and planetary winds. The result is that everywhere within the simulation domain the passive scalar concentration is $0 \ < \ n_{pass} \ < \ 1$.

7.2.5 Accretion rate

To determine the deposition of material onto stellar surface, we calculate the flux through a surface, S, of a sphere centred around the star. For simplicity, we assume a spherical coordinate system with the three cardinal directions r, θ, ϕ. The flux is given by the integral over S of the velocity vector projected onto the direction normal to S and the density. Mass-flux is given by

$$f_{\mathrm{mass}} = \int_{\mathrm{S}} \rho\left(\theta,\phi\right)_R \boldsymbol{v}_{\perp}\left(\theta,\phi\right)_R \mathrm{d}S \tag{7.11}$$

The subscript $_R$ means the quantity is evaluated at the radius, R, of the sphere whose surface is S. ρ is the mass per unit volume and $\boldsymbol{v}_{\perp} = \boldsymbol{v}\cdot\boldsymbol{n}$ is the component of the velocity in the direction normal to S. This definition specifies that the flux of quantities in and out of the sphere is negative and positive respectively.

7.2.6 Numerical modelling

Using the public MHD code PLUTO (version 4.2) (Mignone et al., 2007, 2012), the MHD equations (7.1 - 7.4), were solved numerically using a 2nd order accurate scheme with linear spatial reconstruction (Van Lear limiter), 2nd order Runga-Kutta time-stepping and the HLLD Riemann solver. The zero divergence condition of the magnetic field was provided by the GLM method of Dedner et al. (2002), see Mignone et al. (2010); Mignone & Tzeferacos (2010) for the PLUTO version.

Two types of numerical grids were employed in this study, the first, Cartesian, was designed to capture the global evolution of the extended wind of both the star and planet. Using adaptive mesh refinement (AMR), the Cartesian grid preserves and increases resolution at all radii from the stellar surface and where fluid features require a finer grid.

The second grid, spherical polar, was used in only one simulation for model **S2P1**. The aim was to study the behaviour of material as it approaches the close in stellar magnetosphere, where material interacts with stellar surface. To capture this behaviour a spherical grid is superior as the common *staircasing* effect which Cartesian grids suffer from when representing smooth or curved surfaces at low resolution is avoided.

There were a number of methods available to us to avoid the *staircasing* effect. These included the brute force method of simply increasing the number of AMR levels at the stellar surface until the surface was approximately smooth over the dynamic length scale of the simulation. This option was however prohibitively computationally expensive. Another is the Level-set method which allows for the computation of smooth surfaces on numerical grids (Osher & Sethian, 1988). The Level-set method is not a native feature in PLUTO therefore using a spherical grid proved more time-efficient for overcoming the *staircasing* issue.

The following describes the two grid types, their extent and resolution. Examples of which are shown in Fig. 7.2.

7.2.6.1 Cartesian grid

The Cartesian grid extended from $x, y \in \{-32\ R_\odot, 32\ R_\odot\}$ and $z \in \{-16\ R_\odot, 16\ R_\odot\}$ with an initial resolution of $128^2 \times 64$ cells. This initial grid was then successively refined to a maximum of 5 AMR levels resulting in an effective resolution of $4096^2 \times 2048$ giving 64 cells/R_*. The initial grid setup is shown in the lower plot of Fig. 7.2. Refinement of cells is determined by the gradient of the density across the cell, if the gradient exceeds a pre-specified amount, then the cell is marked for refinement. PLUTO uses the patch based method for the grid infrastructure and as such the regions marked for refinement have applied a patch of higher resolution cells covering a greater physical extent than the local cell which was marked for refinement.

7.2.6.2 Spherical polar grid

The spherical polar grid employed for model **S2P1** is defined by $r \in \{1\ R_\odot, 16\ R_\odot\}$, $\theta \in \{0.02\pi, 0.98\pi\}$ and $\phi \in \{0, 2\pi\}$ with a resolution of $178 \times 156 \times 252$. The grid at the θ boundaries is effectively clipped so that the grid does not touch the polar axis. This is done to avoid restrictive time-step sizes as the cell size diminishes at the poles, hence the range specified above.

As the planet is not at the centre of the coordinate system and due to the curvilinear nature of spherical polar grids, individual computational cells occupy different physical volumes on the day and night sides of the planet. High resolution is therefore required to

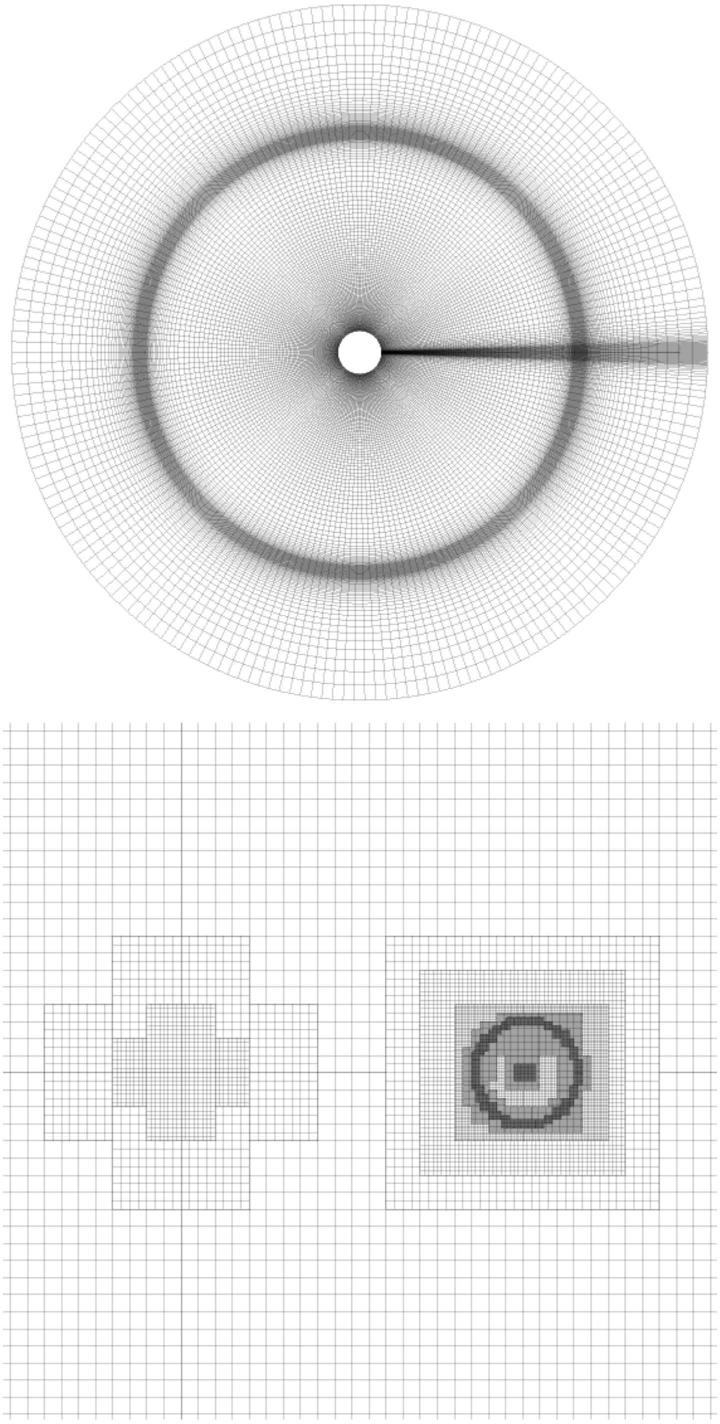

Figure 7.2: Examples of the grids used in the simulations. Top: grid for the spherical polar simulation bands of darker lines indicate high resolution strips which coincide at the planet, allowing higher resolution where it is needed with minimal computational cost. Bottom: zoom in of the grid used for the Cartesian AMR simulations (the full grid is not shown here). The star is situated to the left and the planet to the right. The nested high resolution patches are clustered at points of high density gradient such as the stellar and planetary surfaces and the transition point between the stellar and planetary winds. The physical extent of both grids, as displayed here, are not to scale and are simply illustrative.

avoid grid effects, as AMR is not used in this grid arrangement, the grid is stretched to ensure sufficient resolution at the planet to resolve the planetary outflow and minimise the difference in cell size between the day and night side. There are five distinct grid regions in all three spherical directions which are either stretched or uniform, allowing for the high resolution to be centred on the planet. An illustration of the stretched spherical polar grid is shown in the top image of Fig. 7.2. In contrast to the Cartesian grid, the only region held constant in the spherical grid is within the planetary boundary, as the radial coordinate begins at the stellar surface, the star is effectively outside the grid and therefore not held constant.

7.2.6.3 Boundary conditions

The computational mesh is initialised everywhere according to the equations presented in Section 7.2.2 for the stellar wind. A region of $10R_{\circ}$ around the planet is initialised for the planetary wind in the same manner.

In the Cartesian simulations, both the stellar and planetary bodies act as internal boundaries with stellar, planetary and wind parameters held constant out to 1.5 R_* ($R_{\circ}$), see Daley-Yates & Stevens (2018) for more details. The outer boundaries are set to outflowing insuring that edges of the computational domain do not influence the solution. This situation can change if the velocity begins to point inwards at the edge of the domain, resulting in the simulation being swamped by spurious material entering from the boundaries. This can be avoided by specifying that if $v_r < 0$ then override with $v_r = 0$. This condition was however not encountered in this study.

For the spherical polar grid, the inner radial boundary is set to the values given by equation (7.7) for $\xi = 1$. The velocity here is held constant and positive to ensure inflow at the correct mass-loss rate for the star. The outer radial boundary is set to out-flowing. Both the upper and lower θ boundaries are set to reflective and the upper and lower ϕ boundaries are set to periodic to allow for material to flow between them.

7.3 Results and discussion

The following sections detail the results of the three models, describes the global behaviour of the wind-wind interaction, the surface dynamics, accretion rates and finally places these results in the context of observable signatures.

7.3.1 Global evolution

First the global evolution of the models will be analysed to asses the extent to which the initial conditions have been dissipated and whether the simulation has reached quasi-steady state.

Fig. 7.3 shows a cross-section in the xy plane of the simulation domain for all three models. Both the large scale structure of the star-planet interacting wind is shown on the left and on the right, a close up of the region directly ahead of the planets orbit which includes the stellar surface. This is an important region, as accreting material needs to pass through this area to reach the stellar surface and the morphology of developing structures here determines the rate and spacial location of accretion. The three columns show, from top to bottom, slices from models **S0P0**, **S2P1** and **S2P0** respectively.

Comparing the three models, only **S2P1** has developed a coherent accretion stream where material reaches the stellar surface, predominately through one conduit, only breaking up when reaching the inner magnetosphere. Model **S2P0** exhibits similar filamentary structure but has not developed into a single stream. Model **S0P0** has not developed any coherent streams through which material is transferred to the surface, the differing physical regime under which the simulation is conducted, HD rather than MHD, sets **S0P0** aside from the other two models.

The planetary wind rapidly expands spherically to fill the planets Roche lobe and continues until it collides with the stellar wind. All three models develop a tear-drop like structure around the HJ, this structure is a result of the balance between outward ram pressure of the planetary wind and the large scale stellar wind. Beyond this, the

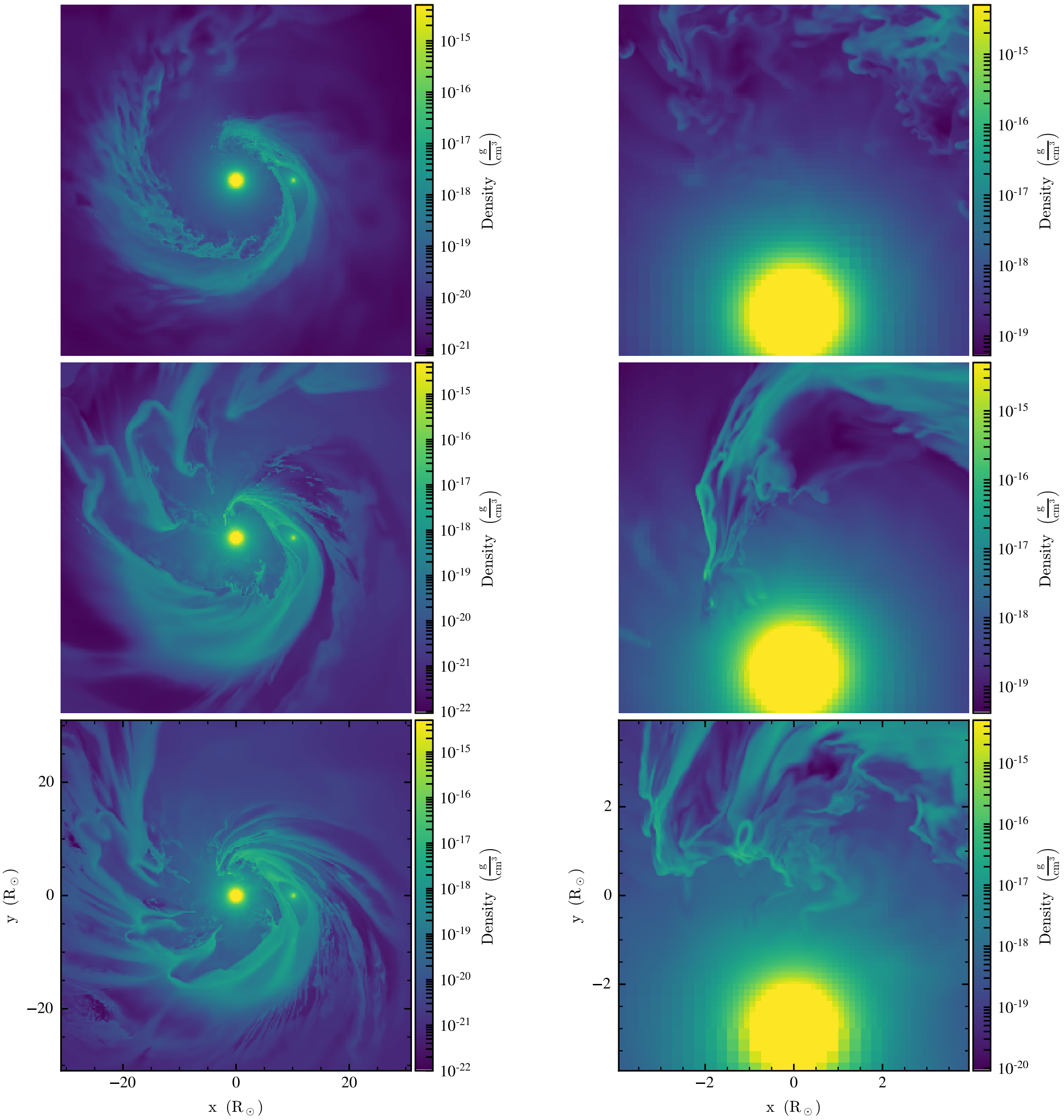

Figure 7.3: Left column: large scale structure of the star-planet interacting wind. Right: close up of the region directly ahead of the planets orbit including the stellar surface. Accreting material needs to pass through this region to reach the stellar surface, structures which develop here determine the morphology of the accretion stream. The three columns show, from top to bottom, data from models **S0P0**, **S2P1** and **S2P0** respectively.

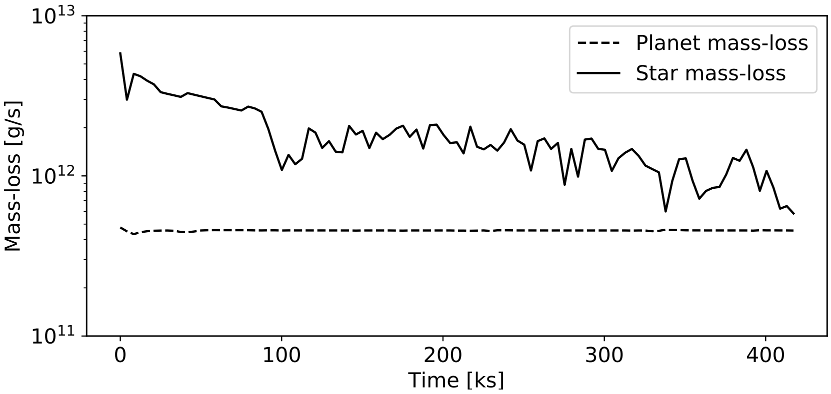

Figure 7.4: Mass-loss as a function of time for both the star and HJ in model **S2P1**. Mass-loss for the star, $\dot{M}_*$, undergoes a decrease from its initial value to $\sim 10^{12}$ g/s. The curve exhibits fluctuations in its profile after $\sim$ 100 ks, beyond this point material from the planet advects close enough to the star to influence the mass-loss calculation. In the HJs case, $\dot{M}_\circ$ is constant from the beginning of the simulation at a value of 4.6×10^{11} g/s.

planetary wind is forced to collimate into a steam ahead of the planet where it spirals into the inner stellar magnetosphere, and behind the planet where it expands in an open fan like structure until it reaches the outer boundary of the simulation.

For these three models, **S2P1**, **S2P0** and **S0P0**, only the first, **S2P1**, forms a coherent accretion stream. The material forming the steam itself can only be followed to within 1.5 R_* of the stellar surface, as the simulation in this region is held constant to ensure the wind is initialised properly (see Section 7.2.6.3). To overcome this, model **S2P1** was also simulated using a statically refined spherical polar grid, allowing material to be traced all the way down to the stellar surface. The next sections details the results of both the Cartesian and spherical polar version of model **S2P1**, starting with the mass lost by the two bodies and a consideration of the possible transfer of mass from one body to the other.

7.3.2 Mass-loss

Mass-loss from the star are determined by evaluating equation (7.11) over a surface S encompassing the star. We perform the analysis for the planetary mass-loss in the same manner and the results for both are plotted in Fig. 7.4.

The stellar mass-loss profile exhibits fluctuations after $\sim$ 100 ks which continue to the end of the simulation with $\dot{M}_* \sim 10^{12}$ g/s. in the HJ case $\dot{M}_\circ$ is virtually static throughout the simulation at $\dot{M}_\circ = 4.6 \times 10^{11}$ g/s. The explanation for the lack of fluctuating HJ mass-loss is that, within the immediate vicinity of the HJ, the planetary wind is entirely dominant and radially outward, with no material form the stellar wind approaching the surface S where $\dot{M}_\circ$ is calculated.

Calculation of both $\dot{M}_*$ and $\dot{M}_\circ$ is conducted above the stellar or planetary surface to avoid boundary condition effects. Therefore, the fluctuation in the $\dot{M}_*$ profile does not necessarily correspond to planetary material accreting directly on to the stellar surface (see in Section 7.3.4 for the calculation of this quantity). Material can be swept back by the stellar wind before making contact and the stellar wind can be stalled by the incoming HJ material. As the magnitude of the fluctuations are not of the order of the HJ mass-loss rate, there is some other form of iteration accounting for this variability.

7.3.3 Inner magnetosphere

To assess the exact position and extent of the accretion in model **S2P1**, a spherical polar grid is employed allowing the stellar surface to be a dynamic region in the simulation rather than a static boundary as is the case in the Cartesian version of the model.

Fig. 7.5 illustrates the expansion of planetary atmospheric material into the inner magnetosphere of the star. By using the passive scalars to select only the planetary wind, it can be seen that arcing material makes fall on the stellar surface ahead of the planet's orbit. The planet can not be seen in this image as it is embedded in the cloud of material in the background, behind the star which is the yellow sphere at the centre of the image.

Stellar magnetic field lines are either drawn open and contorted by the wind to form a spiral structure or remain closed and retain their dipolar structure. The division between these two regions is a function of the stellar wind ram-pressure and strength of the stellar dipole. At equilibrium, there exists a latitudinal angle specifying the transition between

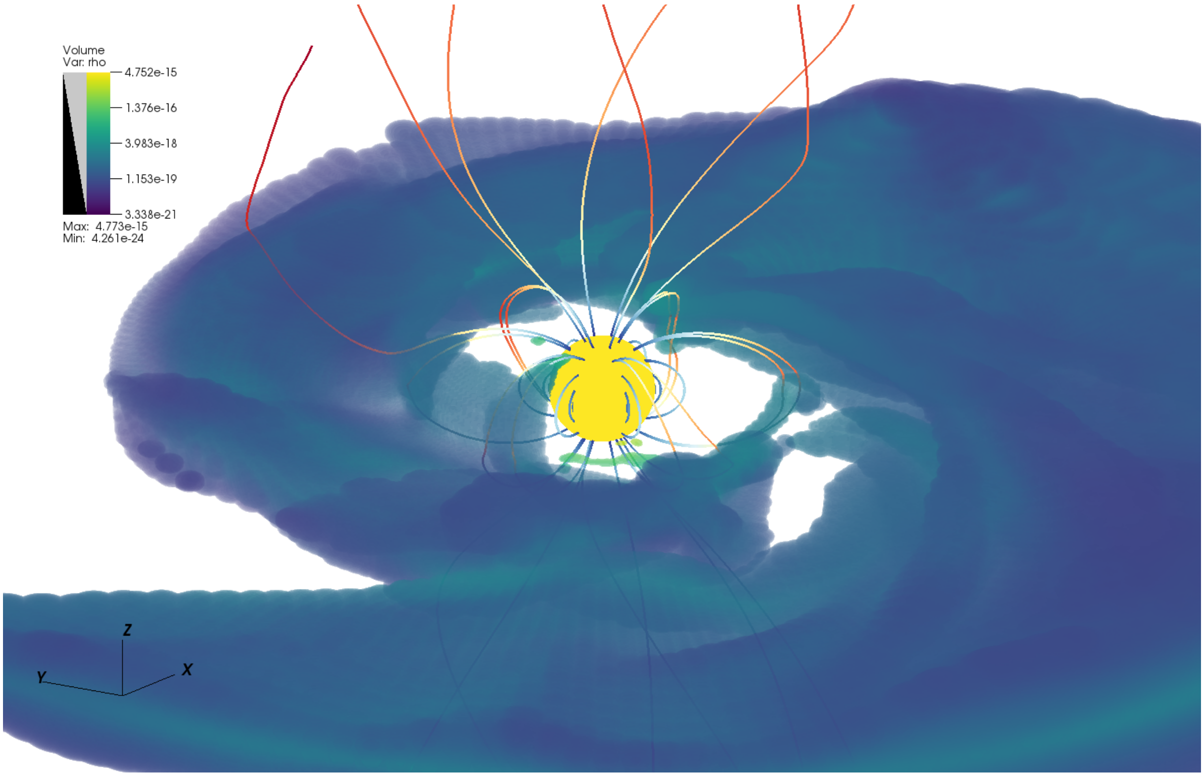

Figure 7.5: Volume rendering of the interaction between planetary mass-loss and the magnetic field of the host star. The planet is embedded in the cloud of material in the background, behind the star which is the yellow sphere at the centre of the image. Magnetic field lines originating in the polar regions of the stellar surface are drawn open and contorted by the wind to form a spiral structure, while field lines in the equatorial region remain closed. The field line colour scheme represents the strength of the magnetic field, from stronger field (blue) to weaker field (dark red).

open and closed field lines and is given by

$$\sin^2\left(\Theta_{\mathrm{m}}\right) = \frac{R_*}{r_{\mathrm{m}}}. \tag{7.12}$$

Where R_* is the stellar radius, r_{m} is the radial distance from the centre of the star to the apex of the longest closed field line and Θ_{m} is the corresponding angle between the z-axis and the point where the longest field line makes contact with the surface (Jardine et al., 2006). Equation (7.12) assumes no deformation of the field lines due to either stellar rotation or gas motion, an assumption which is largely accurate in the innermost region ($< 1.5 R_*$ above the stellar surface) of the magnetosphere (see below). A physically motivated estimate for r_{m} is needed in order to use equation (7.12). Jardine et al. (2006) describe a model in which gas pressure is balanced with magnetic pressure to provide a parameterised estimate for r_{m} for a T Tauri stellar magnetosphere (although the model is general for stellar magnetospheres). In the context of the present study, we can estimate this radius via visual inspection of Fig. 7.5 and 7.6. From this we will assume for simplicity $r_{\mathrm{m}} = 3\ R_*$, yielding a latitudinal angle of 55°. This angle will be compared directly to the accretion latitude from the simulations.

Planetary material in Fig. 7.5 can be seen spiralling into the stellar magnetosphere from the planetary orbital radius, this material then interacts with the closed field lines where magnetic tension acts to support the material. It is then confined to follow these field lines down to the stellar surface. Therefore, the position where these closed field lines intersect the stellar surface determines the exact location where planetary material makes foot-fall and therefore the exact surface position at which accretion takes place (see Section 7.3.4).

To further investigate the interplay between the accreting planetary material and the magnetic field of the star, we plot the planetary material and magnetic field lines in a region directly above the stellar surface. Fig. 7.6 shows this interplay. Magnetic field lines are coloured according to the strength of magnetic tension, given by $|\left(\mathbf{B}\cdot\nabla\right)\mathbf{B}/4\pi|$,

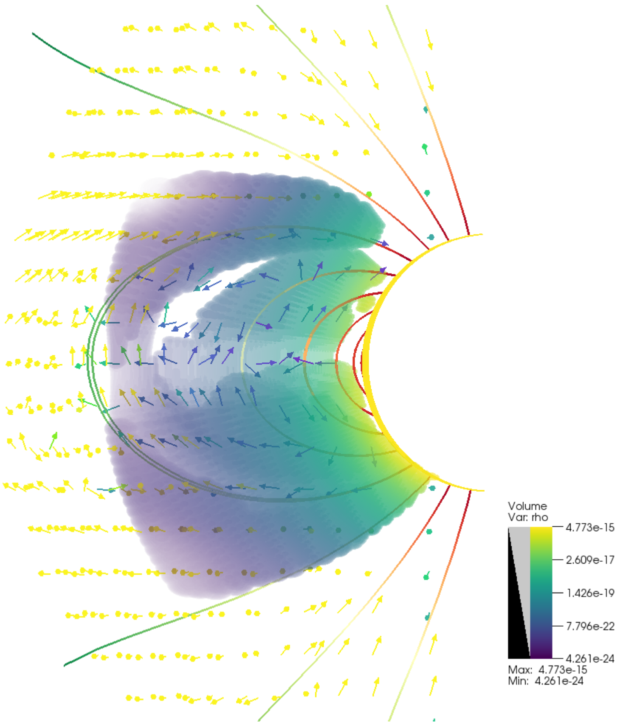

Figure 7.6: Volume rendering of the density of planetary material suspended in the magnetosphere of the star. magnetic field lines are coloured to indicate the magnitude of magnetic tension. Field lines close to the stellar surface exhibit the strongest tension and are therefore experience the smallest perturbation away from the initial dipole. The material structure and velocity vectors can clearly be seen to form arcs corresponding to the field lines, with arrows pointing along filed lines. This indicates that material close to the stellar surface is dominated by magnetic pressure. What is shown is material where the n_{pass} concentration is above 1%.

which acts to restore the magnetic field lines to the lowest energy configuration. In the case of a pure dipole, the magnetic tension is balanced by magnetic pressure resulting in a force free field. For the star in our simulations, this dipole structure is largely preserved out to the Alfvén surface. Beyond this, the field is drawn open by the expanding stellar wind.

Stellar rotation also acts to warp field lines, this acts in the ϕ-direction and laterally stresses the field line. As can be seen in Fig. 7.6 and at a larger scale in Fig. 7.5. This effect grows as the radial distance form the star increases, as field lines which protrude further into the wind are azimuthally contorted to a greater degree. Velocity arrows are annotated in Fig. 7.6 to illustrate the direction of material. In the equatorial region, the velocity is directed along the field lines.

The net effect of the stellar magnetic field is to guide the incoming planetary material towards the stellar poles rather than to accrete directly onto the equatorial region. This is consistent with the frozen in condition of ideal MHD. increasing the stellar dipole strength will lead to accretion at higher latitude and inversely, weaker dipole strength will lead to accretion at lower latitude, in agreement with equation (7.12). If non-ideal plasma physics are incorporated, such as resistivity or other dissipative mechanisms, then a departure from this behaviour maybe seen.

Our results are consistent with simulations conducted by Long et al. (2007) who investigated the accretion of protoplanetary disc material onto the magnetospheres of dipole and non-dipole early type low mass stars. Long et al. (2007) find that the accretion occurs in predominately ring like patterns, parallel to the equator or individual spots close to the poles. The precise pattern of accretion which occurs in our study is described in the next section.

7.3.4 Stellar surface evolution

In the following sections, when referring to locations on the stellar surface, latitude and longitude are given as θ and ϕ and a distinction is made from the spherical grid coordinates used in Section 7.2.6, by following the angle with compass directions. For example, the position $\theta = 30°$N and $\phi = 40°$E refers to the point on the stellar surface which is both 30° above and 40° ahead of the subplanetary point.

Fig. 7.7 and 7.8 depict the stellar surface at time $t = 417.3$ ks (the final time of the simulation), in orthographic form for both the complete surface and the region in which planetary n_{pass} are present. ρ, T, $v_{\rm r}$ and $B_{\rm r}$ show the impact of the accreting material, resulting in a departure from the ambient stellar surface conditions. The location of accretion is displayed in the right hand column. Here, the accretion point is located at approximately $\phi = 133°$W and $\theta = 53°$S. This shows that the accretion stream loops almost completely around the star before making contact. This stellar surface position differs from results found by Pillitteri et al. (2015) who conducted a limited simulation to provide a physical mechanism in support of observational evidence for SPMI. In their study, an accretion stream, which makes contact with the stellar surface at $\phi \sim 70°$E, is described in detail including a knee like structure where the stream is swept back in, counter to the orbital direction. This is due to the slower rotation of the star compared to the orbital rotation of the planet they simulate. However, as the star in our simulation rotates at the same frequency as that of the orbit, the inner accretion stream does not experience the drag which Pillitteri et al. (2015) describe and no knee feature develops, as can be see in the features of the right hand column of Fig. 7.3. This indicates that the precise location of the accretion spot is strongly influenced by the rotation of the star itself. A more detailed comparison with this study is discussed in Section 7.3.5.

The largest perturbation to the stellar surface quantities actually occurs ahead of the accretion point, outside the region marked by the passive scalers. This feature has the highest density and temperature and lowest radial velocity on the stellar surface. A possible explanation is that as the accretion stream approaches the stellar surface it pushes ahead of it a bow shock of stellar wind material and that the most significant perturbation to the surface is in fact of stellar origin via interaction with HJ material.

As previously stated, the highest concentration of accreting material is found $\phi = 133°$W

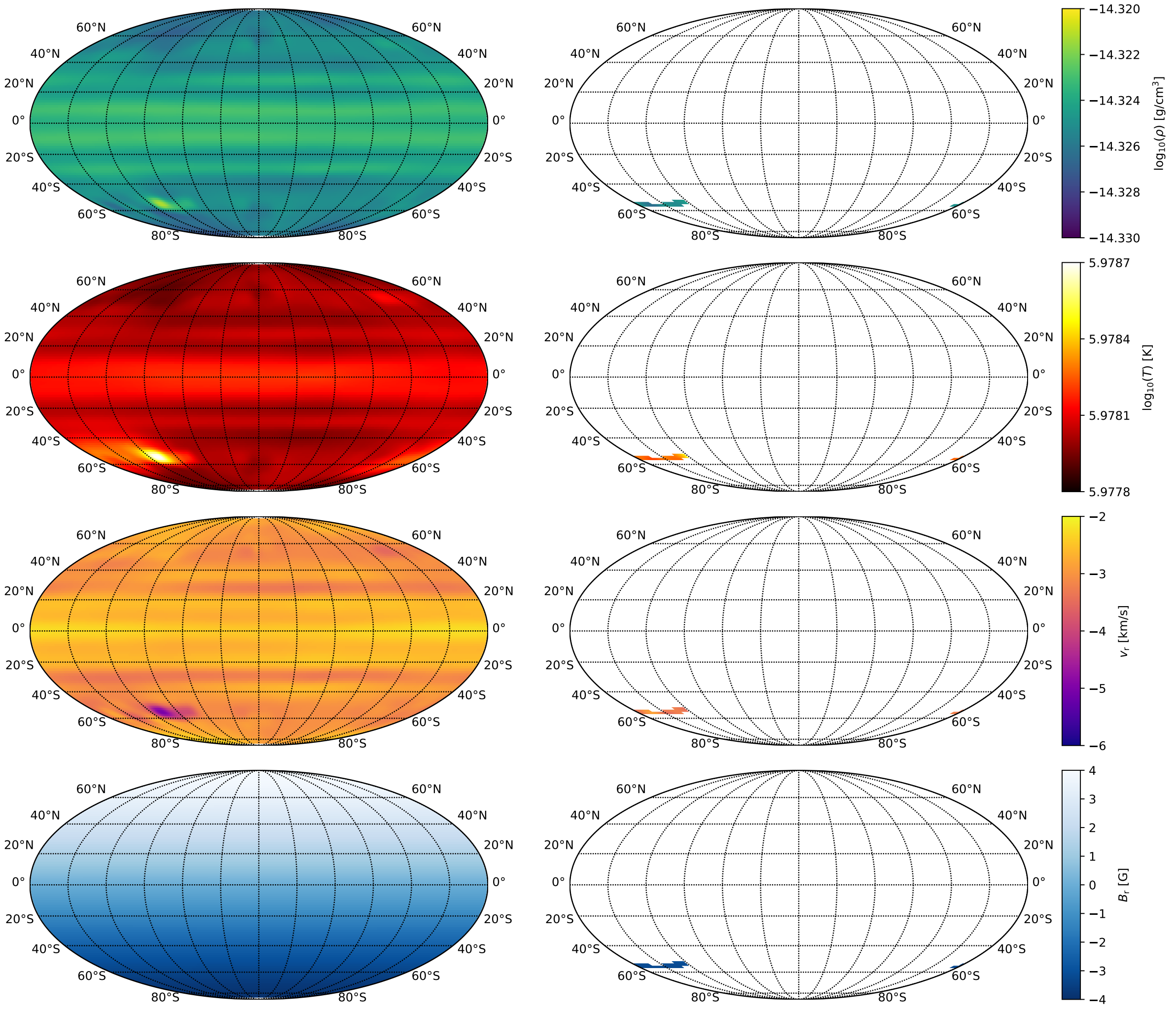

Figure 7.7: Left column: stellar surface values for ρ, T, $v_{\rm r}$ and $B_{\rm r}$. This column shows the total material, both from the stellar and planetary winds. Right column: planetary wind values only; the regions displaying data are where n_{pass} are present. Lines of latitude and longitude mark equal distances on the stellar surface (20° in latitude and 30° in longitude). Zero latitude and zero longitude corresponds to sub-planetary position, the centre of each plot. The extrema of longitude are the opposite side of the star. Not only do the n_{pass} show what the magnitude of the accreting quantities, but also the spacial location at which the accretion takes place; $\phi = 133°$W and $\theta = 53°$S.

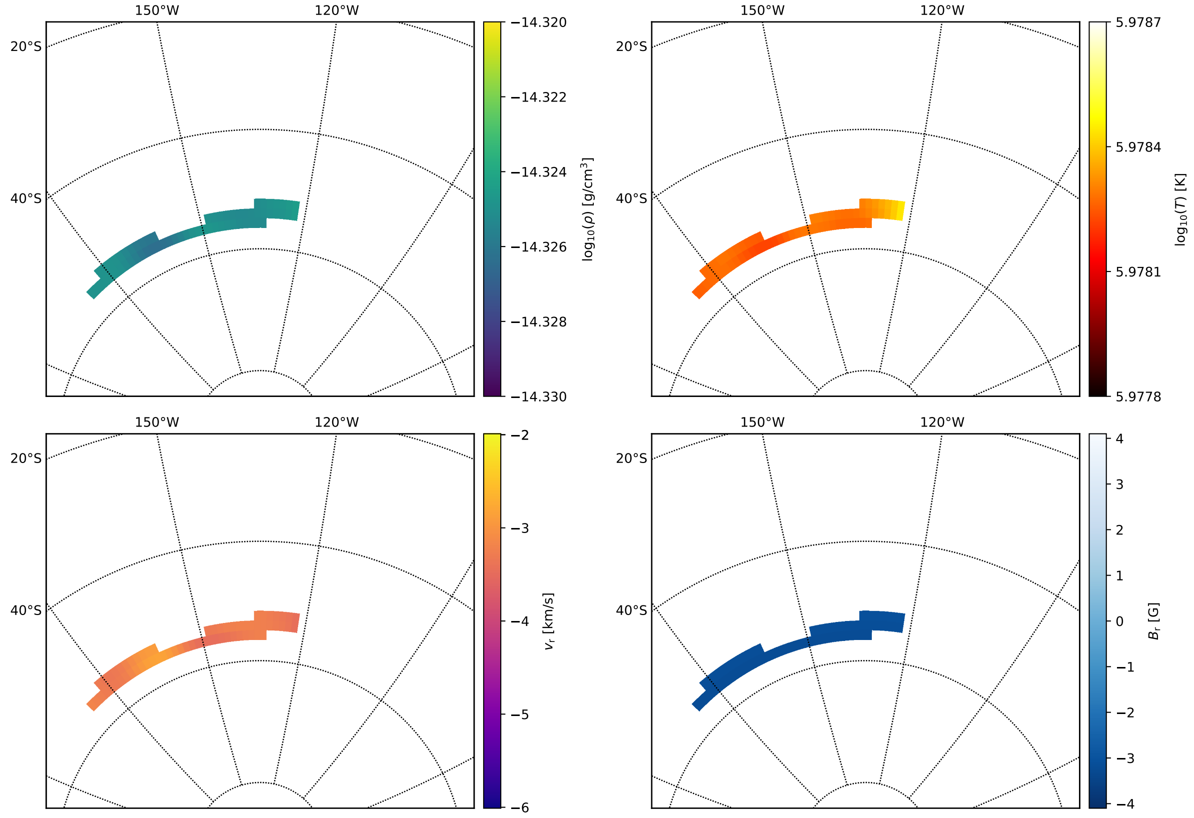

Figure 7.8: Close up of the accretion point located at $\phi = 133°$ behind the sub-planetary point and $\theta = -53°$ below the orbital plane. Starting at top left and going clockwise, the plots are ρ, T, $v_{\rm r}$ and $B_{\rm r}$. The accretion point resembles a narrow strip and less like a spot. The cutoff for n_{pass} is conservative and one should assume that the accretion region extends beyond this strip, however, we exclude regions where the n_{pass} concentration is less than 1% of the planetary surface concentration.

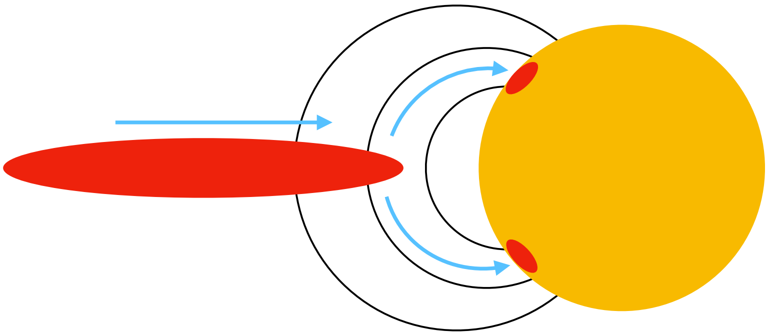

Figure 7.9: Cartoon illustrating the motion and position of incoming accreting material. The thin accretion stream makes its way into the outer magnetosphere remaining coherent until interacting with the closed field lines close to the stellar surface, here the magnetic tension consts the incoming material to follow magnetic field lines down to the stellar surface. The precise location of which will depend on the local plasma-β value.

of the sub planetary point and $\theta = 53°\mathrm{S}$ below the orbital plane. This value is in good agreement with the predicted value of $\Theta_{\mathrm{m}} = 55°\mathrm{N/S}$ (either north or south) from Section 7.3.3, equation (7.12) and therefore our estimate of $r_{\mathrm{m}} = 3\ R_*$.

To further illustrate the trajectory of the accreting planetary material, Fig. 7.9 shows a cartoon diagram of the motion as it enters the stellar magnetosphere and interacts with the field lines for model **S2P1**. The thin accretion stream remains coherent as it approaches the stellar surface, at a given point the gas ram pressure of the accretion stream is balanced by the magnetic pressure of the magnetosphere. At this point material is confined to follow the stellar magnetic field lines down to the surface, resulting in the accretion spot seen in Fig. 7.7 and 7.8 at the latitude given by equation (7.12).

Both Fig. 7.9 and equation (7.12) predict that accretion should take place on both the northern and southern hemispheres simultaneously, they are symmetric about the equator. As we only see accretion on the southern hemisphere in our simulation we can conclude that the symmetry is broken by dynamic properties of the MHD flow.

The coordinates of the accretion spot stated above are instantaneous and capture no information about the intermittent nature of the accretion or how its spacial location changes. To determine this, both the flux of accreted material and the accretion coordinates are plotted as a function of time. This allows us to make quantitative statements about the impact of the accretion stream on the stellar surface and possible observable signatures.

To achieve this, we take the ambient surface condition from the early stages of the simulation, when the stellar surface has relaxed from a Parker wind to a magnetospheric configuration but no planetary material has yet interacted with the surface. This average, ambient stellar surface is then used to normalise the density and temperature in the accretion spot with the result being the over or under density and temperature of the spot, giving the net effect of the planetary accretion stream. The normalised values can therefore be thought of as the percentage increase (or decrease) in surface fluid quantities due to the action of accreting planetary material.

Beginning at 207 ks, when accretion commences, the evolution of the spot latitude, longitude, size and the normalised quantities, along with the average radial velocity and magnetic field in the spot are plotted in Fig. 7.10.

From Fig. 7.10 we can make some attempt to quantify the stability of the accretion stream. We can see that while the latitude of accretion is stable at $\sim 50°$S, the longitude processes round the star from $\sim 138°$E to $\sim 133°$W, with a sudden jump from positive to negative as the spot crosses the point opposite the stellar sphere from the sub-planetary point. The spot size undergoes a periodic variation between $5 \times 10^{-4}\ A_*$ and $3 \times 10^{-3}\ A_*$, where A_* is the stellar surface area, indicating a pulsing in the accretion rate and a periodicity in the stream stability of 67 ks (taking the peak to peak value of the maxima). This variation however only last for two maxima and one minima before the simulation ends, as such it is unclear whether this will continue.

The average quantities over the final 50 ks are: spot area $= 1.78 \times 10^{-3}\ A_*$, $\rho_{\rm norm} = 1.02$, $T_{\rm norm} = 0.99$, $v_{\rm r} = -3.66$ km/s, $B_{\rm r} = -3.17$ G and mass-flux $= 1.49 \times 10^{10}$ g/s. $T_{\rm norm}$ and $\rho_{\rm norm}$ are the spot temperature and density normalised by the stellar surface values without accretion; allowing us to determine the extent to which the stellar surface is perturbed by accretion.

The spot temperature being 99% of the stellar wind temperature is consistent with

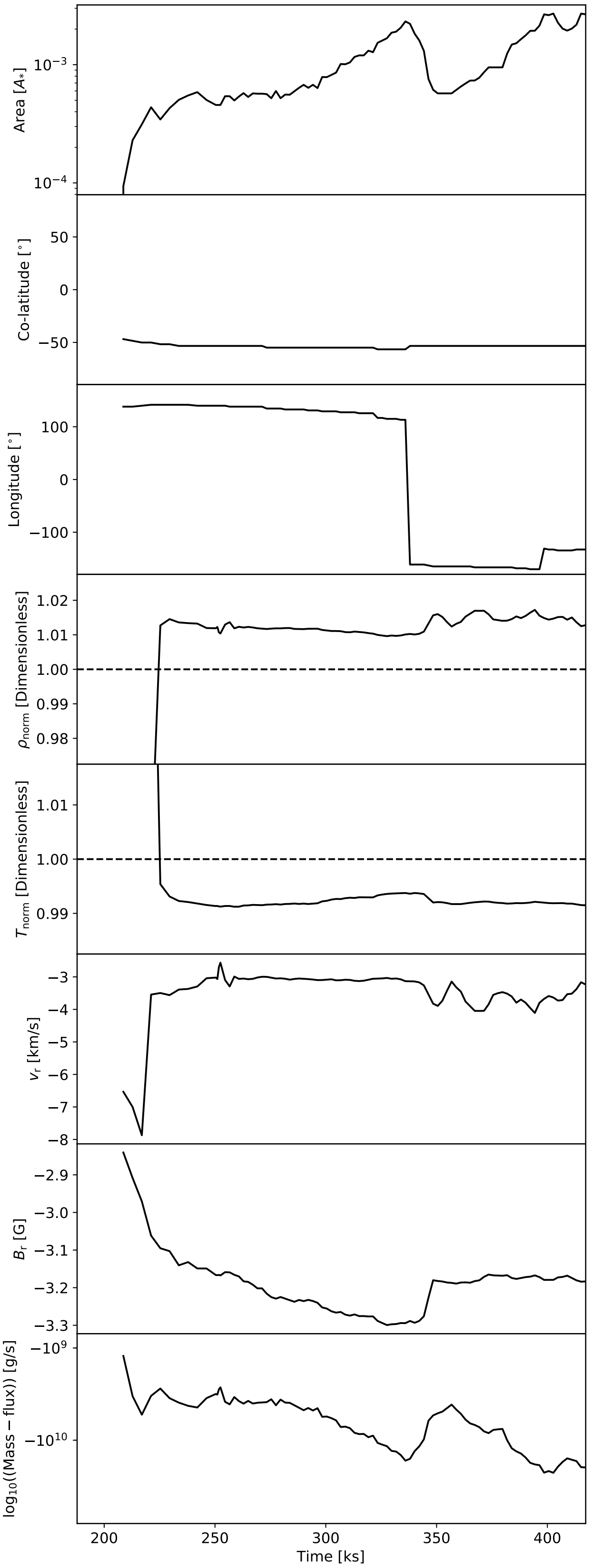

Figure 7.10: From top to bottom, accretion spot size, location, fluid quantities ρ, T, v_{r}, B_{r} and Mass-flux through spot. Accretion begins at 207 ks. ρ and T are normalised to the base, ambient values. The average quantities over the final 50 ks of the simulation are: Spot Area $= 1.78 \times 10^{-3}\, A_*$, $\rho_{\mathrm{norm}} = 1.02$, $T_{\mathrm{norm}} = 0.99$, $v_{\mathrm{r}} = -\,3.66$ km/s, $B_{\mathrm{r}} = -\,3.17$ G and $\mathrm{Mass-flux} = -\,1.49 \times 10^{10}$ g/s.

the threshold passive scaler concentration of 1% used to separate the HJ and stellar material. As the simulation is quasi-isothermal, this indicates there is a large amount of mixing between the stellar and planetary winds. This together with the very small velocity values (in comparison to the stellar escape velocity ∼ 100 km/s) implies that the accreting HJ material slowly sinks rather than free-falls to the stellar surface.

Of the above quantities, the only one to exhibit large fluctuations is the spot size, the average density remains approximately constant at 1% above ambient density, implying that the accretion stream feeds material to the stellar surface at a constant density despite the variability in the size of the accretion spot. Together they result in the time-varying Mass-flux seen in the bottom plot of Fig. 7.10 with the same period as the accretion spot size. The negative Mass-flux indicates that material is flowing into the star, see Section 7.2.5. If we compare this mass-flux to the mass-loss of the planet, we find that the mass-flux is 3.2% of the planetary mass-loss. This is in marked contrast to the crude estimate of 50% based on the planets proximity to the L_1 and L_2 points made in Section 7.2.3. The remaining 46.8% must interact with the stellar wind in such a manner that it is eventually removed form the inner Roche potential and out to the outer simulation boundary.

Finally, to gain a global perspective of the motion of the accretion material described above, we use the approach of ud-Doula et al. (2008) and ud-Doula et al. (2013) to calculate the time-dependent radial distribution of mass via the following equation:

$$\frac{\mathrm{d}m\left(r,t\right)}{\mathrm{d}r} = r^2 \int_0^{2\pi} \int_{\frac{3}{4}\pi}^{\frac{1}{4}\pi} \rho\left(r,\theta,\phi,t\right)\sin(\theta)\mathrm{d}\theta\mathrm{d}\phi. \tag{7.13}$$

Here r, θ and ϕ are the three spherical polar coordinates and $\rho\left(r,\theta,\phi,t\right)$ is the density distribution. By integrating $\rho\left(r,\theta,\phi,t\right)$ first over θ between the limits $\frac{1}{4}\pi$ and $\frac{3}{4}\pi$ and then over ϕ in the full azimuthal range $0 \rightarrow 2\pi$, we are left with $\mathrm{d}m\left(r,t\right)/\mathrm{d}r$ which is the radial distribution of mass for a given time t. by calculating equation (7.13) for each simulation snapshot, we build a picture of the global radial motion of mass. $\mathrm{d}m\left(r,t\right)/\mathrm{d}r$

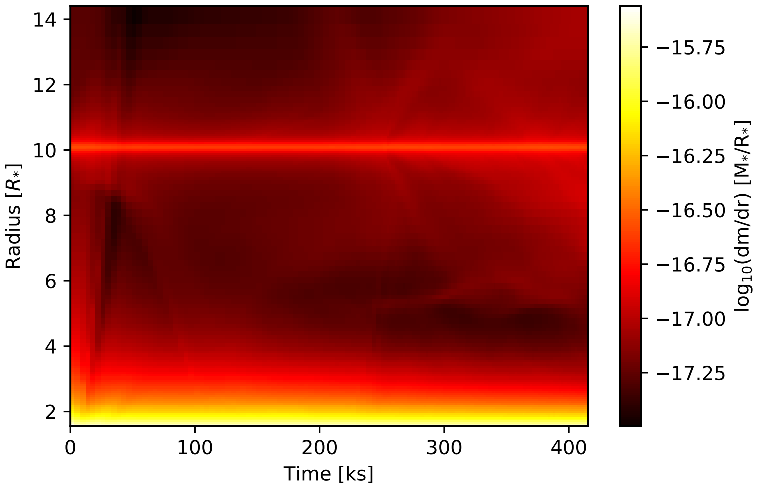

Figure 7.11: Time-dependency of the radial mass distribution, $\mathrm{d}m\,(r,t)\,/\mathrm{d}r$. Two features at 1 R_* and 10 R_* are the stellar surface and planet respectively. The majority of the material in the system is stationary with respect to time. Faint features are however apparent and represent motion towards or away from the stellar surface.

is plotted in Fig. 7.11 in units of $[M_*/R_*]$. Any features whose radial distance changes with time are an indication of net flows either away or toward the stellar surface. Two features are immediately apparent at 1 R_* and 10 R_* and are the stellar surface and planet respectively. As most features remain at constant radius and there is no distinctive change at 207 ks, when accretion commences we can conclude that the majority of material is not involved in the accretion process.

The next section will evaluate these results in the context of existing literature and observations.

7.3.5 Implications for observable signatures

Cranmer & Saar (2007) conducted theoretical work modelling SPMI between a HJ and a solar type star. Their work predicted that the precise nature of the accretion spot will vary from cycle to cycle if the star both rotates at a different frequency to the orbit and if the stars magnetic geometry is non-cylindrically symmetric, for example an oblique dipole or quadrupole, result in the predicted light curve not repeating exactly.

Shkolnik et al. (2008) report that SPI is intermittent and mimics cyclic variability of the host star and characterise this as the on/off nature of SPI. A striking result from the observations of Shkolnik et al. (2008) is that the leading longitude of activity seen on the stellar surface, attributed to the action of the HJ, is at a longitude of $\phi \sim 70°$E for HD 189733, HD 179949 and τ Boo, three out of their seven targets. For the latter, this phase is preserved over 5 yr implying steady SPI over this time-period. However, without knowing the mass loss rates of the targets, it is difficult to determine whether the form of SPI is due to direct magnetic connection between star and planet or due to an accretion stream.

Based on our results for the accretion spot location and the evolution of the spot size, the on/off nature of the planetary accretion described by Shkolnik et al. (2008) maybe attributed to the accretion stream either pulsing in size or precessing round the star to be out of phase with the planet's orbit or being obscured to the observer.

All the planets studied by Shkolnik et al. (2008) are orbiting within the Alfvén surface of their host stars. The planets in our models are all orbiting outside the Alfvén surface and therefore in the super Alfvénic region of the stellar wind. As such we classify our simulated systems as interacting via SPWI rather than SPMI. This is an important distinction as magnetic perturbations induced at the planetary orbit are unable to travel back to the stellar surface. This means that there is no heating of the stellar surface due to directly connected field lines between the star and the planet.

The HJ hosting system HD 189733 has been the focus of a number of studies in the context of SPMI (Fares et al., 2010; Majeau et al., 2012; Pillitteri et al., 2015) observational and via MHD simulations. The system serves as an example of the complexity involved in studying SPMI systems. Fares et al. (2010) investigate the system using spectropolarimetry and reconstruct the magnetic map of the stellar surface with the result that it has a predominately toroidal surface magnetic field with a strength up to 40 G (a departure from the simple dipole used in the present study). They conclude that stellar activity is mainly modulated by stellar rotation and find no evident of SPMI.

For the HJ, HD 189733 b, Majeau et al. (2012) reconstruct a secondary eclipse map of the surface and allow them to deduce that the planet has both small obliquity and atmospheric winds which circulate in the atmosphere, described as *super-rotating* winds.

More recently Pillitteri et al. (2015) studied this system with the Cosmic Origins Spectrograph on board Hubble Space Telescope (HST) and supported their observations with MHD simulation based on the work by Matsakos et al. (2015) and hence are similar in nature to those conducted here. Their observations show a high degree of variability in emission lines in Si, C, N, and O. They deduce that this enhanced activity is directly a consequence of the planetary material accreting onto the stellar surface. The point of accretion is inferred to be between longitudes $70° - 90°$E. Their simulations are however hampered by the numerical prescription which restricts the dynamic evolution of the simulation to be no closer than 1.5 R_* to the stellar surface and therefore the precise location of the accretion spot on the surface is unknown, a limitation not exhibited by the work presented here. The location of our accretion spot, $\phi = 133°$W, does not agree with their reported position. The difference can be attributed to the fact that our planetary and stellar parameters are not the same as HJ, HD 189733 b and while a similar accretion longitude is reported for HD 179949 and τ Boo, there remains several factors which could lead to the difference. Firstly the rotational rate of HD 189733 is slower than the orbital rotation leading to the a swept back accretion stream as it interacts with the slower rotating stellar wind in the inner magnetosphere, a property our simulations lack due to the fixed rotational rate. Secondly, the shorter orbital period of the HD 189733 b makes the distance travelled by the accretion stream shorter and the stream would also have less AM. This reduced arc distance would result in a trajectory for the accretion stream that would bring it close to the inner stellar magnetosphere just ahead of the sub-planetary point, as seen in their observations.

The SPMI occurring in HD 189733 is attributed to two different physical processes by Shkolnik et al. (2008) and Pillitteri et al. (2015). For the former, SPMI is via direct magnetic field line connection between the stellar and HJ magnetospheres. Such interaction have been modelled by Strugarek et al. (2015b); Strugarek (2016). As has already been discussed, Pillitteri et al. (2015) attribute the interaction to an accretion stream from the HJ to the star, the same form of interaction as our models, SPWI.

The accretion spot quantities presented in Fig. 7.10 provide the necessary detail to calculate the resulting observable signatures of the SPWI. The enhanced density and reduced temperature will lead to absorption and emission features that differ from those of the ambient stellar surface. The precise enhancements due to the accretion stream we simulate will also increase the surface abundances of metals. The precise values will however be a function of the composition of the HJ wind. However, the magnitude of the surface perturbation to both the density and temperature make detection unlikely. This is especially problematic for observations of spectral lines as the accretion spot temperature will result in ionisation of the heavier elements present in the HJ wind.

As our simulations only account for stellar surface increases due to accreting material, enhanced fine grained magnetic behaviour can not be captured and only large scale perturbations to the stellar dipole are present and, as we have discussed in Section 7.3.3, negligible. As such heating due to magnetic effects are not captured and could account for the decrease in surface temperature in the accretion spot.

Calculating specific observable signatures is however beyond the scope of this study, as our initial intention was to determine the nature of the accretion stream, specifically the stellar surface location and to demonstrate that a stable bridge of material between the two bodies can be formed.

7.4 Conclusions

We have simulated a suite of mixed geometry, high resolution 3D MHD simulations which characterise the behaviour of interacting stellar and planetary wind material in the context of SPWI for a representative HJ hosting system.

Our results show that the pressence of a planetary magnetic field plays a central role in forming accretion streams between the star and HJ and that the nature of the accretion is variable both in location and in rate. The leading longitude of accretion in our simulation, $\phi \sim 133°$W, differs from reports in the literature which suggest a stable $\phi \sim 70°$E for a number of systems. This difference is attributed to specifics of the HJ system parameters. The accretion spot itself has been found to vary between occupying 0.05% to 0.3% of the stellar surface, a variation with a period of 67 ks. Within the spot there is a 1% decrease in temperature and 2% increase in surface density. We predict this perturbation will lead to negligible observational signatures in spectral lines, as the temperature profile will ionise heavier elements. This is not in agreement with Pillitteri et al. (2015). We have illustrated that magnetic fields cannot be ignored as the relatively modest field strengths used in our three models have lead to a dramatic difference in wind structure and determine the establishment of the accretion stream itself.

This difference in behaviour indicates that the establishment of an accretion stream is highly dependent upon the magnetic field of both the HJ and the host. While in all cases SPWI occurs and there are unique fluid features in the inter planetary medium due to SPWI, the accretion stream itself appears to require aligned dipole-dipole combination. The authors acknowledge that the parameter space investigated in the present study is limited and further modelling is required to draw more precise conclusions.

The authors intend to further expand the theoretical basis for SPWI and the role stellar and planetary magnetic fields play in shaping its behaviour through the study of two specific HJ systems which directly compares SPMI with SPWI. This can be done by selecting a HJ whose orbit lies within its host's Alfvén surface and one which lies outside.

There are now multiple HJ hosting systems exhibiting SPMI and little numerical modelling of specific systems. A concerted effort to systematically model these systems and deduce the stellar surface signatures of SPMI would allow for the classification and parameterisation of many HJ properties which remain ill constrained such as the nature of their magnetic fields.

8

Thesis summary and conclusions

"Yeah well... y'know... that's just like, err... your opinion man...."

– The Dude (Jeff Bridges), *The Big Lebowski*

8.1 Thesis summary

Understanding the winds of hot massive stars and hot giant planets provides us with a mechanism for understanding how the interstellar medium is enriched and the history behind planetary system formation. This thesis presented four related studies of the winds of both these astronomical bodies though the simulation of magnetised and non-magnetised massive star winds and the star-planet interactions of solar type stars and their hosted hot Jupiter (HJ) type exoplanets.

In the case of non-magnetised massive star winds, investigated in Chapter 4, I have found that the spectral index, α, is not constant in the Atacama Large Millimeter Array (ALMA) frequency range due to the effect of wind acceleration.

If the stellar wind is clumped, then the spectral flux, S_ν, is modified in the same manner as in the case of wind acceleration. At ALMA wavelengths this effect leads to a degeneracy between clumped and smooth wind models even when different velocity laws are considered. However, as there is sparse data at the frequencies considered in this study, the degeneracy between models can be lifted, especially with observational data from within the ALMA range (100 GHz $< \nu <$ 1000 GHz) is required.

Building on the non-magnetised stellar wind models presented in Chapter 5, a 3D isothermal Magnetohydrodynamics (MHD) simulation of a magnetic rotating massive star has been conducted. This simulated star was given a non-zero dipole obliquity, a feature which leads to the breakdown of symmetry. From this simulation, the radio/sub-mm radio light curves and continuum spectra have been predicted for frequencies within the ALMA range. From this synthetic radio emission an inferred mass-loss rate has been derived. A strong dependence on inclination and phase has been found for both the synthetic spectral flux and corresponding inferred mass-loss rate, which variability of factors between 2 and 3 over a stellar rotation. Such variability illustrates the importance of modelling non-symmetric winds. The gradient of S_ν, known as the spectral index, can be approximated as having a constant value in the low frequency range ($\nu < 10^3$ GHz). At higher frequencies ($\nu > 10^3$ GHz) this assumption breaks down and a non-constant spectral index needs to be accounted for.

Thermal emission dominated the discussion of massive stars due to the high density found in their winds. In the case of hot Jupiters (HJs) and their host systems, the density is 4 orders of magnitude lower and as such, thermal emission from these systems is negligible. Non-thermal emission due to magnetic interactions are however a viable route to observing these systems as radio emission due to the Electron Cyclotron Maser Instability (ECMI) process in HJ exoplanets is expected to be considerable. However, to the contrary of numerous theoretical works, no repeatable detections have been made to date. I explored this emission mechanism in Chapter 6 through the use of MHD simulations which I applied to the global evolution and the circumplanetary environment of a HJ hosting system via rigorous treatment of both the stellar and planetary winds and magnetic field. This allowed me to to determine the efficiency of the ECMI process at producing detectable radio emission. The frequency of emission has been determined to be in the range 3.88 MHz $< \nu_{\rm ce} <$ 5.60 MHz for a HJ with a 1 G equatorial magnetic field.

Both the Earth's ionospheric cutoff frequency and detection limits of current instruments are above this range. However, HJs with field strength larger than 1 G may result in emission above this cut-off point. Whether the frequency range is detectable on earth or not, the ECMI process is completely inhibited by the expanding HJ atmosphere. A considerably larger magnetic field than that employed here would be needed for such an exoplanet to produce detectable emission. Results presented in Chapter 6 do not rule out radio emission from HJs which experience energetic or transient events such as a Coronal Mass Ejection (CME) or reconnection events.

HJ radio emission via ECMI is one form of Star-Planet Interaction (SPI) and a possible important observable signature, but there is also a range of other possible SPI types. In HJ systems the expanding planetary atmosphere can, if the planetary mass-loss is sufficient, form magnetised density structures which interact directly with the surface of the host star.

In Chapter 7, I pursued this paradigm as a possible signature of SPI via a suite of high resolution 3D MHD simulations, characterising the behaviour of interacting stellar and planetary wind material in the context of a representative HJ hosting system and distinguish this type SPI as Star-Planet Wind Interaction (SPWI).

Accretion between the HJ and the host star was found to be highly dependent on the presence of magnetic fields in both objects. The longitudinal location of accretion was found to differ from report in the literature. Instead of accreting at $\phi \sim 70°$E, which has been reported for a number of HJ hosting systems, the accretion occurred at $\phi \sim 133°$W and occupied between $\sim 0.05\%$ and 0.3% of the stellar surface with a period of 67 ks. This intermittent stream results in the variation of both temperature and density at the point of accretion. SPWI is found to occur in all models simulated, however the presence of a coherent accretion stream appears to require a dipole-dipole configuration of the stellar and HJ system.

To conclude, the surroundings of hot stars and planets form dynamic environments where magnetic fields, wind ram pressure, radiation and centrifugal forces act to channel material, forming structures that directly lead to observable signatures.

In the case of hot stars, both magnetic and non-magnetic, the spectral index of thermal emission is modified over several dex in frequency, leading to departures from early model predictions. The work here highlights the necessity for encompassing detailed dynamic wind physics when interpreting observations of massive stars conducted at radio/sub-mm frequencies.

Hot planets orbiting solar type stars provide a fertile setting to test theories of planetary characteristics and internal structure models. Previous studies argue that ECMI emission can be used to probe these properties, but, as has been demonstrated, this is not the case for low magnetic field strength HJs. SPWI however, forms an alternative channel, allowing for the indirect observation of the impact of HJs on their host stars. The extent and periodicity of this impact will shed light on many HJ properties which are currently ill constrained.

8.2 Future prospects

To understand observations provided by collaborations such as the Magnetism in Massive Stars (MiMeS) project and the more recent Binary MagnetIc Stars (BinaMIcS) project, a general purpose suite for simulating magnetic massive stars is required and needs to support single and binary magnetic stars and making use of Cartesian numerical grids. Such a suite would overcome the limitations described in Chapter 5 concerning the boundary conditions and allow for lifting the isothermal limitation.

Large scale simulations of hot Jupiter systems are currently limited by crude planetary atmosphere models, in which planetary outflow is imposed analytically rather than calculated self-consistently; such models are employed in Chapters 6 and 7. For simulations to compliment the high quality data coming from mission such as Kepler 2 (K2) and Transiting Exoplanet Survey Satellite (TESS), atmosphere models developed to study small scale dynamics need to be paired with large scale global star-planet interaction simulations. The synergy between these two branches of planetary study will lead to a greatly enhanced understanding of the star-planet interaction paradigm.

The interaction of CME with the extended planetary magnetosphere of hot Jupiters is an important transient event, which will produce distinct observational signatures such as the amplification of the ECMI process. It has been demonstrated in the literature that the inclusion of a non-constant stellar wind, or space weather, as well as CME is important to fully capture exoplanet environments (Nicholson et al., 2016). Developing a prescription for including stellar CME in simulations to study their interaction with an exoplanetary atmosphere will be a vital step towards realistic simulations of in situ HJs.

Finally, current simulations are almost exclusively limited to two-body systems in which the exoplanet is constrained to move in a circular orbit. Projecting into the future, simulations will need to employ the flexibility allowed by the novel non-fixed grid methods, described in Chapter 3, to investigate the role of orbital eccentricity, binary host stars, and exomoons in the dynamical evolution of exoplanet systems.

References

Abbott D. C., Bieging J. H., Churchwell E., 1981, ApJ, 250, 645

Abbott D. C., Telesco C. M., Wolff S. C., 1984, ApJ, 279, 225

Albrow M. D., et al., 2018, ApJ, 858, 107

Alexander R. D., Wynn G. A., Mohammed H., Nichols J. D., Ercolano B., 2015, MNRAS, 456, 2766

Alvarado-Gómez J. D., Hussain G. A. J., Cohen O., Drake J. J., Garraffo C., Grunhut J., Gombosi T. I., 2016, A&A, 588, A28

Alvarado-Montes J. A., Zuluaga J. I., Sucerquia M., 2017, MNRAS, 471, 3019

Aschwanden M. J., Poland A. I., Rabin D. M., 2001, ARA&A, 39, 175

Baker G. A., 1977, MC, 31, 45

Balsara D. S., Kappeli R., 2018, arXiv:1804.06731

Barlow M. J., Cohen M., 1977, ApJ, 213, 737

Bieging J. H., Abbott D. C., Churchwell E. B., 1989, ApJ, 340, 518

Blomme R., Prinja R. K., Runacres M. C., Colley S., 2002, A&A, 382, 921

Blomme R., van de Steene G. C., Prinja R. K., Runacres M. C., Clark J. S., 2003, A&A, 408, 715

Bonfils X., et al., 2012, A&A, 546, A27

Bouret J.-C., Lanz T., Hillier D. J., 2005, A&A, 438, 301

Bourrier V., Lecavelier des Etangs A., 2013, A&A, 557, A124

Bourrier V., Lecavelier des Etangs A., Ehrenreich D., Tanaka Y. A., Vidotto A. A., 2016, A&A, 591, A121

Braes L. L. E., Habing H. J., Schoenmaker A. A., 1972, Nature, 240, 230

Cantiello M., 2009, PhD thesis, Utrecht University

Cantiello M., et al., 2009, A&A, 499, 279

Carroll-Nellenback J., Frank A., Liu B., Quillen A. C., Blackman E. G., Dobbs-Dixon I., 2017, MNRAS, 466, 2458

Castor J. I., 1974, MNRAS, 169, 279

Castor J. I., Lamers H. J. G. L. M., 1979, ApJS, 39, 481

Castor J. I., Simon T., 1983, ApJ, 265, 304

Castor J. I., Abbott D. C., Klein R. I., 1975, ApJ, 195, 157

Ceverino D., Klypin A., 2009, ApJ, 695, 292

Chadney J., Galand M., Unruh Y., Koskinen T., Sanz-Forcada J., 2015, Icarus, 250, 357

Chang Y.-L., Bodenheimer P. H., Gu P.-G., 2012, ApJ, 757, 118

Clementel N., Madura T. I., Kruip C. J. H., Paardekooper J.-P., Gull T. R., 2015a, MNRAS, 447, 2445

Clementel N., Madura T. I., Kruip C. J. H., Paardekooper J.-P., 2015b, MNRAS, 450, 1388

Cohen M., V. Kuhi L., J. Barlow M., 1975, A&A, 40, 291

Cox N. L. J., et al., 2012, A&A, 537, A35

Cranmer S. R., Owocki S. P., 1995, ApJ, 440, 308

Cranmer S. R., Saar S. H., 2007, arXiv:astro-ph/0702530

Crowther P. A., Hillier D. J., Evans C. J., Fullerton A. W., Marco O. D., Willis A. J., 2002, ApJ, 579, 774

D'Angelo C. V., Esquivel A., Schneiter M., Sgró M. A., 2018, arXiv:1806.02259

Daley-Yates S., Stevens I. R., 2017, Astron. Nachr., 338, 881

Daley-Yates S., Stevens I. R., 2018, MNRAS

Daley-Yates S., Stevens I. R., Crossland T. D., 2016, MNRAS, 463, 2735

Dang L., et al., 2018, Nature Aston., 2, 220

Das B., Chandra P., Wade G. A., 2017, MNRASL, 474, L61

Davidson K., Humphreys R. M., 1997, ARA&A, 35, 1

De Becker M., 2007, A&A Rev, 14, 171

Dedner A., Kemm F., Kröner D., Munz C.-D., Schnitzer T., Wesenberg M., 2002, J. Comput. Phys., 175, 645

Dmitruk P., Matthaeus W. H., Seenu N., 2004, ApJ, 617, 667

Drew J. E., 1989, ApJS, 71, 267

Dulk G. A., 1985, ARA&A, 23, 169

Elmegreen B. G., Elmegreen D. M., 1978, ApJ, 220, 1051

Fall S. M., Krumholz M. R., Matzner C. D., 2010, ApJ, 710, L142

Fambri F., Dumbser M., Zanotti O., 2017, CPC, 220, 297

Fares R., et al., 2010, MNRAS, 406, 409

Fares R., et al., 2017, MNRAS, 471, 1246

Fogg M. J., Nelson R. P., 2005, A&A, 441, 791

Frank A., Jones T. W., Ryu D., Gaalaas J. B., 1996, ApJ, 460, 777

Fryxell B., et al., 2000, ApJS, 131, 273

Gayley K. G., 1995, ApJ, 454, 410

Gayley K. G., 2009, ApJ, 703, 89

Gayley K. G., Owocki S. P., 2000, ApJ, 537, 461

George S. J., Stevens I. R., 2007, MNRAS, 382, 455

Gingold R. A., Monaghan J. J., 1977, MNRAS, 181, 375

Godunov S. K., 1959, MSNS, 47, 271

Grießmeier J.-M., et al., 2004, A&A, 425, 753

Grießmeier J.-M., Zarka P., Spreeuw H., 2007, A&A, 475, 359

Guillet T., Pakmor R., Springel V., Chandrashekar P., Klingenberg C., 2018, arXiv:1806.02343

Guo J. H., 2011, ApJ, 733, 98

Gurdemir L., Redfield S., Cuntz M., 2012, PASA, 29, 141

Harmanec P., 1988, AIC, 39, 329

Harten A., Lax P. D., van Leer B., 1983, SIAMRev, 25, 35

Hebb L., et al., 2009, ApJ, 693, 1920

Hess S. L. G., Zarka P., 2011, A&A, 531, A29

Hillier D. J., Miller D. L., 1999, ApJ, 519, 354

Hopkins P. F., 2015, MNRAS, 450, 53

Hopkins P. F., 2016, MNRAS, 462, 576

Ignace R., 2016, MNRAS, 457, 4123

Intema H. T., van der Tol S., Cotton W. D., Cohen A. S., van Bemmel I. M., Röttgering H. J. A., 2009, A&A, 501, 1185

Jardine M., Cameron A. C., Donati J.-F., Gregory S. G., Wood K., 2006, MNRAS, 367, 917

Karakus A., Chalmers N., Swirydowicz K., Warburton T., 2018, arXiv:1801.00246v2

Kashi A., Soker N., 2010, ApJ, 723, 602

Kee N. D., Owocki S., Sundqvist J. O., 2016, MNRAS, 458, 2323

Khodachenko M. L., Shaikhislamov I. F., Lammer H., Prokopov P. A., 2015, ApJ, 813, 50

Kivelson M., et al., 1997, ASR, 20, 193

Knapp M., Winterhalter D., Lazio J., 2016, in AAS. p. 122.30

Kritsuk A. G., et al., 2011, ApJ, 737, 13

Krtička J., 2014, A&A, 564, A70

Krtička J., Kubát J., 2012, MNRAS, 427, 84

Kulsrud R. M., 2004, Plasma Physics for Astrophysics. Princeton University Press, https://www.ebook.de/de/product/2854976/russell_m_kulsrud_plasma_physics_for_astrophysics.html

Kurapati S., et al., 2016, MNRAS, 465, 2160

Lamers H. J. G. L. M., Cassinelli J. P., 1999, Introduction to Stellar Winds. CAMBRIDGE UNIV PR, https://www.ebook.de/de/product/3779761/henny_j_g_l_m_lamers_joseph_p_cassinelli_introduction_to_stellar_winds.html

Lammer H., Selsis F., Ribas I., Guinan E. F., Bauer S. J., Weiss W. W., 2003, ApJ, 598, L121

Lecavelier des Etangs A., Sirothia S. K., Gopal-Krishna Zarka P., 2013, A&A, 552, A65

Leitherer C., Robert C., 1991, ApJ, 377, 629

Leitherer C., Robert C., Drissen L., 1992, ApJ, 401, 596

Leto P., et al., 2018, MNRAS, 476, 562

Liepmann H. W., Roshko A., 2002, Elements of Gas Dynamics. DOVER PUBN INC, https://www.ebook.de/de/product/3359850/h_w_liepmann_a_roshko_elements_of_gas_dynamics.html

Llama J., Vidotto A. A., Jardine M., Wood K., Fares R., Gombosi T. I., 2013, MNRAS, 436, 2179

Long M., Romanova M. M., Lovelace R. V. E., 2007, MNRAS, 374, 436

Lozinskaya T., 1997, ApSS, 252, 199

Lucy L. B., 1977, AJ, 82, 1013

Lucy L. B., Solomon P. M., 1970, ApJ, 159, 879

Maiz-Apellaniz J., Walborn N. R., Galue H. A., Wei L. H., 2004, ApJS, 151, 103

Majeau C., Agol E., Cowan N. B., 2012, ApJ, 757, L32

Manousakis A., Walter R., 2015, A&A, 584, A25

Manzanero J., Ferrer E., Rubio G., Valero E., 2018, arXiv:1805.10519

Matsakos T., Uribe A., Königl A., 2015, A&A, 578, A6

Matt S., Pudritz R. E., 2008, ApJ, 678, 1109

Mayor M., Queloz D., 1995, Nature, 378, 355

Melrose D. B., Dulk G. A., 1982, ApJ, 259, 844

Mignone A., Tzeferacos P., 2010, J. Comput. Phys., 229, 2117

Mignone A., Bodo G., Massaglia S., Matsakos T., Tesileanu O., Zanni C., Ferrari A., 2007, ApJS, 170, 228

Mignone A., Tzeferacos P., Bodo G., 2010, J. Comput. Phys., 229, 5896

Mignone A., Zanni C., Tzeferacos P., van Straalen B., Colella P., Bodo G., 2012, ApJS, 198, 7

Miller B. P., Gallo E., Wright J. T., Pearson E. G., 2015, ApJ, 799, 163

Miyoshi T., Kusano K., 2005, J. Comput. Phys., 208, 315

Monaghan J. J., 2005, RPP, 68, 1703

Montes G., González R. F., Cantó J., Pérez-Torres M. A., Alberdi A., 2011, A&A, 531, A52

Montes G., Alberdi A., Pérez-Torres M. A., González R. F., 2015, RMAA, 51, 209

Müller P. E., Vink J. S., 2008, A&A, 492, 493

Murphy T., et al., 2014, MNRAS, 446, 2560

Murray-Clay R. A., Chiang E. I., Murray N., 2009, ApJ, 693, 23

Nichols J. D., Milan S. E., 2016, MNRAS, 461, 2353

Nicholson B. A., et al., 2016, MNRAS, 459, 1907

Nordström B., et al., 2004, A&A, 418, 989

Nugis T., Crowther P. A., Willis A. J., 1998, A&A, 333, 969

O'Connor C. E., Hansen B. M. S., 2018, MNRAS, 477, 175

Orszag S. A., Tang C.-M., 1979, JFM, 90, 129

Osher S., Sethian J. A., 1988, J. Comput. Phys., 79, 12

Oskinova L. M., Hamann W.-R., Feldmeier A., 2007, A&A, 476, 1331

Owen J. E., Adams F. C., 2014, MNRAS, 444, 3761

Owocki S., 2004, EAS, 13, 163

Owocki S. P., Cohen D. H., 2006, ApJ, 648, 565

Owocki S. P., Sundqvist J. O., 2018, MNRAS, 475, 814

Owocki S. P., ud Doula A., 2004, ApJ, 600, 1004

Owocki S. P., Castor J. I., Rybicki G. B., 1988, ApJ, 335, 914

Owocki S. P., Cranmer S. R., Blondin J. M., 1994, ApJ, 424, 887

Owocki S. P., ud Doula A., Sundqvist J. O., Petit V., Cohen D. H., Townsend R. H. D., 2016, MNRAS, 462, 3830

Panagia N., Felli M., 1975, A&A, 39, 1

Pantolmos G., Matt S. P., 2017, ApJ, 849, 83

Parker E. N., 1958, ApJ, 128, 664

Petit V., et al., 2013, MNRAS, 429, 398

Petrovich C., Tremaine S., 2016, ApJ, 829, 132

Pillitteri I., Maggio A., Micela G., Sciortino S., Wolk S. J., Matsakos T., 2015, ApJ, 805, 52

Pittard J. M., 2009, MNRAS, 396, 1743

Pittard J. M., 2010, MNRAS, 403, 1633

Prinja R. K., Howarth I. D., 1988, MNRAS, 233, 123

Quirk J. J., 1994, InJNMF, 18, 555

Ramiaramanantsoa T., et al., 2017, MNRAS, 473, 5532

Reed W., Hill T., 1973, PANS

Runacres M. C., Owocki S. P., 2002, A&A, 381, 1015

Rybicki G. B., Lightman A. P., 1985, Radiative Processes in Astrophysics. John Wiley and Sons Ltd, `https://www.ebook.de/de/product/3635699/george_b_rybicki_alan_p_lightman_radiative_processes_in_astrophysics.html`

Ryu D., Jones T. W., Frank A., 2000, ApJ, 545, 475

Sairam L., Schmitt J. H. M. M., Dash S., 2018, MNRAS

Salz M., Czesla S., Schneider P. C., Schmitt J. H. M. M., 2016, A&A, 586, A75

Schaal K., Bauer A., Chandrashekar P., Pakmor R., Klingenberg C., Springel V., 2015, MNRAS, 453, 4279

Schmid-Burgk J., 1982, A&A, 108, 175

Schneiter E. M., Esquivel A., DÁngelo C. S. V., Velázquez P. F., Raga A. C., Costa A., 2016, MNRAS, 457, 1666

Schnurr O., Crowther P. A., 2008, in Hamann W.-R. e., Feldmeier A. e., Oskinova L. M. e., eds, Clumping in hot-star winds : proceedings of an international workshop held in Potsdam, Germany, 18. - 22. June 2007. p. 89

Schwartz J. C., Kashner Z., Jovmir D., Cowan N. B., 2017, ApJ, 850, 154

Seaquist E. R., Gregory P. C., 1973, Nature, 245, 85

Shaikhislamov I. F., Khodachenko M. L., Sasunov Y. L., Lammer H., Kislyakova K. G., Erkaev N. V., 2014, ApJ, 795, 132

Shkolnik E., Bohlender D. A., Walker G. A. H., Cameron A. C., 2008, ApJ, 676, 628

Shultz M., Wade G. A., Alecian E., Collaboration B., 2015, MNRASL, 454, L1

Slee O. B., Wilson W., Ramsay G., 2008, PASA, 25, 94

Smith G. R., Hunten D. M., 1990, Rev. Gp, 28, 117

Sobolev V. V., 1960, SA, 4, 372

Springel V., 2010, MNRAS, 401, 791

Stevens I. R., 1993, MNRAS, 265, 601

Stevens I. R., 1995, MNRAS, 277, 163

Stevens I. R., 2005, MNRAS, 356, 1053

Stevens I. R., Blondin J. M., Pollock A. M. T., 1992, ApJ, 386, 265

Stevenson D. J., 2003, Earth Planet Sci. Lett., 208, 1

Stone J. M., Gardiner T. A., Teuben P., Hawley J. F., Simon J. B., 2008, ApJS, 178, 137

Strugarek A., 2016, ApJ, 833, 140

Strugarek A., Brun A. S., Matt S. P., Réville V., 2014, ApJ, 795, 86

Strugarek A., Brun A. S., Matt S. P., Reville V., 2015a, PIAU, 11, 14

Strugarek A., Brun A. S., Matt S. P., Réville V., 2015b, ApJ, 815, 111

Sundqvist J. O., Owocki S. P., Puls J., 2018, A&A, 611, A17

Sánchez-Vizuet T., Solano M., 2018, arXiv:1712.04148v3

Tarango-Yong J. A., Henney W. J., 2018, MNRAS, 477, 2431

Teyssier R., 2002, A&A, 385, 337

Thum C., Neri R., Báez-Rubio A., Krips M., 2013, A&A, 556, A129

Tilley M. A., Harnett E. M., Winglee R. M., 2016, ApJ, 827, 77

Toro E. F., 2009, Riemann Solvers and Numerical Methods for Fluid Dynamics. Springer-Verlag GmbH, `https://www.ebook.de/de/product/3186408/eleuterio_f_toro_riemann_solvers_and_numerical_methods_for_fluid_dynamics.html`

Toro E. F., Spruce M., Speares W., 1994, SW, 4, 25

Townsend R. H. D., Owocki S. P., 2005, MNRAS, 357, 251

Townsend R. H. D., Owocki S. P., Ud-Doula A., 2007, MNRAS, 382, 139

Tremblin P., et al., 2017, ApJ, 841, 30

Treumann R. A., 2006, A&AR, 13, 229

Trigilio C., Leto P., Umana G., Buemi C. S., Leone F., 2011, ApJ, 739, L10

Tripathi A., Kratter K. M., Murray-Clay R. A., Krumholz M. R., 2015, ApJ, 808, 173

Turner J. D., Grießmeier J.-M., Zarka P., Vasylieva I., 2017, arXiv:1710.04997v1

Van Hoof P. A. M., Williams R. J. R., Volk K., Chatzikos M., Ferland G. J., Lykins M., Porter R. L., Wang Y., 2014, MNRAS, 444, 420

Van Loo S., Runacres M. C., Blomme R., 2004, A&A, 418, 717

Van Loo S., Runacres M. C., Blomme R., 2006, A&A, 452, 1011

Velasco-Romero D. A., Veiga M. H., Teyssier R., Masset F. S., 2018, MNRAS

Vidotto A. A., Jardine M., Helling C., 2010, ApJ, 722, L168

Vidotto A. A., Jardine M., Helling C., 2011, MNRAS, 414, 1573

Vidotto A. A., Fares R., Jardine M., Moutou C., Donati J.-F., 2015, MNRAS, 449, 4117

Vink J. S., de Koter A., Lamers H. J. G. L. M., 2000, A&A, 362, 295

Voronoi G., 1908, JM, 1908

Wade G. A., et al., 2013, PIAU, 9, 265

Wade G. A., et al., 2015, ASPC, 494, 30

Wade G. A., et al., 2016, MNRAS, 456, 2

Walder R., Folini D., Meynet G., 2012, SSRev, 166, 145

Weber E. J., Davis L. J., 1967, ApJ, 148, 217

Weber C., et al., 2017, MNRAS, 469, 3505

White C. J., Stone J. M., Gammie C. F., 2016, ApJS, 225, 22

Wilkin F. P., 1996, ApJ, 459

Williams P. K. G., 2017, arXiv:1707.04264v1

Williams P. M., van der Hucht K. A., Sandell G., The P. S., 1990, MNRAS, 244, 104

Wise A. W., Dodson-Robinson S. E., 2018, ApJ, 855, 145

Wright A. E., Barlow M. J., 1975, MNRAS, 170, 41

Wright J. T., Gaudi B. S., 2012, in , Planets, Stars and Stellar Systems. Springer Netherlands, pp 489–540

Wright A. E., Fourikis N., Purton C. R., Feldman P. A., 1974, Nature, 250, 715

Xia C., Teunissen J., Mellah I. E., Chané E., Keppens R., 2018, ApJS, 234, 30

Yadav R. K., Thorngren D. P., 2017, ApJ, 849, L12

Zanotti O., Fambri F., Dumbser M., Hidalgo A., 2015, arXiv:1412.0081

Zarka P., 1998, JGR, 103, 20159

Zarka P., 2007, PSS, 55, 598

Zhang M., et al., 2018, AJ, 155, 83

ud-Doula A., Owocki S. P., 2002, ApJ, 576, 413

ud-Doula A., Owocki S. P., Townsend R. H. D., 2008, MNRAS, 385, 97

ud-Doula A., Owocki S. P., Townsend R. H. D., 2009, MNRAS, 392, 1022

ud-Doula A., Sundqvist J. O., Owocki S. P., Petit V., Townsend R. H. D., 2013, MNRAS, 428, 2723

ud-Doula A., Owocki S. P., Kee N. D., 2018, MNRAS